

# **Optical measurements for quality control in photodynamic therapy**

Paulo Rodrigues Bargo

B.S., Electrical Engineering, Instituto Nacional de Telecomunicacoes – Brazil (1992)

M.S., Electrical Engineering, Universidade do Vale do Paraiba – Brazil (1995)

A dissertation submitted to the faculty of the  
OGI School of Science and Engineering  
at Oregon Health & Science University  
in partial fulfillment of the  
requirements for the degree  
Doctor of Philosophy  
In  
Electrical and Computer Engineering

July 2003

The dissertation “Optical measurements for quality control in photodynamic therapy” by Paulo Rodrigues Bargo has been examined and approved by the following Examination Committee:

---

Steven L. Jacques  
Professor  
Thesis Research Advisor

---

Scott A. Prahl  
Assistant Professor

---

J. Fred Holmes  
Professor Emeritus

---

Rodger A. Slevin  
Medical Doctor  
Providence Health Systems

Michael W. Macon  
Assistant Professor  
Posthumous

## **Dedication**

To my wife, Leda, for she is my beloved accomplice.

To my children, Laura and Felipe, for they are my dearest and greatest creation.

To my parents, Amador and Maria, for they are my trusty mentors.

## Acknowledgements

First, I would like to thank my advisor, Professor Steven L. Jacques. Steve always encouraged me since I informed him about my interest in coming to OGI in 1997. He taught me how to perform my best and to be independent. He also taught me how to conduct good research, how to interpret results and draw the right conclusions, and how to present them adequately. My career success will rest in these gifts. I also thank Professor Scott A. Prahl, who I also regard as my advisor. His patience and willingness to help were invaluable. My gratitude to Scott cannot be expressed enough in these words, for his door was always opened. By combining the two outstanding, but very distinct points of view and philosophies from Steve and Scott I earned a very balanced education that is by far greater than all the knowledge I had when I first came to Portland. This work could not have been done without their help and guidance.

I would also like to acknowledge Dr. Kenton W. Gregory, the Director of the Oregon Medical Laser Center, where I conduct my research, for providing me the facilities and the opportunity to work in a great environment with excellent researchers. Also, I would like to thank all the OMLC present and past staff. They contributed in many different ways to my success in this endeavor, by helping with administrative needs, or giving tips on how to operate equipment or sharing their knowledge or by just sharing a smile. Your names are carved in my heart. Particularly, I would like to thank nurse coordinator Teresa Goodell for her help in recruiting patients for this study and her work on the PDT program. The clinical application is one of the aspects of my work that I am most proud of, and would not have happened without her support. In this same lines I would like to thank the doctors that performed the clinical procedures. Doctors Rodger A. Slevin, Gregory P. Blair, George Koval, Peter E. Andersen and Douglas A. Shumaker thank you for your excellent work and for allowing/trusting me to use my gadgets in your patients. Special thanks to doctor Slevin who stepped up in the last minute to be part of

my committee and had to give up office hours to accommodate my thesis presentation in his tight schedule. My gratitude to all Providence St. Vincent staff. Special thanks go to the staff at the endoscopy and bronchoscopy departments. None of the clinical work would be done without the patients and their relatives generosity and willingness to help. My most heartfelt thanks for consent in participating in this study.

Living in the same boat and fighting the same battles were my fellow students, who I regard as my brothers and sisters. Former student now Dr. John A. Viator was the first person I meet when I came to Portland. He helped me to establish my career goals, lent me his books and always provided good pie. Jessica was always the perfect listener to my frustrations, as she understood them so well. She was also very easy to annoy which was a great relaxing therapy. I wouldn't finish my thesis on time without her help typing the thesis. I would like to thank Ted for all our discussions, particularly the ones about the Blazers. I also thank the other students Rob, Abe, Kirstin, Yin-Chu, Deb, Dan, Jon, Li and Laurel. Thank you for your friendship.

I must thank the faculty and staff at OGI, in particular those from the Electrical and Computer Engineering Department, Biochemistry and Molecular Biology Department, Library and Registrar Office for their excellence in performing their jobs. My deepest thank to Professors Fred Holmes and Mike Macon for being members of my thesis committee. I would like to thank Professor Casperson from Portland State University for the outstanding course on Laser Principles, the best course I had during my graduate studies. Also, I would like to thank my former professors and friends at Universidade do Vale do Paraiba, Brazil. Their support was essential for the awarding of my scholarship.

I must thank CAPES – Ministry of Education, Brazil for my graduate studies scholarship. I also thank the support by the Collins Foundation and the NIH EB00224.

I thank all my friends who supported me in so many ways, including Helvio, Daniela and their daughters, Henrique and Sonia, Ilka and Yazid, Patrick, Andre and Adriana. Last, but not least, I thank my wife, my children, my parents and my family for their support, kindness and for believing in me. I love you very much.

# Contents

<b>Dedication</b> .....	iii
<b>Acknowledgements</b> .....	iv
<b>Abstract</b> .....	xx
<b>1 Introduction</b> .....	1
1.1 Motivation .....	4
1.2 PDT dosimetry .....	5
1.2.1 The basics of PDT dosimetry .....	5
1.2.2 How blood perfusion influences the depth of PDT treatment .....	8
1.2.3 How photosensitizer fluorescence predicts photosensitizer concentration ..	10
1.3 The current state of PDT dosimetry .....	13
1.3.1 Drug concentration measurements .....	13
1.3.2 Optical penetration depth .....	14
1.4 Goals .....	16
<b>2 PDT efficiencies for photooxidation of substrate using a photosensitizer</b> .....	19
2.1 Introduction .....	19
2.2 Materials and Methods .....	20
2.3 Results .....	22
2.3.1 Background Experiments .....	22
2.3.2 Kinetics of Oxidation .....	24
2.3.3 Photobleaching .....	28
2.4 Discussion .....	29
2.4.1 Comparison between NADPH photo-oxidation and Photofrin fluorescence in different solvents .....	29
2.4.2 Determining the quantum yield of interaction .....	30
2.4.3 Population of oxidizable sites .....	32
2.5 Conclusion .....	34
<b>3 Collection efficiency of a single optical fiber in turbid media</b> .....	35
3.1 Introduction .....	35
3.2 Theory .....	36
3.3 Materials and Methods .....	41
3.3.1 Acrylamide Gel Optical Phantoms .....	41

3.3.2 Single fiber Reflectance Measurements .....	41
3.3.3 Monte Carlo Simulations.....	46
3.4 Results.....	47
3.5 Discussion .....	56
<b>4 Optical properties effects upon the collection efficiency of optical fibers .....</b>	<b>61</b>
4.1 Introduction .....	61
4.2 Material and Methods .....	64
4.2.1 Optical Phantoms Preparation and Calibration .....	64
4.2.2 Reflectance Measurements and Analysis .....	65
4.2.3 Monte Carlo simulations .....	66
4.3 Results.....	69
4.4 Discussion .....	74
4.5 Conclusions .....	76
<b>5 <i>In vivo</i> determination of optical penetration depth and optical properties.....</b>	<b>78</b>
5.1 Introduction .....	78
5.2 Theory.....	80
5.3 Material and Methods .....	83
5.3.1 Probe preparation.....	83
5.3.2 Reflectance measurements .....	84
5.3.3 Empirical forward light transport model.....	86
5.3.3.1 Preparation and calibration of the tissue phantom gel matrix.....	87
5.3.3.2 Probe calibration.....	93
5.3.4 Modeling of tissue reflectance with the empirical/spectral model .....	98
5.3.5 Validation of the model.....	102
5.3.6 Patients .....	104
5.4 Results.....	105
5.4.1 Bovine muscle <i>in vitro</i> .....	105
5.4.1 Human tissue <i>in vivo</i> .....	106
5.5 Discussion .....	123
<b>6 Determination of drug concentration and photodynamic dose .....</b>	<b>127</b>
6.1 Introduction .....	127
6.2 Theory .....	131
6.2.1 Determination of photosensitizer concentration from fluorescence .....	131
6.2.2 Determination of oxidizing radicals .....	133
6.3 Material and Methods .....	134
6.3.1 Fluorescence measurements .....	134
6.3.2 Experimental validation of the model .....	135
6.3.3 Patients .....	137
6.3.4 Patient measurements .....	138
6.3.5 Fluorescence Analysis .....	138
6.3.6 Fluorescence Monte Carlo code .....	140

6.3.7 Calculating drug concentration from the measured fluorescence .....	144
6.4 Results .....	146
6.4.1 Tests of the Monte Carlo code .....	146
6.4.2 Validation of model with phantoms .....	148
6.4.3 Results from patient measurements .....	149
6.5 Discussion .....	156
6.6 Conclusion.....	159
<b>7 General discussion and conclusions .....</b>	<b>161</b>
7.1 Photochemical assay for determination of quantum efficiency of oxidation.....	162
7.2 Collection efficiency of a single optical fiber .....	162
7.3 Collection efficiency of multiple fibers .....	163
7.4 Determination of optical properties with reflectance spectroscopy .....	163
7.5 Determination of drug concentration and photodynamic dose <i>in vivo</i> .....	164
<b>Appendix A: Calibration of stock solutions.....</b>	<b>166</b>
A.1 Stock solutions and chapters 3 and 5 .....	166
A.2 Stock solutions and chapters 4 and 6 .....	167
<b>Appendix B: Matlab code to determine coefficients <math>C_1</math>, <math>C_2</math> and <math>L_1</math> .....</b>	<b>169</b>
<b>Appendix C: Study consent form.....</b>	<b>175</b>
<b>Bibliography .....</b>	<b>179</b>
<b>Biographical Note .....</b>	<b>190</b>

## List of Tables

5.1	Coefficients of the polynomial fits to $C_1$ , $L_1$ and $C_2$ at 630 nm.....	98
5.2	Values of $a$ , $b$ , $f_v$ , $SO_2$ , $A$ , $B$ and optical properties at 630 nm for normal sites of non-PDT patients.....	111
5.3	Values of $a$ , $b$ , $f_v$ , $SO_2$ , $A$ , $B$ and optical properties at 630 nm for normal sites of non-PDT patients.....	112
5.4	Values of $a$ , $b$ , $f_v$ , $SO_2$ , $A$ , $B$ and optical properties at 630 nm for tumor sites of non-PDT patients.....	113
5.5	Mean and standard deviations for $f_v$ , $SO_2$ , and $a$ , $s'$ and $\delta$ at 630 nm. PDT patient data exclude measurements in skin (see text).....	122
6.1	Composition of optical phantoms.....	136
6.2	Optical properties of phantoms at excitation (440 nm) and emission (630 nm) wavelengths.....	137
6.3	Results for Monte Carlo code tests. Absorption and scattering coefficients are in $cm^{-1}$ . Reflectance results for the Monte Carlo code are compared to the adding-doubling (AD) method. Fluorescence results for the Monte Carlo code are compared to Eq. 6.8. The parameter $g$ is the average cosine or anisotropy index of refraction of the sample (ns).....	147
6.4	Fluorescence scores and rhodamine concentration for tissue phantoms. The standard deviation for measured concentration was $\pm 0.3$ and $\pm 0.05$ g/ml for the absorbing-only samples and the scattering samples respectively.....	148
6.5	Mean and standard deviation of normal and tumor sites fluorescence scores at 630 nm ( $FS_{630}$ ) and of normal and tumor sites drug concentration. ....	151

## List of Figures

1.1 Mechanism of Photodynamic therapy. Light excites photosensitizer dye molecules that react with oxygen molecules to produce singlet oxygen radicals or other oxidizing species. If oxidative damage to essential cell targets (e.g., mitochondria) exceeds a critical threshold, the cell dies.....	2
1.2 PDT window. Light exposure and drug concentration should be above a critical threshold to achieve necrosis at a given depth. Too much drug leads to dark toxicity. Too much light leads to drug photobleaching. Curves were calculated rearranging Eq. 1.1 and plotting the drug concentration as a function of light dose ( $E_0 t$ [ $J/cm^2$ ]). Other parameters were assumed: $\delta = 0.25$ cm, $\epsilon = 3$ $cm^{-1}$ (mg/ml) $^{-1}$ , $\lambda = 630$ nm, $c = 3 \cdot 10^8$ m/s, $h = 6.6 \cdot 10^{-34}$ J s, $k = 3$ , $R_{th} = 10^{18}$ ph/g [13] and $\Phi_{ox} = 1$ . Data for patient #E6 (same as Fig. 1.3) is also shown. Photobleaching and dark toxicity levels are qualitative only.....	3
1.3 Optimal PDT outcome. Patient with an early stage adenocarcinoma nodule was treated using the standard FDA approved PDT protocol. Pictures were taken before, 2 days after and 3 weeks after treatment. ....	4
1.4 Theoretical example of how the blood perfusion changes the tissue optical penetration depth. The volume fraction of blood in the tissue is varied from 0.1-12%. ....	9
2.1 Experimental setup for irradiation (step 1), fluorescence (step 2) and absorbance (step 3).....	21
2.2 Control experiment shows no change in NADPH absorbance during irradiation by light over 90 minute period.....	23
2.3 Kinetics of photo-oxidation of NADPH by Photofrin in solution with and without sodium azide (a singlet oxygen scavenger). Photobleaching of Photofrin is shown in the bottom curve. [NADPH] = 1mM. [Photofrin] = 50mM. [sodium azide] = 5mM.....	24

2.4	Typical decay in absorbance at 340 nm due to oxidation of NADPH. Data fitted to a decaying exponential.....	27
2.5	Quantum yield of oxidation of NADPH by Photofrin in TRIZMA and MeOH solutions. Curve fit is an exponential approximation for the diffusion of the singlet oxygen. Error bars are the standard deviations of three measurements and are shown for all points, but are smaller than the symbols in some cases.....	28
2.6	Fluorescence spectra of Photofrin in two different solvents (a) MeOH and (b) TRIS buffer.....	29
2.7	Jablonski diagram of the oxidation of NADPH by PDT. Laser light with energy $h\nu$ excites the photosensitizer molecule to excited state $S_2$ . A fraction $\phi_T$ of the energy undergo intersystem crossing to triplet state $T_2$ . The remaining energy will become heat or fluorescence with energy $h\nu'$ . Energy in triplet state will either phosphoresce with energy $h\nu''$ or transfer to another molecule. A fraction $\phi$ will transfer to oxygen molecules producing singlet oxygen $^1O_2$ . A fraction $f_R$ of the singlet oxygen molecules oxidizes NADPH to $NADP^+$ .....	31
3.1	Diagram of the possible return paths of light incident from a single optical fiber. Light that reaches the fiber face with an angle smaller than the half angle of the acceptance cone will be guided through the fiber to the detector ( $R_{core}$ ). Light that reaches the fiber face with an angle greater than the half angle of the acceptance cone will escape through the fiber cladding ( $R_{clad}$ ). $R_{air}$ is the light that leaves the tissue outside the fiber and $r_{sp}$ is the Fresnel reflection due to the fiber/tissue index of refraction mismatch. Light can also be absorbed by the tissue.....	38
3.2	Diagram of the single optical fiber reflectance system. A single 600 m optical fiber is connected to the distal end of a bifurcated fiber bundle composed of two 300 m optical fibers. One fiber has the proximal end connected to a tungsten-halogen white lamp and the other is connected to a spectrophotometer. The distal end of the 600 m optical fiber is placed in contact with the gel samples through a drop of water. OD filters are used to avoid detector saturation.....	42
3.3	Setup of the integrating sphere experiment. White light guided through a 600 m optical fiber positioned 5 mm away from the sample surface is used to illuminate a 3-mm diameter spot on the sample. Diffuse reflectance from the sample is trapped in an 8"-dia. integrating sphere. Light is collected by an optical fiber positioned at a 1/4" diameter port of the sphere and guided to a spectrophotometer. Spectralon standards are used to calibrate the diffuse reflectance from the samples.....	45

- 3.4 Fraction of collected light ( $f_{\text{core}}$ ) determined by Monte Carlo (empty symbols) and experiments (filled symbols) for three  $s'$  ( $\diamond = 7$ ,  $\square = 14$ , and  $O = 28 \text{ cm}^{-1}$ ) and six  $a$  (0.01, 0.1, 0.4, 0.9, 2.5 and  $4.9 \text{ cm}^{-1}$ , greater  $a$  to the left). The fiber diameter was  $600 \text{ m}$  and the numerical aperture was 0.22.  $f_{\text{core}}$  [dimensionless] is plotted as a function of the dimensionless parameter  $X = \delta \cdot \text{mfp}'/d^2$ , where  $d$  is fiber diameter,  $\delta = (3 a(a+s'))^{-1/2}$  and  $\text{mfp}' = 1/(a+s')$ . Vertical lines are the standard deviation of the data for three measurements. .... 48
- 3.5 Comparison between the experimental and theoretical (Monte Carlo) values for  $f_{\text{core}}$ . Symbols  $\diamond$ ,  $\square$ , and  $O$  represent reduced scattering coefficient of 7, 14 and  $28 \text{ cm}^{-1}$  for six  $a$  (same as figure 3.4). .... 49
- 3.6 (A) Monte Carlo simulations of  $f_{\text{core}}$  for three optical fiber diameters  $200 \text{ m}$  ( $O$ ),  $600 \text{ m}$  ( $\square$ ) and  $2000 \text{ m}$  ( $\diamond$ ), for  $s'$  of  $10 \text{ cm}^{-1}$  (empty symbols) and  $20 \text{ cm}^{-1}$  (filled symbols) and for  $a$  ranging from 0.01 to  $50 \text{ cm}^{-1}$ . The solid line is hyperbolic tangent function that follows the form  $f_{\text{core}} = C(1 - (1 + \tanh(A(\ln(X)+B)))/2)$ . For a fiber  $\text{NA} = 0.39$  and the above range of optical properties  $A = 0.278$ ,  $B = 1.005$  and  $C = 0.0835$ . (B) Same data of Fig. 3.6.A for  $s'$  of  $10 \text{ cm}^{-1}$  (empty symbols) plotted against the reduced mean free path ( $\text{mfp}'$ ) for comparison. .... 51
- 3.7 (A) Plot of Monte Carlo simulations of the collected light as a function of the collection angle bin ( $\theta$ ) for three  $s'$  ( $70$ ,  $10$  and  $1 \text{ cm}^{-1}$ , top to bottom) and  $a$  of  $0.05 \text{ cm}^{-1}$ . Dashed lines are proportional to  $\cos(\theta)\sin(\theta)$  (see eq. 3.10 in discussion) and show the similarities of the data to this simple expression for higher scattering and the differences for low scattering. (B) Integral of figure 3.7.A over  $\theta$ , representing the fraction of the total incident light that couples to the fiber core ( $R_{\text{core}}$  for a given angle). The dashed line is proportional to  $\sin^2(\theta)$  (see text). The dotted line at  $\theta = 15$  degrees and  $R_{\text{core}} = 0.0266$  for  $s' = 70 \text{ cm}^{-1}$  correspond to a  $600\text{-m}$ -dia optical fiber with  $\text{NA} = 0.22$ . .... 52
- 3.8 Monte Carlo simulations of the collection efficiency  $\eta_c$  for a fiber diameter of  $600 \text{ m}$  immersed in a medium with index of refraction of 1.35. (A)  $\eta_c$  as a function of  $s'$  and (B)  $\eta_c$  as a function of  $a$  for  $\text{NA} = 0.39$  (acceptance angle of  $16.8^\circ$ ). (C)  $\eta_c$  as a function of  $s'$  and (D)  $\eta_c$  as a function of  $a$  for  $\text{NA} = 0.22$  (acceptance angle of  $9.38^\circ$ ). Values of  $\eta_c$  equal 0.0835 (A and B) and 0.0266 (C and D) are shown for comparison with equation 3.10 (see text). .... 53

3.9 (A) Collection efficiency $\eta_c$ determined by Monte Carlo simulations for anisotropies of 0.9 (O) and 0.95 ( $\square$ ) plotted as a function of the $\eta_c$ for anisotropy of 0.83. (B) $f_{\text{core}}$ determined by Monte Carlo simulations for anisotropies of 0.9 (O) and 0.95 ( $\square$ ) plotted as a function of $f_{\text{core}}$ for anisotropy of 0.83. $\mu_a$ ranged from 0.5 to 5 $\text{cm}^{-1}$ and $\mu_s'$ from 1 to 20 $\text{cm}^{-1}$ . Fiber diameter was 600 $\mu\text{m}$ and NA = 0.39.....	54
3.10(A) Collection efficiency $\eta_c$ determined by Monte Carlo simulations as a function of the angular distribution of the launched photons. (B) $f_{\text{core}}$ determined by Monte Carlo simulations as a function of the angular distribution of the launched photons. NA of collection was fixed to 0.39. Data for absorption coefficient of 1 $\text{cm}^{-1}$ , reduced scattering coefficients of 5 $\text{cm}^{-1}$ (empty symbols) and 40 $\text{cm}^{-1}$ (filled symbols), and the optical fiber diameters of 200 $\mu\text{m}$ (O), 600 $\mu\text{m}$ ( $\square$ ) and 2000 $\mu\text{m}$ ( $\diamond$ ).....	55
4.1 Diagram of the possible return paths of light in a 2-fiber configuration. Light that reaches the fiber face with an angle smaller than the half angle of the acceptance cone will be guided through the fiber to the detector ( $R_{\text{core}}$ ). Light that reach the fiber face with an angle greater than the half angle of the acceptance cone will escape through the fiber cladding ( $R_{\text{clad}}$ ). $R_{\text{air}}$ is the light that leaves the tissue outside the fiber and $r_{\text{sp}}$ is the Fresnel reflection due to the fiber/tissue index of refraction mismatch. Light can also be absorbed by the tissue. ....	63
4.2 Diagram of the experimental setup. A single 600 $\mu\text{m}$ optical fiber is connected to a tungsten-halogen white lamp and the other is connected to a spectrophotometer. The space between the fibers is 2.5 mm. Fiber tips are aligned at the same depth 1.5 cm inside the sample. OD filters are used to avoid detector saturation.....	65
4.3 Normalized upward flux as a function of the absorption coefficient. The reduced scattering coefficients at 633 nm were 4, 8 and 17 $\text{cm}^{-1}$ (top to bottom). Vertical lines for the experiment and for the MC-diffusion model are the standard deviation of 5 measurements.....	69
4.4 Collection efficiency ( $\eta_c$ ) determined by Monte Carlo simulations plotted as a function of optical properties for a 2-fibers configuration embeded in a infinite medium. These values were used to modify the diffusion model into the MC-diffusion model shown in figure 4.3. Error bars are the standard deviation of 5 Monte Carlo runs with different random number seeds. The separation between the source and collection fibers was 2.5 mm, fiber diameters were 600 $\mu\text{m}$ and the NA was 0.39.....	70

4.5 Comparison between the collection efficiency determined by Monte Carlo simulations for 2 fibers in contact to an infinite medium with no boundaries (empty symbols), 2 fibers in contact to a semi-infinite medium with an air/medium boundary (filled symbols) and a multiple fiber probe with a central source fiber surrounded by an annular detection ring placed on the surface of a semi-infinite medium with air/medium boundary (doubled symbols). Data for the infinite medium configuration are plotted artificially skewed of $-0.2 \text{ cm}^{-1}$ and data for the multiple fiber probe are plotted artificially skewed of $+0.2 \text{ cm}^{-1}$ to help visualization. Error bars are the standard deviation of 5 Monte Carlo runs. The separation between the source and collection fibers was 2.5 mm, fiber diameters were 600 $\mu\text{m}$ and the NA was 0.39.....	71
4.6 Collection efficiency determined by Monte Carlo simulations as a function of optical fiber separation for the multiple fiber probe with a central source fiber surrounded by an annular detection ring placed on the surface of a semi-infinite medium with air/medium boundary. Fig. 4.6.A is the special case of a single fiber used as source and detector. Drawings on top of the figures represent a front view of the face of the probes.....	72
4.7 Influence of the diameter of the collection optical fiber on $\eta_c$ determined for the multiple fiber probe configuration. The source fiber was kept with a diameter of 600 $\mu\text{m}$ , separation between the source and collection fibers was 2.5 mm and the NA was 0.39. Values of $\eta_c$ for $s'$ of $2.5 \text{ cm}^{-1}$ (empty symbols) and for $s'$ of $10 \text{ cm}^{-1}$ (filled symbols) are shown. Error bars are the standard deviation of 5 Monte Carlo runs and in most cases are smaller than the symbols. ....	73
4.8 Collection efficiency plotted as a function of numerical aperture of commercially available optical fibers (NA = 0.22, 0.39 and 0.48). The numerical apertures were corrected by the refractive index of the medium ( $n_{\text{sample}} = 1.335$ ) to account for the effective cone of collection of the optical fiber. Dashed lines are the values obtained from Eq. 4.8 (in discussion section) for the corrected NAs. Fiber diameter was 600 $\mu\text{m}$ and fiber separation was 2.5 mm. ....	74
5.1 Comparison of diffusion analytical solution and Monte Carlo simulations of the spatially resolved radiative transport. White circles: $n_{\text{fiber}} = 1$ , all escaping light detected. Black circles: $n_{\text{fiber}} = 1.45$ , all escaping light detected. Black diamonds: $n_{\text{fiber}} = 1.45$ , but only light collected within numerical aperture of fiber is detected.....	82

5.2	Two-fiber probe for reflectance measurements. A 45°-polished steel mirror directs source light from one 600 μm optical fiber 90° out the side of the fiber and a second mirror and fiber collect light for detection. Source-collector separation is 2.5 mm. Probe is passed through working channel of endoscope .....	84
5.3	Reflectance system setup. Light from a tungsten lamp is guided through an optical probe (see probe preparation). Reflectance spectra is acquired with a spectrophotometer and recorded in a laptop.....	85
5.4	Typical reflectance raw data for normal (3 sites), tumor (3 sites) and Intralipid .....	86
5.5	Picture of the 8x8 acrylamide gel matrix. Rows from top to bottom have final Intralipid concentrations of 7, 5, 3.5, 2.5, 1.5, 1.0, 0.5 and 0.25%. Columns from left to right have final absorption coefficients at 630 nm of 0.01, 0.1, 0.4, 0.9, 1.6, 2.5, 4.9 and 6.4 cm <sup>-1</sup> . All samples have 18% acrylamide gel concentration (see text for detail) and a final volume of 100 ml.....	88
5.6	Setup of the integrating sphere used for calibration of the acrylamide samples. White light from a tungsten halogen lamp is guided through an 600-m-diameter optical fiber positioned 5 mm away from the sample, inside the integrating sphere, forming a 3-mm diameter spot. Reflectance spectra is detected through an 600- m-diameter optical fiber with a diode array spectrophotometer. Spectralon standards are used to calibrate the reflectance measurements.....	89
5.7	Flow Chart of the minimization process to determine the Intralipid absorption coefficient ( $a_0$ ) and the reduced scattering coefficient ( $s'$ ) for each wavelength $\lambda_j$ and for each Intralipid concentration. The samples with five lowest dilutions of ink ( $i = 1$ to 5) were used to determined $a_0$ and $s'$ . Least square minimization is performed between the reflectance calculated with adding-doubling and the reflectance experimentally measured. ....	90
5.8	A. Setup for the collimated transmission measurements. Light from a 543 nm He-Ne laser is shined onto a 150 mm thick glass cuvette containing the Intralipid sample. A 1-cm-diameter silica detector coupled to a pico-ampmeter and positioned 80 cm away from the cuvette is used for detection of the collimated transmitted light. The iris positioned in front of the detector limited the detection to a 5 mm diameter spot. A 2-mm-diameter iris was positioned between the laser and the sample to prevent any non-coherent light from reaching the sample. ....	91

5.9. A) Scattering coefficient of 1, 2, 5, 7 and 20% Intralipid solution determined from collimated transmission at 543 nm. Experimental setup is showed in figure 5.8.....	92
5.9 B) Measurement of light detected by the 1-cm-diameter silica detector with a 5 mm aperture iris translated perpendicularly to the collimated beam in steps of 5 mm for a 20% Intralipid concentration sample. The collimated transmission is approximately 500-fold greater than the diffused light measured by the detector.....	92
5.10 Reduced scattering coefficient determined from integrating sphere measurements for 7, 5, 3.5, 2.5, 1.5, 1.0 0.5 and 0.25% Intralipid-acrylamide-gel samples.....	93
5.11 Making of the light transport maps used as forward model for the reflectance measurements. This is an example for one wavelength (630 nm). (A) Log base 10 of the normalized measurement $M$ for the 64 samples at 630 nm displayed in a grid of absorption and reduced scattering coefficient. (B) Linear interpolation of the 8 data points with the lowest $a$ in figure A. (C) Log base 10 of the normalized measurement obtained from the linear interpolation in figure B. The point highlighted inside the white box are shown in figure D. (D) Exponential fit according to Eq. 5.8 of data highlighted in figure C. The bottom red curve and symbols represent Eq. 5.8. The data points with coefficient $C_2$ subtracted are shown for comparison. (E) Light transport map at 630 nm constructed with the coefficients shown in Fig.5.12. and Eq. 5.8. ....	96
5.12 Coefficients $C_1$ , $L_1$ and $C_2$ used to reconstruct the map on Fig. 5.11.E (630 nm). The coefficients were fitted to polynomials (lines) to speed the calculation of the light transport (see text).....	97
5.13 Spectra of tissue chromophores used in Eq. 5.9 .....	100
5.14 Data from Fig. 5.4 normalized by the measurement $M_{std}$ as an example of the normalization given by Eq.5.7.....	101
5.15 Reduced scattering ( $\mu'_s$ , top) and absorption ( $\mu_a$ , bottom) coefficients determined for bovine muscle determined by the empirical/spectral model (diamonds) in comparison to the optical properties determined by the wavelength-by-wavelength model described in section 5.3.5 (circles). (A) Average and standard deviations for three different sites measured at one sample. (B) Average and standard deviations for all sites measured (three sites per sample for three different samples).....	106

5.16 A) Normalized data for normal site 1, patient #E6 (same as Fig. 5.14) in comparison to the predicted values (circles) determined using the fitted parameters $a$ , $b$ , $f_v$ , $SO_2$ , $A$ and $B$ shown, and Eqs. 5.8, 5.9, 5.10 and 5.11. Bottom curves show the percentage residual errors [(predicted-measured)/measured times 100%]. Bloodless tissue curves are shown in black dashed lines, based on setting the factor $f_v$ equal to zero for $a$ in Eq. 5.9.....	107
5.16 B) Same as Fig. 5.16.A for normal site 2, patient #E6 .....	107
5.16 C) Same as Fig. 5.16.A for normal site 3, patient #E6.....	108
5.16 D) Same as Fig. 5.16.A for tumor site 1, patient #E6.....	108
5.16 E) Same as Fig. 5.16.A for tumor site 2, patient #E6. The system was not able to record data bellow 600 nm because of the blood absorption in that spectral range. Only data above 600 nm was used for fitting. Values of $a$ , $b$ and $B$ were assumed to be the same of those for tumor site 1 in Fig. 5.16.D (see text).....	109
5.16 F) Same as Fig. 5.16.E for tumor site 3, patient #E6.....	109
5.17 A) Optical properties of three normal sites from patient #E6. (Top) Reduced scattering coefficient. (Bottom) Absorption coefficient.....	114
5.17 B) Optical properties of three tumor sites from patient #E6. (Top) Reduced scattering coefficient. (Bottom) Absorption coefficient. Identical reduced scattering coefficients are obtained for all three tumor sites (see text).....	114
5.18 A) Fraction of whole blood for normal esophageal tissue of non-PDT (patient #N1-N9) and PDT patients (patients #E6-E9).....	115
5.18 B) Blood oxygen saturation for normal esophageal tissue of non-PDT (patient #N1-N9) and PDT patients (patients #E6-E9).....	116
5.18 C) Reduced scattering coefficient ( $\mu'_s$ ) at 630 nm for normal esophageal tissue of non-PDT (patient #N1-N9) and PDT patients (patients #E6-E9).....	116
5.18 D) Absorption coefficient ( $\mu_a$ ) at 630 nm for normal esophageal tissue of non-PDT (patient #N1-N9) and PDT patients (patients #E6-E9).....	117
5.18 E) Optical penetration depth ( $\delta$ ) at 630 nm for normal esophageal tissue of non-PDT (patient #N1-N9) and PDT patients (patients #E6-E9).....	117

5.19 A) Fraction of whole blood for normal (O) and tumor (V) sites of esophageal, lung, oral cavity and skin PDT patients. ....	118
5.19 B) Blood oxygen saturation for normal (O) and tumor (V) sites of esophageal, lung, oral cavity and skin PDT patients. ....	118
5.19 C) Reduced scattering coefficient ( $\mu_s'$ ) at 630 nm for normal (O) and tumor (V) sites of esophageal, lung, oral cavity and skin PDT patients. ....	119
5.19 D) Absorption coefficient ( $\mu_a$ ) at 630 nm for normal (O) and tumor (V) sites of esophageal, lung, oral cavity and skin PDT patients. ....	119
5.19 E) Optical penetration depth ( $\delta$ ) at 630 nm for normal (O) and tumor (V) sites of esophageal, lung, oral cavity and skin PDT patients.....	120
5.20 Histograms of optical penetration depth at 630 nm of the esophageal screening and soft-tissue PDT patients. Data is also presented in Figs. 5.18.E and 5.19.E.....	121
6.1 Relation between relative fluorescence intensities (F.I.) and drug concentration in a clear medium. (TOP) Spectra of increasing concentration of photofrin in aqueous solution. (BOTTOM) Peak fluorescence at 630 nm as a function of photosensitizer concentration.....	128
6.2 Photographs of fluorescence of Photofrin from three different media. In a clear medium (left) excitation light goes through the sample and emission comes as a line from across the sample. In a turbid medium (center) excitation light creates a diffusion glow ball at the sample. In a turbid/absorbing medium (right) the fluorescence glow ball is decreased in size and intensity due to the absorption of excitation and emission light.....	129
6.3 Fluorescence system setup. A nitrogen pumped dye laser excites tissue fluorescence, which is collected through the same, disposable, 600- m core diameter optical fiber and detected with an OMA system. ....	135
6.4 Typical <i>in vivo</i> fluorescence raw data from normal and tumor tissue. Thin black curves are a fit of the data by one side of a Gaussian curve that represents the background tissue autofluorescence.....	138
6.5 Typical <i>in vivo</i> photosensitizer fluorescence spectrum for normal and tumor tissue after subtraction of tissue autofluorescence.....	140
6.6 Extinction coefficient ( $\epsilon$ ) of Photofrin diluted in water. $\epsilon_{440} = 10.8$ [ $\text{cm}^{-1}$ ( $\text{mg/ml})^{-1}$ ] from figure.....	146

6.7 Dependence of the lumped parameter $\eta_c\chi$ with the ratio between the absorption coefficient of the fluorophore and the total absorption coefficient at excitation.....	148
6.8 Comparison between normalized fluorescence for normal tissue of PDT (solid line) and non-PDT (dashed line) patients. ....	149
6.9 Example of the conversion of fluorescence scores into drug concentration for one patient. LEFT: fluorescence score for normal and tumor sites of patient #E6. CENTER: fluorescence score after correction by the light transport factor and the fiber field of view ( $\eta_c\chi$ ). RIGHT: drug concentration <i>in situ</i> .....	150
6.10 A) Fluorescence scores for all patients.....	152
6.10 B) Corrected fluorescence for all patients. Measurements of the optical properties of the first 5 esophageal and first lung patient were not possible due to the configuration of the previous reflectance probe hence data points for these patients are not shown.....	152
6.10 C) Drug concentration for all patients. Measurements of the optical properties of the first 5 esophageal and first lung patient were not possible due to the configuration of the previous reflectance probe hence drug concentrations for these patients are not shown. ....	153
6.11 Distribution of logarithm of drug concentration for normal and tumor tissue sites from Fig.6.10.C. The log of the concentration is used because the values span more than two orders of magnitude. ....	154
6.12 Photodynamic dose at different depths determined using Eq. 6.3. Red line is the threshold photodynamic dose ( $10^{18}$ [ph/g]) for tissue necrosis determined by Patterson <i>et al.</i> [13]. Tissue sites with photodynamic dose above the threshold would become necrotic. ....	155
A.1 Optical property spectra determined for the 1.03 $\mu$ m diameter microspheres solution at a concentration of 8%. Absorption coefficients of water (dashed line) and the lowest ink aliquot are shown for comparison. Empty circles represent the reduced scattering coefficients determined by Mie theory for this sphere diameter.....	168

# Abstract

## Optical measurements for quality control in photodynamic therapy

Paulo Rodrigues Bargo

OGI School of Science and Engineering  
Oregon Health and Science University

Supervising Professor: Steven L. Jacques

The evolution of Photodynamic Therapy (PDT) to a fully developed treatment modality requires the development of appropriate dosimetry to ensure proper quality control during treatments. The parameters measured for PDT quality control were the drug accumulation and the optical penetration depth. These methods were tested *in vitro* in photochemical assays and in tissue simulating phantoms. Pilot clinical trials were conducted and *in vivo* measurements were performed in patients undergoing endoscopic screening for esophageal diseases and photodynamic therapy of esophagus, lung, oral cavity and skin.

A system and model to measure the relative drug concentration *in vivo* for patients undergoing endoscopic PDT are presented. Fluorescence measurements from tissue were corrected by the light transport of the excitation and emission light derived from Monte Carlo simulations. The mean error between the concentration

determined from measurements in optical tissue simulating phantoms and was 10%. The non-corrected relative fluorescence data showed differences of 2-3 fold when comparing samples with the same drug concentration but different optical properties. The range of concentrations measured for all patients span over 2 orders of magnitude highlighting the need of dosimetry in individual basis.

Blood perfusion was the main variable that affected the optical penetration depth of treatment light and the depth of treatment. The fraction of blood ranged from 0.1% to 30% and was typically greater for tumor tissue compared with normal tissue for a given patient. The increased blood fraction accounted for a higher absorption coefficient hence a reduced optical penetration depth in tumor tissue. Values of  $\delta$  ranged from 1.3-3.6 mm for the overall normal sites (mean  $\pm$  sd = 2.2  $\pm$  0.5 mm) and from 0.6-3.6 cm for the tumor sites (mean  $\pm$  sd = 1.6  $\pm$  0.7 mm).

Models were developed to help understand light propagation from optical fibers to tissue and vice versa. These models were used to improve the development of instrumentation and to modify existing well-established theories to accurately interpret data.

# Chapter 1

## Introduction

Photodynamic therapy (PDT) is a Food and Drug Administration (FDA) approved procedure for treatment of esophageal, lung and skin cancer as well as for wet Age-related Macular Degeneration (AMD) of the retina. The procedure involves the administration of a photosensitizing drug that accumulates in the treatment region and the activation of the drug with light. The main mechanism of cell death occurs by the transference of energy from the activated drug to oxygen molecules producing singlet oxygen radicals that attack important parts of the cells (e.g., mitochondria) [1, 2]. If the oxidative damage exceeds a threshold the cell will die by either direct damage cell to membranes [3] or apoptosis (programmed cell death) [4, 5]. Other important mechanisms of cell death for *in vivo* PDT are of a vascular nature such as the vasoconstriction of blood vessels [6, 7]. A simple diagram of PDT events is shown in Fig. 1.1.

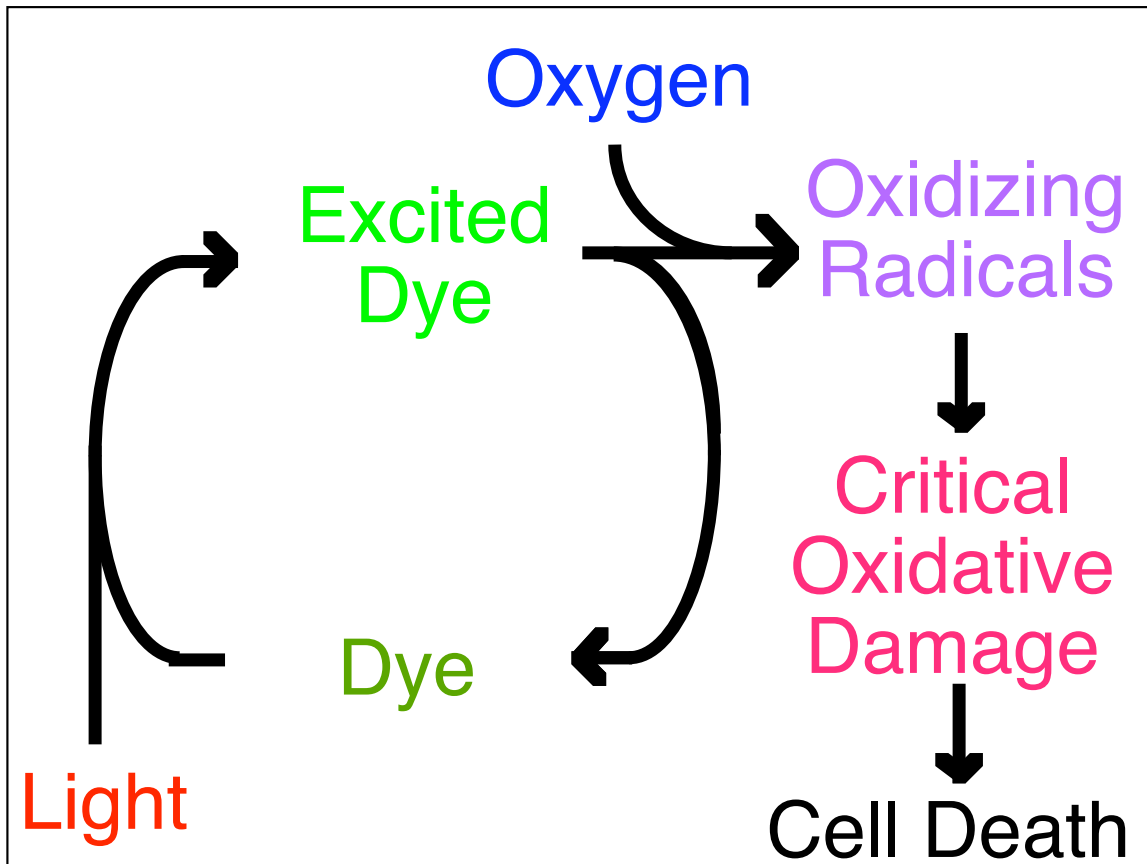


**Fig. 1.1.** - Mechanism of Photodynamic therapy. Light excites photosensitizer dye molecules that react with oxygen molecules to produce singlet oxygen radicals or other oxidizing species. If oxidative damage to essential cell targets (e.g., mitochondria) exceeds a critical threshold, the cell dies.

The success of a PDT procedure is directly related to the availability of drug, light and oxygen. Some of each of these three elements must be present at the tissue during treatment, but excessive drug may cause dark toxicity or excessive light exposure may cause photobleaching of the drug. This sets the frame of a window where PDT is optimized. Figure 1.2 show a diagram of the PDT treatment window. Drug and light doses are parameters that can easily be changed to improve the outcome of the procedure as long as they remain within the treatment window.

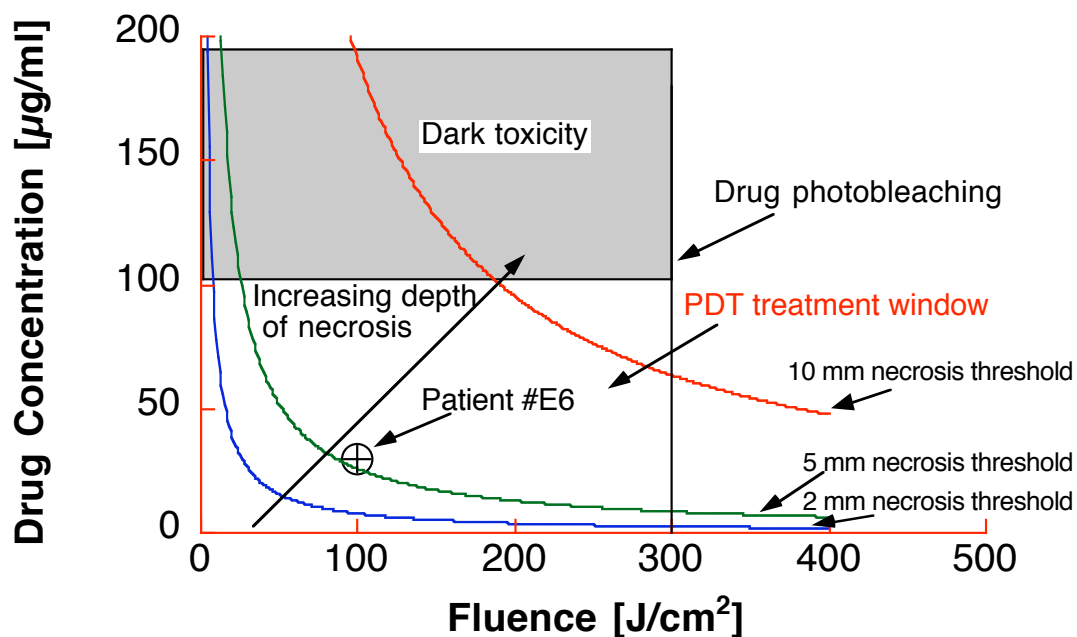


**Fig. 1.2.** – PDT window. Light exposure and drug concentration should be above a critical threshold to achieve necrosis at a given depth. Too much drug leads to dark toxicity. Too much light leads to drug photobleaching. Curves were calculated rearranging Eq. 1.1 and plotting the drug concentration as a function of light dose ( $E_0 t$  [ $J/cm^2$ ]). Other parameters were assumed:  $\delta = 0.25$  cm,  $\epsilon = 3$   $cm^{-1}$  ( $mg/ml$ ) $^{-1}$ ,  $\lambda = 630$  nm,  $c = 3 \cdot 10^8$  m/s,  $h = 6.6 \cdot 10^{-34}$  J s,  $k = 3$ ,  $R_{th} = 10^{18}$  ph/g [13] and  $\Phi_{ox} = 1$ . Data for patient #E6 (same as Fig. 1.3) is also shown. Photobleaching and dark toxicity levels are qualitative only.

The availability of oxygen also plays an important role in the success of the treatment [8-10]. Modulation of oxygen levels by hyperbaric oxygenation has also been attempted [11].

An example of an optimum treatment outcome where the conditions for drug, light and oxygen were met is shown in Fig. 1.3 for a patient treated in our PDT program at Providence St. Vincent Medical Center who had a localized (T1) esophageal adenocarcinoma nodule. The patient was treated with the standard FDA protocol and has remained without cancer for 2 years.

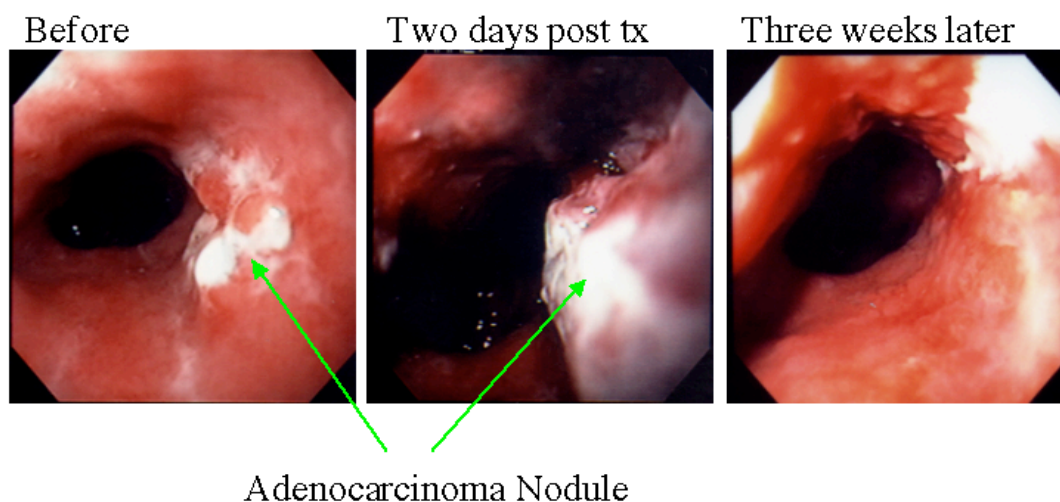


**Fig. 1.3.** – Optimal PDT outcome. Patient with an early stage adenocarcinoma nodule was treated using the standard FDA approved PDT protocol. Pictures were taken before, 2 days after and 3 weeks after treatment.

## 1.1 Motivation

The evolution of radiation therapy into an accepted and important clinical treatment modality depended on the development of dosimetry: the measurement of the dosages of radiation that achieved a desired effect. Now as photodynamic therapy (PDT) gains Food and Drug Administration (FDA) approval and clinical applications grow, the full development of PDT as a treatment modality requires development of the appropriate dosimetry to ensure proper quality control during treatments.

The FDA treatment protocol uses a single drug and light dose for all patients in a given disease modality and photosensitizer. For example, for esophageal tumors treated with Photofrin a dose of 2 mg/kg of body weight of drug is administered intravenous and a light dose of 288 J/cm of cylindrical diffuser of 630 nm laser light is applied 48 hours after drug injection. Although the same amount of drug is administered to every patient each individual will have different amounts of drug *in situ* in different organs due to the person-to-person variations in drug pharmacokinetics. Different light penetration due to different tissue optical properties will change the amount of light that reaches the drug in the tissue and different amounts of excited drug are achieved. Also the tissue oxygenation status will be different for every patient. Drug accumulated rather than administered drug, light penetration rather than delivered light and tissue oxygenation status should be

determined in order to achieve accurate PDT dosimetry. In this sense methods to determine light penetration, drug and oxygen concentration *in situ* in an individual basis have to be developed.

This report describes optical measurements implemented via optical fibers to provide PDT dosimetry in esophageal, lung, oral cavity and skin cancer patients *in vivo*. Reflectance spectroscopy was used to document the optical properties of the tissue (normal and tumor sites) and to specify the optical penetration depth of the treatment light at 630-nm wavelength. Fluorescence spectroscopy was used to characterize the amount of photosensitizing drug (Photofrin II) that had accumulated in the tissues. An optical fiber based system becomes necessary to access some tissue sites (esophagus and lung) through an endoscope. These optical tools were tested and validated in tissue simulating phantoms and improved optical models for analysis of optical fiber measurements were developed. An *in vitro* experiment was conducted to determine the quantum efficiency of oxidation, a parameter that could be used to study the formation of oxidizing species in a cellular environment. This report does not address the quantification of oxygen concentration *in vivo* although the importance of those measurements is recognized. Other researchers have been conducting experiments to perform these measurements [10, 12].

## **1.2 PDT Dosimetry**

### **1.2.1 The basics of PDT dosimetry**

A seminal paper in the field of PDT dosimetry was the report by Patterson, Wilson and Graff in 1990 [13]. In this report rat livers were loaded with a photosensitizing drug and exposed to different wavelengths of light for various radiant exposures (product of irradiance and exposure time) to yield variable-sized zones of necrosis. After accounting for the wavelength dependence of light transport in the liver and for the wavelength dependence of light absorption by the photosensitizer, the authors demonstrated that the margin of necrosis always corresponded to a threshold value for the

number of photons absorbed by photosensitizer per gram of tissue ([ph/g]). This value is called the PDT threshold dose, and is now known to vary for different photosensitizers and different tissues over the range of  $10^{18}$ - $10^{20}$  ph/g. The paper illustrated that despite variation between patients in the optical properties of a tissue or the accumulation of photosensitizing drug in a tissue, there was a practical dosimetry factor, which predicted the onset of necrosis.

Jacques [14-16] offered a simple rule of thumb for the dosimetry that specifies the depth of tissue necrosis during PDT. When irradiating a tissue with a broad uniform illumination, the depth of tissue necrosis is related to the simple exponential decay of treatment light as it penetrates into the tissue. At the margin of necrosis, the production of oxidizing species by the PDT drops to the threshold value required to elicit necrosis. At the margin, the dosimetry relationship is:

$$R_{th} = E_0 k t \exp\left(\frac{-z_{necrosis}}{\delta}\right) \epsilon C b \Phi_T \Phi_{\Delta} f_R \quad (1.1)$$

where

$E_0$	[W/cm <sup>2</sup> ]	irradiance of treatment light onto the tissue surface,
$t$	[s]	exposure time for treatment light,
$\delta$	[cm]	optical penetration depth of treatment light,
$k$	[dimensionless]	augmentation of light at surface due to backscatter,
$z_{necrosis}$	[cm]	depth of the margin for zone of necrosis,
$\epsilon$	[cm <sup>-1</sup> /(mg/g)]	extinction coefficient of photosensitizing drug,
$C$	[mg/g]	concentration of photosensitizing drug,
$b$	[ph/J]	photons per joule of light energy at treatment wavelength,
$\Phi_T$	[dimensionless]	quantum efficiency for triplet formation,
$\Phi$	[dimensionless]	quantum efficiency for generation of oxidizing species,
$f_R$	[dimensionless]	fraction of oxidizing species that attack critical cell sites,
$R_{th}$	[ph/g]	threshold of oxidizing species concentration leading to cell death.

In the above, the concentration  $C$  is expressed as mg photosensitizer per gram of tissue, or [mg/g], and the concentration component of the extinction coefficient  $\epsilon$  is similarly expressed, [ $\text{cm}^{-1}/(\text{mg/g})$ ]. It should be emphasized that the units of concentration used in  $C$  and  $\epsilon$  can vary as long as these two factors both use the same units. The product  $\epsilon C$  will cancel the units and hence the choice of units no longer affects a calculation using Eq. 1.1. The tissue concentration of photosensitizing drugs is often specified as [mg/g]. The value of  $b$  equals  $\lambda/hc$  where  $h$  is Planck's constant [J s],  $c$  is the speed of light in *vacuum* [m/s] and  $\lambda$  is the wavelength of light [m].

In the above, the quantum efficiency for generation of oxidizing species  $\Phi$  describes the efficiency for an excited state photosensitizer to transfer its energy to molecular oxygen to create singlet oxygen or some other type of oxidizing species. This  $\Phi$  is usually dependent on the tissue concentration of oxygen [9]. The parameter  $f_R$  describes the fraction of oxidizing radicals that damage important cell sites, such as the cell membranes or the mitochondria, which lead to cell death.

Rearranging Eq. 1.1 yields a prediction for this 1-dimensional case of the depth of necrosis:

$$z_{necrosis} = \delta \ln \left( \frac{E_0 t k \epsilon C b \Phi_T \Phi_{\Delta} f_R}{R_{th}} \right) \quad (1.2)$$

Note that  $z_{necrosis}$  is linearly proportional to the optical penetration depth  $\delta$  but proportional to the logarithm of all other factors. Hence, to double the size of  $z_{necrosis}$ , one must double  $\delta$  but must alter any other factor by a factor of 7.4. The practical consequence of Eq. 1.2 is that the tissue optical properties influence  $\delta$  and have a primary effect on the depth of treatment. For example, a tissue that is highly inflamed has a high blood content whose hemoglobin absorbs the treatment light and attenuates the light penetration into the tissue. Patients who present target tissues with variable degrees of

inflammation are expected to have variable PDT treatment zones if all other PDT dosimetry factors are constant. The applicability of Eq. 1.2 in vivo derives from the original experimental demonstration of Patterson et al. [13].

The above 1-dimensional case (planar zone under a broad illumination) can be adapted to the 2-dimensional case (cylindrical zone around a cylindrical fiber source) and 3-dimensional case (spherical zone around an imbedded single fiber source), and Eq. 1.2 will be slightly altered. However, the basic form of Eq. 1.2 remains the same and it provides a simple rule of thumb to guide PDT dosimetry. For example, for a 2-dimensional case with a cylindrical isotropic diffuser embedded in an infinite medium the only change in Eq. 1.1 will be the different fluence rate distribution of light. If the distance  $r$  where the generation of oxidizing species is being determined is much greater than the optical penetration depth  $\delta$  ( $r \gg \delta$ ) the modified Eq. 1.1 for the cylindrical geometry becomes [17]:

$$R_{th} = kt\epsilon Cb\Phi_T\Phi_\Delta\Phi_R \frac{3E'_0(\mu_a + \mu'_s)}{\sqrt{8\pi \frac{z_{necrosis}}{\delta}}} \exp\left(-\frac{z_{necrosis}}{\delta}\right) \quad (1.3)$$

where

$E'_0$  [W/cm] power delivered per length of diffuser,

$s'$  [ $\text{cm}^{-1}$ ] reduced scattering coefficient,

and the other parameters are the same described before.

## 1.2.2 How blood perfusion influences the depth of PDT treatment

The tissue optical properties that influence light transport in tissue are the absorption coefficient,  $\mu_a$  [ $\text{cm}^{-1}$ ], and the reduced scattering coefficient,  $\mu'_s$  [ $\text{cm}^{-1}$ ] [18]. The optical penetration depth,  $\delta$  [cm], is related to  $\mu_a$  and  $\mu'_s$ :

$$\delta = \frac{1}{\sqrt{3\mu_a(\mu_a + \mu'_s)}} \approx \frac{1}{\sqrt{3\mu_a\mu'_s}} \quad (1.4)$$

The value  $\mu'_s$  is usually at least 10-fold greater than the value of  $\mu_a$ . If  $\mu'_s$  is comparable to or less than  $\mu_a$ , then optical diffusion theory no longer applies and  $\delta$  approaches the value  $1/\mu_a$  rather than  $1/\mu_a/\sqrt{3}$ . If  $\mu'_s$  exceeds  $\mu_a$  a change in the blood content of a tissue will cause a proportional change in  $\mu_a$ , and  $\delta$  will change as the square root of the change in blood content. Since the PDT treatment zone is proportional to  $\delta$ , the treatment zone will vary as much as 10-fold depending on the degree of tissue inflammation. An example of change in optical penetration depth with blood perfusion is shown in Fig. 1.4.

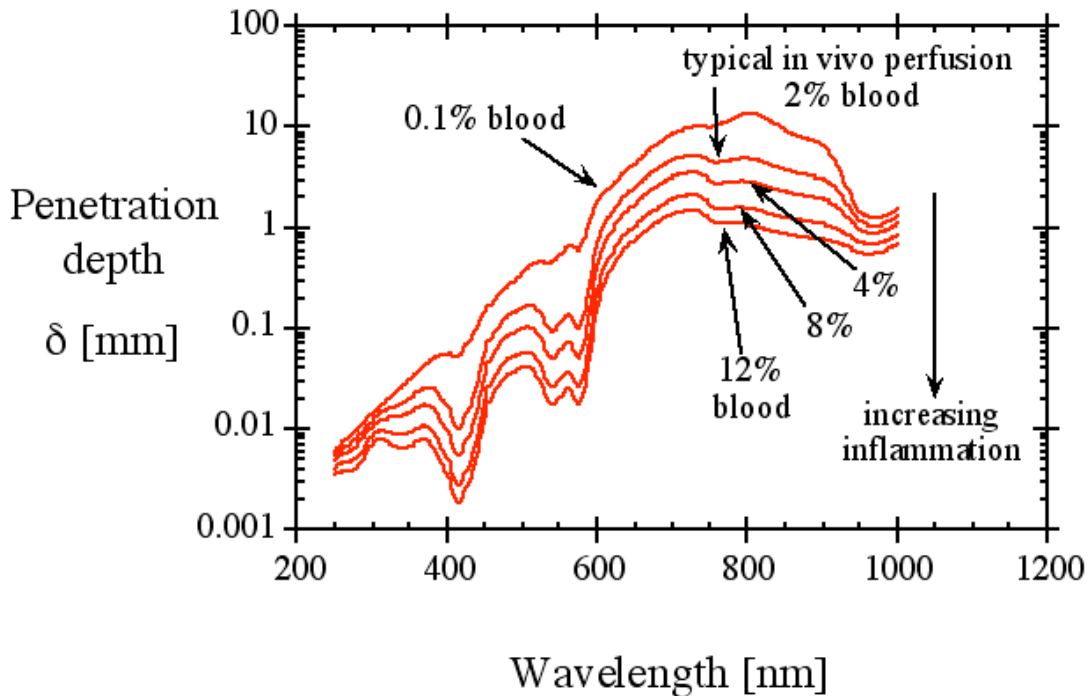


**Fig. 1.4.** – Theoretical example of how the blood perfusion changes the tissue optical penetration depth. The volume fraction of blood in the tissue is varied from 0.1-12%.

The above discussion of PDT dosimetry pertains to bulk tumors such as esophageal cancer that extend over mm or cm in size, in contrast to superficial cancer

which presents as a thin layer on top of otherwise normal tissue. In superficial cancer, one is not concerned with the depth of PDT treatment, but rather is concerned with exceeding the threshold dose required to kill the superficial cancer. The light delivered to the tissue surface is basically the light seen by the tumor. There is an augmentation of the light dose due to backscatter from the underlying normal tissue. The effective irradiance of treatment light,  $E$  [ $\text{W}/\text{cm}^2$ ], seen by a superficial tissue is:

$$E = E_0 \left( 1 + 2R \frac{(1 + r_i)}{(1 - r_i)} \right) \approx E_0 (1 + 6R) \quad (1.5)$$

where  $r_i$  is the total internal reflection of light attempting to escape at the air/tissue surface which is usually about 0.5. The fraction of incident light that escapes the tissue as observable reflectance is denoted by  $R$  and is typically about 0.30-0.60. Hence the factor  $(1 + 6R)$  varies from 2.8-4.6. This surface augmentation phenomenon was early recognized by Star *et al.* [19] and was demonstrated by Andersen *et al.* [20]. Hence, backscatter significantly affects the treatment light dose. However, as long as one exceeds the threshold amount of light appropriate for a given concentration of photosensitizing drug in the superficial tissue, the zone of cancer necrosis does not change because the cancer is a limited superficial volume. Of course, there may be a variable zone of damage in the underlying normal tissue that depends on the underlying tissue optical properties, but that is a different issue. In summary, Eqs. 1.1, 1.2 and 1.3 pertain to bulk tumors, not to superficial tumors.

### **1.2.3 How photosensitizer fluorescence predicts photosensitizer concentration**

Normally, photosensitizers are administered as mg photosensitizer per kg body weight of patient, or [ $\text{mg}/\text{kg.b.w.}$ ]. But the key factor is how much photosensitizer accumulates in the tissue,  $C$  [ $\text{mg}/\text{g}$ ]. If the body were simply a bag of water, the administered drug would distribute uniformly. But in reality, the pharmacokinetics of

photosensitizer distribution in the body is variable for different tissues, and indeed for different times after drug administration [21]. One needs to document the amount of photosensitizer that has accumulated in a target tissue to ensure that sufficient photosensitizer is present for treatment.

Photosensitizing drugs are often fluorescent which offers a means of assaying the amount of photosensitizing drug that accumulates in a tissue. One uses a shorter wavelength of light,  $\lambda_x$  [nm], to excite the photosensitizer fluorescence that emits over a range of longer wavelengths, any one of which is denoted  $\lambda_m$  [nm]. For an optically homogeneous tissue with a uniform distribution of fluorescent photosensitizer, the observed fluorescence,  $F$  [ $\text{W}/\text{cm}^2$ ], at wavelength  $\lambda_m$  escaping the tissue is expressed:

$$F = \int_V E_{0x} T_x \ln(10) \epsilon C \Phi_f T_m \eta_c dV \quad (1.6)$$

$$= E_{0x} \ln(10) \epsilon C \eta_c \Phi_f \int_V T_x T_m dV = E_{0x} \ln(10) \epsilon C \Phi_f \eta_c \chi$$

where

$E_{0x}$	[ $\text{W}/\text{cm}^2$ ]	irradiance of excitation light onto the tissue surface,
$T_x$	[dimensionless]	light transport factor for excitation light,
$\epsilon$	[ $\text{cm}^{-1}/(\text{mg}/\text{g})$ ]	extinction coefficient of photosensitizing drug,
$C$	[ $\text{mg}/\text{g}$ ]	concentration of photosensitizing drug,
$\Phi_f$	[dimensionless]	fluorescence quantum efficiency,
$T_m$	[ $1/\text{cm}^2$ ]	light transport factor for escape of fluorescence at surface,
$V$	[ $\text{cm}^3$ ]	Integration volume accounting for the optical fiber dimensions and geometry of excitation and collection,
$\eta_c$	[dimensionless]	collection factor to account for the numerical aperture of the fiber (see chapters 3 and 4),
$\chi$	[ $\text{cm}$ ]	lumped effective transport length for excitation into and emission out of tissue, equal to the integral of $T_x T_m$ over tissue volume

The above Eq. 1.6 indicates that an effective transport length  $\chi$  characterizes the penetration of excitation light into tissue and the escape of fluorescence out of tissue. The parameter  $\chi$  depends on the optical properties of the tissue at  $\lambda_x$  and  $\lambda_m$  and on the area of collection of the detector. Gardner *et al.* [22] demonstrated the role of  $\chi$  in fluorescence spectroscopy of light-scattering tissue phantoms with an experimental setup that did not use optical fibers. The observed photosensitizer fluorescence specifies the concentration of photosensitizer according to:

$$C = \frac{F}{E_{0x} \ln(10) \epsilon \Phi_f \eta_c \chi} \quad (1.7)$$

Consider two tissues with the same concentration  $C$  of photosensitizer, one tissue is highly inflamed and the other is normal. In the inflamed tissue the high blood content attenuates penetration and escape of light and the value of  $\chi$  is decreased. The observed fluorescence  $F$  is lower than observed in the normal tissue. But the factor  $\chi$  in Eq. 1.7 corrects for the differences in  $F$  and Eq. 1.7 predicts the same  $C$  for both tissues.

The factor  $\Phi_f$  is not necessarily a well behaved factor. The  $\Phi_f$  can vary several fold depending on the microenvironment of the photosensitizer, for example, is the photosensitizer dissolved in an aqueous phase, adsorbed to a protein or aggregated with another photosensitizer. The quenching of fluorescence by the microenvironment is a variable that awaits experimental comparison of observed fluorescence,  $F$ , versus the true concentration  $C$  determined by chemical extraction from biopsied tissue samples and subsequent well-controlled assay. Some work in this venue has been presented by Mang *et al.* [23].

## 1.3 The current state of PDT dosimetry

### 1.3.1 Drug concentration measurements

Pharmacokinetics of photosensitizers have been studied in cell [24] and animal models [25, 21] and in human clinical trials [26, 27] to determine the distribution of administered drug in different organs such as liver, skin, muscle and vessels. Bellnier *et al.* [25] and Baumgartner *et al.* [21] studied the distribution of Photofrin in mice and rats using scintigraphic and fluorescence methods. Bellnier and Dougherty [26] determined the mean ( $\pm$  SEM) serum concentrations of Photofrin 48 after injection of 0.875, 1, or 2 mg Photofrin/kg to be  $2.7 \pm 0.5$ ,  $4.0 \pm 0.7$ , and  $3.5 \pm 1.0$  micrograms Photofrin/ml, respectively. Although these values represent an estimate of the drug concentrations that should be expected *in situ* they do not accurately represent patient-to-patient variation of drug concentration.

Fluorescence spectroscopy has been used to determine relative drug concentration *in situ* since most of the photosensitizers used in PDT are also fluorescent. The main difficulties in making quantitative measurements are the dependence of the fluorescence measurements on the tissue optical properties and the photochemical changes in the photosensitizer quantum yield and extinction coefficient due to the microenvironment where the drug is bound. Some authors have simply disregarded these problems [28]. Other researchers have suggested methods to overcome the fluorescence optical properties dependence. Practical approaches were suggested by Andersen-Engels *et al* [29] who performed comparison of fluorescence of two different fluorescence species present in the tissue and by Sinaasapel *et al* [30] and Lam *et al* [31] who suggested the use of relative fluorescence as a ratio of two wavelengths. Models based on Kubelka-Munk [32] photon migration [33] and Monte Carlo [22, 34] have been proposed. An interesting approach was given by Gardner *et al* [22] where Monte Carlo simulations were used to correct the measured fluorescence and quantitative measurements of drug concentrations were achieved. This model was not suited for optical fibers and was limited to one-dimension light delivery. Pogue and Burke [35] demonstrated a fiber optic

method where small diameter optical fibers were used to diminish the effects of the absorption coefficient in the measurements. In this method the fluorescence still has to be corrected for variations in the scattering coefficient and calibration could be particularly difficult due to the complex behavior of the measured fluorescence at low scattering coefficients. Soft tissues such as the esophagus and photosensitizers fluorescing in the near infrared are typical cases where low scattering situations can occur [36].

### 1.3.2 Optical penetration depth

The optical penetration can be inferred from measurements of tissue optical properties such as the reduced scattering coefficient and the absorption coefficient as shown in Eq.1.4. The main chromophores that affect the absorption coefficient in the visible spectral range in tissue are blood and melanin [37] whereas changes in collagen fibers are the main tissue constituent responsible for changes in scattering [38]. Many authors have proposed experimental techniques for the determination of tissue optical properties as well as light transport models to accurately recover these optical properties. Jacques and Prahl [39] used integrating spheres to measure total reflectance and total transmission in addition to collimated transmission to determine the optical properties from models based on the diffusion approximation. Prahl [40, 41] developed Monte Carlo and adding-doubling theories for application of light transport in tissue. Monte Carlo methods were also developed by Wang *et al* [42]. Wilson and Jacques [18] discussed several methods for tissue diagnostics and dosimetry. A great review of optical properties was given by Cheong *et al* [36]. Farrell *et al.* [43] proposed a model based on the spatially resolved steady-state diffuse reflectance to determine the optical properties and compare the results to Monte Carlo simulations. Pickering *et al.* used a method based on two integrating spheres [44, 45] to determine the optical properties of slowly heated myocardium [46]. Patterson *et al.* [47] proposed time resolved methods for non-invasive measurements of tissue optical properties. Anderson-Engels *et al.* [48] developed a multispectral time domain system based on diffusion theory. Frequency domain measurements were also proposed [49, 50]. Another technique for determination of

optical properties is based on photoacoustics [51] and authors have also proposed its use for the determination of the depth of necrosis in PDT [52].

The practicality of implementing any of the above experimental techniques will depend on the type of tissue being studied and its location in the body. For two of the tissues that concern this report (esophagus and lung) remote access is necessary hence methods based on an integrating sphere are not suited for these measurements. Time resolved measurements such as time or frequency domain techniques have advantage over steady state diffuse reflectance techniques because no a priori information is need to recover tissue optical properties [50]. On the other hand, time resolved techniques are complex and require the use of sophisticated and expensive equipment such as fast response detectors and short pulse sources. Steady state diffuse reflectance is much simpler but at least two independent factors must be supplied by measurements to determine the two optical parameters,  $\mu_a$  and  $\mu'_s$ . Sufficient information can be obtained by either doing spatially resolved measurements at several distances or by doing wavelength dependent measurements.

A few authors have used steady state diffuse reflectance *in vivo*. Nielsson *et al.* [53] made measurements with a single 300  $\mu$ m optical fiber at two depths *in vivo* to determine the optical penetration depth of light in rat liver and muscle during PDT. These measurements were further related to optical properties by correlating them to *ex-vivo* measurements of the total diffuse reflectance and transmission made with integrating spheres and measurements of collimated transmission. Kim *et al.* [54] developed a diffuse reflectance probe based on two side-viewing optical fibers with 7 preset translation positions between source and detector that was used to determined optical properties of dog prostate. A similar device was developed by Bays *et al.* [55] but the dimensions were slightly bigger than the internal diameter of the working channel of an endoscope and could not be used during regular endoscopic procedures. The authors developed a different configuration where a 15-mm diameter probe was developed and positioned in the esophagus without visualization by the physician. Using this device the authors measured an average reduced scattering coefficients of  $7 \text{ cm}^{-1}$  and an average

effective attenuation coefficient ( $\mu_{\text{eff}} = 1/\delta$ ) of  $2.4 \text{ cm}^{-1}$  for normal esophagus. Kienle *et al.* [56] developed a camera based system and Nichols *et al.* [57] developed a fiber based system for applications in skin. Mourant *et al.* [58, 59] used small fiber separations for the determination optical properties of tissue phantoms. Moffitt and Prahl [60] developed a method based on sized-fiber spectroscopy where two fibers, one with a small diameter and other with a large diameter, were used to determine the optical properties. The small diameter of this probe potentially allows use in endoscopic measurements. In summary, although several experimental techniques have been developed for the determination of optical properties, none of them were systematically used during standard endoscopic procedures.

#### 1.4 Goals

Dosimetry in photodynamic therapy relies on the development of methods for the determination of light penetration, drug concentration and tissue oxygenation status *in vivo*. Without this information treatment planning can only rely on the current FDA-approved protocols. Although these protocols are based on clinical trials to ensure safety and efficacy for a large population of patients, they do not consider patient-to-patient variation. If PDT treatment for a particular patient fails, there currently are no tests to document that sufficient photosensitizer accumulated in the tumor or that sufficient light penetrated the tissue to achieve the desired depth of treatment. This dissertation focuses on the determination of the tissue optical properties to determine the penetration depth of treatment light, and on measurement of photosensitizer fluorescence to specify the photosensitizer concentration in the tissue.

Chapter 2 introduces measurements of the quantum efficiency of oxidation and the efficiency of interaction between singlet oxygen and target molecules during *in vitro* PDT. These measurements will allow the determination of the parameters  $\Phi$  and  $\Phi_R$  in Eq. 1.1. The photosensitizer was Photofrin II and the target was nicotinamide adenine dinucleotide phosphate (NADPH). Spectrophotometric and spectrofluorometric assays were implemented to determine the oxidation of NADPH into  $\text{NADP}^+$  after irradiation of

Photofrin by 488 nm laser light and to determine photobleaching rates of photosensitizer. The efficiency of interaction between PDT-formed singlet oxygen and NADPH was derived based on assumptions for efficiencies of triplet-state and singlet oxygen formation derived from literature values. Parameters derived from this method ( $\Phi$  and  $\Phi_R$ ) could be extrapolated to *in vivo* measurements and be used in Eq. 1.1 to 1.3 to estimate the number of singlet oxygen radicals formed for a given irradiation scheme.

Chapter 3 presents correction methods for optical measurements based on single optical fiber probes. These probes are small and widely used in the biomedical field particularly for fluorescence measurements. The collection efficiency ( $\eta_c$ ) of single optical fibers is studied experimentally and theoretically and its dependence on the optical properties of the medium is demonstrated. Analytical equations and numerical methods are derived for the collection efficiency. These studies are used in the analysis of experimental data in later chapters and may also facilitate development of new optical fiber systems.

Chapter 4 extends the studies of chapter 3 to multiple fiber probes. Experimental and theoretical analysis of the optical fiber collection efficiency is made for different probe configurations. Collection-efficiency-corrected diffusion theory analysis of light transport is compared to simple diffusion theory and to experimental data for a two-fiber probe with 2.5-mm separation between source and detector. Effects of changes on optical fiber diameter, numerical aperture of collection, numerical aperture of launching and medium anisotropy are also evaluated. The use of multiple fiber probes increases the sample volume, which facilitates the determination of tissue optical properties in the clinical trails. These types of probes were used in Chapter 5.

Chapter 5 uses spatially resolved steady-state diffuse reflectance to determine the optical properties of esophageal, lung, oral cavity and skin's tissues. A side viewing optical fiber probe was developed for endoscopic measurements of diffuse reflectance. The probe was calibrated and tested with tissue simulating optical phantoms made of Intralipid (scattering), India ink (absorber) and acrylamide gels. Measurements on normal sites were performed in 9 patients undergoing endoscopic screening for esophageal

diseases. Normal and tumor sites were measured in 11 patients undergoing PDT treatment of esophagus, lung, oral cavity and skin. Optical properties were derived from a least square minimization of the reflectance arising from different combinations of chromophores and scattering. The optical properties obtained were comparable to those of similar tissues reported by other researchers. The optical penetration depth for each tissue site was then determined based on these optical properties. Distribution of the data demonstrated the patient-to-patient variability.

Finally, in Chapter 6, a method for determination of fluorophore concentrations based on the correction of optical fiber fluorescence measurements by optical properties is presented. A fluorescence Monte Carlo code was implemented to determine the transport of excitation light out of the fiber and emission light back into the fiber. Measurements of fluorescence phantoms were made for both non-scattering and turbid media cases. Errors between values predicted by the model and the concentration determined by titration of the stock solution were 4 % and 10 %, respectively. Fluorescence measurements for the same PDT patients of chapter 5 were also taken immediately after the reflectance measurements were made. Optical properties derived for each patient in chapter 5 were used with the fluorescence Monte Carlo code to determine the lumped parameter  $\eta_c\chi$  which accounts for the optical fiber field of view and the fluorescence correction parameter. These corrections compensated for the high blood perfusion of tumor sites due to inflammation; these increased the measured drug concentrations and increased the separation between diseased and normal tissue. Histogram plots of the drug concentration demonstrated that the concentration values span more than two orders of magnitude emphasizing the need for individual dosimetry measurements. Using the values determined for optical penetration depth and drug concentration allowed the determination of the photodynamic dose based on Eq. 1.1 for several tissue depths.

## Chapter 2

### PDT efficiencies for photooxidation of substrate (NADPH) using a photosensitizer (Photofrin II).

#### 2.1 Introduction

\*Singlet oxygen generation is well established as one of the major intermediates in Photodynamic Therapy (PDT). Several groups [61-63] have shown singlet oxygen production during *in vitro* and *in vivo* PDT and its implication in cell damage and microvascularization collapse. Spectroscopic and electrochemical methods have been used to evaluate different photosensitizers in cuvette solutions, cell suspensions, and animals.

Understanding the kinetics of oxidation in cuvette solutions can provide significant information regarding the interaction of singlet oxygen and molecular targets. Although cuvette experiments are attractive because of their simplicity, extrapolating these results to more complex *in vivo* models is problematic because photosensitizers can bind to substances present in cells (such as proteins in cell membranes) that modify monomeric or oligomeric forms of the photosensitizer and change its photochemistry.

Nevertheless, extrapolation of the cuvette solution model can still be applied to determine *in vivo* processes by assuming that the photosensitizer in a cell environment is in a quasi-monomeric state. We will show that the quantum yield for photooxidation

---

\* Part of this chapter was published in Proc. SPIE, vol. 3909, 2000.

using Photofrin as the photosensitizer reaches a limiting value in the limit of high target molecule concentration (which may correspond to the cell environment). We will also show that the difference in the quantum yield of oxidation between a monomeric state solution and an oligomeric state solution is not great, which may justify the assumption of photosensitizer being in the monomeric form. The possibility of extrapolating these *in vitro* results to a cell environment will be discussed.

## 2.2 Materials and Methods

NADPH ( $\beta$ -Nicotinamide Dinucleotide Phosphate, reduced form, Sigma Chemical Co.), used as a target substrate, was diluted in a 50 mM solution of Trizma buffer (Trizma - pre-set crystals, Sigma Chemical Co.) or in 50:50 MeOH:water solution. (Fisher). Concentrations ranged from 0.4 to 10 mM. The final volume was 5 ml and the solutions were kept in ice after preparation.

Photofrin II(QLT PhotoTherapeutics), was used as the photosensitizer. The stock solution, 2.5 mg/ml, was stored at  $-20^{\circ}\text{C}$  and thawed prior to use. A fixed concentration of 50  $\mu\text{g/ml}$  ( $\sim 50\ \mu\text{M}$ ) was prepared by adding 100  $\mu\text{l}$  of Photofrin stock to 4.9 ml of NADPH solution. Solutions were returned to ice and also kept in the dark until irradiated.

Absorbance spectra of the solutions were taken prior to irradiation to ensure repeatability and to measure the extinction coefficients of NADPH at 340 nm and Photofrin at 488 nm.

Experiments were done in three steps for each solution as shown in figure 2.1.

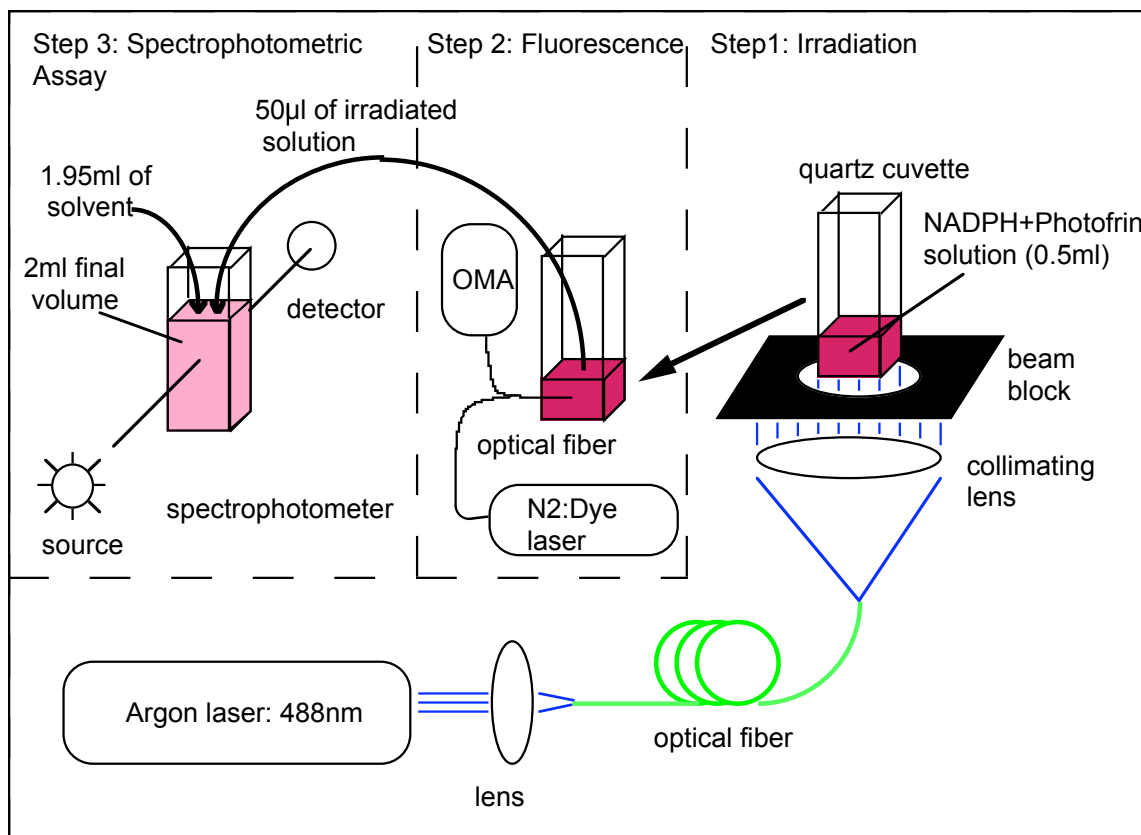


**Fig. 2.1.** - Experimental setup for irradiation (step 1), fluorescence (step 2) and absorbance (step 3).

**STEP 1, Irradiation:** A continuous wave argon ion laser, operating at 488nm, was used to irradiate the samples. Aliquots of 500  $\mu$ l of solutions were placed into quartz cuvettes (1cm pathlength) for irradiation, forming an effective sample volume of 1 cm x 1 cm x 0.5 cm. Laser power was 100mW, guided through a 600- $\mu$ m core diameter optical fiber and the output was collimated with a bi-convex lens ( $f = 50$ mm), forming a 13-mm diameter uniform spot. The irradiation was delivered through the bottom of the cuvette to avoid meniscus influence. The effective irradiation area was 1 cm<sup>2</sup>, yielding a final irradiation power of 75 mW. Irradiation time ranged from 0 to 90 minutes. No temperature elevation was observed using a thermocouple.

**STEP 2, Fluorescence Measurement:** After irradiation, fluorescence spectra of non-diluted samples were measured from 540 to 800 nm to assay Photofrin photobleaching.

An Optical Multichannel Analyzer, OMA (Princeton Instruments), recorded spectra excited by a nitrogen-pumped dye laser (Laser Science) operating at 440nm and energy of 20 $\mu$ J per pulse. Excitation and collection was performed through a 600- $\mu$ m core diameter optical fiber. Accumulations of 50 pulses were necessary to record the faint fluorescence from Photofrin in TRIZMA solution. Accumulations of 5 pulses were used to record fluorescence from Photofrin in MeOH solution.

**STEP 3, Spectrophotometric Assay:** Absorbance measurements were taken in the 250–820 nm spectral range with a spectrophotometer (Hewlett Packard). Solutions were diluted 1:40 (50  $\mu$ l of irradiated solution into 1.95 ml of Trizma buffer or 1.95 ml of 50% MeOH solution) and placed into quartz cuvettes (1-cm pathlength). Spectra were recorded and absorbance at 340 nm was measured to assay the kinetics of NADPH oxidation.

Several sets of experiments were conducted according to this three-step assay. Samples of NADPH alone (1 mM) and Photofrin alone (50 g/ml) were tested for auto-oxidation and photobleaching, respectively. Samples of NADPH (0.4 to 10 mM) + Photofrin (50 g/ml) in TRIZMA and 50% MeOH were tested for PDT-mediated oxidation of NADPH. Samples of NADPH (1mM) + sodium azide (5mM) + Photofrin (50 g/ml) tested the influence of singlet oxygen in the PDT process since sodium azide is a singlet oxygen scavenger. A minimum of three repetitions per test was performed.

## 2.3 Results

### 2.3.1 Background Experiments

To confirm the oxidation process, control samples of NADPH without Photofrin were exposed to laser light according to the same irradiation protocol. Results showed negligible oxidation of NADPH, which can be observed by the invariance of the absorbance peak at 340nm (Fig. 2.2) as a function of time.

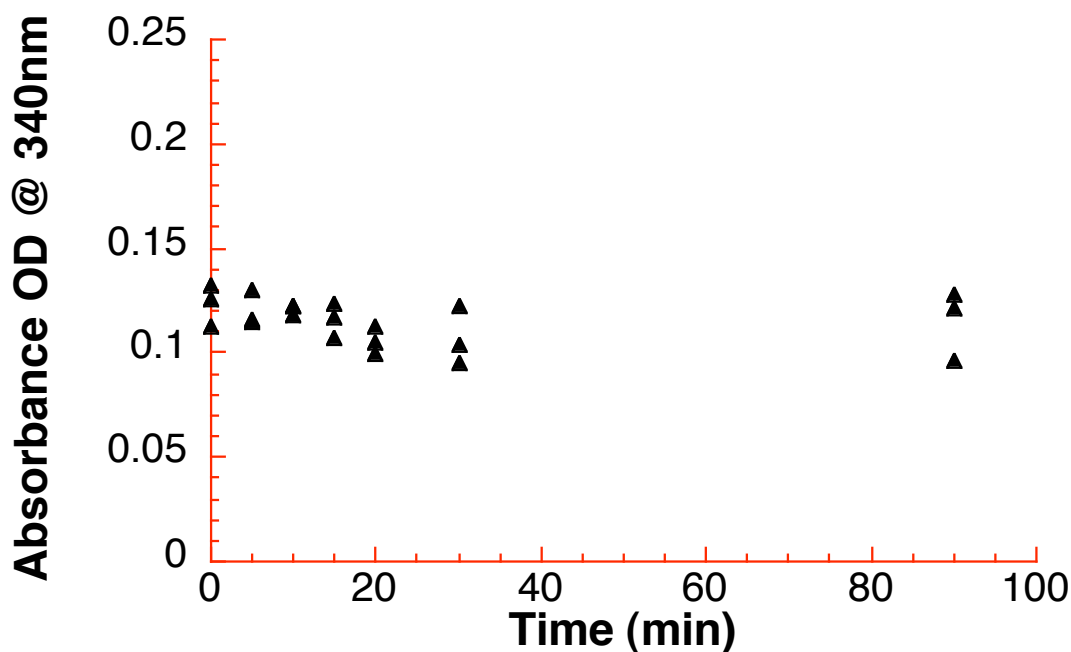


**Fig. 2.2.** – Control experiment shows no change in NADPH absorbance during irradiation by light over 90 minute period.

Experiments with Photofrin alone (50 g/ml) showed negligible photobleaching effects. Results are shown in figure 2.3 (bottom curve) where a variation of the absorbance peak at 340 nm is less than 5% after 90 minutes laser exposure. In this experiment, 90 min of 100-mW irradiation at 488 nm delivered through a 0.5 cm thickness of a 50 g/ml solution of Photofrin (85% transmission) would yield less than 1% photobleaching if the quantum yield of photobleaching (photobleaching per photon absorbed) were 100%. But the quantum yield of photobleaching is relatively low and so the lack of observable photobleaching is expected.

Oxidation involving Photofrin as the oxidant agent is shown in literature to be a type II process requiring the formation of singlet oxygen. This was confirmed by adding sodium azide (5 mM), a singlet oxygen scavenger, to the solutions. The kinetics of

oxidation were affected (Fig. 2.3, top 2 curves) by sodium azide. The time constant for oxidation was increased due to the competition between NADPH and sodium azide for reacting with the singlet oxygen.

Extinction coefficients of NADPH and Photofrin were also experimentally measured based on transmission measurements through dilute non-scattering solutions (graphs not shown).

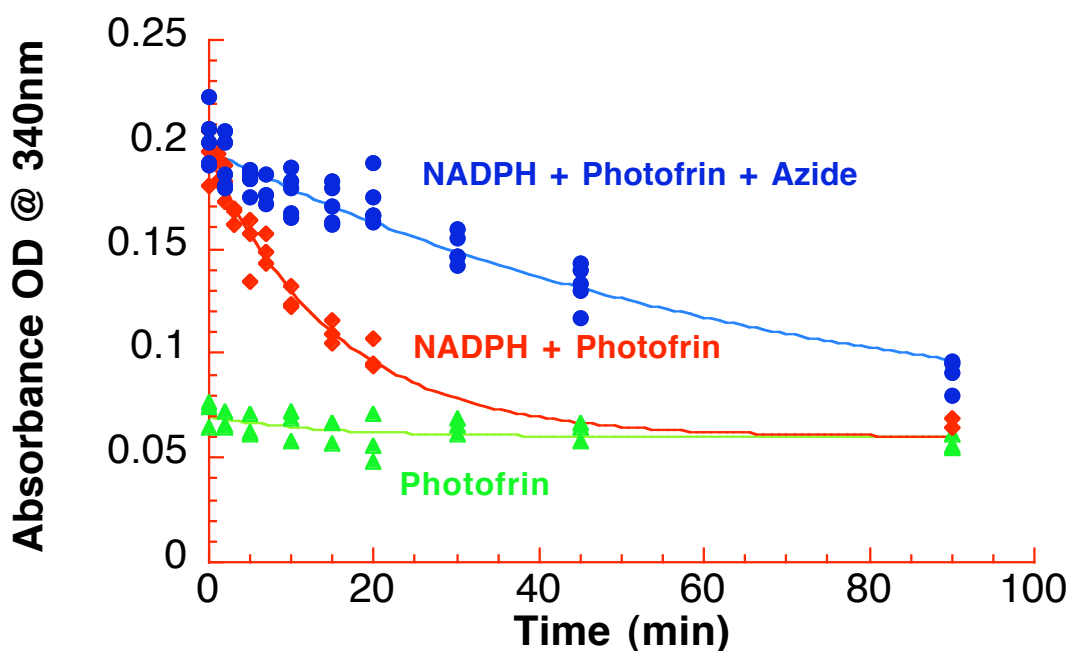


**Fig. 2.3.** – Kinetics of photo-oxidation of NADPH by Photofrin in solution with and without sodium azide (a singlet oxygen scavenger). Photobleaching of Photofrin is shown in the bottom curve. [NADPH] = 1mM. [Photofrin] = 50mM. [sodium azide] = 5mM.

### 2.3.2 Kinetics of Oxidation

Absorbance measurements from step 3 were used to verify the kinetics of NADPH oxidation. The data points were fitted with exponential decay curves to determine  $A$  (change in absorbance at 340 nm) and  $\tau$  (time at which the absorbance dropped to  $1/e$  of its initial value). The parameter  $A$  was used to quantify the number of

oxidized NADPH molecules and  $\tau$  was used to quantify the number of photons absorbed by Photofrin at time equals  $\tau$ .

The quantum yield of oxidation is defined as the number of target molecules oxidized ( $N_{ox}$ ) per number of photons absorbed by photosensitizer ( $N_{abs}$ )

$$\phi_{ox} = \frac{N_{ox}}{N_{abs}} \quad (2.1)$$

The exponential fit for the decay in absorbance in figure 2.4 is given by:

$$A = A_{Photofrin} + A_{nadph} \exp(-t / \tau) \quad (2.2)$$

where

A	[OD]	absorbance at 340 nm
$A_{Photofrin}$	[OD]	absorbance of Photofrin molecules at 340 nm
$A_{nadph}$	[OD]	absorbance of NADPH molecules at 340 nm
t	[minutes]	time
$\tau$	[minutes]	time constant to $A_{nadph}$ decay to 1/e of its initial value

The concentration of oxidized NADPH molecules measured with the spectrophotometric assay is

$$C_{nadph} = \frac{\Delta A}{\epsilon_{nadph @ 340} \cdot L_{sp}} \quad (2.3)$$

where

$C_{nadph}$	[M]	concentration of NADPH molecules in the measurement cuvette
$A$	[OD]	NADPH absorbance decay at 340nm ( $= A_{nadph} \exp(-\tau / \tau)$ )
$\epsilon_{nadph@340}$	[cm <sup>-1</sup> mM <sup>-1</sup> ])	NADPH extinction coefficient at 340 nm (5.1)**
$L_{sp}$	[cm]	cuvette pathlength for spectrophotometer measurement (1)

The number of oxidized NADPH molecules ( $N_{ox}$ ) in the irradiated cuvette can be determined by converting  $C_{nadph}$  from molar concentration to number of molecules according to equation 2.4

$$N_{ox} = \frac{\Delta A \cdot N_{av} \cdot V_{sp}}{\epsilon_{nadph @ 340} \cdot L_{sp}} \frac{1}{f} \quad (2.4)$$

$N_{av}$	[molec/mol]	Avogadro's number ( $6.02 \times 10^{23}$ )
$V_{sp}$	[ml]	sample volume measured in the spectrophotometer (2)
$f$	[-]	dilution fraction ( $= 50 / 500 = 0.1$ )

The number of absorbed photons is calculated:

$$N_{abs} = P \cdot \tau \cdot b \cdot \left(1 - 10^{-A_{488}^{PF}}\right) \quad (2.5)$$

$P$	[W]	irradiated power (0.075)
$\tau$	[sec]	time constant (converted to seconds from Fig. 2.4)
$b$	[ph/J]	conversion factor: Joules to # of photons ( $2.5 \times 10^{18}$ ) at 488nm
$A_{488}^{PF}$	[OD]	Photofrin absorbance at 488 nm

---

\*\* in parenthesis are the actual used values

The term  $(1 - 10^{-A_{488}^{PF}}) = (1 - T) = Abs$  corresponds to the absorption of photons by Photofrin at 488 nm ( $Abs = absorption$ ;  $T = transmission$ ). The Photofrin absorbance ( $A_{488}^{PF}$ ) can be determined by

$$A_{488}^{PF} = \epsilon_{488}^{PF} C_{irr} L_{irr} \quad (2.6)$$

$\epsilon_{488}^{PF}$	$[\text{cm}^{-1}(\text{mg/ml})^{-1}]$	Photofrin extinction coefficient at 488 nm (6.3)
$C_{irr}$	$[\text{g/ml}]$	Photofrin concentration (50)
$L_{irr}$	$[\text{cm}]$	irradiated path length (0.5)

### Typical Absorbance kinetics as a function of exposure time

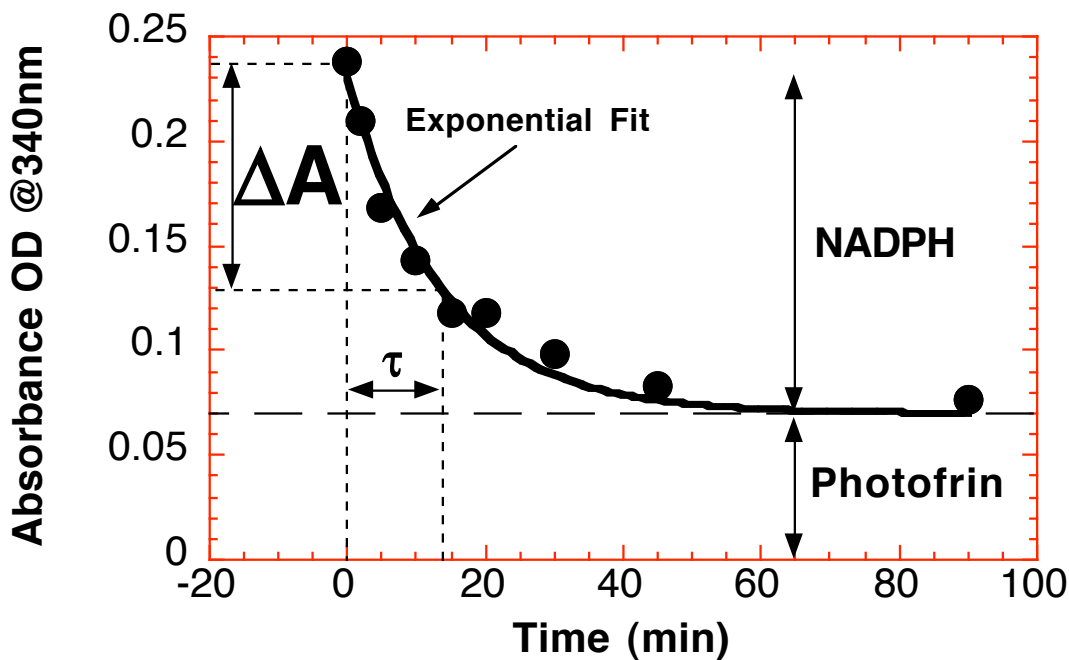
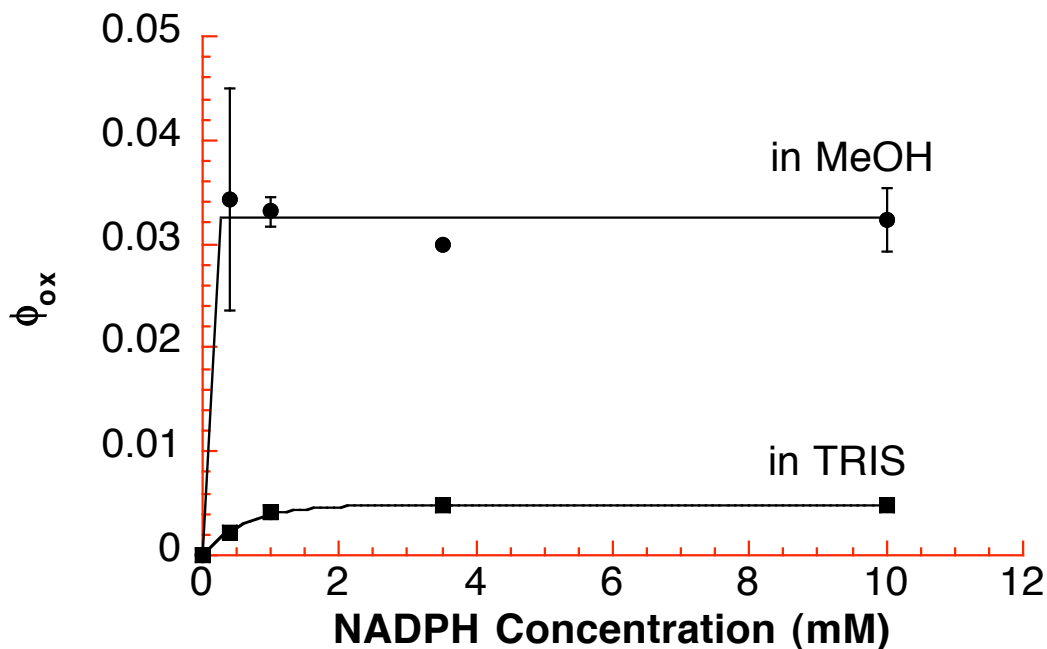


Fig. 2.4. - Typical decay in absorbance at 340 nm due to oxidation of NADPH. Data fitted to a decaying exponential.

Figure 2.5 shows the calculated quantum yield of oxidation ( $\phi_{ox}$ ) of NADPH in TRIZMA buffer and 50% MeOH. It can be observed that  $\phi_{ox}$  reaches a steady state as the concentration of oxidizable targets increase for both cases.



**Fig. 2.5.** - Quantum yield of oxidation of NADPH by Photofrin in TRIZMA and MeOH solutions. Curve fit is an exponential approximation for the diffusion of the singlet oxygen. Error bars are the standard deviations of three measurements and are shown for all points, but are smaller than the symbols in some cases.

A 7-fold increase in  $\phi_{ox}$  is observed when comparing TRIZMA and MeOH solutions. This increase is tentatively attributed to the availability of extra Photofrin in monomeric state with potential to interact with NADPH.

### 2.3.3 Photobleaching

Fluorescence measurements from step 2 were used to verify Photofrin photobleaching. Fluorescence spectra showed little photobleaching effect on Photofrin for shorter exposure times (<5%). Sodium azide had negligible influence on

photobleaching. A 70-fold increase in the fluorescence was observed for Photofrin in MeOH in comparison with TRIZMA solutions (Fig. 2.6).

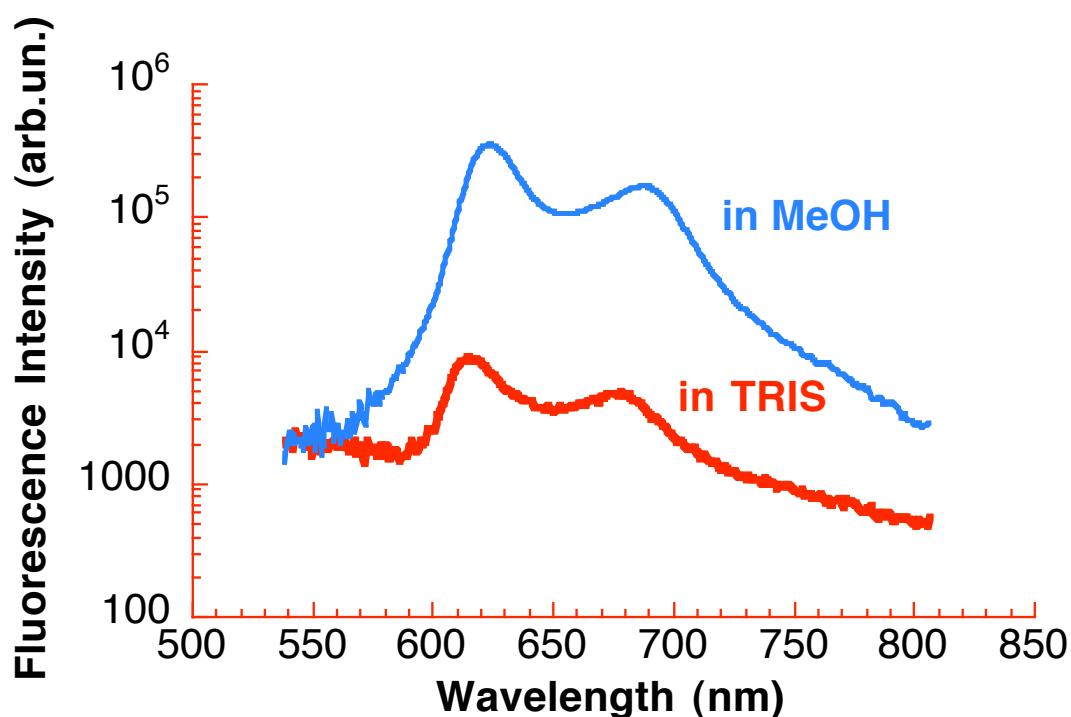


Fig. 2.6 – Fluorescence spectra of Photofrin in two different solvents (a) MeOH and (b) TRIS buffer.

## 2.4 Discussion

### 2.4.1 Comparison between NADPH photo-oxidation and Photofrin fluorescence in different solvents

The efficiency of oxidation of NADPH in MeOH was 7 fold greater than the efficiency of oxidation of NADPH in TRIS buffer. The fluorescence intensity of Photofrin in MeOH was 70-fold greater the PII in TRIS buffer. One could attribute the 7-fold increase on  $\phi_{ox}$  to a 7-fold increase on the availability of Photofrin in monomeric form in MeOH solution. However, a 7-fold increase on the availability of Photofrin in

monomeric form in MeOH solution should also represent a 7-fold increase in the fluorescence signal, but instead the augmentation in the fluorescence signal was 70 fold. This suggests two possibilities. There is an additional 10-fold increase in production of singlet oxygen during PDT in MeOH and this additional singlet oxygen attacks some other species in the solution. Alternatively the quantum efficiencies of oxidation and fluorescence are nonlinear functions of the concentration of monomeric form of the photosensitizer and hence no additional singlet oxygen is formed. Since no additional photobleaching of Photofrin was observed for the PDT of Photofrin alone in MeOH solution the first hypothesis is unlikely.

#### 2.4.2 Determination of the quantum yield of interaction

Figure 2.7 shows a Jablonski diagram in which the quantum yield of oxidation ( $\phi_{ox}$ ) can be obtained by multiplying the quantum efficiency of Photofrin triplet state generation ( $\phi_T$ ), the efficiency of singlet oxygen production ( $\phi$ ) and the fraction of the singlet oxygen reacting with NADPH ( $f_R$ ):

$$\phi_{ox} = \phi_T \phi_{\Delta} f_R \quad (2.7)$$

Furthermore, the fraction of the singlet oxygen reacting with NADPH ( $f_R$ ) can be split into two quantities: the efficiency of diffusion of singlet oxygen ( $\phi_D$ ) to an NADPH molecule and the efficiency of interaction with a NADPH molecule ( $\phi_I$ )

$$f_R = \phi_D \phi_I \quad (2.8)$$

The efficiency of singlet oxygen interaction with NADPH ( $\phi_I$ ) can be stated:

$$\phi_I = \frac{\phi_{ox}}{\phi_T \phi_{\Delta} \phi_D} \quad (2.9)$$

The behavior of  $\phi_{ox}$  as a function of concentration (converging to a steady-state) suggests that the most important component in the oxidation process of NADPH, at higher concentrations, is the interaction between the singlet oxygen and the target molecule (Fig. 2.5). For this case  $\phi_D$  can be approximated to 1 since the lifetime of a singlet molecule is very short [64].

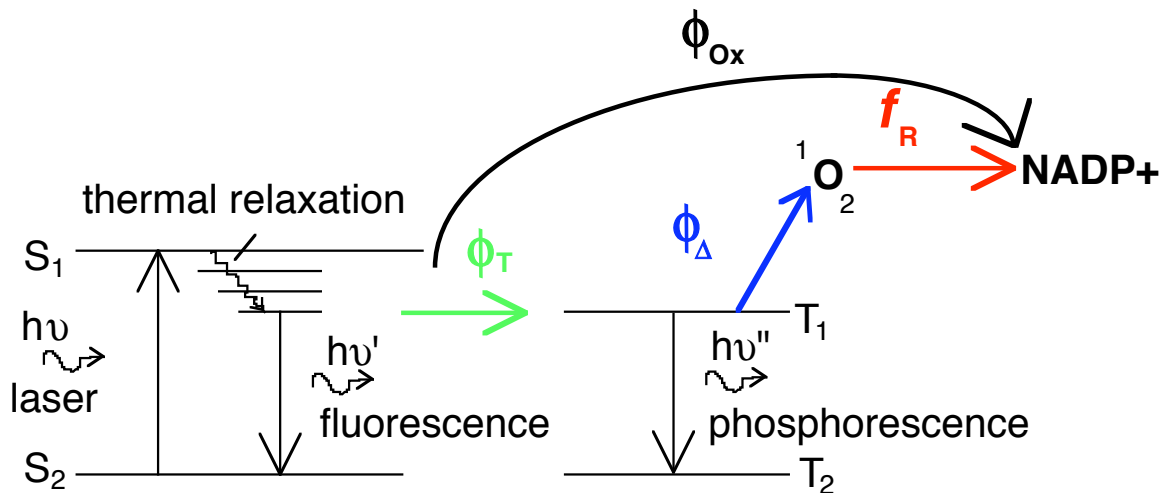


**Fig. 2.7.** – Jablonski diagram of the oxidation of NADPH by PDT. Laser light with energy  $h\nu$  excites the photosensitizer molecule to excited state  $S_2$ . A fraction  $\phi_T$  of the energy undergo intersystem crossing to triplet state  $T_2$ . The remaining energy will become heat or fluorescence with energy  $h\nu'$ . Energy in triplet state will either phosphoresce with energy  $h\nu''$  or transfer to another molecule. A fraction  $\phi$  will transfer to oxygen molecules producing singlet oxygen  $^1O_2$ . A fraction  $f_R$  of the singlet oxygen molecules oxidizes NADPH to  $NADP^+$ .

Using typical values found in the literature for  $\phi_T$  and  $\phi$  (0.63 from Reddi *et al.* [65] and 0.32 from Lambert *et al.* [66], respectively) in aqueous solutions and  $\phi_{ox} = 0.005$  (from Fig.2.5), we estimated the efficiency of interaction of singlet oxygen with NADPH for a target saturated solution to be  $\phi_I = 0.025$ .

For lower concentrations of NADPH, singlet oxygen diffusion becomes an important factor in the oxidation process and its behavior may be modeled with molecular diffusion theory.

At higher NADPH concentrations, the oxidation process is dominated by the efficiency of interaction between the singlet oxygen and the target, not by the efficiency of singlet oxygen diffusion to the target.

### 2.4.3 Population of oxidizable sites

In cells and tissues, where many targets exist, a simple linear approximation to how the singlet oxygen interact to multiple targets can help understanding the importance of a particular species in the oxidation process.

*In vitro* results could be extrapolated to cells by considering a model in which the total number of oxidation events is specified by the number of oxygen radicals generated in the cell. These radicals will attack various sites in the cell according to the local concentration ( $C$ ) of a particular site in the cell and the efficiency of interaction ( $\phi_i$ ) for singlet oxygen reaction with that site.

$$N_{radicals} = f_n \sum_{j=1}^N C_j \phi_{Ij} \quad (2.10)$$

where the number of types of oxidizable species or sites equals  $N$ , the concentration of the  $j^{\text{th}}$  species is  $C_j$ , and the efficiency of singlet reaction with each  $j^{\text{th}}$  species is  $\phi_{Ij}$ . The factor  $f_n$  is a normalization factor, units of volume, that causes the summation to equal  $N_{radical}$ , the number of singlet oxygen radical generated by PDT. The efficiency of oxidation of a particular  $k^{\text{th}}$  species in the cell ( $\phi_k$ ) is given by the ratio of the number of radicals oxidizing the  $k^{\text{th}}$  ( $N_k$ ) species over  $N_{radicals}$  (Eq. 2.9).

$$\phi_k = \frac{N_k}{N_{radicals}} = \frac{C_k \phi_{Ik}}{\sum_{j=1}^N C_j \phi_{Ij}} \quad (2.11)$$

where  $C_k$  is the concentration of the  $k^{\text{th}}$  species in the cell and  $\phi_{Ik}$  is the efficiency of reaction of singlet oxygen with the  $k^{\text{th}}$  species.

If one could specify the denominator of Eq. 2.11, one would have characterized the population of oxidizable sites (POS) in the cell. This could be done by determining the concentration  $C_k$  in the cell (e.g., by fluorescence microscopy), the efficiency of oxidation of the  $k^{\text{th}}$  species ( $\phi_k$ ) in the cell (e.g., by fluorescence spectroscopy) and the efficiency of interaction ( $\phi_{Ik}$ ) of singlet oxygen to the  $k^{\text{th}}$  species (e.g., by the *in vitro* assay demonstrated in this report). Rearranging Eq. 2.11. and solving for POS (Eq. 2.12).

$$POS = \sum_{j=1}^N C_j \phi_{Ij} = \frac{C_k \phi_{Ik}}{\phi_k} \quad (2.12)$$

Direct determination of the efficiency of oxidation for most oxidizing species (e.g.,  $\phi_i$  for the  $i^{\text{th}}$  species) in the cell is difficult since an assay (chemical or photochemical) for its determination may not be trivial. On the other hand, determination of the efficiency of interaction of singlet oxygen to this specie ( $\phi_{Ii}$ ) with a method similar to the described in this report is generally simple. If one can determine the concentration of the  $i^{\text{th}}$  species in the cell one could use the term POS determined for the  $k^{\text{th}}$  species to determine  $\phi_i$  indirectly by using Eq. 2.11.

Pogue *et al.* [67] determined the efficiency of oxidation of NADH after PDT in mice leg muscle *in vivo* using benzoporphyrin derivative monoacid ring (BPD) as photosensitizer. In this study the efficiency of oxidation of NADH was 22% determined by fluorescence spectroscopy. Let's assume for the sake of argument that the same assay for Photofrin as photosensitizer would determine a similar efficiency of oxidation for NADPH as oxidizing species. If the concentration of NADPH in the cell equals 0.15 mM [68] the term  $POS = (0.00015 \times 0.025) / 0.22 = 0.000017$ . Our work on measuring  $\phi_{Ij}$  for targets begins to approach the complex problem encountered in cells and tissues.

## 2.5. Conclusion

*In vitro* experiments in a cuvette can yield information on the efficiency of reaction of singlet oxygen with targets for oxidation. The results indicate likely efficiencies in cells and tissues.

The quantum efficiency of oxidation of NADPH by Photofrin in TRIS and MeOH was 0.005 and 0.032, respectively. The efficiency of interaction of singlet oxygen and NADPH for a target saturated solution was determined to be 0.025.

Discrepancies between the augmentation in the efficiency of oxidation and the production of fluorescence suggest that these parameters are nonlinear functions of concentration of the monomeric form of photosensitizer.

# **Chapter 3**

## **Collection Efficiency of a Single Optical Fiber in Turbid Media**

### **3.1 Introduction**

\*Single optical fibers have been commonly used as light delivery and collection tools for optical diagnosis. Authors have proposed their use to determine tissue optical properties [60], measure relative chromophore concentration [35, 69, 70] and monitor drug pharmacokinetics [28]. Changes in tissue optical properties will affect single-fiber measurements by either modifying the light transport in the tissue (e.g., less light would return to the fiber when comparing measurements on inflamed versus non-inflamed tissues) or by changing the light coupling to an optical fiber. Studies on how optical properties affect the intensity of light traveling through a media have resulted in improved light transport models [22, 30, 33, 71] but little work has been done on light coupling to an optical fiber. Some investigators consider the light coupling to an optical fiber to be part of the light transport model (e.g., including the optical fiber boundaries to Monte Carlo simulations [35, 60]) and don't separate these two factors. Two advantages of separating the light transport problem from the fiber-coupling problem are (1) implementation of simpler models for light transport and (2) better understanding of the

---

\* This chapter was published in Applied Optics-OT, Vol. 42, pp.3187-97, 2003.

influences of the fiber on the detection scheme. The latter may guide the development of improved optical-fiber-based systems. This paper addresses the coupling of light from turbid media to a single, bare optical fiber in contact with a semi-infinite homogenous medium used simultaneously for delivery and collection, by determining how the *optical fiber collection efficiency* varies as a function of optical properties. The optical fiber collection efficiency is a parameter that determines how much of the light returning to the optical fiber face couples into the fiber core, and is guided to the detector. A single, bare optical fiber used as source and collector is the simplest case of practical importance. These fibers are simple and inexpensive to make, are small, and might be used in endoscopic or minimally invasive procedures. The optical fiber collection efficiency for multi-fiber probes and for fluorescence measurements will be the subjects of further reports.

### 3.2 Theory

Consider the measurement of light from a semi-infinite medium when the power  $P_o$  [W] is delivered as a collimated beam at the origin, and the specular reflectance due to the refractive index mismatch at the interface is  $r_{sp}$  [dimensionless]. The total power escaping the medium is:

$$P_{esc} = P_o r_{sp} + P_o (1 - r_{sp}) \int_0^{\infty} T(r) 2\pi r dr = P_o r_{sp} + P_o (1 - r_{sp}) R_{diffuse} \quad (3.1)$$

where the transport factor from the fiber through the tissue to a position  $r$  on the surface is  $T(r)$  [ $\text{cm}^{-2}$ ] and  $R_{diffuse}$  is a dimensionless factor called the total diffuse reflectance. If light is both delivered and collected over an aperture of diameter  $d$ , the power collected by the aperture is:

$$P_{collected} = P_o r_{sp} + P_o (1 - r_{sp}) \int_0^{\frac{d}{2}} \int_0^{\frac{d}{2}} T(r, r') dA' dA = P_o r_{sp} + P_o (1 - r_{sp}) R_{collected} \quad (3.2)$$

where  $R_{\text{collected}}$  is the diffuse light collected by the aperture, and  $dA$  and  $dA'$  indicate the incremental aperture area for delivery and collection. In a practical application the aperture could be a single optical fiber or an optical fiber bundle.

Saidi [72] defined the fraction of collected light by a 2-mm-dia. mixed fiber bundle of small randomly mixed source and collection fibers as the power collected divided by the total diffuse light that escaped the medium. In the case of Saidi's mixed fiber bundle the source and collection fibers were separate, the power that entered the tissue was  $P_o(1-r_{sp})$  but the collection fibers did not collect the factor  $P_o r_{sp}$ . The light fraction  $P_o r_{sp}$  did not interact with the sample and hence was excluded from the problem. Therefore, the collection fraction  $f$  was:

$$f = \frac{P_{\text{collected}}}{P_{\text{esc}} - P_o r_{sp}} = \frac{R_{\text{collected}}}{R_{\text{diffuse}}} \quad (3.3.a)$$

In contrast to Saidi's experiment, this study will consider the delivery and collection of light using a single optical fiber. A portion of our collected light is specular reflectance from the fiber tip. Therefore, the collection fraction  $f$  in our case should be defined:

$$f = \frac{P_{\text{collected}} - P_o r_{sp}}{P_{\text{esc}} - P_o r_{sp}} = \frac{R_{\text{collected}}}{R_{\text{diffuse}}} \quad (3.3.b)$$

Another distinction between Saidi's report and this study is that Saidi did not consider that only light reaching the optical fiber face within the fiber cone of acceptance couples to the fiber. Thus his measurements of the fraction of collected light were normalized so that the maximum value of  $f$  approached unity. If a mixed fiber bundle or a single optical fiber is used the fraction of light collected by an optical fiber should remain low (ranging from 0.03-0.20). The term  $R_{\text{collected}}$  should be split into the light that enter

the optical fiber with an angle smaller than the half angle of the acceptance ( $R_{\text{core}}$ ) plus the light that enter the fiber with an angle greater than the half angle of acceptance ( $R_{\text{clad}}$ ),  $R_{\text{collected}} = R_{\text{core}} + R_{\text{clad}}$ .  $R_{\text{core}}$  is guided to the detector by the fiber core and  $R_{\text{clad}}$  escapes the fiber through the fiber clad. Figure 3.1 shows a schematic of the possible light paths.

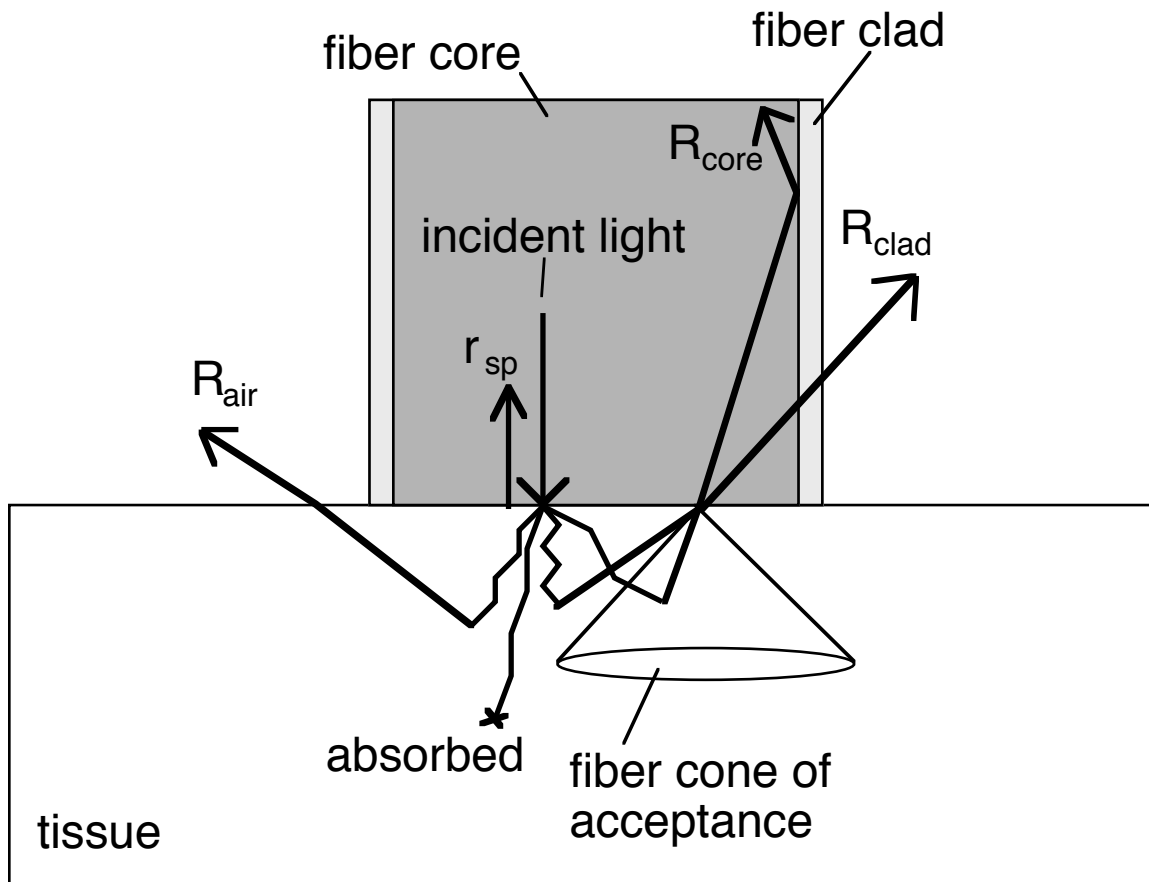


**Fig. 3.1.** – Diagram of the possible return paths of light incident from a single optical fiber. Light that reaches the fiber face with an angle smaller than the half angle of the acceptance cone will be guided through the fiber to the detector ( $R_{\text{core}}$ ). Light that reaches the fiber face with an angle greater than the half angle of the acceptance cone will escape through the fiber cladding ( $R_{\text{clad}}$ ).  $R_{\text{air}}$  is the light that leaves the tissue outside the fiber and  $r_{\text{sp}}$  is the Fresnel reflection due to the fiber/tissue index of refraction mismatch. Light can also be absorbed by the tissue.

The fraction of light that couples into the fiber core ( $f_{\text{core}}$ ) is given by:

$$f_{core} = \frac{R_{core}}{R_{diffuse}} \quad (3.4)$$

The total diffuse reflectance ( $R_{diffuse}$ ) exiting the medium can be experimentally measured, i.e., with an integrating sphere [44]. The term  $R_{core}$  can be measured experimentally by normalizing the optical fiber measurement of the sample by the measurement of a known nonscattering standard, such as water, and multiplying this ratio by the fiber/water Fresnel reflection due to the index of refraction mismatch [73]. If a mixed fiber bundle is used there is no contribution from the specular reflection to the measurements. For a measurement in which a single fiber touching the sample perpendicular to its surface is used to deliver and collect light, one should also take a baseline measurement from a clear medium with the same index of refraction as the sample (e.g., water or gel) and subtract that to account for the specular reflection. Both  $R_{diffuse}$  and  $R_{core}$  can be determined numerically using Monte Carlo simulations [40, 42, 74].

This study considers of  $f_{core}$  as a function of the optical properties using Monte Carlo simulations and experiments on tissue simulating phantoms. A single 600-  $\mu$ m core diameter optical fiber was used as source and collector of light.  $f_{core}$  was calculated by dividing the single optical fiber measurements on the samples (calibrated by measurements in water) by the total diffuse reflectance ( $R_{diffuse}$ ) measured with an integrating sphere. A Monte Carlo model was compared with these experiments. Good agreement was obtained between experiment and model with a mean error of 4%. An empirical expression was determined for the theoretical  $f_{core}$  that gives a first approximation to its value.

A new parameter that describes the coupling of light to a single optical fiber when the fiber is used as source and collector was introduced. This parameter is named the *optical fiber collection efficiency* ( $\eta_c$ ). Although the cone of collection of an optical fiber depends only on its numerical aperture (NA), the amount of light that couples to the fiber core depends on the angular dependence of photons entering the optical fiber which in

turn, depends on the tissue optical properties. The NA is defined by the indices of refraction of the optical fiber core ( $n_1$ ), clad ( $n_2$ ), and medium that the fiber face is in contact with ( $n_0$ ), and is given by:  $NA = (n_1^2 - n_2^2)^{1/2} = n_0 \sin(\theta_a)$ ; where  $\theta_a$  is the half angle the cone of acceptance [75]. The optical fiber collection efficiency ( $\eta_c$ ) is defined as the light that couples to the fiber core ( $R_{core}$ ) divided by the light that simply enters the fiber ( $R_{collected} = R_{core} + R_{clad}$ ) as stated in equation 3.5. Monte Carlo simulations were used to determine  $\eta_c$  since direct experimental determination of the light that couples to the fiber clad ( $R_{clad}$ ) is difficult.

$$\eta_c = \frac{R_{core}}{R_{coll}} = \frac{R_{core}}{R_{core} + R_{clad}} \quad (3.5)$$

The fraction of light collected by the fiber core ( $f_{core}$ ) is related to the  $f$  determined by Saidi by:

$$f_{core} = f \cdot \eta_c = \frac{R_{coll}}{R_{diffuse}} \cdot \frac{R_{core}}{R_{coll}} = \frac{R_{core}}{R_{diffuse}} \quad (3.6)$$

Analysis of the collection efficiency as a function of the angular distribution of the photons that couple to the optical fiber demonstrate the origin of the collection efficiency for turbid media. In this paper a simple analytical expression (Eq. 3.10) was derived to estimate  $\eta_c$  when the reduced mean free path of scattering is much smaller than the fiber diameter ( $mfp' = 1/s' < \text{fiber diameter}$ ; where the reduced scattering coefficient  $s' = s(1-g)$  and  $g$  is the anisotropy). For low scattering samples the Monte Carlo model must be used since  $\eta_c$  can vary as much as 2-3 fold depending on the optical properties and the NA of the optical fiber. Variation on the launching scheme showed minimal effects on the results.

### 3.3 Material and Methods

#### 3.3.1 Acrylamide Gel Optical Phantoms

A 6x3 matrix of different optical property acrylamide gel phantoms was prepared using Intralipid as the scattering agent and India ink as the absorber. Samples were prepared by mixing under a hood calibrated (see Appendix A) stock Intralipid-20%, stock India ink, stock 40% acrylamide solution and water. Stock 40% acrylamide solution was prepared by diluting 1kg of acrylamide acid 99<sup>+</sup>% (electrophoresis grade) plus 50 g of BIS-acrylamide (40:1 ratio) in 2.5 liters of water (reagents from Fisher Scientific, Pittsburgh, PA). Solutions had absorption coefficients ( $\mu_a$ ) of 0.01, 0.1, 0.4, 0.9, 2.5 and 4.9  $\text{cm}^{-1}$  and reduced scattering coefficients ( $\mu_s'$ ) of 7, 14 and 28  $\text{cm}^{-1}$  at 630 nm with a final acrylamide concentration of 20% by volume and a final volume of 100 ml. Gels were prepared by adding, 400 mg of ammonium persulphate, and 0.1 ml of TEMED (Fisher Scientific, Pittsburgh, PA) to each 100-ml solution while stirring at room temperature. Samples gelled after approximately 3 minutes. Each sample was 5 cm in diameter and 4 cm in height and assumed to be a semi-infinite homogeneous medium for the purpose of modeling.

#### 3.3.2 Single fiber Reflectance Measurements

Samples were measured by contacting the surface with a single 600- m optical fiber (UV600/660, quartz/quartz, Ceramoptec, Longmeadow, MA) coupled to a bifurcated optical bundle through SMA connectors (Thorlabs, Newton, NJ). The bifurcated bundle was composed of two 300- m optical fibers (FT300ET, Thorlabs, Newton, NJ) coupled to a single 600- m SMA connector at the distal end and two 300- m SMA connectors at the proximal ends. One fiber was connected to a tungsten-halogen white lamp (LS-1, Ocean Optics, Inc., Dunedin, FL) and the other to a spectrometer

(S2000, Ocean Optics, Inc., Dunedin, FL) controlled by a laptop computer. The fiber distal end was fixed to a clear acrylic rectangular support (25x25x6 mm) through a hole in the center of the support's largest dimension and aligned flush to its contact surface. The support had a 5x5x2 mm groove surrounding the fiber where it touched the surface of the sample forming a region with air/gel interface. The glow ball of the light exiting the sample was always smaller than this region. The experimental setup is shown in Fig. 3.2. with a zoomed view of the fiber support. Acquisition time was 200 ms. A 1-OD filter (03FNG057, Melles Griot, Irvine, CA) was used with all samples and water measurements to avoid detector saturation. A 2-OD filter (03FNG065, Melles Griot, Irvine, CA) was used when the signal from the air/fiber was being measured.

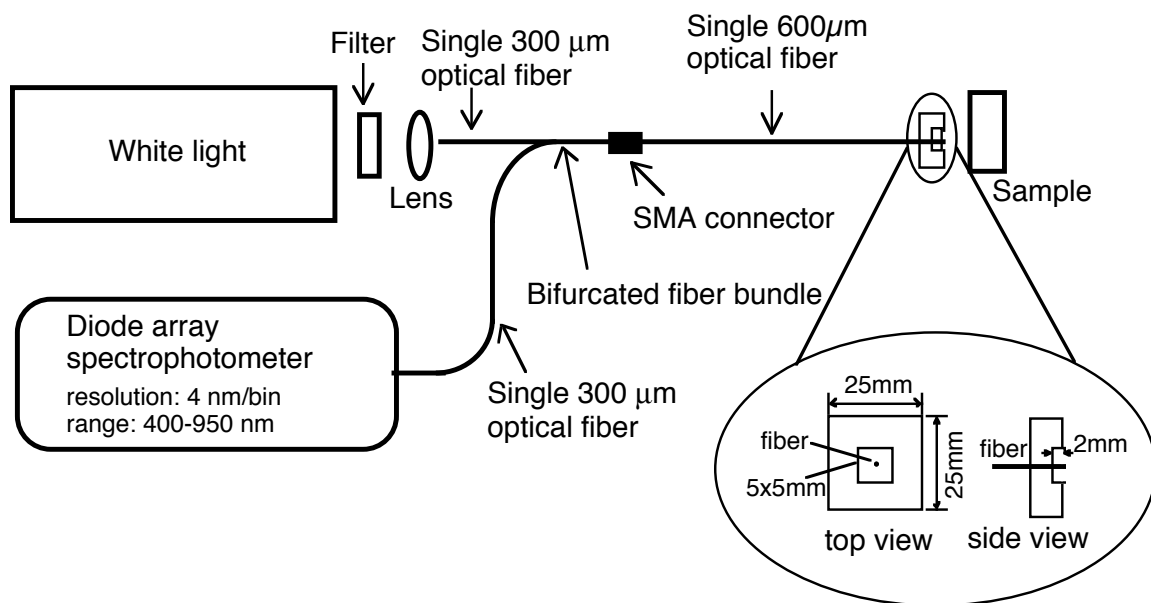


**Fig. 3.2.** – Diagram of the single optical fiber reflectance system. A single 600 μm optical fiber is connected to the distal end of a bifurcated fiber bundle composed of two 300 μm optical fibers. One fiber has the proximal end connected to a tungsten-halogen white lamp and the other is connected to a spectrophotometer. The distal end of the 600 μm optical fiber is placed in contact with the gel samples through a drop of water. OD filters are used to avoid detector saturation.

Measurements of water, air and a clear acrylamide gel sample were taken to evaluate the calibration of the system. Water was placed in a container with its interior painted black to avoid any reflections from the container boundaries that would

contaminate the signal. The Fresnel reflection from the optical fiber face due to the index of refraction mismatch between the fiber core and water was measured. The fiber core is made of pure fused silica [76] and the index of refraction at 630 nm is 1.458 [77]. The index of refraction of water and the clear gel measured with a refractometer (Abbe model. 3L, Fisher Scientific, Pittsburgh, PA) were 1.335 and 1.362, respectively. The influence of the water meniscus on the reproducibility of the measurement  $M_{\text{water}}$  was tested by positioning the fiber below and above the surface in increments of 25  $\mu\text{m}$ . Deviation between the measurements was less than 1%. Air measurements were taken with the fiber pointing away from any object. Gel measurements were taken by positioning the whole acrylic support in contact with the gel. The best way to assure reproducible measurements was to position the support slowly onto the gel surface with the help of a micrometer and observe the change in the reflectance of the surface as the support progressively came in contact with the gel. Since the gel is never perfectly flat or perpendicular to the support the contact always started from one corner. Water was chosen to be the normalization standard because the contact with the fiber is always reproducible and the meniscus showed no effect in the water measurements. As a calibration test the Fresnel reflections for the fiber/air and fiber/clear-gel interfaces were calculated based on the measured indices of refraction ( $R = (n_t - n_i)^2 / (n_t + n_i)^2$ ) [73] and were compared to the Fresnel reflection determined from the water-normalized measurements. These errors were 3 and 5% for the fiber/air and fiber/clear-gel interfaces, respectively.

$R_{\text{core}}$  for each sample was determined by normalizing the sample measurements ( $M_{\text{sample}}$ ) by a measurement of water ( $M_{\text{water}}$ ) at the surface to cancel the effects of source and detector spectral response and multiplying the result by the Fresnel reflection from the fiber/water interface ( $R_{\text{water}}$ ). As stated in the introduction, when a single optical fiber is used the specular reflection has to be subtracted from the sample measurement. This was done by subtracting the measurement of a clear acrylamide gel sample ( $M_{\text{clear}}$ ) from the sample measurement ( $M_{\text{sample}}$ ) as shown in Eq. 3.7:

$$R_{core} = \frac{M_{sample} - M_{clear}}{M_{water}} R_{water} \quad (3.7)$$

Measurements of the total diffuse reflectance ( $R_{diffuse}$ ) for the samples were made with an integrating sphere (IS-080, Labsphere Inc., North Sutton, NH) in a reflectance mode configuration [44], as shown in Fig.3.3. The sphere diameter was 8 inches. Samples were placed at the 1-inch diameter port of the integrating sphere presenting a sample/air boundary. A 600-  $\mu$ m diameter optical fiber (FT600ET, Thorlabs, Newton, NJ) was inserted in a stainless steel tube and held inside the sphere 5 mm away from the sample producing a 3-mm diameter spot on the sample. The outer side of the stainless steel tube was painted white to match the characteristics of the sphere's inner surface. A tungsten-halogen lamp (LS-1, Ocean Optics, Inc., Dunedin, FL) was used to illuminate the samples. Another 600-  $\mu$ m diameter optical fiber (FT600ET, Thorlabs, Newton, NJ) was positioned at a 1/4 inch diameter port of the sphere and the detected signal was guided to a spectrometer (S2000, Ocean Optics, Inc., Dunedin, FL) controlled by a laptop computer. The sphere had a baffle positioned between the sample port and the detection port to avoid direct reflections from the sample striking the detection fiber. Spectralon<sup>TM</sup> reference standards with 2, 20, 50, 75 and 99% reflectance (models: SRS-02-010, SRS-20-010, SRS-50-010, SRS-75-010 and SRS-99-010, Labsphere Inc., North Sutton, NH) were measured to calibrate the sphere and normalize the data from the samples. A clear gel sample was measured to account for the Fresnel reflectance due to the air/gel interface and subtracted from the sample measurements.

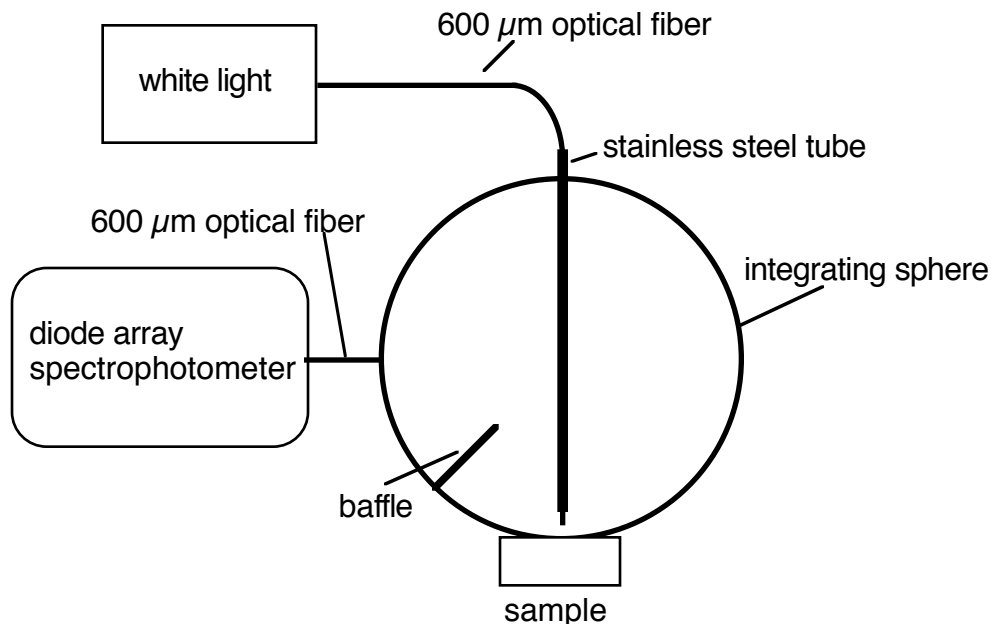


**Fig. 3.3.** – Setup of the integrating sphere experiment. White light guided through a 600  $\mu\text{m}$  optical fiber positioned 5 mm away from the sample surface is used to illuminate a 3-mm diameter spot on the sample. Diffuse reflectance from the sample is trapped in an 8"-dia. integrating sphere. Light is collected by an optical fiber positioned at a 1/4" diameter port of the sphere and guided to a spectrophotometer. Spectralon standards are used to calibrate the diffuse reflectance from the samples.

The experimental  $f_{\text{core}}$ , calculated using Eq. 3.4 and the experimentally determined  $R_{\text{core}}$  and  $R_{\text{diffuse}}$ , was plotted as a function of the dimensionless parameter  $X$  [69, 72] (Figs. 3.4 and 3.6).  $X$  is a function of the optical penetration depth ( $\delta = 1/\mu_{\text{eff}} = (3\mu_a(\mu_a + \mu_s'))^{-1/2}$ ), the reduced mean free path ( $\text{mfp}' = 1/\mu_t' = 1/(\mu_a + \mu_s')$ ) and the optical fiber diameter ( $d$ ) and is given by Eq. 3.8:

$$X = \frac{\delta \cdot \text{mfp}'}{d^2} = \frac{1}{(\mu_{\text{eff}} d)(\mu_t' d)} \quad (3.8)$$

The advantage of plotting against  $X$  was shown by Jacques [69] to be that these plots are independent of optical fiber diameter and all data points tend to collapse to a single sigmoidal-like curve.

### 3.3.3 Monte Carlo Simulations

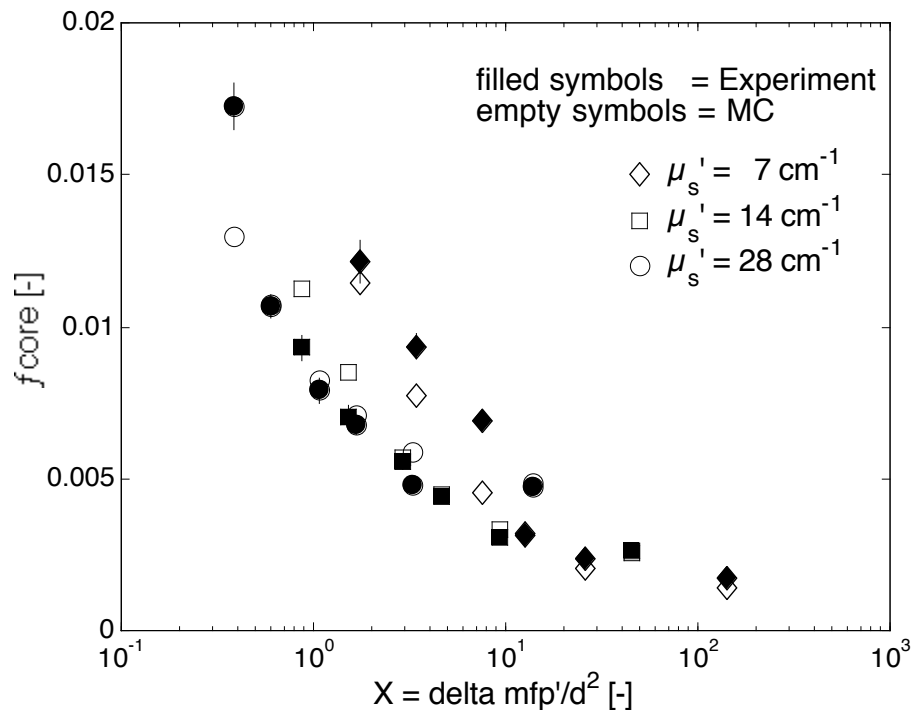
Monte Carlo simulations were performed for a set of optical properties to establish  $f_{\text{core}}$  and  $\eta_c$ . Monte Carlo is well accepted as a model for light transport close to sources and boundaries [40, 42, 74]. Photons ( $\geq$  than 1,000,000) were randomly launched within the radius of the fiber forming a collimated beam into a homogenous semi-infinite medium. Each photon was assigned a weight  $(1-r_{\text{sp}})$  prior to launching and propagated in the medium a random distance ( $\ell = \ln(\text{rnd}) / (a + s)$ ), where rnd was a pseudo-random number uniformly distributed between 0 and 1. After every propagation step the weight of the photon was multiplied by 1-albedo  $(1-a)$ , where  $a = s / (a + s)$ . A new direction was randomly assigned according to the Henyey-Greenstein scattering function. The average cosine of the angle of photon deflection by a single scattering event (or anisotropy,  $g$ ) was set to 0.83 (as measured by Flock [78] for Intralipid) for most of the runs, except when the effects of the anisotropy were being tested (see Fig.3.9). If a photon crossed a boundary (air/sample or fiber/sample) a fraction  $1-r_i$  ( $r_i$  = internal specular reflection which varies with angle of escape according to Fresnel equations) of its weight was recorded in one of three groups. If the position was outside the fiber diameter with any propagation angle, the photon was added to  $R_{\text{air}}$ . If the position was inside the fiber diameter with an angle smaller than the angle defined by the NA of the fiber (e.g., NA = 0.39), the photon was added to  $R_{\text{core}}$ . If the position was within the fiber diameter with an angle greater than the angle defined by the NA of the fiber, the photon was added to  $R_{\text{clad}}$ . Exit angles were corrected according to Snell's law<sup>12</sup>. The photon was returned to the tissue with the remaining weight ( $r_i$  times the weight before crossing the boundary) and was propagated until being terminated according to the roulette method<sup>13-15</sup> in order to conserve energy. Theoretical  $f_{\text{core}}$  and  $\eta_c$  were determined by combining the values of the bins  $R_{\text{core}}$ ,  $R_{\text{clad}}$  and  $R_{\text{air}}$  according to equations 3.6 and 3.5, where  $R_{\text{diffuse}}$  for the Monte Carlo simulations equals the sum of  $R_{\text{core}}$ ,  $R_{\text{clad}}$  and  $R_{\text{air}}$ . Simulations were made for fibers with diameters of 200  $\mu\text{m}$ , 600  $\mu\text{m}$  and 2000  $\mu\text{m}$  and the numerical aperture was set to 0.22 or 0.39. For comparison with the experimental data (figures 3.4 and 3.5) the index of refraction of the sample ( $n_s$ ) and fiber ( $n_f$ ) were set to 1.362 and 1.458, respectively, as

discussed in the previous section. For all other simulations the index of refraction of the sample ( $n_s$ ) and fiber ( $n_f$ ) were set to 1.35 and 1.45.

In a second type of simulation the Monte Carlo code was modified to determine the angular distribution of the photons that return to the fiber. Photons were sorted according to escape angle within the fiber in relation to the normal of the fiber face. Photons with angles between 0 and 5 degrees were assigned to one bin. Photons with angles between 5 and 10 degrees were assigned to another bin, and so forth up to 90 degrees. For these simulations  $\mu_s'$  was set to 70, 10 and 1  $\text{cm}^{-1}$ ,  $\mu_a$  was set to 0.05  $\text{cm}^{-1}$  and fiber diameter was 600  $\mu\text{m}$ . The effect of the angular distribution of launching was determined in a third type of simulation where photons were launched in a uniform angular distribution in a cone configuration with cones having different solid angles to mimic fibers with different NAs. Cone half angles vary from 0 to 50 degrees. Reduced scattering coefficients were 5 and 40  $\text{cm}^{-1}$ ,  $\mu_a$  was set to 1  $\text{cm}^{-1}$  and fiber diameters of 200, 600 and 2000  $\mu\text{m}$ .

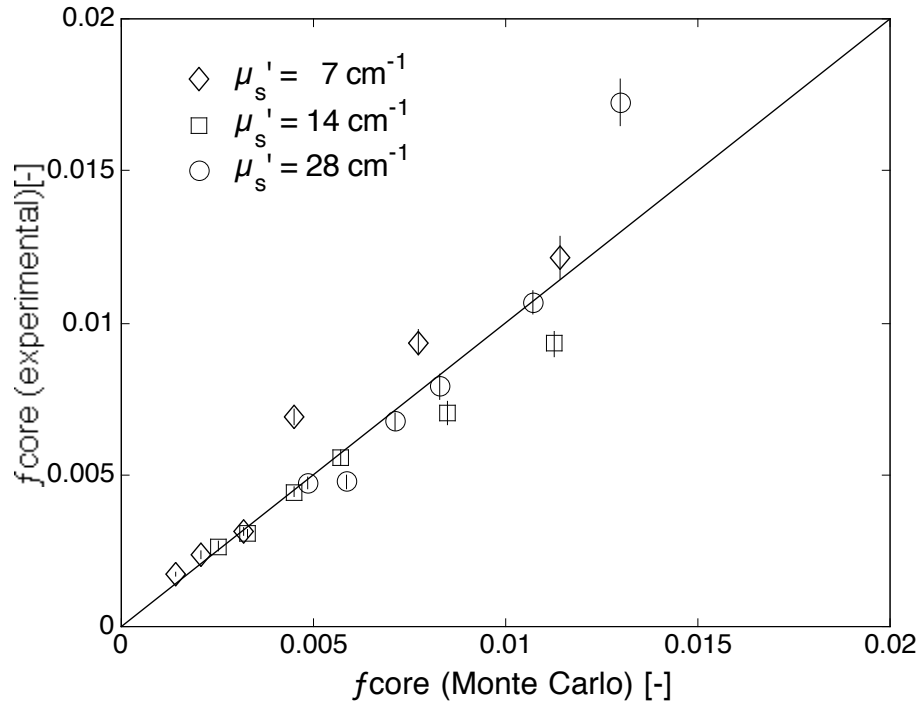
### 3.4 Results

Figure 3.4 shows the results for  $f_{\text{core}}$  determined by Monte Carlo (empty symbols) and experiments (filled symbols) for three  $\mu_s'$  ( $\diamond = 7$ ,  $\square = 14$ , and  $\circ = 28 \text{ cm}^{-1}$ ) and six  $\mu_a$  (0.01, 0.1, 0.4, 0.9, 2.5 and 5  $\text{cm}^{-1}$ , greater  $\mu_a$  to the left). The numerical aperture was 0.22. Experimental data is the mean of seven measurements with standard deviations shown as the vertical bars. The standard errors for all the Monte Carlo data are smaller than the symbols, and hence they are not shown.  $f_{\text{core}}$  is plotted as a function of the non-dimensional parameter  $X$  equal  $(\delta \text{ mfp}')/d^2$  described in materials and methods.



**Fig. 3.4.** – Fraction of collected light ( $f_{\text{core}}$ ) determined by Monte Carlo (empty symbols) and experiments (filled symbols) for three  $\mu_s'$  ( $\diamond = 7$ ,  $\square = 14$ , and  $\circ = 28 \text{ cm}^{-1}$ ) and six  $\mu_a$  (0.01, 0.1, 0.4, 0.9, 2.5 and  $4.9 \text{ cm}^{-1}$ , greater  $\mu_a$  to the left). The fiber diameter was 600  $\mu\text{m}$  and the numerical aperture was 0.22.  $f_{\text{core}}$  [dimensionless] is plotted as a function of the dimensionless parameter  $X = \delta \cdot \text{mfp}' / d^2$ , where  $d$  is fiber diameter,  $\delta = (3 \mu_a (\mu_a + \mu_s'))^{-1/2}$  and  $\text{mfp}' = 1 / (\mu_a + \mu_s')$ . Vertical lines are the standard deviation of the data for three measurements.

The same data from Fig. 3.4 is shown in Fig. 3.5 where the experimental values of  $f_{\text{core}}$  are plotted against the Monte Carlo  $f_{\text{core}}$ . Reduced scattering coefficients ( $\mu_s'$ ) and absorption coefficients ( $\mu_a$ ) are the same of those in Fig. 3.4.



**Fig. 3.5.** – Comparison between the experimental and theoretical (Monte Carlo) values for  $f_{core}$ . Symbols  $\diamond$ ,  $\square$ , and  $\circ$  represent reduced scattering coefficient of 7, 14 and 28  $\text{cm}^{-1}$  for six  $a$  (same as figure 3.4).

Figure 3.6.A shows the theoretical  $f_{core}$  for three optical fiber diameters, an extended set of  $a$  (0.01, 0.05, 0.1, 0.5, 1, 5, 10, 20, 50  $\text{cm}^{-1}$ ) and for  $s'$  of 10  $\text{cm}^{-1}$  (empty symbols) and 20  $\text{cm}^{-1}$  (filled symbols) plotted against  $X$ . Optical fiber diameters are 200  $\mu\text{m}$  (circles), 600  $\mu\text{m}$  (squares) and 2000  $\mu\text{m}$  (diamonds) and the NA was 0.39. Figure 3.6.B shows the same data of figure 3.6.A for  $s'$  of 10  $\text{cm}^{-1}$  (empty symbols) plotted against the reduced mean free path (mf $\mu$ '), demonstrating how the data for different optical fiber diameters spreads if not plotted against  $X$ . The solid line in Fig. 3.6.A is a hyperbolic tangent function that fit the data and can be used to estimate the value of  $f_{core}$ . The hyperbolic tangent function follows the form:

$$f_{core} = C \left( 1 - \frac{1 + \tanh(A(\ln(X) + B))}{2} \right) \quad (3.9)$$

where  $C$  is a term related to  $\eta_c$  (discussed in the next section). For a fiber NA of 0.39, an aqueous gel ( $n = 1.35$ ) and the above range of optical properties  $A = 0.278$ ,  $B = 1.005$  and  $C = 0.0835$ .

Figure 3.7.A illustrates how the optical properties affect the angular dependence of the light collection by plotting the fraction of collected light as a function of the collection angle ( $\theta$ ) for three  $s'$  ( $\diamond = 70$ ,  $\square = 10$  and  $O = 1 \text{ cm}^{-1}$ ) and  $a$  of  $0.05 \text{ cm}^{-1}$ . In the same figure, the dashed lines are plots of  $\cos(\theta)\sin(\theta)$  (see Eq. 3.10 in discussion) and show the similarities of the data to this simple expression for higher scattering and the differences for low scattering. Figure 3.7.B is the integral of Fig. 3.7.A over  $\theta$  and represents the fraction of light that couples to the fiber core for a given acceptance angle (index of refraction of the medium = 1.35). For an acceptance angle of  $15^\circ$  Fig. 3.7.B gives  $R_{\text{core}}$  as defined in the Monte Carlo section of materials and methods. The dashed line is a function of  $\sin^2(\theta)$  as will be shown in equation 3.10 in the discussion.

Theoretical optical fiber collection efficiencies ( $\eta_c$ ) based on Monte Carlo simulations are shown in Fig. 3.8 for a fiber diameter of  $600 \text{ m}$  in contact with a medium with index of refraction of 1.35. Figures A and C show the dependency of the  $\eta_c$  on  $s'$  for different  $a$  (different symbols) and numerical apertures of 0.39 and 0.22, respectively. Using Snell's law the equivalent acceptance angles in the medium are:  $\sin^{-1}(0.39/1.35) = 16.8^\circ$  and  $\sin^{-1}(0.22/1.35) = 9.38^\circ$ . For  $s'$  above  $5 \text{ cm}^{-1}$   $\eta_c$  approaches values of 0.0835 (NA = 0.39) and 0.0266 (NA = 0.22). Figures B and D show the dependency of  $\eta_c$  on  $a$  for different  $s'$  (different symbols) and numerical apertures of 0.39 and 0.22 (in air), respectively.

Changes in the anisotropy ( $g$ ) showed negligible effects on  $\eta_c$  as shown in Fig. 3.9.A. Figure 3.9.B showed a slight decrease in  $f_{\text{core}}$  due to changes in  $g$ . The optical properties ranged from  $a$  of  $0.5$  to  $5 \text{ cm}^{-1}$  and  $s' = 1$  to  $20 \text{ cm}^{-1}$ , fiber diameter was  $600 \text{ m}$  and results for anisotropies of 0.9 (O) and 0.95 ( $\square$ ) were plotted as a function of the results for the same size fiber and anisotropy of 0.83.

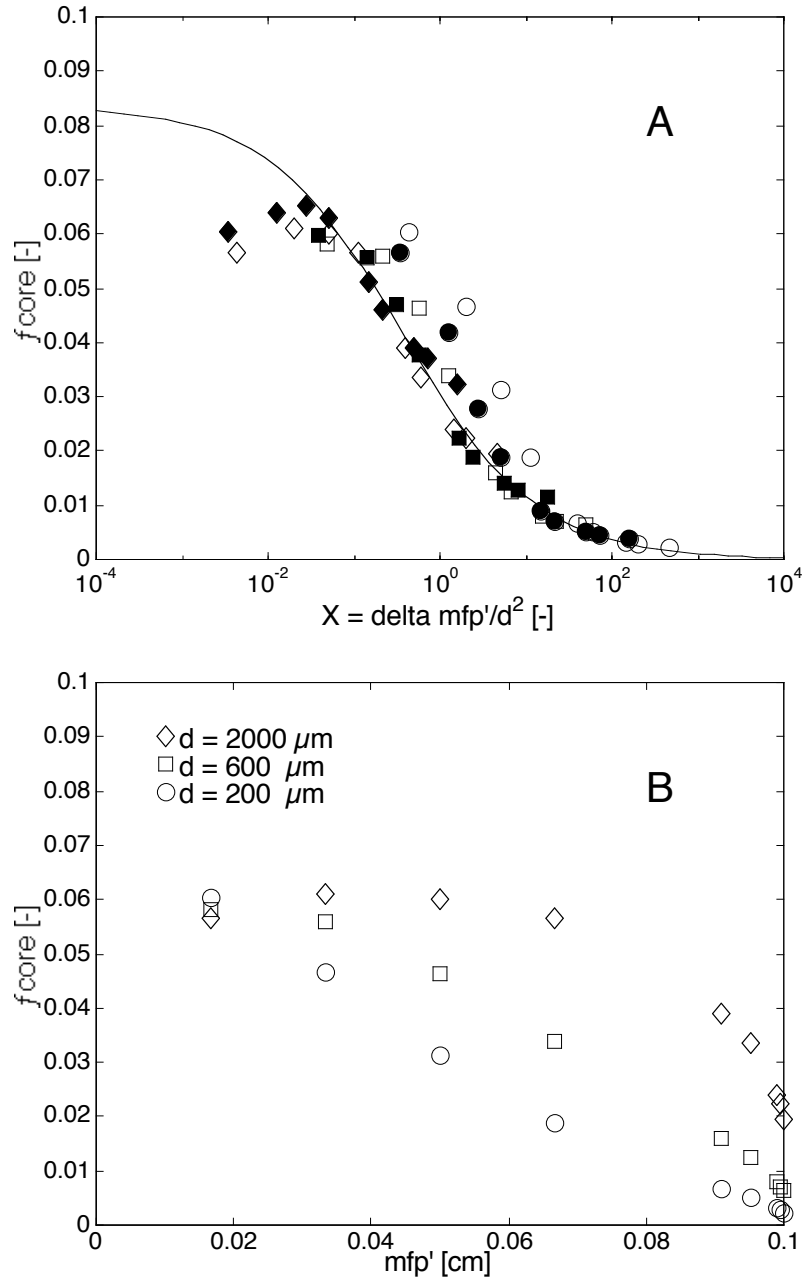


**Fig. 3.6.** – (A) Monte Carlo simulations of  $f_{core}$  for three optical fiber diameters 200  $\mu\text{m}$  (O), 600  $\mu\text{m}$  ( $\square$ ) and 2000  $\mu\text{m}$  ( $\diamond$ ), for  $s'$  of 10  $\text{cm}^{-1}$  (empty symbols) and 20  $\text{cm}^{-1}$  (filled symbols) and for  $a$  ranging from 0.01 to 50  $\text{cm}^{-1}$ . The solid line is hyperbolic tangent function that follows the form  $f_{core} = C(1 - (1 + \tanh(A(\ln(X) + B))) / 2)$ . For a fiber NA = 0.39 and the above range of optical properties  $A = 0.278$ ,  $B = 1.005$  and  $C = 0.0835$ . (B) Same data of Fig. 3.6.A for  $s'$  of 10  $\text{cm}^{-1}$  (empty symbols) plotted against the reduced mean free path ( $\text{mfp}'$ ) for comparison.

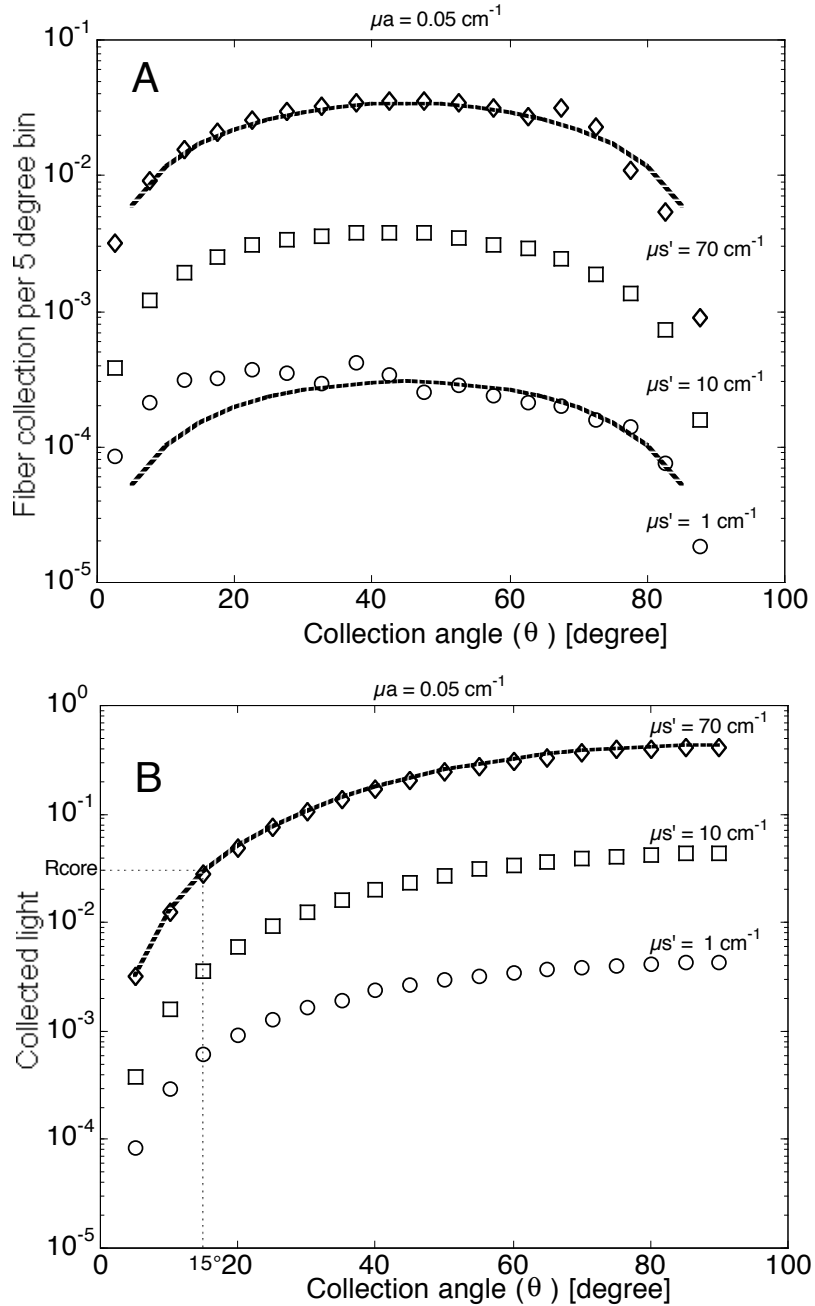


**Fig. 3.7.** – (A) Plot of Monte Carlo simulations of the collected light as a function of the collection angle bin ( $\theta$ ) for three  $\mu_s'$  (70, 10 and  $1 \text{ cm}^{-1}$ , top to bottom) and  $\mu_a$  of  $0.05 \text{ cm}^{-1}$ . Dashed lines are proportional to  $\cos(\theta)\sin(\theta)$  (see Eq. 3.10 in discussion) and show the similarities of the data to this simple expression for higher scattering and the differences for low scattering. (B) Integral of figure 3.7.A over  $\theta$ , representing the fraction of the total incident light that couples to the fiber core ( $R_{\text{core}}$  for a given angle). The dashed line is proportional to  $\sin^2(\theta)$  (see text). The dotted line at  $\theta = 15$  degrees and  $R_{\text{core}} = 0.0266$  for  $\mu_s' = 70 \text{ cm}^{-1}$  correspond to a 600-  $\mu\text{m}$ -dia optical fiber with  $\text{NA} = 0.22$ .

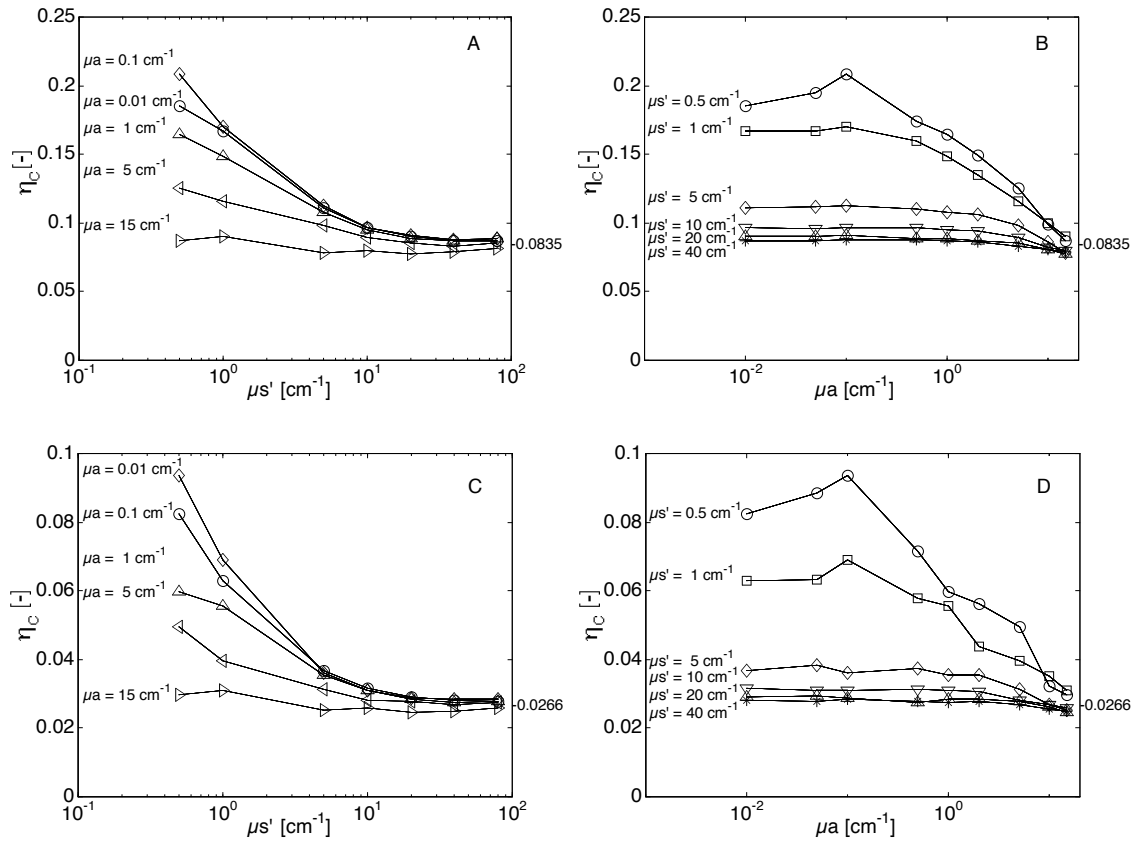


**Fig. 3.8.** – Monte Carlo simulations of the collection efficiency  $\eta_c$  for a fiber diameter of 600 m immersed in a medium with index of refraction of 1.35. (A)  $\eta_c$  as a function of  $s'$  and (B)  $\eta_c$  as a function of  $a$  for NA = 0.39 (acceptance angle of 16.8°). (C)  $\eta_c$  as a function of  $s'$  and (D)  $\eta_c$  as a function of  $a$  for NA = 0.22 (acceptance angle of 9.38°). Values of  $\eta_c$  equal 0.0835 (A and B) and 0.0266 (C and D) are shown for comparison with equation 3.10 (see text).

Figure 3.10.A shows the effect of the angular distribution of the launched photons on  $\eta_c$  for a fixed NA of collection (NA = 0.39). Photons were launched in a uniform angular distribution with a maximum angle given by the maximum launching angle. Data for an absorption coefficient of 1 cm<sup>-1</sup>, reduced scattering coefficients of 5 cm<sup>-1</sup> (empty symbols) and 40 cm<sup>-1</sup> (filled symbols), and the optical fiber diameters of 200 m (O), 600 m (□) and 2000 m (◇) are presented. Figure 3.10.B shows how  $f_{\text{core}}$  changes as a function of the launching angle for the same optical properties and fiber diameters of figure A. The effects of the launching angle are only noticed for angles greater than 30° and are more evident for the lower scattering and small fiber diameters.

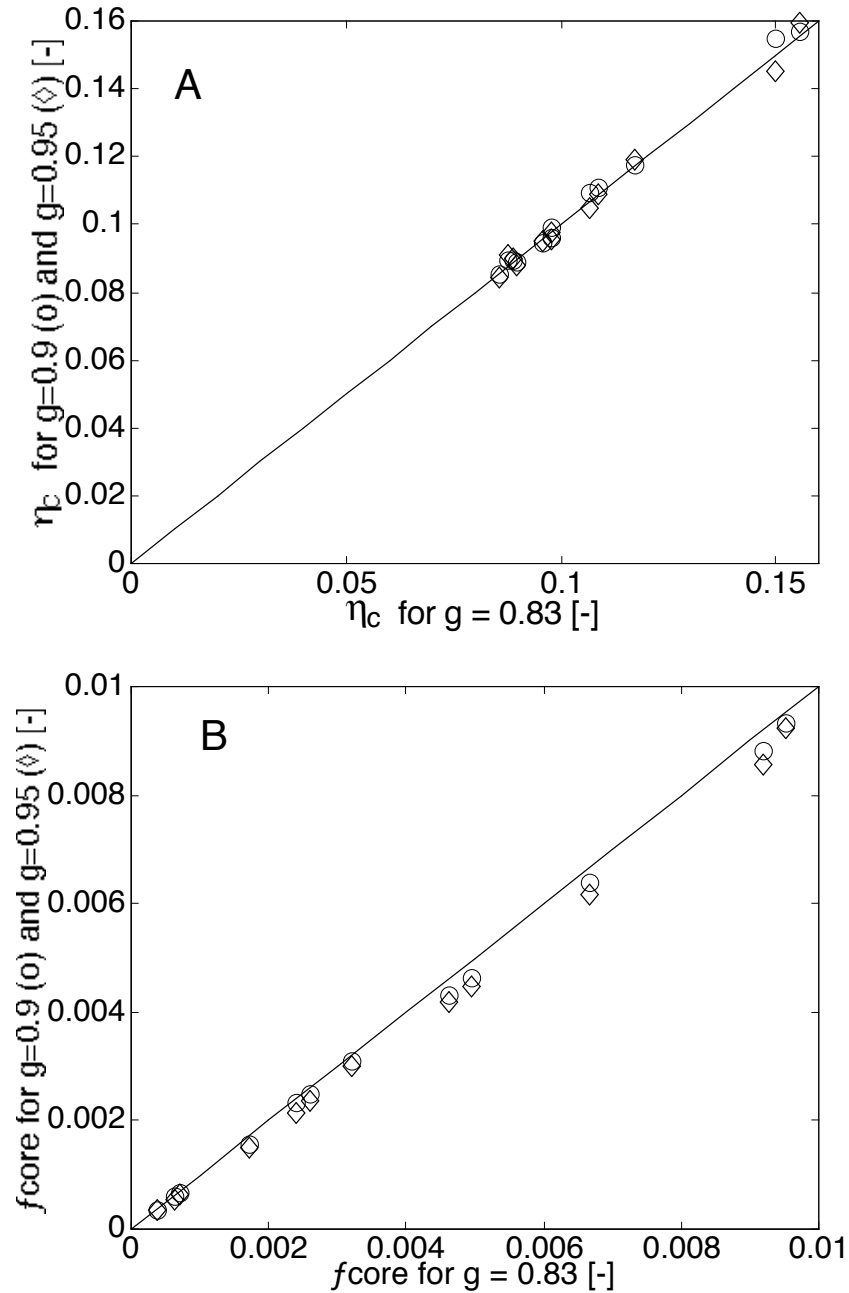


**Fig. 3.9.** – (A) Collection efficiency  $\eta_c$  determined by Monte Carlo simulations for anisotropies of 0.9 (O) and 0.95 ( $\square$ ) plotted as a function of the  $\eta_c$  for anisotropy of 0.83. (B)  $f_{\text{core}}$  determined by Monte Carlo simulations for anisotropies of 0.9 (O) and 0.95 ( $\square$ ) plotted as a function of  $f_{\text{core}}$  for anisotropy of 0.83.  $a$  ranged from 0.5 to 5  $\text{cm}^{-1}$  and  $s$  from 1 to 20  $\text{cm}^{-1}$ . Fiber diameter was 600  $\mu\text{m}$  and  $\text{NA} = 0.39$ .

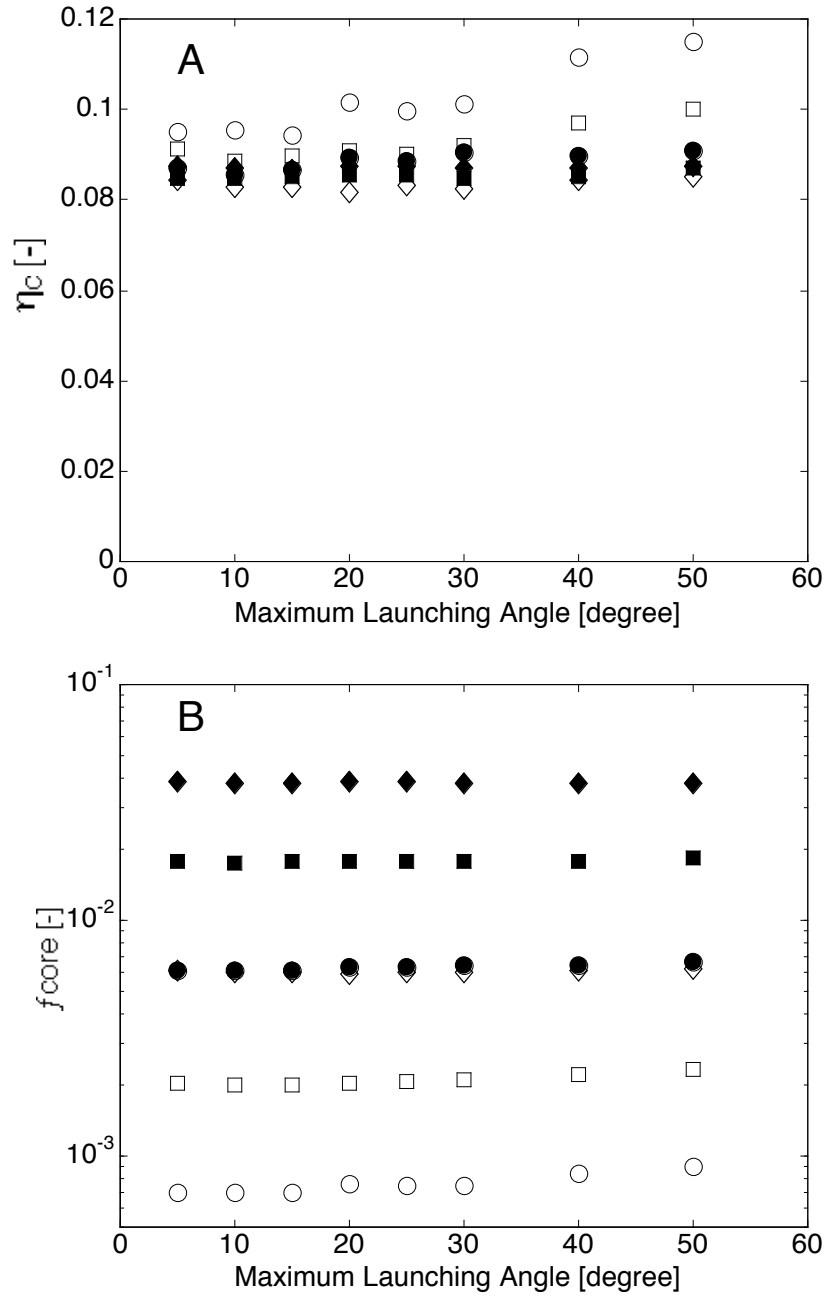


**Fig. 3.10.** – (A) Collection efficiency  $\eta_c$  determined by Monte Carlo simulations as a function of the angular distribution of the launched photons. (B)  $f_{\text{core}}$  determined by Monte Carlo simulations as a function of the angular distribution of the launched photons. NA of collection was fixed to 0.39. Data for absorption coefficient of 1  $\text{cm}^{-1}$ , reduced scattering coefficients of 5  $\text{cm}^{-1}$  (empty symbols) and 40  $\text{cm}^{-1}$  (filled symbols), and the optical fiber diameters of 200  $\mu\text{m}$  (O), 600  $\mu\text{m}$  ( $\square$ ) and 2000  $\mu\text{m}$  ( $\diamond$ ).

### 3.5 Discussion

When performing single optical fiber measurements on scattering samples the specular reflection of launched photons due to the index of refraction mismatch between the optical fiber and the sample is an important fraction of the signal. For that reason the fiber has to be carefully polished and cleaned, and measurements from a clear sample with the same index of refraction should be subtracted from the sample measurements. Three different configurations for the contact between the fiber face and the samples were tested. In a first configuration the fiber was held 2 cm away from its face and the fiber was placed in contact to the sample with the help of a micrometer. The signal detected ( $R_{\text{core}}$ ) varied by as much as 30% depending on the proximity of the fiber face to the surface. The variation was caused by the fiber tip being surrounded by the sample, which violated the flat-surface semi-infinite boundary conditions, drastically changing the detected signal. The second configuration was described in the materials and methods section and used for all the measurements in this study. The fiber was placed in an acrylic support, the fiber face flush with the contact surface, and with a 5x5x2 mm groove surrounding the fiber tip, forming a region of air/gel interface. This configuration had a maximum measurement variation of 5% and an average of 3%. Assuming a maximum variation on the integrating sphere measurements of 3% the propagated maximum experimental error of  $f_{\text{core}}$  was 6% and the average error was 4%. An alternate configuration was the insertion of the optical fiber in the acrylic block without the groove. This configuration showed results equivalent to the second configuration. This configuration, however requires a precise characterization of the material used in the support (acrylic in our case) to account for the proper boundary conditions for the Monte Carlo model.

Comparison between Monte Carlo (empty symbols) and experimental (filled symbols)  $f_{\text{core}}$  in Fig. 3.4 shows agreement for a large range of optical properties. The mean error calculated by  $(f_{\text{core}}^{\text{exp}} - f_{\text{core}}^{\text{MC}}) / f_{\text{core}}^{\text{MC}}$  was 4%. Larger errors (up to 50%) were observed for the measurements on the higher absorption samples (left-most points) for all

sets of reduced scattering samples, probably due to the reduced signal/noise ratio for those measurements. The difference between experiments and model can be better observed in Fig. 3.5.

In general, if the reduced mean free path (mfp') is less than half the optical fiber diameter (d), then  $f_{\text{core}}$  tends to approach a sigmoidal curve when plotted against the non-dimensional parameter X  $((\delta \text{ mfp}')/d^2)$ . Plotting  $f_{\text{core}}$  against X becomes very attractive since minimal effects of the optical fiber diameter can be observed. Plotting  $f_{\text{core}}$  against mfp' alone shows how the data for different fiber diameters spread, as observed in Fig. 3.6.B. A greater advantage of plotting  $f_{\text{core}}$  against X is that the resulting sigmoidal curve is readily approximated by a hyperbolic function (Eq. 3.9), as first proposed by Saidi [72] and Jacques [69]. Their proposed empirical expression was modified by the introduction of the multiplication constant C, which accounts for the maximum fraction of light that can couple to a fiber due to the numerical aperture of the fiber. For mfp' smaller than the fiber diameter the value of C can be approximated by the optical fiber collection efficiency ( $\eta_c$ ).

The parameter  $\eta_c$  (Eq. 3.5) can also be interpreted as the total fraction of light that couples to the optical fiber with an angle smaller than the acceptance angle defined by the fiber NA ( $\theta_a$ ) divided by the total light that enters the fiber face at all angles (Eq. 3.10). As demonstrated in Fig. 3.7.B and in Eq. 3.10,  $\eta_c$  follows the form  $\sin^2(\theta_a)$ .

$$\eta_c = \frac{R_{\text{core}}}{R_{\text{coll}}} = \frac{\int_0^{2\pi} d\phi \int_0^{\theta_a} \cos(\theta) \sin(\theta) d\theta}{\int_0^{2\pi} d\phi \int_0^{\frac{\pi}{2}} \cos(\theta) \sin(\theta) d\theta} = \frac{\pi \sin^2(\theta) \Big|_0^{\theta_a}}{\pi \sin^2(\theta) \Big|_0^{\frac{\pi}{2}}} = \sin^2(\theta_a) \quad (3.10)$$

For numerical apertures of 0.39 and 0.22, and a medium with index of refraction of 1.35,  $\theta_a$  equals  $16.8^\circ$  and  $9.38^\circ$  respectively (see results section). Applying these angles in equation 3.10 gives  $\eta_c$  equal to 0.0835 and 0.0266, respectively. The values of  $\eta_c$  calculated from equation 3.10 are a good first approximation for most optical properties

(especially high reduced scattering coefficients), as shown in Fig. 3.8 A and C. But this equation fails for small values of  $s'$ . In fact,  $\eta_c$  may vary as much as 2 (NA = 0.39) or 3 fold (NA = 0.22) when comparing data for low reduced scattering with data for high reduced scattering.

The usefulness of the parameter  $\eta_c$  in interpreting experimental data is probably best implemented by a theoretical lookup table to account for the coupling of light to the optical fiber since measurement of the light lost in the cladding is difficult. Knowledge of the optical property dependency of  $\eta_c$  can guide the choice of optical fiber systems where  $\eta_c$  is less sensitive to changes in the optical properties (e.g., changing the optical fiber diameter or the optical fiber NA). For a fiber diameter of 600  $\mu\text{m}$  and a  $\mu_a$  of  $0.1\text{ cm}^{-1}$ , the ratios of the collection efficiency between  $s'$  of 1 and  $20\text{ cm}^{-1}$  are 1.87 (NA of 0.39) and 2.41 (NA of 0.22), as shown in Figs. 3.8 A and C. Also, the collection efficiency can be used to understand differences between experimentally measured data and predicted values determined by models that do not account for the effects of the optical fiber. In a practical example, consider a single optical fiber probe being used to detect light from a soft tissue such as the esophagus, with optical properties of  $s' = 5\text{ cm}^{-1}$  and  $\mu_a = 0.5\text{ cm}^{-1}$  at 630 nm [55]. For a 600- $\mu\text{m}$  optical fiber with NA of 0.39 the collection efficiency from Fig. 3.8.B is 0.11, representing a 1.32-fold increase in the light that couples to the optical fiber in comparison to what the fiber NA would predict ( $\eta_c = 0.0835$  from Eq. 3.10). This means that light couples 32% more efficiently to the optical fiber in a medium with these optical properties than it would to a higher scattering medium. The increase in collected light could erroneously be attributed to the light transport in the tissue. For tissues with lower reduced scattering the collection efficiency could be 2-3 fold greater than the predicted by the NA, depending on the optical fiber diameter and the numerical aperture.

The factor  $f_{\text{core}}$  can be used to account for the light coupling to an optical fiber when the total diffuse reflectance is used to normalize the measured data. The advantage of using  $f_{\text{core}}$ , calculated either by the hyperbolic expression or a look up table generated by Monte Carlo simulations, is the reduction of complexity of the model used for interpretation of a single fiber measurement. For example, a simple Monte Carlo code

(not accounting for the optical fiber boundaries) could be used to generate the fluence rate distribution at the surface. This code would be at least 10-fold faster than a Monte Carlo with the optical fiber boundaries because the maximum coupling factor is less than 10% for most commercial optical fibers. Multiplying the fluence rate at the air/tissue boundary by the fiber area and the fiber collection efficiency ( $\eta_c$ ) would give the light coupled to the optical fiber.

The cone of collection of an optical fiber (defined by the fiber NA) is dependent only on the indices of refraction of the fiber core/clad and the medium where the fiber is in contact [75]. Changes in the optical fiber collection efficiency for turbid media arises from differences in the angular distribution of the photons that reach the fiber for different optical properties, as observed in Fig. 3.7.A for low scattering (bottom curve). These changes are not caused by an intrinsic parameter of the optical fiber but arise from its use in a turbid media, like biological tissues. Moffitt and Prahl [60] proposed, as a rule of thumb, that the fraction of collected light by an optical fiber should obey an expression  $1-\cos(\theta_a)$ , with  $\theta_a$  being the fiber acceptance angle defined by NA. Though this expression fits the data for small collection angles,  $\sin^2(\theta_a)$  should be used since it gives a better estimate of the collected light for a larger range of optical properties and NA. In general, if the tissue has a high  $\mu_s'$ , then  $mfp'$  is small and light will be concentrated in front of the optical fiber. However, the angular distribution of the photons escaping the tissue will be closer to uniform and since the collection efficiency is typically a small value (<10% for commercial NA of optical fibers), the amount of light that couples to the fiber is small. On the other hand, if the tissue has a low  $\mu_s'$ , then  $mfp'$  is large and most light coupling to the optical fiber comes from larger depths, thus having shallow angles (smaller than the angle defined by the NA). For that reason a greater proportion of the light that reaches the fiber couples to the fiber and the collection efficiency is greater. The optical fiber collection efficiency has a counter action to the light transport.

The effects of the anisotropy on the collection efficiency of the optical fiber are negligible as long as the reduced scattering coefficient remains the same and the anisotropy is close to 1 (Fig. 3.9.A). Although there is negligible influence of the

anisotropy on the collection efficiency of the fiber, there exists a slight influence in  $f_{\text{core}}$  as observed in Fig. 3.9.B.

The optical fiber collection efficiency ( $\eta_c$ ) was minimally affected by the distribution of launching photons, with negligible effects for maximum launching angles smaller than  $30^\circ$  (which accounts for most commercial optical fibers). Keijzer *et al* [79] showed that the fluence rate distribution is independent of the launching scheme. Our results for an optical fiber confirm those of Moffitt and Prahl [60]. Application of the Monte Carlo model to small size fibers and low reduced scattering showed that, although minimal, the effects of the launching scheme should be considered when working with optical fibers of dimensions close to or smaller than the reduced mean free path. These effects can be observed for a small 200-  $\mu\text{m}$  diameter optical fiber and small reduced scattering ( $s' = 5 \text{ cm}^{-1}$ ) for the empty circles in Fig. 3.10.A. The fraction of collected light for a given fiber diameter is also of importance when defining an optical fiber based system, which can be observed in Fig. 3.10.B when comparing the fraction of collected light for 200  $\mu\text{m}$  (O), 600  $\mu\text{m}$  ( $\square$ ) and 2000  $\mu\text{m}$  ( $\diamond$ ) fiber diameters.

The effects of the optical properties on the optical fiber collection efficiency were examined both experimentally and theoretically. Analytical expressions to determine  $f_{\text{core}}$  and  $\eta_c$  were derived. In both cases prediction of the collection efficiency for low reduced scattering coefficients with the analytical formulas produced poor results (e.g., for  $s' < 7 \text{ cm}^{-1}$  the error between the analytical expression and MC is greater than 30%) highlighting the need for numerical models (e.g., Monte Carlo simulations). The collection efficiency was shown to be an intrinsic problem of the usage of optical fibers in turbid media because the angular distribution of the photons that return to the optical fiber is different for different optical properties. This distribution behaves as  $\cos(\theta_a)\sin(\theta_a)$ , and the amount of collected light behaves as  $\sin^2(\theta_a)$  for high reduced scattering samples ( $s' > 7 \text{ cm}^{-1}$ ). The anisotropy and launching configuration had minimal effects on the collection efficiency. The parameter  $\eta_c$  can be used as a practical guide for choosing optical fiber based systems for biomedical applications.

## **Chapter 4**

# **Optical properties effects upon the collection efficiency of optical fibers in different probe configurations**

### **4.1 Introduction**

\* Optical fibers are an important tool for remote optical measurements and have been extensively used as light delivery and collection tools for optical diagnosis. They have been used in various configurations for the quantitative determination of chromophore concentration [35, 69, 70], tissue optical properties [55, 60], particle sizes [80] and to monitor pharmacokinetics [28]. Two major factors affect the measurement of collected light: (1) light transport from the source to the fiber, and (2) light coupling into the optical fiber (which depends on the angular distribution of photons at the fiber face). Studies of how optical properties affect the intensity of light traveling through a medium have resulted in improved light transport models [22, 30, 33, 71, 81] but little work has been done on light coupling into an optical fiber. Some investigators consider the light coupling to an optical fiber to be part of the light transport model (e.g., including the optical fiber boundaries in Monte Carlo simulations [35, 60]) and don't separate these two factors. Two advantages of separating the light transport problem from the fiber-coupling problem are (1) implementation of simpler models for light transport, and (2)

---

\* This chapter was accepted for publication at IEEE-JSTQE, 2003

better understanding of the influences of the fiber on the detection scheme. The latter may guide the development of improved optical–fiber–based systems.

We have previously demonstrated how the light coupling changes for different optical properties when a single optical fiber is used as source and detector [82] by determining the *optical fiber collection efficiency* ( $\eta_c$ ) as a function of optical properties. The optical fiber collection efficiency was defined for a single optical fiber [82] as the fraction of light that couples to the optical fiber within the fiber's acceptance solid angle ( $R_{core}$ ) divided by all the light that enters the fiber's face ( $R_{core}+R_{clad}$ ). This is illustrated in figure 4.1 and stated in equation 4.1.

$$\eta_c = \frac{R_{core}}{R_{core} + R_{clad}} \quad (4.1)$$

where  $R_{core}$  represents the light that enters the optical fiber core with an angle smaller than the fiber's half angle of acceptance (defined by the numerical aperture, NA) and  $R_{clad}$  represents the light that enters the optical fiber core with an angle greater than the fiber's half angle of acceptance or enters the fiber clad with any angle (hence this portion of the light defined by  $R_{clad}$  escapes through the fiber cladding and is not guided to the detector). The sum  $R_{core} + R_{clad}$  accounts for all the light that enters the fiber face. The same definition of the collection efficiency can be used to multiple fiber configurations.

The parameter  $R_{core}$  can be determined by integrating the radiance (in [W/(cm<sup>2</sup>sr)]) within the solid angle of acceptance ( $\Omega_a$ ) and the fiber-core area ( $S_{core}$ ):

$$R_{core} = \int_{S_{core}} \int_{\Omega_a} L(\vec{r}, \vec{s}) d\Omega dS \quad (4.2)$$

where  $\mathbf{r}$  is the position in the medium and  $\mathbf{s}$  is the direction unit vector.

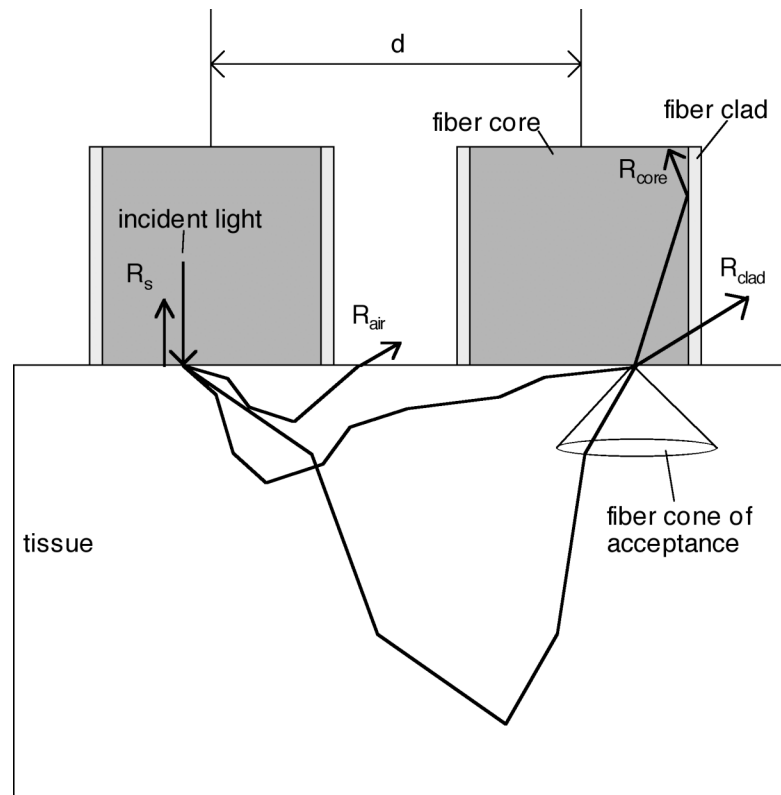


**Fig. 4.1.** – Diagram of the possible return paths of light in a 2-fiber configuration. Light that reaches the fiber face with an angle smaller than the half angle of the acceptance cone will be guided through the fiber to the detector ( $R_{\text{core}}$ ). Light that reach the fiber face with an angle greater than the half angle of the acceptance cone will escape through the fiber cladding ( $R_{\text{clad}}$ ).  $R_{\text{air}}$  is the light that leaves the tissue outside the fiber and  $R_{\text{sp}}$  is the Fresnel reflection due to the fiber/tissue index of refraction mismatch. Light can also be absorbed by the tissue.

The total light that enters the fiber face is determined by integrating the radiance at the fiber face within a solid angle of  $2\pi$  steradians. The collection efficiency will depend on the optical properties and on the probe geometry since the radiance probed by the optical fiber depends on the medium optical properties, the fiber position and the viewing direction. The average depth from which a photon takes its final unscattered step and escapes a highly scattering medium will be concentrated close to the fiber face when the mean free path ( $\text{mfp} = 1/(a + s)$ ) is small in comparison to the fiber diameter. When the photons have been scattered many times the angular distribution of the photons escaping the medium within the area of collection of the fiber will be nearly uniform events. In this case the influence of the medium absorption coefficient and the geometry

imposed by the source-detector fiber separation on the collection efficiency are minimal. However, in a low-scattering medium, the average depth from which a photon takes its final unscattered step and escapes the medium is much deeper in the medium. A greater number of escaping photons within the area of the collection fiber will escape with preferred angles (depending on the probe configuration) making the angular distribution of the escaping photons non-uniform. The fraction of escaping photons entering the fiber within the cone of collection will be strongly influenced by the number of scattering events and by the probe configuration.

Experimental measurements of the light transport for a fixed source-detector fiber separation are compared to models based on the diffusion approximation of the steady-state radiative transport with and without correction for the collection efficiency determined from Monte Carlo simulations. These models will be designed MC-diffusion and diffusion respectively. We demonstrate that by accounting for the collection efficiency the mean square error between model and experiment is reduced from 7.9% to 1.4% as the absorption coefficient varies from 0.1 to 5  $\text{cm}^{-1}$  and the reduced scattering coefficient varies from 4 to 17  $\text{cm}^{-1}$ . The influence of parameters such as the probe configuration, the collection fiber diameter, the numerical aperture, anisotropy of scattering and launching configuration on the collection efficiency was also tested by Monte Carlo simulations.

## **4.2 Material and Methods**

### **4.2.1 Optical Phantoms Preparation and Calibration**

Optical phantoms were prepared using latex microspheres (5100B, 1.03  $\mu\text{m}$  diameter, Duke Scientific, Palo Alto, CA) as scattering elements and India ink (No. 4415, Higgs, Lewisburg, TN) as the absorber. The absorption coefficient of the stock ink was determined with a UV-VIS spectrophotometer (model 8452A, Hewlett-Packard, Palo Alto, CA). The optical properties of the stock microspheres were determined by added-absorber spatially resolved steady-state diffuse reflectance measurements [83] as

discussed in Appendix A. Samples were prepared with microspheres concentrations of 8, 4 and 2% ( $\mu$ ' of 17, 8 and 4  $\text{cm}^{-1}$  at 630 nm) forming three sets with seven samples for each concentration. Different aliquots of India ink were added resulting in final absorption coefficients at 630 nm of 0.1, 0.3, 0.7, 1.0, 2.0 and 5.0  $\text{cm}^{-1}$  for each scattering set. The final sample volume was 40 ml held in a 3-cm diameter by 3-cm height container.

#### 4.2.2 Reflectance Measurements and Analysis

Samples were measured by inserting two independent 600- $\mu\text{m}$  optical fibers (FT600ET, Thorlabs, Newton, NJ), held by a fixed support with a separation distance of 2.5 mm between them, 1.5 cm below the surface inside the media. Fiber tips were carefully aligned to the same height. One fiber was connected to a tungsten-halogen white lamp (LS-1, Ocean Optics, Inc., Dunedin, FL) and the other to a spectrometer (S2000, Ocean Optics, Inc., Dunedin, FL) controlled by a laptop computer. The experimental setup is shown in Fig. 4.2. Acquisition time was 200 ms. Neutral density filters with 1- OD or 2- OD (03FNG057 and 03FNG065, Melles Griot, Irvine, CA) were used to avoid detector saturation.

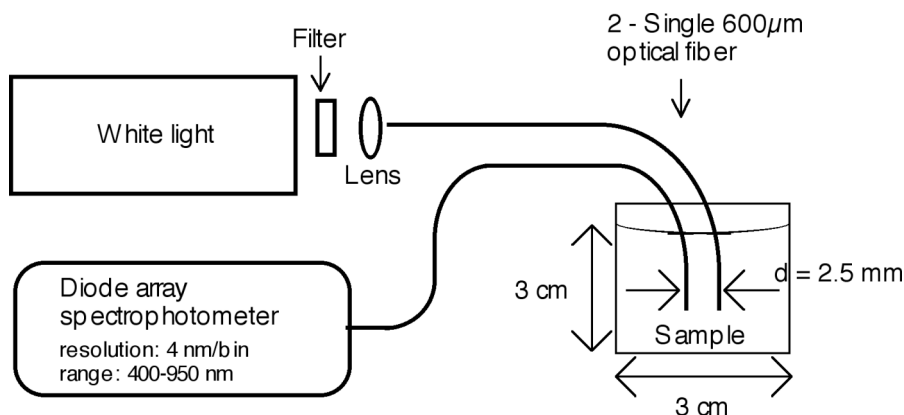


**Fig. 4.2** – Diagram of the experimental setup. A single 600  $\mu\text{m}$  optical fiber is connected to a tungsten-halogen white lamp and the other is connected to a spectrophotometer. The space between the fibers is 2.5 mm. Fiber tips are aligned at the same depth 1.5 cm inside the sample. OD filters are used to avoid detector saturation.

For each microsphere concentration, the experimental measurements were normalized by the measurement of the sample with the lowest absorption coefficient (0.1

cm<sup>-1</sup>). Normalized data were compared to the normalized upward flux at the face of the fiber determined by [17]

$$F_{z^-} = \frac{\phi(r)}{4} - \frac{F(r) \cdot \hat{z}}{2} \quad (4.3)$$

where  $\phi(r)$  is the radial fluence rate and  $F(r)$  is the net flux determine by

$$\phi(r) = \frac{\exp\left(-\frac{r}{\delta}\right)}{4\pi D r} \quad (4.4)$$

$$F(r) = -D\nabla\phi(r) = \frac{z_o}{4\pi} \left(\frac{1}{\delta} + \frac{1}{r_1}\right) \frac{\exp\left(-\frac{r_1}{\delta}\right)}{r_1^2} \quad (4.5)$$

where  $z_o = 1/(a + s)$ ,  $D = z_o/3$ ,  $\delta^2 = D/a$  and  $r_1^2 = z_o^2 + r^2$ . The reference depth ( $z = 0$ ) was assumed to be the fiber face on this analysis. The diffusion upward flux was normalized by the upward flux obtained for the optical properties of the lowest absorption samples for each set of microspheres concentration. The normalized experimental flux was also compared with a Monte Carlo-corrected diffusion equation (MC-diffusion model). For the MC-diffusion model the collection efficiency ( $\eta_c$ ) of the optical fiber obtained from Monte Carlo simulations was used as a multiplicative correction factor on the diffusion model. The MC-diffusion model was normalized in the same way for comparison with the data.

### 4.2.3 Monte Carlo Simulations

Monte Carlo simulations were performed for a set of optical properties to establish  $\eta_c$ . The MC model was described elsewhere [82]. Briefly, photons ( $\geq$  than 1,000,000) were randomly launched uniformly within the radius of the fiber forming a collimated beam into a homogenous medium. Proper boundary conditions were assigned

depending on the medium being infinite or semi-infinite and the probe configuration being a single fiber, two fibers or multiple fibers. Each photon was assigned a weight  $(1-r_{sp})$ , where  $r_{sp}$  is the specular reflectance at the fiber tip, prior to launching and was propagated in the medium by steps with a random stepsize  $d = -\ln(\text{RND})/(a + s)$ , where  $\text{RND}$  was a pseudo-random number uniformly distributed between 0 and 1. After every propagation step the weight of the photon was multiplied by  $(1-a)$ , where  $a = s/(a + s)$ . A new direction was chosen according to the Henyey-Greenstein scattering function [84, 85] in equation 4.6.

$$\cos(\theta) = \frac{1}{2g} \left[ 1 + g^2 - \left( \frac{1 - g^2}{1 - g + 2g\text{RND}} \right)^2 \right] \quad (4.6)$$

The average cosine of the angle of photon deflection by a single scattering event (or anisotropy,  $g$ ) was set to 0.83 for most runs. Different anisotropies were tested to evaluate the model dependence on this parameter.

If a photon crossed an air/sample boundary (in the semi-infinite case) with any escaping angle then the variable  $R_{\text{air}}$  was incremented by a value  $W(1-r_i)$  where  $r_i$  is the internal specular reflection which varies with angle of escape according to Fresnel equations (Eq. 4.7, for unpolarized light) [73] and  $W$  was the photon weight at the moment of escape.

$$R(\theta) = \frac{1}{2} \left[ \frac{\sin^2(\theta_i - \theta_t)}{\sin^2(\theta_i + \theta_t)} + \frac{\tan^2(\theta_i - \theta_t)}{\tan^2(\theta_i + \theta_t)} \right] \quad (4.7)$$

If the photon crossed a sample/fiber boundary with an escaping angle smaller than the half angle defined by the NA of the fiber (e.g.,  $\text{NA} = 0.39$ ), the escaping photon weight incremented the variable  $R_{\text{core}}$ . If the photon crossed a sample/fiber boundary with an escaping angle greater than the angle defined by the NA of the fiber, the escaping photon weight incremented the variable  $R_{\text{clad}}$ . In the Monte Carlo code the size of optical

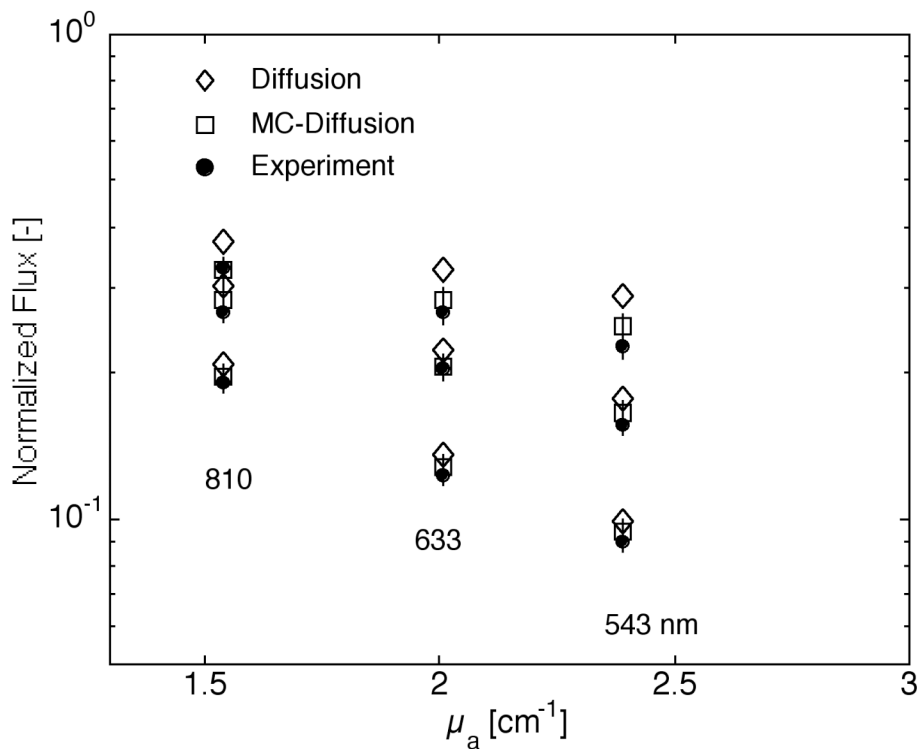
fiber cladding was neglected for simplification. Escaping angles were corrected according to Snell's law to account for the refractive index mismatched at the boundary. The photon was returned to the tissue with the remaining weight ( $r_iW$ ) and continued propagating until being terminated according to the roulette method [40, 42, 74] to conserve energy. Values of  $\eta_c$  were determined by combining the values of the bins  $R_{core}$  and  $R_{clad}$  according to equation 4.1.

In a first experiment  $\eta_c$  was determined for a large range of optical properties with the same parameters of the experimental setup (two-fibers configuration in an infinite medium, fiber separation of 2.5 mm, fiber diameter 600  $\mu$ m and NA of 0.39). In a second test the two-fiber configuration in an infinite medium was compared to the two-fiber configuration in contact with a semi-infinite medium and with a multiple-fiber configuration in contact with a semi-infinite medium. The multiple-fiber configuration was implemented by a central source fiber surrounded by a ring of collection fibers. The other parameters were kept the same. The influence of the fiber separation was determined in a third experiment with the multiple-fiber configuration in contact with a semi-infinite medium. Distance between the source and collection fibers was varied from 0 to 5 mm. The condition for the separation equals to zero is equivalent to the special case of a single fiber used as source and detector. Fiber diameter was 600  $\mu$ m and the NA was 0.39. A fourth experiment was done to evaluate the influence of the collection fiber diameter on  $\eta_c$ . For this test the diameter of the source fiber was kept constant at 600  $\mu$ m and the diameter of the collection fiber was varied from 100  $\mu$ m to 2 mm. These tests were performed for the multiple-fiber configuration in contact with a semi-infinite medium and separation between the central fiber and the center of the ring of 2.5 mm. The NA was kept constant at 0.39. A fifth experiment was done to evaluate the influence of the numerical aperture on  $\eta_c$ . This experiment was performed for the multiple-fiber configuration in contact with a semi-infinite medium, with separation between the central fiber and the center of the ring of 2.5 mm and with source and collection fiber diameters of 600  $\mu$ m. Simulations were also made to evaluate the influence of the anisotropy and

the launching configuration in the source fiber. For all simulations the index of refraction of the sample ( $n_s$ ) and fiber ( $n_f$ ) were fixed at 1.335 and 1.458, respectively.

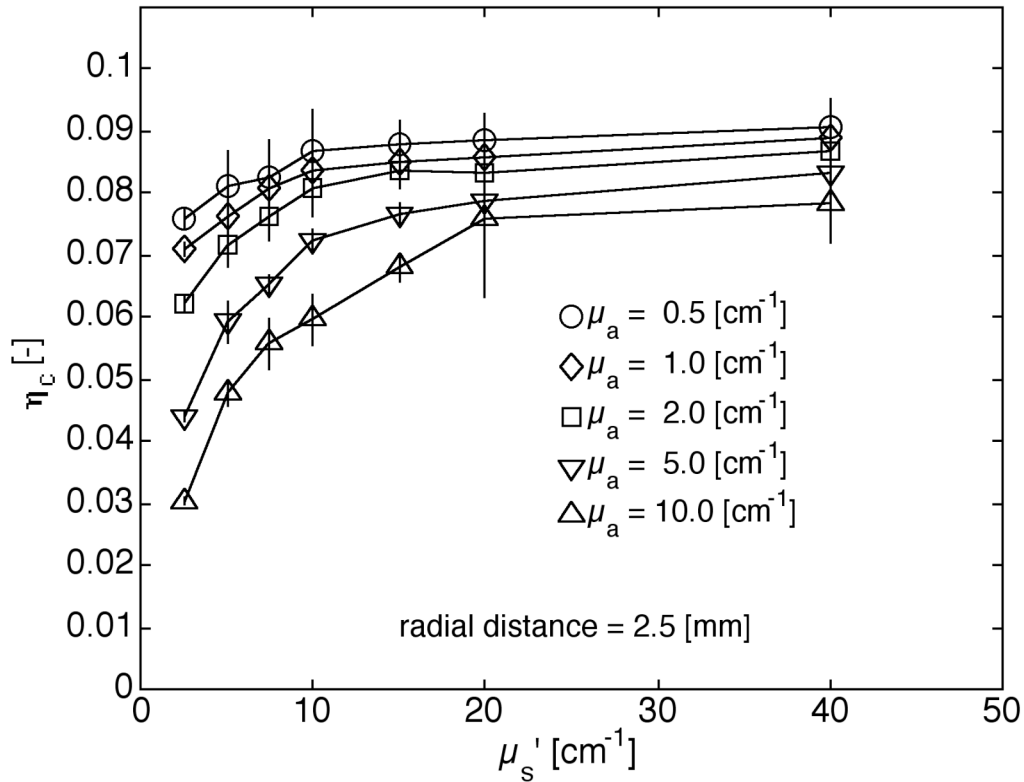
### 4.3 Results

Figure 4.3 shows the results for the normalized upward flux as a function of the absorption coefficient. Each cluster of three different symbols represents the normalized upward flux determined by experiment ( $\bullet$ ), diffusion approximation ( $\diamond$ ) and by the MC-diffusion model ( $\square$ ). Measurements on 3 samples of the 3x6 matrix are shown with three wavelengths (532, 633 and 810 nm) for each sample. The reduced scattering coefficients at 633 nm were 4, 8 and 17  $\text{cm}^{-1}$  (top to bottom). Error bars are shown for the experiment and for the MC-diffusion model as vertical lines. Mean square errors of 7.9 and 1.4% (with maximum errors up to 93 and 38%) were determined between diffusion and experiment and between MC-diffusion and experiment, respectively.



**Fig. 4.3.** – Normalized upward flux as a function of the absorption coefficient. The reduced scattering coefficients at 633 nm were 4, 8 and 17  $\text{cm}^{-1}$  (top to bottom). Vertical lines for the experiment and for the MC-diffusion model are the standard deviation of 5 measurements.

Collection efficiencies for 2 fibers in an infinite medium with no boundary were determined by Monte Carlo simulations and are shown in Fig. 4.4 for different optical properties. These values were used to modify the diffusion model into the MC-diffusion model shown in figure 4.3. Error bars are the standard deviation of 5 Monte Carlo runs with different random number seeds and 1,000,000 photons launched per run. The separation between the source and collection fibers was 2.5 mm, fiber diameters were 600  $\mu\text{m}$  and the NA was 0.39.



**Fig. 4.4.** – Collection efficiency ( $\eta_c$ ) determined by Monte Carlo simulations plotted as a function of optical properties for a 2-fibers configuration embedded in a infinite medium. These values were used to modify the diffusion model into the MC-diffusion model shown in figure 4.3. Error bars are the standard deviation of 5 Monte Carlo runs with different random number seeds. The separation between the source and collection fibers was 2.5 mm, fiber diameters were 600  $\mu\text{m}$  and the NA was 0.39.

Similar data was obtained for 2 fibers placed on the surface of a semi-infinite medium with an air/medium boundary (filled symbols) and for a multiple fiber probe

with a central source fiber surrounded by an annular detection ring placed on the surface of a semi-infinite medium with air/medium boundary (doubled symbols). These configurations are compared to the 2-fibers configuration in a infinite medium (empty symbols) in Fig. 4.5. Data for the infinite medium configuration are plotted artificially skewed of  $-0.2 \text{ cm}^{-1}$  and data for the multiple fiber probe are plotted artificially skewed of  $+0.2 \text{ cm}^{-1}$  to help visualization. Error bars are the standard deviation of 5 Monte Carlo runs. The separation between the source and collection fibers was 2.5 mm, fiber diameters were 600  $\mu\text{m}$  and the NA was 0.39.

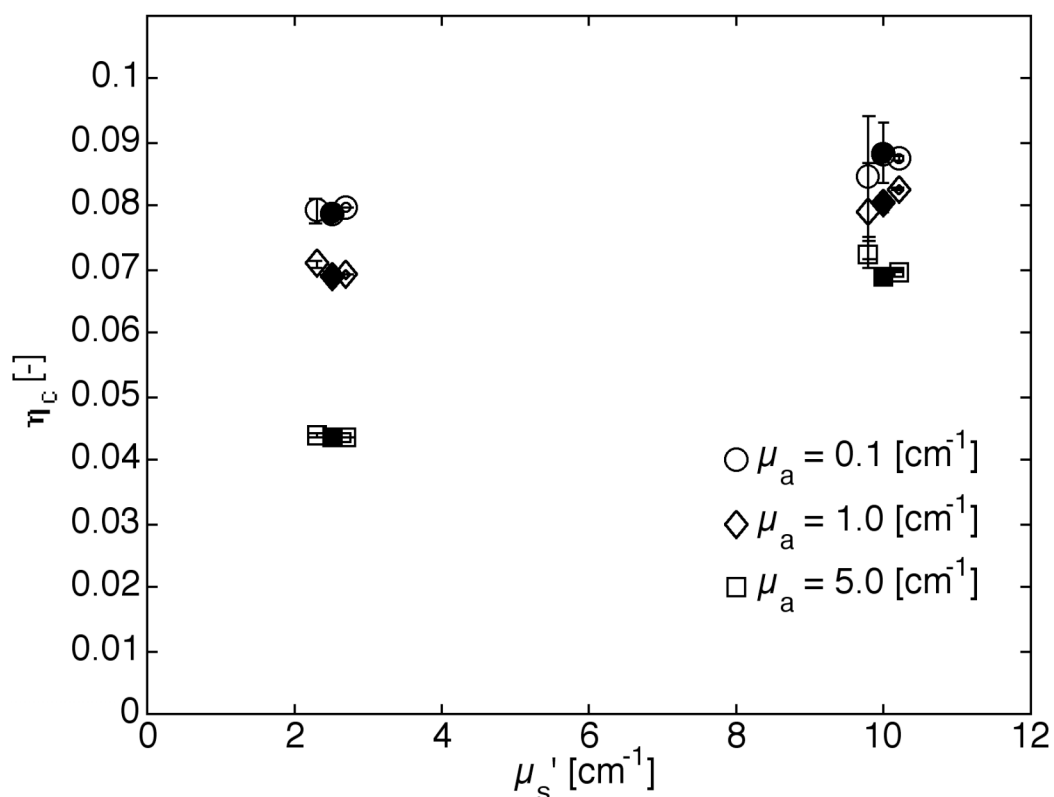


**Fig. 4.5.** – Comparison between the collection efficiency determined by Monte Carlo simulations for 2 fibers in contact to an infinite medium with no boundaries (empty symbols), 2 fibers in contact to a semi-infinite medium with an air/medium boundary (filled symbols) and a multiple fiber probe with a central source fiber surrounded by an annular detection ring placed on the surface of a semi-infinite medium with air/medium boundary (doubled symbols). Data for the infinite medium configuration are plotted artificially skewed of  $-0.2 \text{ cm}^{-1}$  and data for the multiple fiber probe are plotted artificially skewed of  $+0.2 \text{ cm}^{-1}$  to help visualization. Error bars are the standard deviation of 5 Monte Carlo runs. The separation between the source and collection fibers was 2.5 mm, fiber diameters were 600  $\mu\text{m}$  and the NA was 0.39.

Collection efficiencies as a function of optical fiber separation are shown in Fig. 4.6 for the multiple-fiber probe with a central source fiber surrounded by an annular detection ring placed on the surface of a semi-infinite medium with air/medium boundary. Fig. 4.6.A is the special case of a single fiber used as source and detector. Drawings on top of the figures represent a front view of the face of the probes.

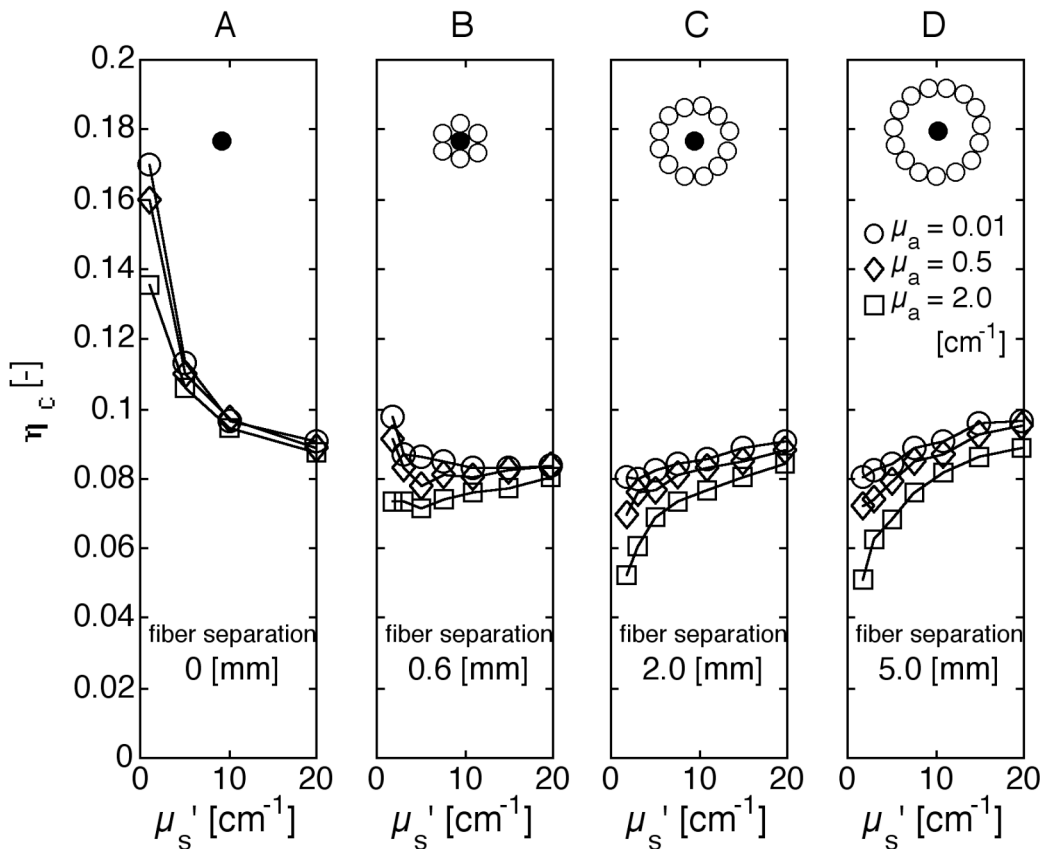


**Fig. 4.6.** - Collection efficiency determined by Monte Carlo simulations as a function of optical fiber separation for the multiple fiber probe with a central source fiber surrounded by an annular detection ring placed on the surface of a semi-infinite medium with air/medium boundary. Fig. 4.6.A is the special case of a single fiber used as source and detector. Drawings on top of the figures represent a front view of the face of the probes.

The influence of the diameter of the collection optical fiber on  $\eta_c$  was determined for the multiple-fiber probe configuration as shown in Fig. 4.7. The source fiber was kept with a diameter of 600  $\mu$ m, separation between the source and collection fibers was 2.5 mm and the NA was 0.39. Coincidentally the values of  $\eta_c$  for  $\mu_s'$  of 2.5 cm<sup>-1</sup> and  $\mu_a$  of 1

$\text{cm}^{-1}$  (empty circles) overlap with the values obtained for  $s'$  of  $10 \text{ cm}^{-1}$  and  $a$  of  $5 \text{ cm}^{-1}$  (filled diamonds).

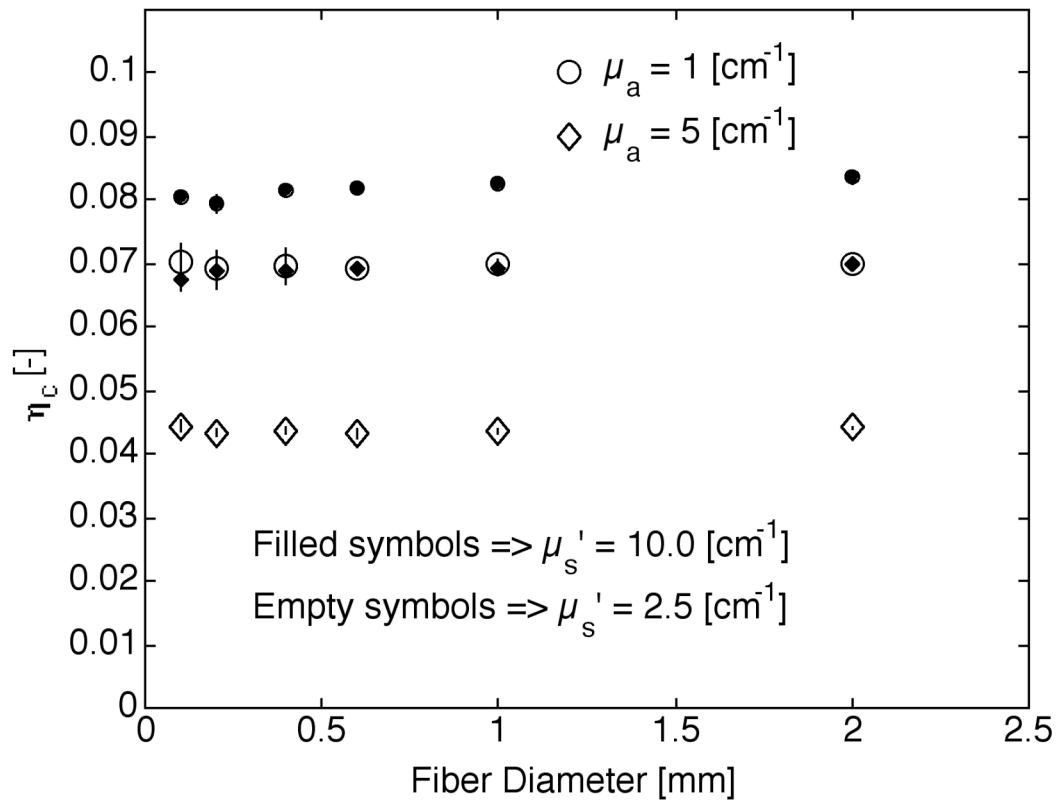


**Fig. 4.7.** - Influence of the diameter of the collection optical fiber on  $\eta_c$  determined for the multiple fiber probe configuration. The source fiber was kept with a diameter of 600  $\mu\text{m}$ , separation between the source and collection fibers was 2.5 mm and the NA was 0.39. Values of  $\eta_c$  for  $s'$  of  $2.5 \text{ cm}^{-1}$  (empty symbols) and for  $s'$  of  $10 \text{ cm}^{-1}$  (filled symbols) are shown. Error bars are the standard deviation of 5 Monte Carlo runs and in most cases are smaller than the symbols.

Fig. 4.8 shows the influence of the numerical aperture on  $\eta_c$ . The chosen NA for these experiments were those of commercial optical fibers (0.22, 0.39 and 0.48) [76]. The numerical apertures were corrected by the refractive index of the medium ( $n_{\text{sample}} = 1.335$ ) to account for the effective cone of collection of the optical fiber. Dashed lines are the values obtained from Eq. 4.8 (in discussion section) for the corrected NAs. Values of  $\eta_c$  for  $s'$  of  $2.5 \text{ cm}^{-1}$  and  $a$  of  $1 \text{ cm}^{-1}$  (empty circles) coincidentally overlap with the values obtained for  $s'$  of  $10 \text{ cm}^{-1}$  and  $a$  of  $5 \text{ cm}^{-1}$  (filled diamonds).

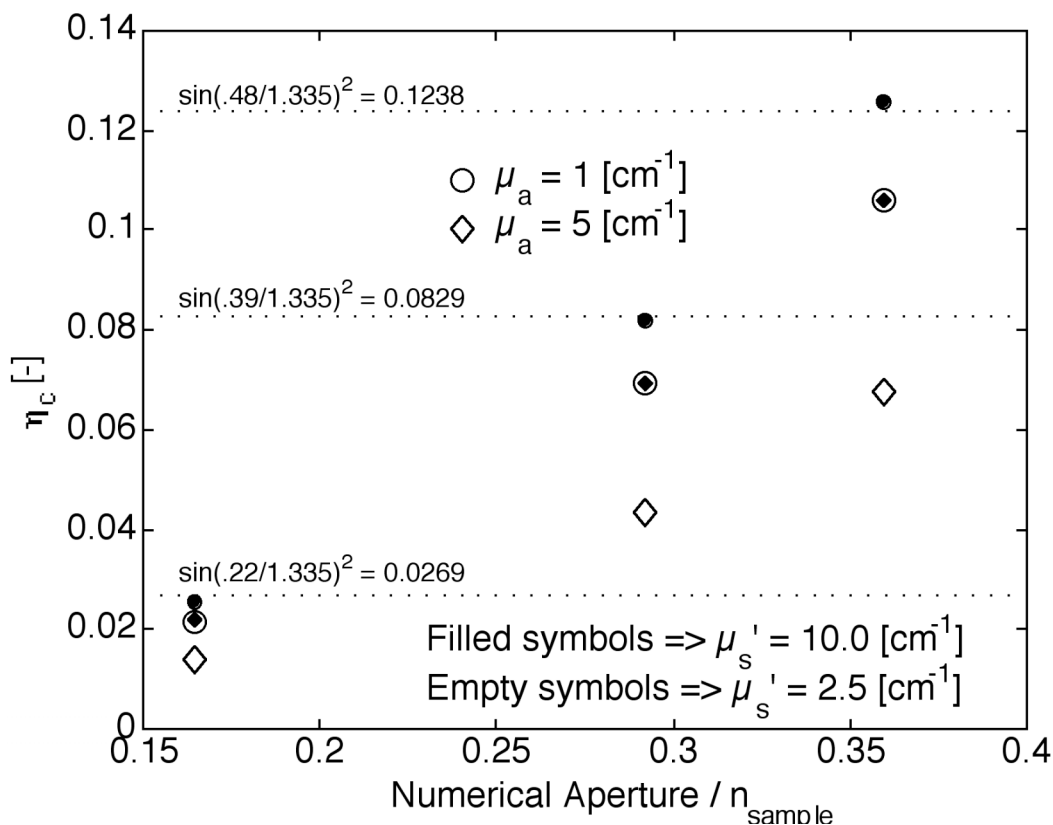


**Fig. 4.8.** – Collection efficiency plotted as a function of numerical aperture of commercially available optical fibers (NA = 0.22, 0.39 and 0.48). The numerical apertures were corrected by the refractive index of the medium ( $n_{\text{sample}} = 1.335$ ) to account for the effective cone of collection of the optical fiber. Dashed lines are the values obtained from Eq. 4.8 (in discussion section) for the corrected NAs. Fiber diameter was 600  $\mu\text{m}$  and fiber separation was 2.5 mm.

#### 4.4 Discussion

The normalized upward flux in Fig. 4.3 showed that the MC-diffusion model predicted experimental values better than the diffusion model. The mean square error for the experimental versus diffusion model comparison was 7.9% and for the experimental versus MC-diffusion was 1.4%. For higher absorption coefficients the square error can increase to as much as 93 and 38% for the diffusion and MC-diffusion comparison, respectively. Larger errors were observed for the measurements on the higher absorption samples for all sets of reduced scattering samples.

The parameter  $\eta_c$  (Eq. 4.1) can be interpreted as the total fraction of light that couples into the optical fiber at an angle smaller than the acceptance angle defined by the fiber NA ( $\theta_a$ ) divided by the total light that enters the fiber face at all angles (Eq. 4.8). We have demonstrated that  $\eta_c$  follows the form  $\sin^2(\theta_a)$  for single fibers used simultaneously as source and detector [82].

$$\eta_c = \frac{R_{core}}{R_{coll}} = \frac{\int_0^{2\pi} d\phi \int_0^{\theta_a} \cos(\theta) \sin(\theta) d\theta}{\int_0^{2\pi} d\phi \int_0^{\frac{\pi}{2}} \cos(\theta) \sin(\theta) d\theta} = \frac{-\pi \sin^2(\theta) \Big|_0^{\theta_a}}{-\pi \sin^2(\theta) \Big|_0^{\frac{\pi}{2}}} = \sin^2(\theta_a) \quad (4.8)$$

For numerical apertures of 0.39 and a medium with index of refraction of 1.33,  $\theta_a$  equals  $17^\circ$ . Applying this angle in equation 4.8 gives  $\eta_c$  equal to 0.086. The values of  $\eta_c$  calculated from equation 4.8 are a good first approximation for most optical properties (especially high reduced scattering coefficients). But they do not agree for small values of  $s'$ . In fact,  $\eta_c$  may vary as much as 2-fold when comparing data for low reduced scattering with data for high reduced-scattering coefficients as observed in Fig. 4.4.

The cone of collection of an optical fiber (defined by the fiber NA) is dependent only on the indices of refraction of the fiber core/clad and the medium where the fiber is in contact [75]. Changes in the optical fiber collection efficiency for turbid media arises from differences in the angular distribution of the photons that reach the fiber for different optical properties. These changes are not caused by an intrinsic parameter of the optical fiber but arise from its use in a turbid media, such as biological tissues. As a rule of thumb the fraction of light collect by an optical fiber in a highly scattering medium can be approximated by the  $\sin^2(\theta_a)$  rule determined for a single fiber used as source and detector. For multiple-fiber probes the  $\sin^2(\theta_a)$  rule is not as accurate as for the single fiber case. This occurs because of the introduction of the extra geometrical parameter of the source detector fiber separation. The discrepancies become greater for increased absorption. For small-diameter single fibers the changes in absorption are less noticeable

especially for high reduced scattering coefficients due to the probing volume being very small so that the pathlength for absorption to exert its effect is short. There exist a transition in behavior of  $\eta_c$  as a function of the separation between source and detector as shown in Fig. 4.6. For large source detector separations the collection efficiency decreases for small reduced scattering coefficients (by as much as 2-fold) and approach the value of  $\sin^2(\theta_a)$  for high reduced scattering coefficients (Figs. 4.6.C and D). For the very common probe with six fibers around one  $\eta_c$  is less dependent on the reduced scattering coefficient (Figs. 4.6.B). For a single fiber used as source and detector  $\eta_c$  behaves differently than for the case of 2 or more fibers with separation. In fact the opposite trend is obtained for low reduced scattering coefficients and a 2-fold increase in  $\eta_c$  can be obtained.

No significant change in  $\eta_c$  was obtained when different multi-fiber probe geometries were tested as shown in Fig. 4.5. The influence of the diameter of the collection fiber on  $\eta_c$  was also negligible (Fig. 4.7). Figure 4.8 shows that independently of the optical fiber numerical aperture  $\eta_c$  approaches the value of  $\sin^2(\theta_a)$  for high reduced scattering coefficients.

The effects of the anisotropy on the collection efficiency of the optical fiber are negligible as long as the reduced scattering coefficient remains the same and the anisotropy is close to 1. We have tested the influence of the launching angle on the optical fiber collection efficiency ( $\eta_c$ ) and verified negligible effects. Keijzer et al. [79] showed that the fluence rate distribution is independent of the launching scheme. Our results for a single optical fiber confirm those obtained independently by Moffitt and Prahl [60].

## 4.5 Conclusions

The parameter  $\eta_c$  is probably best implemented by a Monte Carlo generated lookup table to account for the coupling of light to the optical fiber since measurement of the light lost in the cladding is difficult. Knowledge of the optical property dependency of  $\eta_c$  can guide the choice of optical fiber systems to yield a  $\eta_c$  that is less sensitive to

changes in the optical properties (e.g., changing the optical fiber diameter or the optical fiber NA). Also, the collection efficiency can be used to understand differences between experimentally measured data and predicted values determined by models that do not account for the effects of the optical fiber coupling as shown in figures 4.3. Prediction of the collection efficiency for low reduced scattering coefficients with the analytical formula (Eq. 4.8) produced poor results highlighting the need for numerical models (e.g., Monte Carlo simulations). The collection efficiency is an intrinsic problem for the usage of optical fibers in turbid media deriving from the fact that the angular distribution of the photons that return to the optical fiber is different for different optical properties. For highly scattering samples and a single optical fiber this distribution behaves as  $\cos(\theta_a)\sin(\theta_a)$ , and the amount of collected light behaves as  $\sin^2(\theta_a)$ . For multiple fiber configurations the collection efficiency slightly deviates from this  $\sin^2(\theta_a)$  rule and is particularly influenced by the absorption coefficient of the sample. Nevertheless this rule of thumb provides a good estimate of the collection efficiency of the optical fiber when highly scattering samples are being measured. The collection efficiency behaves similarly for different multiple fiber probe configurations. For a single fiber used as source and detector the behavior of  $\eta_c$  is drastically changed. Negligible changes in  $\eta_c$  were observed for changes in the diameter or the numerical aperture of the collection fiber. The anisotropy of single scattering and the launching configuration had minimal effects on the collection efficiency. The parameter  $\eta_c$  can be used as a practical guide for choosing optical fiber based systems for biomedical applications.

## Chapter 5

# ***In vivo* determination of optical penetration depth and optical properties of normal and tumor tissue with white light reflectance during endoscopy**

### 5.1 Introduction

Determination of tissue optical properties is fundamental for application of light in either therapeutical or diagnostics procedures. Methods to accurately determine optical properties can lead to optical diagnostics tools [86], improvements in laser surgery [15, 46], quantitative determination of chromophore [87] and fluorophore [22] concentrations, drug pharmacokinetics [28] and improvements on Photodynamic Therapy (PDT) dosimetry [14]. The latter is of particular interest for this study.

A simple rule of thumb for PDT dosimetry that specifies the depth of tissue necrosis during PDT was offered by Jacques [14-16]. In a planar geometry the depth of tissue necrosis is related to the natural logarithm of treatment light as it penetrates into the tissue,

$$z_{necrosis} = \delta \ln \left( \frac{E_0 t k \epsilon C b \Phi f}{R_{th}} \right) \quad (5.1)$$

where

$E_o$	[W/cm <sup>2</sup> ]	irradiance of treatment light onto the tissue surface,
$t$	[s]	exposure time for treatment light,
$\delta$	[cm]	optical penetration depth of treatment light,
$k$	[dimensionless]	augmentation of light at surface due to backscatter from tissue,
$z_{\text{necrosis}}$	[cm]	depth of the margin for zone of necrosis,
$\epsilon$	[cm <sup>-1</sup> /(mg/g)]	extinction coefficient of photosensitizing drug,
$C$	[mg/g]	concentration of photosensitizing drug,
$b$	[ph/J]	photons per joule of light energy at treatment wavelength,
$\Phi$	[dimensionless]	quantum efficiency for generation of oxidizing species,
$f$	[dimensionless]	fraction of oxidizing species that attack critical sites that contribute to cell death,
$R_{\text{th}}$	[moles/liter]	threshold concentration of critical oxidation attacks for cell death.

It should be noted that  $z_{\text{necrosis}}$  is linearly proportional to the optical penetration depth  $\delta$  but proportional to the logarithm of all other factors. Hence, to double the size of  $z_{\text{necrosis}}$ , one must double  $\delta$  but must alter any other factor by a factor of 7.4. The practical consequence of Eq. 5.1 is that the optical properties of a tissue influence  $\delta$  and have a primary effect on the depth of treatment. For example, a tissue that is highly inflamed has a high blood content whose hemoglobin absorbs the treatment light and reduces  $\delta$  and therefore  $z_{\text{necrosis}}$ . Patients who present target tissues with variable degrees of inflammation are expected to have variable PDT treatment zones if all other PDT dosimetry factors are constant.

The tissue optical properties that influence light transport in tissue are the absorption coefficient,  $a$  [cm<sup>-1</sup>], and the reduced scattering coefficient,  $s'$  [cm<sup>-1</sup>] [18]. The optical penetration depth,  $\delta$  [cm], is related to  $a$  and  $s'$ :

$$\delta = \frac{1}{\sqrt{3\mu_a(\mu_a + \mu'_s)}} \approx \frac{1}{\sqrt{3\mu_a\mu'_s}} \quad (5.2)$$

The value  $\mu'_s$  is usually at least 10-fold greater than the value of  $\mu_a$  in the diffusion limit. If  $\mu'_s$  is comparable to or less than  $\mu_a$ , then diffusion theory no longer holds and  $\delta$  approaches the value  $1/\mu_a$  rather than the value  $1/\mu_a\sqrt{3}$ . In this report, we will assume that  $\mu'_s$  comfortably exceeds  $\mu_a$ . A change in the blood content of a tissue will cause a proportional change in  $\mu_a$ , and  $\delta$  will change as the square root of the change in blood content. Since the PDT treatment zone is proportional to  $\delta$ , we expect that the treatment zone will vary as much as the square root of the degree of tissue inflammation.

Experimental determination of tissue optical properties has been proposed using different methodologies. Integrating sphere [41, 44-46], frequency domain diffuse reflectance [49, 50], time domain diffuse reflectance [47-49], optoacoustic [51] and spatially resolved steady-state diffuse reflectance [43, 55] are among the most widely used. Each technique has its own advantages and disadvantages. In this work we implemented a spatially resolved steady-state diffuse reflectance method where only two fibers (one source and one detector) spaced 2.5 mm apart are used for the determination of the optical properties. The method relies on the spectral characteristics of the tissue chromophores (water, dry tissue and blood) to determine the absorption coefficient and on a simple wavelength dependent expression ( $\mu'_s = a\lambda^{-b}$ ) [81] for the determination of the reduced scattering coefficient. Advantages of using this method are the inexpensive equipment involved and the simplicity of the measurements.

## 5.2 Theory

When performing the analysis of reflectance measurements one has to decide upon a light transport model to determine how light from the source fiber reaches the collection fiber. A simple approach is to use the diffusion approximation of the steady-state radiative transport equation and calculate the net flux escaping the sample at a radial distance  $r$  from the source as demonstrated by Farrel [43] and shown in equation 5.3.

$$R(r) = z_o \left( \frac{1}{\delta} + \frac{1}{r_1} \right) \frac{e^{-\frac{r_1}{\delta}}}{r_1^2} + (z_o + 4AD) \left( \frac{1}{\delta} + \frac{1}{r_2} \right) \frac{e^{-\frac{r_2}{\delta}}}{r_2^2} \quad (5.3)$$

where  $z_o = 1/(a + s')$ ,  $D = z_o/3$ ,  $\delta^2 = D/a$ ,  $r_1^2 = z_o^2 + r^2$ ,  $r_2^2 = (z_o + 4AD)^2 + r^2$  and  $A = (1 + r_i)/(1 - r_i)$ . The term  $r_i$  is the internal reflection due to the refractive index mismatch at the surface. Walsh (see Ryde [88]) developed an exact analytical expression for the case where  $n_i$  (the refractive index of the medium of the incident ray) is smaller than  $n_t$  (the refractive index of the medium of the transmitted ray) given by Eq.5.4

$$r_i = \frac{1}{2} + \frac{(m-1)(3m+1)}{6(m+1)^2} + \left[ \frac{m^2(m^2-1)^2}{(m^2+1)^3} \right] \ln \left( \frac{m-1}{m+1} \right) - \frac{2m^3(m^2+2m-1)}{(m^2+1)(m^4-1)} + \left[ \frac{8m^4(m^4+1)}{(m^2+1)(m^4-1)^2} \right] \ln(m) \quad (5.4)$$

where  $m = 1/n = n_t/n_i$ . For the case where  $n_i > n_t$  one should (1) calculate  $r_i$  using Eq. 5.4 substituting  $m$  for  $m' = 1/m$  and (2) apply the resulting  $r_i$  in the expression derived by Egan and Hilgaman [89] based on the  $n^2$ -law of radiance (Eq. 5.5) to calculate  $r_i'$ .

$$r_i' = 1 - m^2(1 - r_i) \quad (5.5)$$

A two-fiber Monte Carlo model (as described in chapter 4) where all the light that reaches the collection fiber face is counted (open circles) shows the same result predicted by the diffusion model (line) as shown in Fig. 5.1.

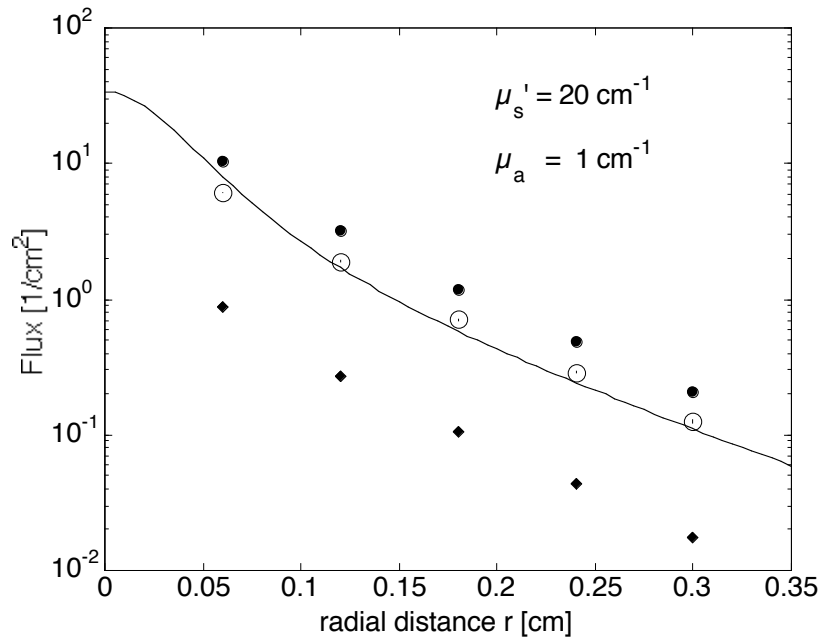


**Fig. 5.1.** – Comparison of diffusion model (Eq. 5.3) and Monte Carlo simulations of the spatially resolved radiative transport. White circles:  $n_{\text{fiber}} = 1$ , all escaping light detected. Black circles:  $n_{\text{fiber}} = 1.45$ , all escaping light detected. Black diamonds:  $n_{\text{fiber}} = 1.45$ , but only light collected within numerical aperture of fiber is detected.

In this example the source and collection fibers have a 600-  $\mu\text{m}$  diameter. The refractive indices of the sample and top medium (air) were set to 1.33 and 1 respectively and the refractive index of the fiber was not considered ( $n_{\text{fiber}} = 1$ ). If the refractive index of the optical fiber is set to its actual value of 1.45 the returning flux (Fig. 5.1 filled circles) is larger. The fiber perturbs the medium by introducing a region where the refractive index is greater than the sample, hence having no critical angle, which increases the escaping flux. To accurately determine the flux collected by the optical fiber, the optical fiber collection efficiency described in chapters 3 and 4 must be taken into account. If only the light that reaches the collection fiber within the angle defined by the numerical aperture is used then the net flux coupling into the fiber is approximately 1/10 (Fig. 5.1. filled diamonds) of that determined by the diffusion model. Moreover, the collection efficiency is dependent on the optical properties of the medium, which in addition to the perturbation of the probe caused by its refractive index makes accurate modeling based on analytical or numerical methods a difficult task. This task is

particularly aggravated when probes composed of more than simply optical fibers (i.e., metal or plastic holders) are used since the presence of additional material close to the fiber tip will result in changes in the local index of refraction. Thus, the assumption of a simple air/medium boundary at the surface becomes flawed. An alternative approach toward characterizing a particular optical fiber device can be based on experimental measurements on optical phantoms with varying absorption and scattering properties to establish an empirical forward light transport model as described in this study.

## **5.3 Material and Methods**

### **5.3.1 Probe preparation**

A two-fiber probe was developed for steady-state diffuse reflectance measurements. Two pieces of 620- $\mu$ m diameter stainless steel rod were cut 12-mm long and one end of each was polished at a 45° angle to create a mirror. Two lengths of stainless steel tubing (I.D. = 660  $\mu$ m, O.D. = 830  $\mu$ m) were cut 8-mm long and a hole was made in each through one side of the tube wall using a 0.025" (635- $\mu$ m diameter) end mill. The holes in the tubing were spaced 2 mm or 4.5 mm from the end for use as the source or the detector fiber, respectively. The polished steel rods were aligned inside the tubing such that the 45° mirror surface would reflect light through the hole. Two optical fibers (silica-silica, 600- $\mu$ m core diameter, 3-m long; Ceramoptec Industries Inc., East Longmeadow, MA) were polished flat and one fiber was inserted through the open end of each tube. The optical fiber, rod/mirror and tube were fixed in place by filling the internal spaces of the tube with clear epoxy (Epo-Tek 301; Epoxy Technology, Billerica, MA), and curing at 60°C for 4 hours. Excess rod was trimmed and filed to remove sharp edges. The source (with hole 2 mm from the end) and detector (with hole 4.5 mm from the end) were aligned side by side and bonded together by epoxy with the two holes facing toward the same side. The remaining 3-m optical fibers were inserted into Teflon tubing (PTFE 17LW; Zeus Industrial Products Inc., Orangeburg, SC). The tip of the probe was sealed with silicone glue and a 2-cm piece of heat-shrink Teflon tubing (14HS; Zeus Industrial

Products Inc., Orangeburg, SC). Figure 5.2 shows the diagram and a picture of the device. The probe was sterilized with ethylene oxide gas prior to patient use.

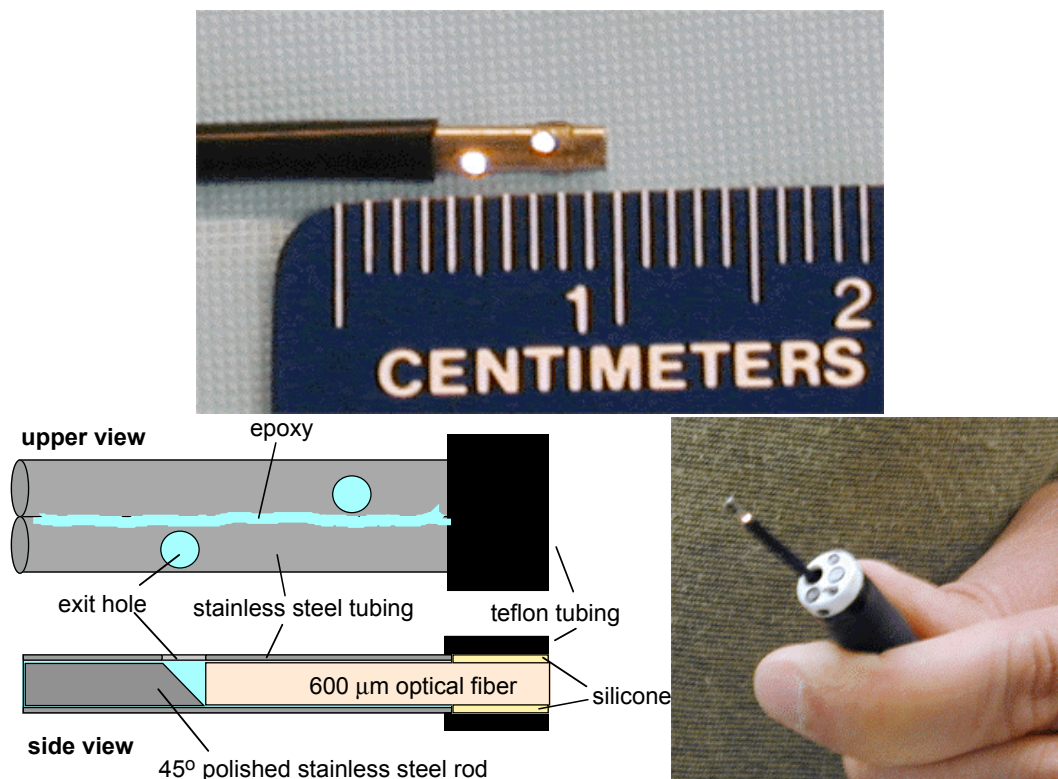


**Fig. 5.2** - Two-fiber probe for reflectance measurements. A 45°-polished steel mirror directs source light from one 600  $\mu\text{m}$  optical fiber 90° out the side of the fiber and a second mirror and fiber collect light for detection. Source-collector separation is 2.5 mm. Probe is passed through working channel of endoscope.

### 5.3.2 Reflectance measurements

Reflectance measurements used the reflectance system shown in Fig. 5.3. White light from a tungsten lamp (QTH6333, Oriel Instruments, Stratford, CT) was used as the light source. The signal was detected with a diode array spectrophotometer (S2000, Ocean Optics Inc., Dunedin, FL). The fiber probe used was described in the previous section.

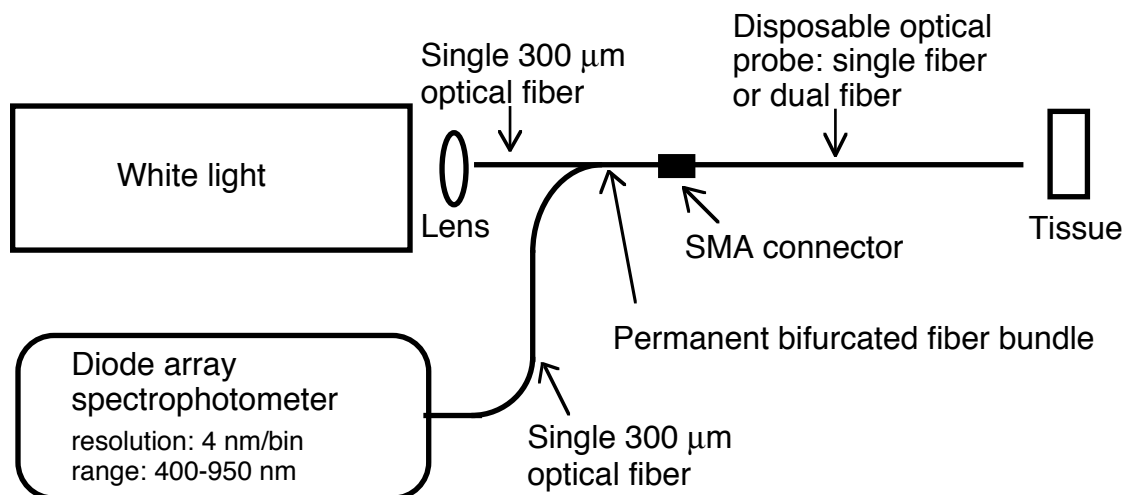


**Fig. 5.3.** - Reflectance system setup. Light from a tungsten lamp is guided through an optical probe (see probe preparation). Reflectance spectra is acquired with a spectrophotometer and recorded in a laptop.

The physician positioned the reflectance probe at normal sites (all patients) and tumor sites (PDT patients) according to his clinical evaluation of the tissue. Three sites were measured per patient/disease, and the reflectance spectra were later analyzed to determine the tissue optical properties. The endoscope illumination was turned off for a few seconds while the spectrum for a given site was acquired (200-ms acquisition time). The probe was calibrated by topical placement on an epoxy/titanium-dioxide solid phantom immediately after the procedure. The solid epoxy standard was previously calibrated with integrating sphere measurements of a thin slice cut from the standard and inverse adding-doubling [40, 41] modeling to specify its optical properties. Figure 5.4 shows the raw reflectance spectra for one of the patients. Lower intensities in the 500-600-nm range are due to blood absorption.

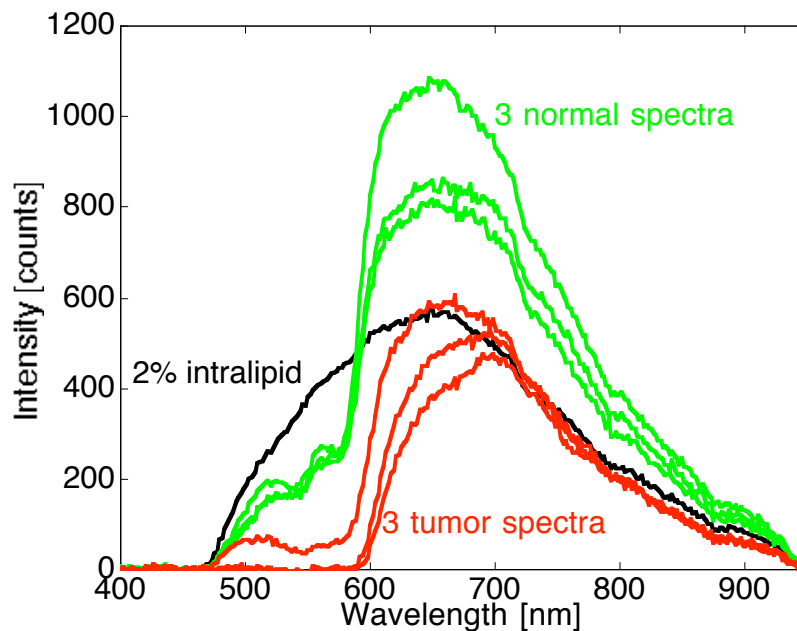


Fig. 5.4. – Typical reflectance raw data for normal (3 sites), tumor (3 sites) and Intralipid

### 5.3.3 Empirical forward light transport model

The decision to use steady state diffuse reflectance, as opposed to time-resolved [47-49] or frequency-domain [49, 50] measurements, was based on the simplicity and low cost of the steady state method. The analysis of reflectance assumes (1) that the reduced scattering coefficient of the tissue behaves as a power of the wavelength [81] and (2) that a linear combination of chromophore spectra can fully approximate the absorption coefficient [81]. The reflectance spectra used an empirical light transport function determined by experimental calibration of the reflectance probe with a matrix of tissue simulating phantom gels, and with the tissue being assumed to be homogeneous, as described in the following sections. This experimentally determined transport function behaves similar to that of diffusion theory with a mismatched air/tissue boundary, but accurately accounts for the performance of the actual probe device with its particular geometry and construction.

### 5.3.3.1 Preparation and calibration of the tissue phantom gel matrix

An 8x8 matrix of acrylamide gel tissue simulating phantoms was prepared using Intralipid (Liposin II, Abbott Laboratories, North Chicago, IL) as scattering element and India ink (No. 4415, Higgs, Lewisburg, TN) as absorber. Intralipid optical properties were determined according to Appendix A. The absorption coefficient of the stock ink was determined with an UV-VIS spectrophotometer (model 8452A, Hewlett-Packard, Palo Alto, CA). A matrix of 64 gels was prepared with all combinations of 8 different reduced scattering coefficients and 8 different absorption coefficients. Samples were prepared to yield final Intralipid concentrations of 7, 5, 3.5, 2.5, 1.5, 1.0, 0.5 and 0.25% (gram lipid/ml solution times 100%). Different aliquots of India ink were added to yield final absorption coefficients at 630 nm of 0.01, 0.1, 0.4, 0.9, 1.6, 2.5, 4.9 and 6.4  $\text{cm}^{-1}$ . Gels were prepared by adding aliquots of Intralipid, India ink, 45 ml of acrylamide solution (40% concentration) and water to a final volume of 100 ml (4 cm height by 5 cm diameter). The final gel was 18% acrylamide. Stock acrylamide was prepared by diluting 1.4 kg of acrylamide acid (BP170-100, 99%, electrophoresis grade, Fisher Scientific, Pittsburgh, PA) and 35 g of bis-acrylamide (BP171-25, Fisher Scientific, Pittsburgh, PA) in water (1:40 ratio) to create a final volume of 3.5 liters (40% contraction). Samples were gelled by adding 0.4 g of ammonium persulfate (BP179-25, Fisher Scientific, Pittsburgh, PA) and 100  $\mu\text{l}$  of TEMED (BP150-20, Fisher Scientific, Pittsburgh, PA) in each 100 ml sample. Figure 5.5 is a picture of the samples.



**Fig. 5.5.** – Picture of the 8x8 acrylamide gel matrix. Rows from top to bottom have final Intralipid concentrations of 7, 5, 3.5, 2.5, 1.5, 1.0, 0.5 and 0.25%. Columns from left to right have final absorption coefficients at 630 nm of 0.01, 0.1, 0.4, 0.9, 1.6, 2.5, 4.9 and 6.4  $\text{cm}^{-1}$ . All samples have 18% acrylamide gel concentration (see text for detail) and a final volume of 100 ml.

Acrylamide did not change the absorbing properties of the added ink (as experimentally verified for an absorbing only gel), however the scattering properties of the added Intralipid were assumed to change when added to the gels. This assumption was based upon experiments done with samples before and after gelling (data not shown). Optical properties of the final gel samples were determined by measuring the total reflectance with an 8-inch-diameter integrating sphere (IS-080, Labsphere Inc., North Sutton, NH). Samples were placed directly at the open port (1-inch diameter) of the integrating sphere. A 600-  $\mu\text{m}$ -diameter optical fiber was positioned inside the integrating sphere through a stainless steel tube 5-mm away from the sample forming a 3-mm diameter spot on the sample. Total diffused light was collected with a 600-  $\mu\text{m}$ -diameter optical fiber positioned in another port of the sphere. Light that would have reflected directly from the sample to the collection port was blocked with a baffle positioned between the two ports. The setup is shown on Fig. 5.6.

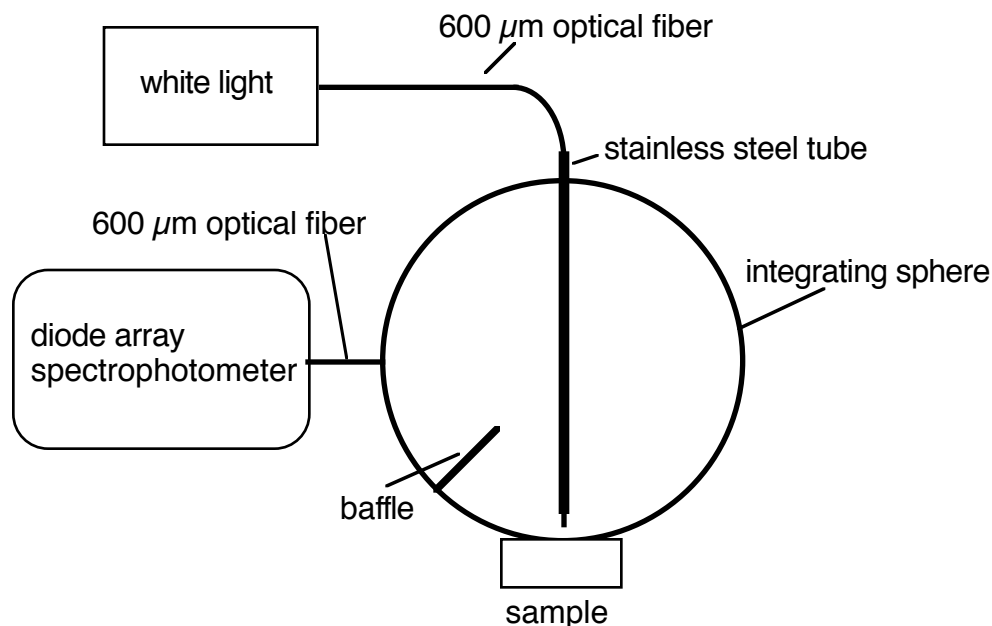


**Fig. 5.6.** – Setup of the integrating sphere used for calibration of the acrylamide samples. White light from a tungsten halogen lamp is guided through an 600-  $\mu\text{m}$ -diameter optical fiber positioned 5 mm away from the sample, inside the integrating sphere, forming a 3-mm diameter spot. Reflectance spectra is detected through an 600-  $\mu\text{m}$ -diameter optical fiber with a diode array spectrophotometer. Spectralon standards are used to calibrate the reflectance measurements.

Measurements of Spectralon standards (Labsphere Inc., North Sutton, NH) were taken to calibrate the sphere. Reduced scattering ( $s'$ ) and absorption ( $a$ ) coefficients were determined using a combination of the added-absorber [83] and adding-doubling [40, 41] methods to predict the total diffuse reflectance ( $R_i^{\text{AD}}$ ) for comparison with the measured total diffuse reflectance ( $R_i^{\text{EXP}}$ ) in a least square minimization routine. Determination of the two parameters  $s'$  and  $a$  with only one measurement of total diffuse reflectance is possible because of the knowledge of the added absorber to all samples. The minimization was done wavelength-by-wavelength using the samples with the five lowest ink concentrations ( $D_i^{\text{ink}} = 0, 0.0003, 0.0010, 0.0024, 0.0040$ , corresponding to 0.01, 0.1, 0.4, 0.9 and  $1.6 \text{ cm}^{-1}$  at 630 nm, respectively) for each Intralipid concentration. Fig. 5.7 shows a flow chart of the minimization. The results of this analysis showed a non-linear relation between the Intralipid concentration and the reduced scattering coefficient.

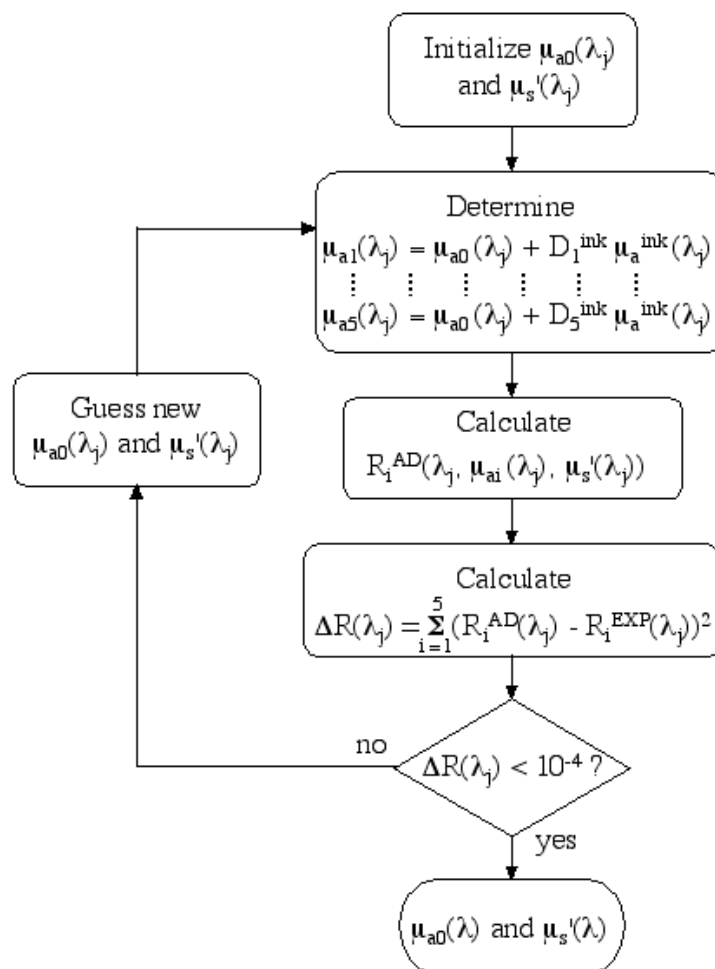


**Fig. 5.7.** – Flow Chart of the minimization process to determine the Intralipid absorption coefficient ( $\mu_{a0}$ ) and the reduced scattering coefficient ( $\mu_s'$ ) for each wavelength  $\lambda_j$  and for each Intralipid concentration. The samples with five lowest dilutions of ink ( $i = 1$  to  $5$ ) were used to determine  $\mu_{a0}$  and  $\mu_s'$ . Least square minimization is performed between the reflectance calculated with adding-doubling and the reflectance experimentally measured.

A collimated transmission measurement (Fig. 5.8) confirmed the non-linear relationship between Intralipid concentration and scattering properties (Fig. 5.9.A). A He-Ne laser (543 nm, Melles Griot) was positioned 15 cm away from a cuvette. The cuvette was made of two glass-slides spaced 150  $\mu$ m with glass cover slips spacers glued on the sides and opened on the top and bottom. A 1-cm-diameter silica detector with a 5 mm aperture iris was positioned 80 cm away from the cuvette and connected to a pico-ammeter.

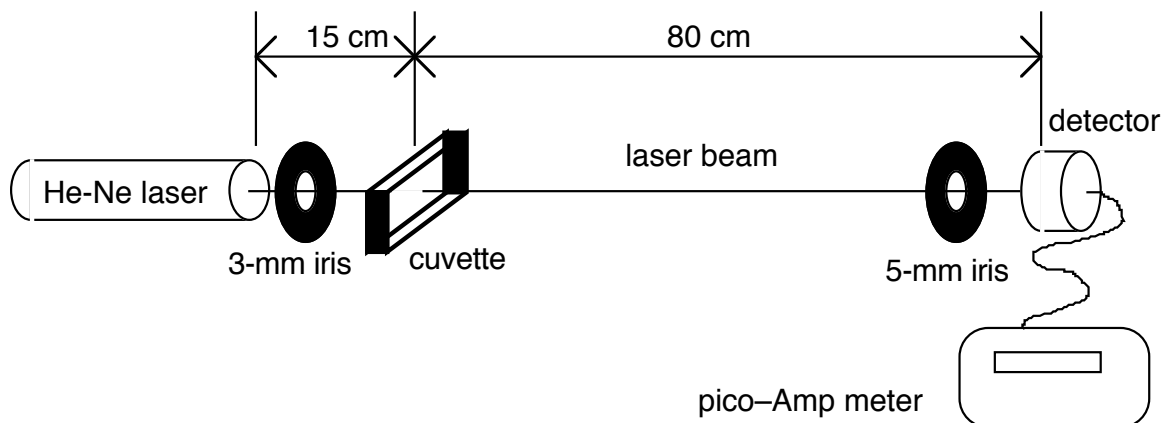


**Fig. 5.8.** – A. Setup for the collimated transmission measurements. Light from a 543 nm He-Ne laser is shined onto a 150 mm thick glass cuvette containing the Intralipid sample. A 1-cm-diameter silica detector coupled to a pico-ammeter and positioned 80 cm away from the cuvette is used for detection of the collimated transmitted light. The iris positioned in front of the detector limited the detection to a 5 mm diameter spot. A 2-mm-diameter iris was positioned between the laser and the sample to prevent any non-coherent light from reaching the sample.

The cuvette was filled with water to determine the transmitted intensity  $I_0$  with the help of neutral density filters to avoid detector saturation. The liquid was held inside the cuvette by surface tension. The cuvette was flushed with acetone and dried with high-pressure air. Intralipid at different concentrations (starting at 20%) was placed in the cuvette and the collimated transmitted light ( $I_c$ ) was measured. The scattering coefficient of the samples was determined using Eq. 5.6. The absorption coefficient of the samples was neglected since it is much smaller than the scattering coefficient.

$$\mu_s = -\ln\left(\frac{I_c}{I_0}\right) \quad (5.6)$$

The collimated transmission setup was tested to check the contamination of the collimated light due to collection of diffused light by the detector. The 20% Intralipid solution was placed in the cuvette and the detector was translated perpendicularly to the collimated beam in half centimeters steps. The measured current is shown in Fig. 5.9.B with a contrast ratio between collimated and diffused light of approximately 500 fold.

Since the greatest intensity of diffused light is expected for the 20% Intralipid concentration all other concentrations have a contrast ratio greater than 500.

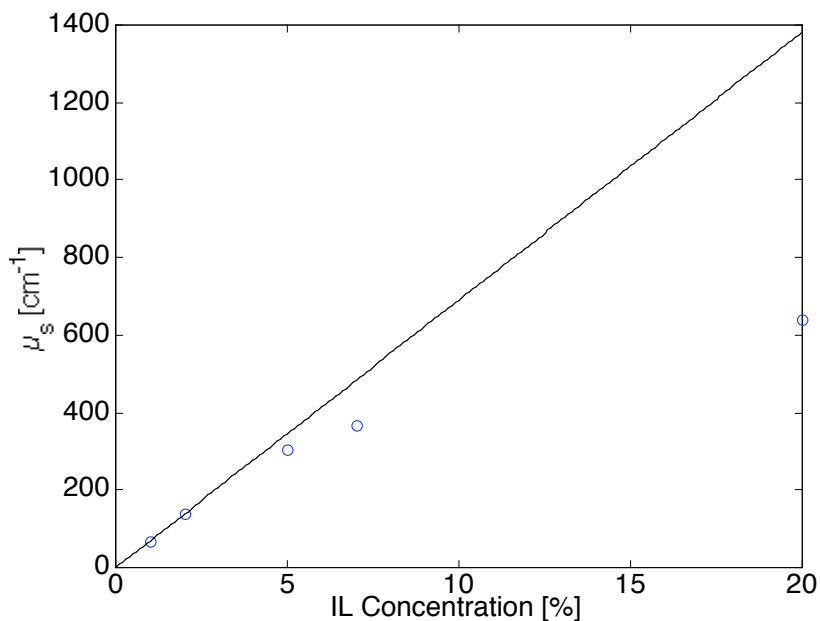


**Fig. 5.9.A.** – Scattering coefficient of 1, 2, 5, 7 and 20% Intralipid solution determined from collimated transmission at 543 nm. Experimental setup is showed in figure 5.8.

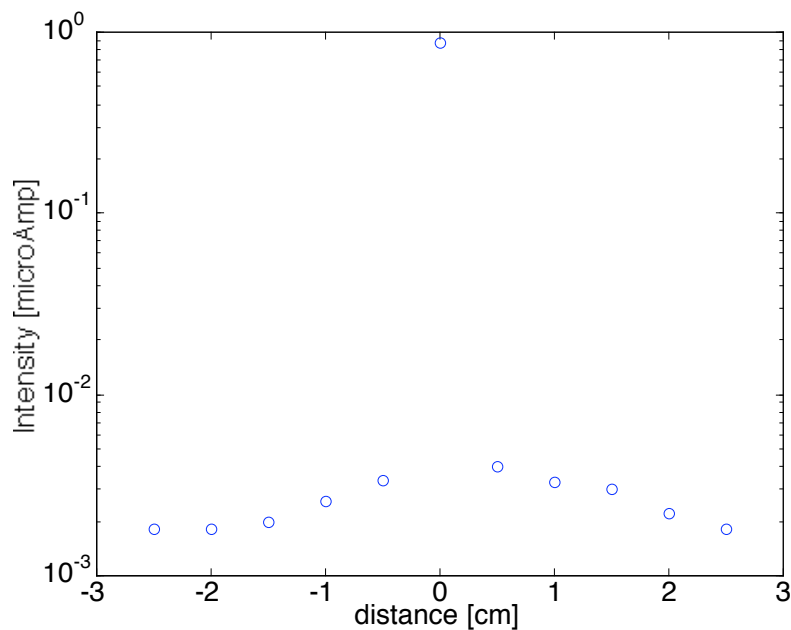


**Fig. 5.9.B.** – Measurement of light detected by the 1-cm-diameter silica detector with a 5 mm aperture iris translated perpendicularly to the collimated beam in steps of 5 mm for a 20% Intralipid concentration sample. The collimated transmission is approximately 500-fold greater than the diffused light measured by the detector.

The results illustrate that the scattering properties of the dilutions of Intralipid were nonlinearly related to the Intralipid concentration. The reason for this non-linearity is not known. The probe calibration simply used the documented final  $\mu_s'$  of the gels based on the integrating sphere measurements as shown in Fig. 5.10.

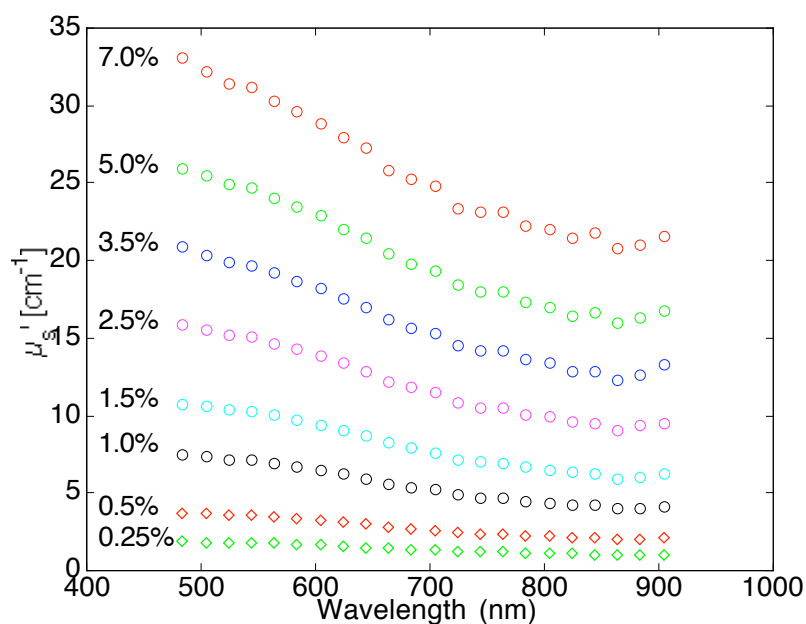


**Fig. 5.10.** – Reduced scattering coefficient determined from integrating sphere measurements for 7, 5, 3.5, 2.5, 1.5, 1.0 0.5 and 0.25% Intralipid-acrylamide-gel samples.

### 5.3.3.2 Probe calibration

All 64 acrylamide gel samples and the epoxy/titanium-dioxide solid standard were measured with the probe. A 2-mm water layer was added to the sample surface to help light coupling. The excess water was dumped after approximately two minutes leaving a moist surface where the fiber was placed in contact. It is acknowledge that the additional water may change the surface optical properties slightly but without this additional water the measurement to measurement variance for a single sample was greater than 20%. With water this variance reduced to less than 5%.

Reflectance measurements on samples ( $M_s$ ) were normalized by the epoxy/titanium-dioxide (epoxy-TiO<sub>2</sub>) solid standard ( $M_{std}$ ). The final spectrum was the ratio  $M$ :

$$M(\lambda) = \frac{M_s(\lambda)}{M_{std}(\lambda)} = \frac{S(\lambda) T_s(\lambda) \eta_c(\lambda) D(\lambda)}{S(\lambda) R_{std}(\lambda) \eta_{c, std}(\lambda) D\eta_c(\lambda)} = \frac{T_s(\lambda) \eta_c(\lambda)}{R_{std}(\lambda) \eta_{c, std}(\lambda)} \quad (5.7)$$

where

$S(\lambda)$	[W]	is the light source power,
$D(\lambda)$	[counts/W]	is the detector sensitivity,
$T_s(\lambda)$	[1/cm <sup>2</sup> ]	is the optical transport into the medium and returning to the sample surface at the collection fiber,
$\eta_c(\lambda)$	[dimensionless]	is the collection efficiency of the optical fiber,
$R_{std}(\lambda)$	[dimensionless]	is the standard reflectance (0.65 at 630 nm)

The terms  $S$  (the source spectral response) and  $D$  (the detector spectral response) are the same for samples and standard measurements and don't vary within a measurement procedure and thus cancel in Eq. 5.7. The normalized measurement,  $M(\lambda)$ , was multiplied by the reflectance of the standard [ $R_{std}(\lambda)$ ] determined with the integrating sphere setup shown in Fig. 5.6 to yield the adjusted normalized measurement  $M^*$  (Eq. 5.7.b).

$$M^*(\lambda) = \frac{M_s(\lambda)}{M_{std}(\lambda)} R_{std}(\lambda) = \frac{T_s(\lambda) \eta_c(\lambda)}{\eta_{c, std}(\lambda)} \quad (5.7.b)$$

This  $M^*$  incorporated the actual light transport of the sample multiplied by the ratio between the optical fiber probe collection efficiency for the sample and the standard ( $\eta_s/\eta_{s, std}$ ). As discussed in chapters 3 and 4 both  $\eta_s$  and  $\eta_{s, std}$  are optical properties

dependent factors and their determination are not trivial for the somewhat complex probe used in this work.

Each phantom gel yielded a spectrum of reflection values ( $\lambda = 480 - 925$  nm). With the knowledge of the optical properties of the samples from the integrating sphere measurements a light transport map was generated for each wavelength by interpolating the 64 normalized measurements ( $M^*$ ) as follows:

1. The 64 measurements for one wavelength (e.g.,  $\lambda = 630$  nm) were plotted on a grid of absorption ( $\mu_a$ ) and reduced scattering ( $\mu'_s$ ) coefficients (Fig. 5.11.A).
2. A linear interpolation of the 8 adjacent points in the reduced scattering dimension was made using the function *interp1* in Matlab as shown in Fig. 5.11.B, i.e.,  $M^*(\mu'_s)$  at each  $\mu_a$ .
3. The result of the linear interpolation was plotted on the same grid of absorption ( $\mu_a$ ) and reduced scattering ( $\mu'_s$ ) coefficients (Fig. 5.11.C).
4. The 8 adjacent points in the absorption dimension were fitted with an exponential curve (Eq. 5.8) as shown in Fig. 5.11.D for each wavelength ,

$$M^*(\mu_a, \mu'_s) = C_1(\mu'_s)e^{-\mu_a L_1(\mu'_s)} + C_2(\mu'_s) \quad (5.8)$$

where the constants  $C_1$ ,  $L_1$  and  $C_2$  are a function of the  $\mu'_s$ .

5. The resulting constants  $C_1$ ,  $L_1$  and  $C_2$  (Fig. 5.11) were used with Eq. 5.8 to create the final light transport shown in Fig. 5.11.E.

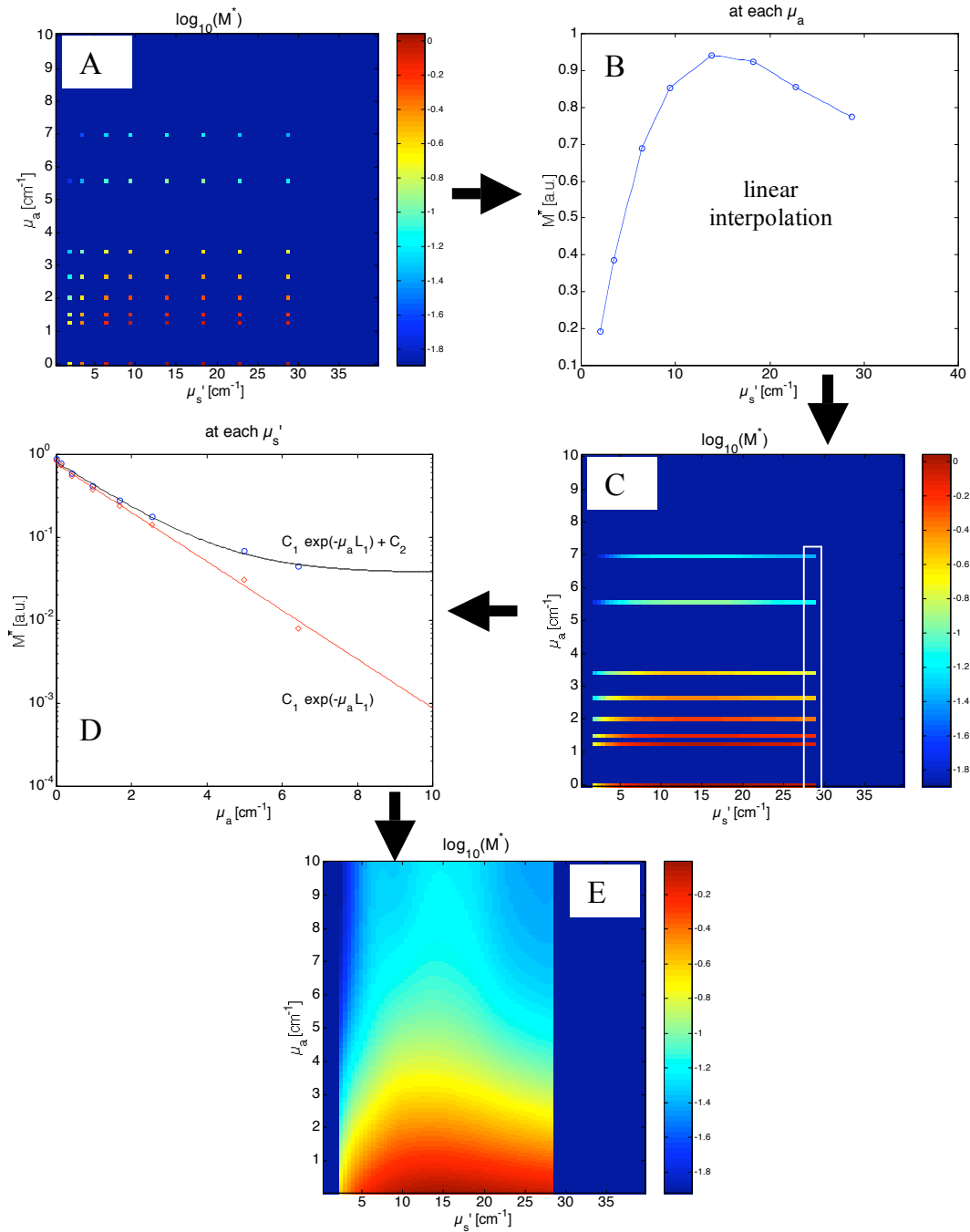


**Fig. 5.11.** – Making of the light transport maps used as forward model for the reflectance measurements. This is an example for one wavelength (630 nm). (A) Log base 10 of the normalized measurement  $M^*$  for the 64 samples at 630 nm displayed in a grid of absorption and reduced scattering coefficient. (B) Linear interpolation of the 8 data points with the lowest  $\mu_a$  in figure A. (C) Log base 10 of the normalized measurement  $M^*$  obtained from the linear interpolation in figure B. The points highlighted inside the white box are shown in figure D. (D) Exponential fit according to Eq. 5.8 of data highlighted in figure C. The data points with coefficient  $C_2$  subtracted are shown in red for comparison. (E) Light transport map at 630 nm constructed with the coefficients shown in Fig.5.12. and Eq. 5.8.

In a first attempt the light transport maps were used as look-up tables to determine the forward transport. Given  $a_s$ ,  $s'$  and wavelength the correspondent light transport value was determined by a 2 dimensional linear interpolation of the light transport map. The *interp2* Matlab function was used for the 2-dimension interpolation. This approach showed to be computationally time consuming. To speed the calculation of the light transport the coefficients  $C_1$ ,  $L_1$  and  $C_2$  were fit to polynomial functions of orders 4, 15 and 15, respectively. The use of high order polynomial functions for  $L_1$  and  $C_2$  were necessary because of the rapid changes in these coefficients as a function of reduced scattering coefficients. Fitted values beyond the limits of maximum and minimum coefficient values were discarded (shadow regions on Fig. 5.12.). The polynomial coefficients for  $C_1$ ,  $L_1$  and  $C_2$  at 630 nm (Fig. 5.12. lines) are shown in table 5.1. The Matlab code used to generate the polynomial coefficients is presented in appendix C.

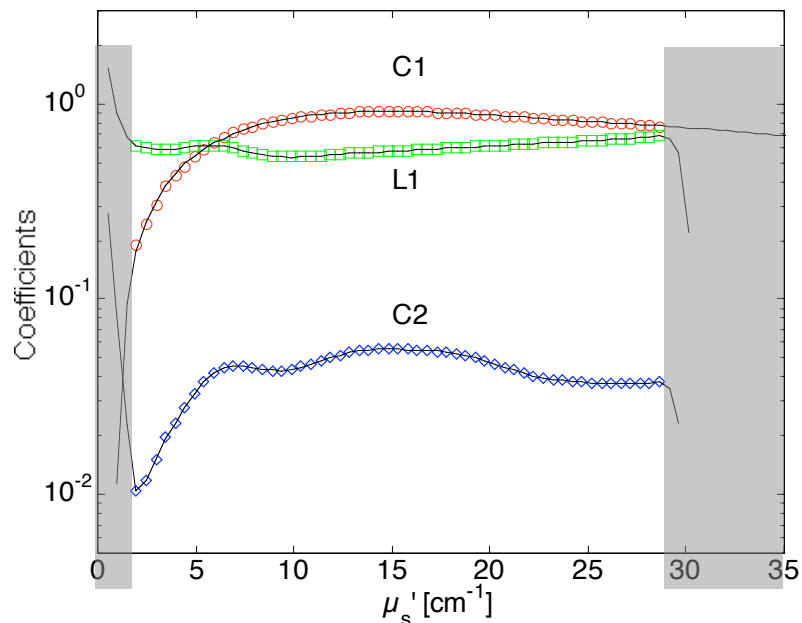


**Fig. 5.12.** – Coefficients  $C_1$ ,  $L_1$  and  $C_2$  used to reconstruct the map on Fig. 5.11.E (630 nm). The coefficients were fitted to polynomials (lines) to speed the calculation of the light transport (see text).

**Table 5.1.** – Coefficients of the polynomial fits to  $C_1$ ,  $L_1$  and  $C_2$  at 630 nm.

Coefficient order	Coefficients for $C_1$	Coefficients for $L_1$	Coefficients for $C_1$
$(s)^0$	$-3.38 \cdot 10^{-06}$	$-3.36 \cdot 10^{-16}$	$-5.43 \cdot 10^{-17}$
$(s)^1$	$3.45 \cdot 10^{-04}$	$7.90 \cdot 10^{-14}$	$1.32 \cdot 10^{-14}$
$(s)^2$	$-1.30 \cdot 10^{-02}$	$-8.44 \cdot 10^{-12}$	$-1.46 \cdot 10^{-12}$
$(s)^3$	$2.01 \cdot 10^{-01}$	$5.42 \cdot 10^{-10}$	$9.71 \cdot 10^{-11}$
$(s)^4$	$-1.75 \cdot 10^{-01}$	$-2.33 \cdot 10^{-08}$	$-4.33 \cdot 10^{-09}$
$(s)^5$		$7.07 \cdot 10^{-07}$	$1.37 \cdot 10^{-07}$
$(s)^6$		$-1.56 \cdot 10^{-05}$	$-3.15 \cdot 10^{-06}$
$(s)^7$		$2.53 \cdot 10^{-04}$	$5.35 \cdot 10^{-05}$
$(s)^8$		$-3.03 \cdot 10^{-03}$	$-6.72 \cdot 10^{-04}$
$(s)^9$		$2.66 \cdot 10^{-02}$	$6.20 \cdot 10^{-03}$
$(s)^{10}$		$-1.68 \cdot 10^{-01}$	$-4.14 \cdot 10^{-02}$
$(s)^{11}$		$7.50 \cdot 10^{-01}$	$1.95 \cdot 10^{-01}$
$(s)^{12}$		-2.27	$-6.26 \cdot 10^{-01}$
$(s)^{13}$		4.44	1.29
$(s)^{14}$		-5.06	-1.51
$(s)^{15}$		3.17	$7.70 \cdot 10^{-01}$

### 5.3.4 Modeling of tissue reflectance with the empirical/spectral model

Tissue absorption was modeled as a linear combination of water ( $a^{\text{water}}$ ), a background spectrum for dry bloodless tissue ( $a^{\text{dry}}$ ), and a variable blood volume fraction ( $f_v$ ) of oxygenated and deoxygenated whole blood ( $a^{\text{oxy}}$ ,  $a^{\text{deoxy}}$ ) at an oxygen saturation ( $SO_2$ ). The amount of dry material and water were kept fixed with the water content being 75%. In principle, the water content could be fitted, but our system was not sufficiently sensitive in the 900-1000 nm spectral region where water strongly influences the spectra.

Tissue scattering can be represented by a simple expression,  $a\lambda^{-b} + c\lambda^{-d}$ . The term  $a\lambda^{-b}$  mimics the Mie scattering from larger tissues structures such as collagen fiber bundles, mitochondria, nuclei and cells. The term  $c\lambda^{-d}$  accounts for Rayleigh scattering (for  $d = 4$ ) at shorter wavelengths from collagen fibril fine structure, small membranes, and other ultrastructure on the 10-100 nm scale [38]. The Rayleigh scattering factor was neglected in this modeling effort because our spectra were acquired above 500 nm and were not sensitive to Rayleigh scattering. The absorption coefficient ( $\mu_a$ ) and reduced scattering coefficient ( $\mu_s'$ ) were specified as:

$$\mu_a(\lambda) = \mu_a^{dry}(\lambda) + f_w \mu_a^{water}(\lambda) + f_v (SO_2 \mu_a^{oxy}(\lambda) + (1 - SO_2) \mu_a^{deoxy}(\lambda)) \quad (5.9)$$

$$\mu_s'(\lambda) = a\lambda^{-b} \quad (5.10)$$

$$\mu_a^{dry}(\lambda) = A \exp(-B\lambda) \quad (5.11)$$

where

$\mu_a(\lambda)$	[ $\text{cm}^{-1}$ ]	total absorption coefficient of tissue <i>in vivo</i>
$\mu_a^{dry}(\lambda)$	[ $\text{cm}^{-1}$ ]	absorption coeff. of dry bloodless tissue
$\mu_a^{water}(\lambda)$	[ $\text{cm}^{-1}$ ]	absorption coeff. of pure water
$\mu_a^{oxy}(\lambda)$	[ $\text{cm}^{-1}$ ]	absorption of fully oxygenated blood (45% hematocrit)
$\mu_a^{deoxy}(\lambda)$	[ $\text{cm}^{-1}$ ]	absorption of fully deoxygenated blood (45% hematocrit)
$f_w$	[dimensionless]	volume fraction of water
$f_v$	[dimensionless]	volume fraction of 45%-hematocrit blood in tissue
$SO_2$	[dimensionless]	oxygen saturation
$A$	[ $\text{cm}^{-1}$ ]	amplitude constant for $\mu_a^{dry}(\lambda)$
$B$	[ $\text{nm}^{-1}$ ]	rate constant for $\mu_a^{dry}(\lambda)$
$\mu_s'(\lambda)$	[ $\text{cm}^{-1}$ ]	reduced scattering coefficient of tissue <i>in vivo</i>
$a$	[ $\text{cm}^{-1}$ ]	factor that characterizes magnitude of scattering
$b$	[dimensionless]	factor that characterizes wavelength dependence of scattering
$\lambda$	[nm]	wavelength

Typical spectra for  $\mu_a^{\text{dry}}$ ,  $\mu_a^{\text{water}}$ , and the  $\mu_a^{\text{oxy}}$  and  $\mu_a^{\text{deoxy}}$  for whole blood at 45% hematocrit are shown in Fig. 5.13.

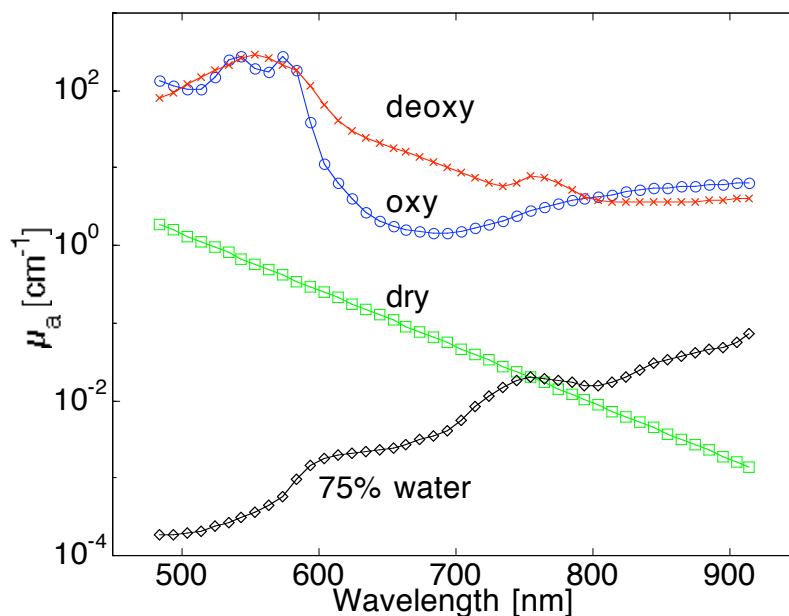
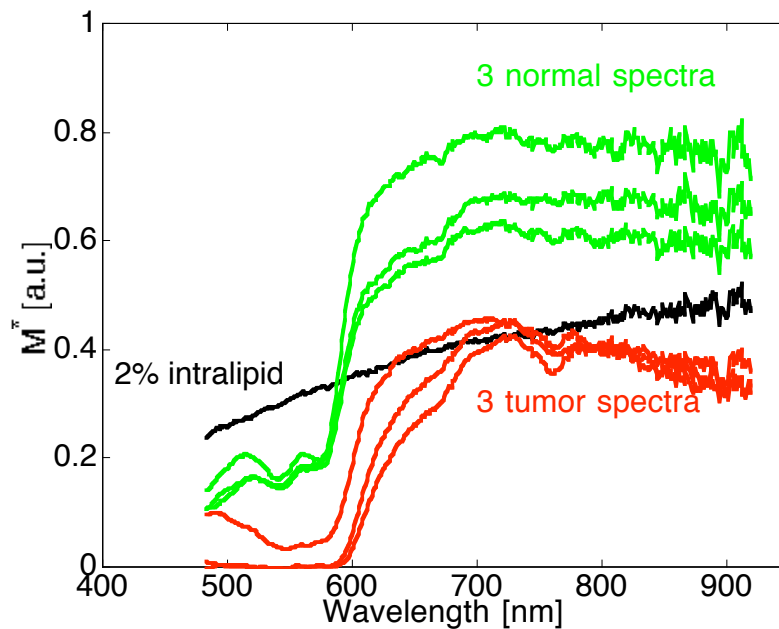


Fig. 5.13. - Spectra of tissue chromophores used in Eq. 5.9

The absorption of dry tissue was assumed to behave as an exponential decay, as suggested by Saidi [72]. In physical terms it represents the absorption coefficient in the visible range due to an ensemble of ultraviolet and blue absorbing chromophores (e.g., tryptophan, collagen fibers, bilirubin, porphyrins, etc.).

Measurements on the solid standard made of epoxy, titanium dioxide ( $\text{TiO}_2$ ) and ink used to normalize the acrylamide gel phantoms (section 5.3.3.2.) were taken to account for day-to-day variations in the wavelength and magnitude dependence of the light source and detector sensitivity. As an example, normalized data from Fig. 5.4 is presented in Fig. 5.14.



**Fig. 5.14.** – Data from Fig. 5.4 normalized by the measurement of the epoxy standard ( $M_{std}$ ) and multiplied by the standard reflectance ( $R_{std}$ ) as an example of the normalization given by Eq.5.7.b to yield  $M^*$ .

Values of  $a$ ,  $b$ , blood fraction ( $f_v$ ), blood oxygen saturation ( $SO_2$ ),  $A$  and  $B$  were determined by a least square minimization routine described below.

1. Variables  $a$ ,  $b$ ,  $f_v$ , and  $A$  and  $B$  are initialized.
2. The parameters  $a$  and  $s'$  are determined using Eqs. 5.9, 5.10 and 5.11 for the isobestic wavelengths (500, 530, 545, 570, 584, 796 nm) and using  $SO_2$  equals to 1.
3. Using the empirical transport model, the predicted normalized measurement was calculated for the isobestic wavelengths. The normalized measurements are determined directly from the empirical model since the model is based on the normalized experimental data.
4. The predicted normalized measurement ( $pM(\lambda)$ ) was compared to the experimental normalized measurement from the patient ( $M(\lambda)$ ) in a least square minimization process by minimizing the square error according to equation 5.12:

$$error = \sqrt{\sum_{\lambda=\lambda_i}^{\lambda_f} ((pM(\lambda) - M(\lambda)) / M(\lambda))^2} \quad (5.12)$$

5. Update variables a, b,  $f_v$ , A and B .
6. Iterate until error is less than 0.001.
7. After determining the variables a, b,  $f_v$ , A and B for the isobestic wavelengths the value of b was fixed and the variables a,  $f_v$ , A and B were used as starting point to fit these variables plus the  $SO_2$  for all the wavelengths
8. The parameters  $a$  and  $s'$  are determined using Eqs. 5.9, 5.10 and 5.11 for the all wavelengths.
9. Using the empirical transport model, the predicted normalized measurement was calculated wavelength-by-wavelength.
10. The predicted normalized measurement ( $pM(\lambda)$ ) was compared to the experimental normalized measurement from the patient ( $M(\lambda)$ ) in a least square minimization process by minimizing the square error according to equation 5.12.
11. Update variables a,  $f_v$ ,  $SO_2$ , A and B .
12. Iterate until error is less than 0.001.

Exception on data analysis using this model was the analysis of the skin patient data. For those the values of A and B were fixed at 27 and 0.006, respectively and a similar algorithm where only a, b,  $f_v$  and  $SO_2$  were fitted was used. These values were chosen based on work by Saidi [72] for neonatal skin.

### 5.3.5 Validation of the empirical/spectral model with a wavelength-by-wavelength theoretical model

Measurements of bovine muscle were made to validate the model. An *in vitro* tissue measurement was preferred to the use of phantoms composed of scatters such as Intralipid or microspheres and absorbers such as India ink or other chemical chromophores because of the model dependence to the spectra of the tissue components (oxy and deoxy blood, water, etc.). Bovine muscle was bought fresh from the local

abattoir and was approximately 24 hours post mortem at the time of the measurements. Tissue was kept refrigerated and wrapped in plastic until the time of use. Three sites in three different samples were measured.

Optical properties of the samples were determined using the empirical/spectral model described in the previous sections and compared to optical properties determined by a wavelength-by-wavelength model based on a total diffuse reflectance measurement ( $R_t$ ) in conjunction to a spatially resolved steady state diffuse reflectance measurement ( $R_d$ ). The measurement  $R_t$  was done with the integrating sphere setup shown in Fig. 5.6. Measurements of Spectralon standards were used to calibrate the sphere. The measurement of  $R_d$  was made with an optical fiber probe composed of five 400- $\mu$ m diameter optical fibers linearly spaced 1.524 mm (0.060") apart. The first fiber was used to illuminate the tissue with a white light tungsten lamp (QTH6333, Oriel Instruments, Stratford, CT). The remaining four fibers were connected to a four-channel diode array spectrophotometer (S2000, Ocean Optics Inc., Dunedin, FL). A measurement of the epoxy-TiO<sub>2</sub> standard referred on section 5.3.3.2 was taken to normalize the tissue measurements. This normalization was done to cancel the source and detector spectral response (Eq. 5.7). Optical properties were determined by fitting the experimental measurements  $R_t$  and  $R_d$  to adding-doubling [40, 41] and diffusion theory [17, 43] models, respectively, wavelength-by-wavelength, as follows:

1. Initialize  $a(\lambda_o)$ ,  $s'(\lambda_o)$  and  $const(\lambda_o)$  for a wavelength  $\lambda_o$  (e.g., 630 nm). The variable  $const$  was used as a multiplication factor to Eq. 5.3 to account for the ratio between  $\eta_s$  and  $\eta_{s, std}$ .
2. Calculate the predicted total diffuse reflectance  $pR_t(\lambda_o)$  using the initial  $a$ ,  $s'$  and the adding-doubling model
3. Calculate the predicted spatial resolved diffuse reflectance  $pR_d(\lambda_o)$  using the initial  $a$ ,  $s'$  and Eq. 5.3
4. Determine the predicted normalized spatially resolved diffuse reflectance  $[pM_d(\lambda_o)]$  by multiplying  $pR_d(\lambda_o)$  by  $const(\lambda_o)$  and divide by the  $R_{d, std}(\lambda_o)$  calculate for the epoxy-TiO<sub>2</sub> standard based on its known optical properties at  $\lambda = \lambda_o$  and Eq.5.3.

5. Compare  $pR_t(\lambda_o)$  to  $R_t(\lambda_o)$  and  $pM_d(\lambda_o)$  to  $M_d(\lambda_o)$  (the normalized spatially resolved diffuse reflectance) in a least square minimization using Eq. 5.13.

$$error = \sqrt{\left(\frac{pR_t(\lambda_o) - R_t(\lambda_o)}{R_t(\lambda_o)}\right)^2} + \sqrt{\left(\frac{pM_d(\lambda_o) - M_d(\lambda_o)}{M_d(\lambda_o)}\right)^2} \quad (5.13)$$

6. Update the variables  $a(\lambda_o)$ ,  $s'(\lambda_o)$  and  $const(\lambda_o)$
7. Iterate until error is less than 0.001.
8. Repeat for all wavelengths.

### 5.3.6 Patients

Patients undergoing endoscopic screening for esophageal diseases and patients undergoing photodynamic therapy for esophageal, lung, oral cavity and skin cancer treatment were recruited for the reflectance measurements. Consent to take part in the study was obtained from all patients. A study protocol was defined and approved by the Providence St. Vincent Medical Center IRB Committee. Detailed written and oral information on the study protocol was given to the patients prior to enrollment (Appendix C). The measurements increased the endoscopic procedure an average of 5 minutes.

A total of nine patients (#N1 to #N9) undergoing the endoscopic procedures for screening purpose were recruited to set baseline values for optical properties at clinically evaluated normal tissue sites. One measurement was taken at three different sites for each patient.

One patient with Barrett's esophagus (patient #E1), eight patients with esophageal tumor (#E2 to #E9), three patients with lung tumor (#L1 to #L3), one patient with oral cavity tumor (#O1) and four patients with skin cancer (#S1 to #S4) scheduled to receive standard FDA and off-label PDT treatment protocols were recruited for this study. All were intravenously injected with 2 mg/(kg body weight) of Photofrin II (Axcan Pharma Inc., Birmingham, AL) 48 hours prior to activation by 630-nm laser light. Measurements of reflectance spectra were taken immediately prior to light treatment. Three clinically evaluated normal sites and three clinically evaluated tumor sites were measured per

patient. Exceptions were lung patient #L3, who had two normal sites and three tumor sites measured and skin patient #S2 who had only one normal and one tumor site measured, due to time constraints during the procedures.

Esophageal patients #E1 to #E5 and lung patient #L1 are not shown in the results section because a different probe made of a single 600-  $\mu$ m-diameter optical fiber was used for the reflectance measurements on these patients. This probe was not able to determine the tissue absorption coefficient due to the small sampling volume limited by its geometry and was replaced by the probe discussed in section 5.3.1.

## 5.4 Results

### 5.4.1 Bovine muscle *in vitro*

Comparison between the optical properties of bovine muscle determined with the empirical/spectral model and by the wavelength-by-wavelength model (section 5.3.4) is shown in Fig. 5.15. Figure 5.15.A shows the average and standard deviations for  $s'$  (top) and  $a$  (bottom) obtained with the two techniques for three different sites of one sample. Similar results are shown in Fig. 5.15.B for all nine sites measured (three sites times three samples).

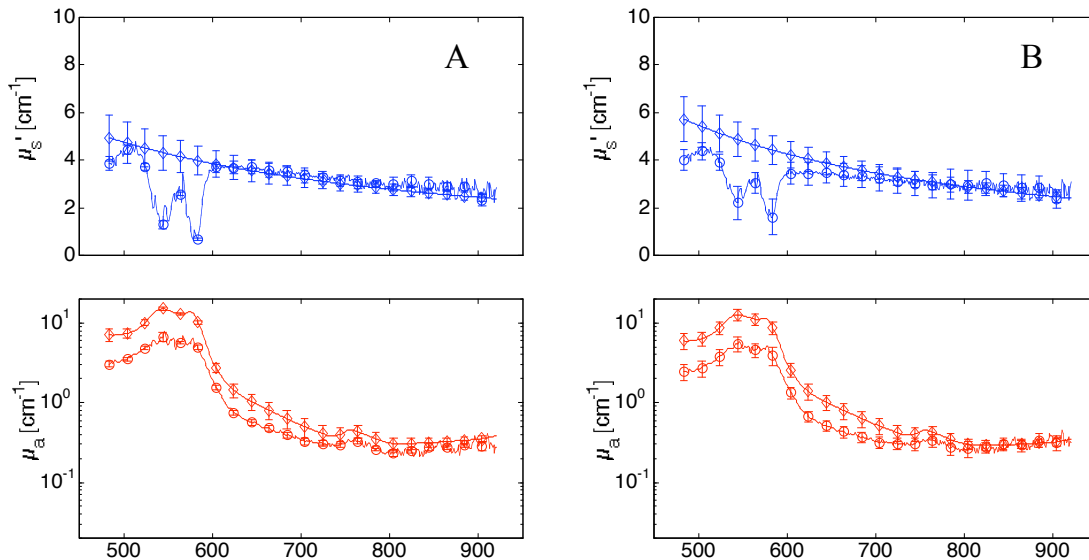


**Fig. 5.15.** – Reduced scattering ( $\mu_s'$ , top) and absorption ( $\mu_a$ , bottom) coefficients determined for bovine muscle determined by the empirical/spectral model (diamonds) in comparison to the optical properties determined by the wavelength-by-wavelength model described in section 5.3.5 (circles). (A) Average and standard deviations for three different sites measured at one sample. (B) Average and standard deviations for all sites measured (three sites per sample for three different samples).

## 5.4.2 Human tissue *in vivo*

Figure 5.16 show results of the empirical/spectral model for esophageal PDT patient #E6 with plots of the experimental and predicted spectra for three normal sites (Figs. A-C) and three tumor sites (Figs. D-F). Experimental curves in Figs. 5.16.A-F are the same shown in Fig. 5.14. Bloodless tissue curves are shown in black dashed lines, based on setting the factor  $f_v$  equal to zero for  $\mu_a$  in Eq. 5.9 and determining the light transport using the bloodless tissue optical properties and Eq. 5.8. The values of  $a$ ,  $b$ ,  $f_v$ ,  $SO_2$ ,  $A$  and  $B$  are specified in the graphs for this patient and in Tables 5.2, 5.3 and 5.4 for sites measured in all patients (PDT and non-PDT). To obtain the optical properties one must use these numbers with equations 5.9, 5.10 and 5.11. The normalized residual error [ (predicted-experimental)/experimental ] is shown below each graph.

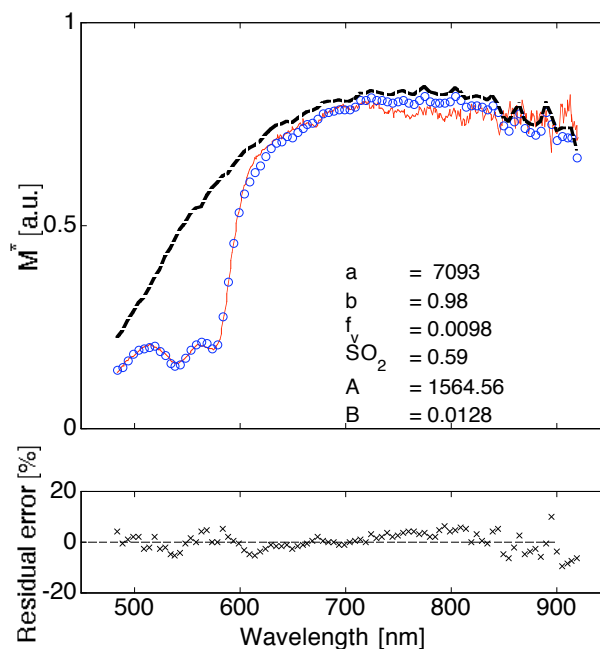


**Fig. 5.16.A** – Normalized data for normal site 1, patient #E6 (same as Fig. 5.14) in comparison to the predicted values (circles) determined using the fitted parameters  $a$ ,  $b$ ,  $f_v$ ,  $SO_2$ ,  $A$  and  $B$  shown, and Eqs. 5.8, 5.9, 5.10 and 5.11. Bottom curves show the percentage residual errors [(predicted-measured)/measured times 100%]. Bloodless tissue curves are shown in black dashed lines, based on setting the factor  $f_v$  equal to zero for  $a$  in Eq. 5.9.

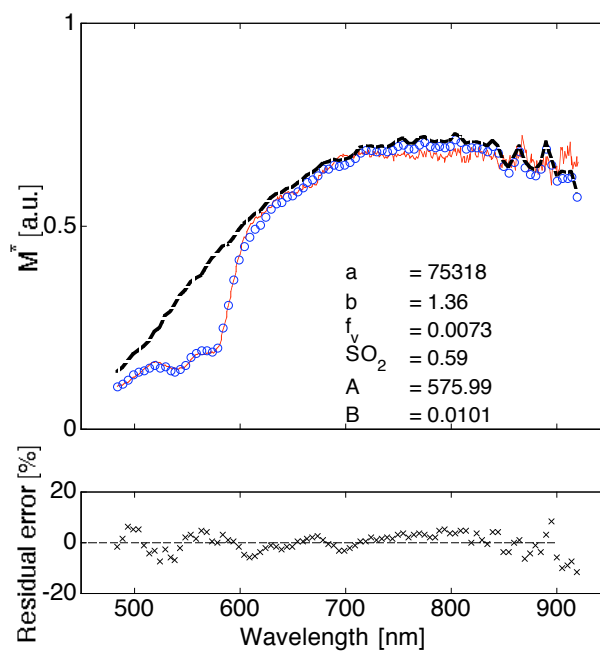


**Fig. 5.16.B** – Same as Fig. 5.16.A for normal site 2, patient #E6.

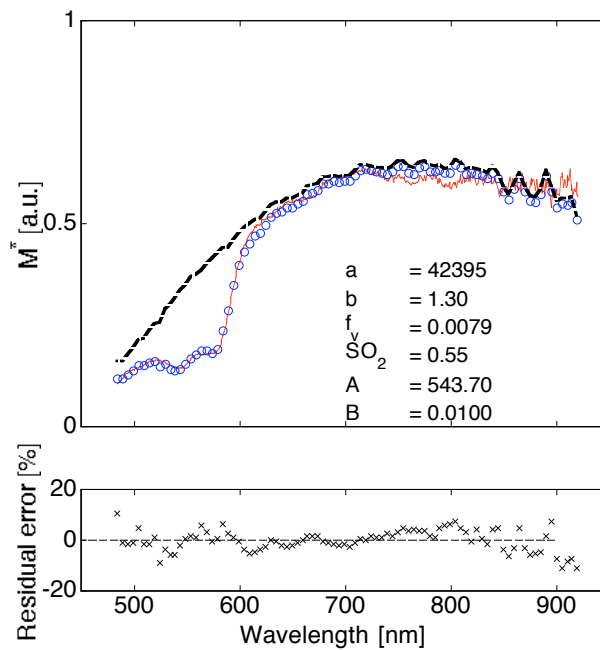


Fig. 5.16.C – Same as Fig. 5.16.A for normal site 3, patient #E6.

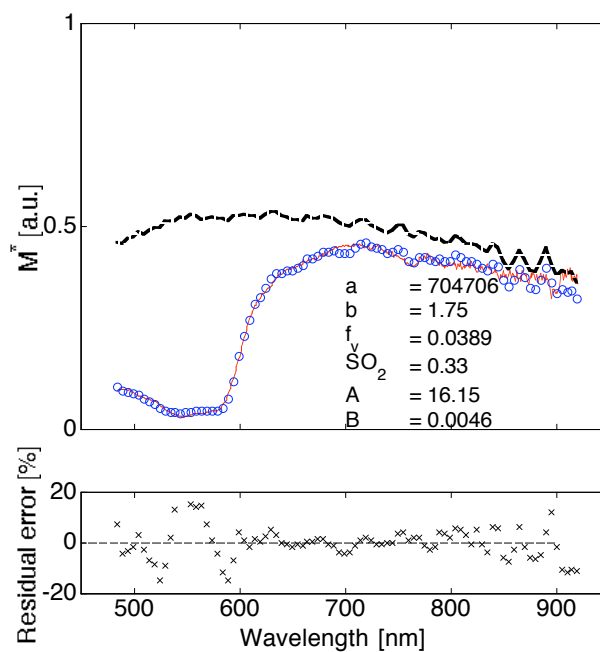
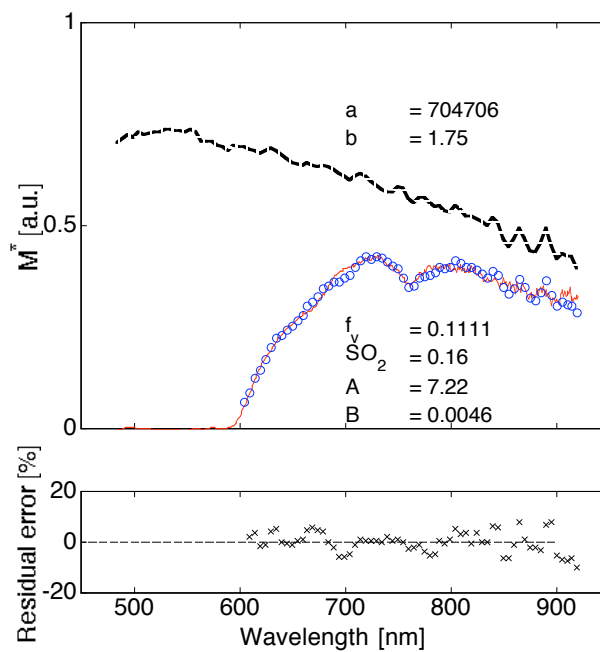
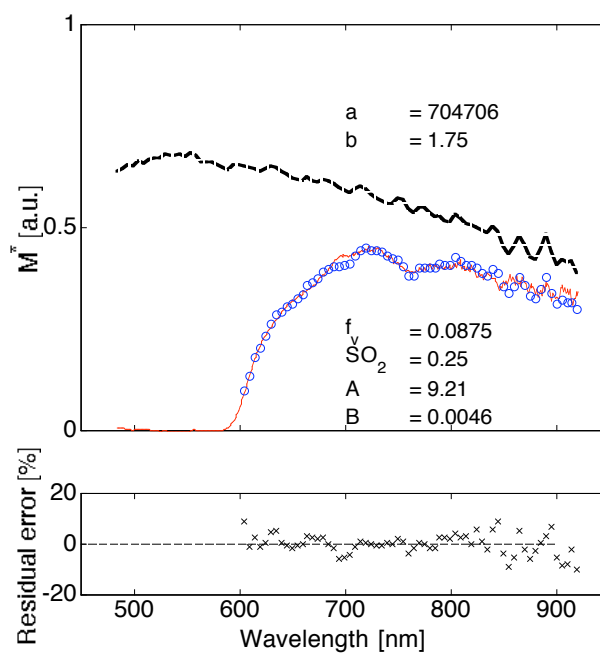


Fig. 5.16.D – Same as Fig. 5.16.A for tumor site 1, patient #E6.



**Fig. 5.16.E** – Same as Fig. 5.16.A for tumor site 2, patient #E6. The system was not able to record data below 600 nm because of the blood absorption in that spectral range. Only data above 600 nm was used for fitting. Values of  $a$ ,  $b$  and  $B$  were assumed to be the same of those for tumor site 1 in Fig. 5.16.D (see text).



**Fig. 5.16.F** – Same as Fig. 5.16.E for tumor site 3, patient #E6.

In some cases the blood content from tumor tissue was so high that zero reflectance was obtained in the 500-600-nm wavelength range. In these cases data were truncated below 600 nm and the same fitting algorithm was attempted. Without the data below 600 nm, the fitting for  $a$  and  $b$  (that describe the reduced scattering coefficient) and  $B$  (that describe the absorption of dry tissue) were not reliable. Therefore, the values of  $a$ ,  $b$  and  $B$  were determined using the average of  $s'$  and  $a^{\text{dry}}$  from the other tumor sites for the same patient and the variables  $f_v$ ,  $SO_2$  and  $A$  were fitted using the data above 600 nm. In the case of patient #E6, i.e., only one other tumor measurement (tumor site #1) did not have zero reflectance values in the 500-600 nm wavelength range. Thus, the values of  $a$ ,  $b$  and  $B$  for this tumor site were used to determine the other variables ( $f_v$ ,  $SO_2$  and  $A$ ) for tumor sites #2 and #3. The sites where the truncated data was used are highlighted in table 5.4.

**Table 5.2.** – Values of  $a$ ,  $b$ ,  $f_v$ ,  $SO_2$ ,  $A$ ,  $B$  and optical properties at 630 nm for normal sites of non-PDT patients.

Pat. #	site	$a$ [ $cm^{-1}$ ]	$b$ [-]	$f_v$ [%]	$SO_2$ [%]	$A$ [ $cm^{-1}$ ]	$B$ [ $nm^{-1}$ ]	$s_s^{630}$ [ $cm^{-1}$ ]	$a_a^{630}$ [ $cm^{-1}$ ]	$\delta^{630}$ [mm]
N1	1	19246	1.22	1.83	54	409	0.011	7.4	0.71	2.4
	2	52738	1.39	3.09	67	326	0.010	7.0	0.94	2.1
	3	30888	1.32	1.33	44	1094	0.013	6.2	0.59	2.9
N2	1	277950	1.56	4.98	39	0.51	0.000	12.0	1.40	1.3
	2	14057	1.19	1.73	40	9681	0.017	6.4	0.56	2.9
	3	251580	1.64	0.69	42	231	0.009	6.5	0.85	2.3
N3	1	8994	1.10	1.92	49	4966	0.015	7.5	0.64	2.5
	2	2904	1.00	1.57	49	6950	0.016	4.7	0.50	3.6
	3	6310	1.05	2.42	70	2698	0.014	7.5	0.64	2.5
N4	1	48580	1.37	1.33	61	361	0.010	7.0	0.67	2.6
	2	118056	1.53	1.49	66	293	0.010	6.3	0.80	2.4
	3	308977	1.62	0.63	52	82	0.007	8.9	0.94	1.9
N5	1	108754	1.47	1.03	51	3234	0.014	8.1	0.60	2.5
	2	144963	1.46	3.55	37	5142700	0.028	11.9	0.74	1.9
	3	69965	1.40	0.84	44	2055	0.013	8.3	0.72	2.3
N6	1	54916	1.38	1.46	58	683	0.011	7.3	0.82	2.2
	2	10312	1.12	1.58	48	1911	0.013	7.4	0.72	2.4
	3	93179	1.45	1.84	55	1117	0.012	8.1	0.72	2.3
N7	1	184459	1.55	1.07	53	97	0.008	8.7	0.83	2.0
	2	143323	1.50	0.99	53	44	0.006	8.8	1.10	1.7
	3	11139	1.15	0.90	45	361	0.011	6.6	0.55	2.9
N8	1	421423	1.69	2.00	58	72	0.007	7.7	1.20	1.8
	2	321110	1.64	1.38	54	36	0.005	8.4	1.35	1.6
	3	207327	1.59	0.92	58	606	0.011	7.4	0.89	2.1
N9	1	183263	1.56	2.19	71	313	0.010	7.6	0.84	2.2
	2	214786	1.63	2.12	59	1643	0.013	6.0	0.71	2.6
	3	119723	1.49	1.63	72	324	0.010	8.1	0.67	2.4

**Table 5.3.** – Values of a, b,  $f_v$ ,  $SO_2$ , A, B and optical properties at 630 nm for normal sites of PDT patients.

Pat. #	site	a [ $cm^{-1}$ ]	b [-]	$f_v$ [%]	$SO_2$ [%]	A [ $cm^{-1}$ ]	B [ $nm^{-1}$ ]	$\mu_s^{630}$ [ $cm^{-1}$ ]	$\mu_a^{630}$ [ $cm^{-1}$ ]	$\delta^{630}$ [mm]
E6	1	7093	0.98	0.98	59	1565	0.013	13.0	0.64	2.0
	2	75318	1.36	0.73	59	576	0.010	12.1	1.10	1.5
	3	42395	1.30	0.79	55	544	0.010	10.0	1.11	1.6
E7	1	163662	1.53	1.57	41	164	0.008	8.3	0.78	2.2
	2	114857	1.52	4.46	58	2773	0.014	6.4	1.10	2.0
	3	329851	1.69	3.59	36	3183	0.014	6.1	1.20	1.9
E8	1	31163	1.33	2.26	78	1426	0.013	6.0	0.64	2.8
	2	10005	1.11	4.28	74	4995	0.017	7.8	0.56	2.7
	3	75554	1.46	2.12	62	2700	0.014	6.4	0.69	2.6
E9	1	99004	1.51	4.23	59	945042	0.025	5.9	0.67	2.8
	2	262333	1.62	3.15	91	53	0.007	7.7	1.07	1.9
	3	29061	1.34	2.72	52	186929	0.022	5.3	0.59	3.1
L2	1	676216	1.74	3.33	84	131	0.008	9.3	1.21	1.6
	2	47908	1.46	2.58	43	17	0.003	4.0	2.97	1.3
	3	81315	1.40	3.30	52	9253	0.016	9.6	0.95	1.8
L3	1	71777	1.45	2.21	79	117	0.008	6.2	0.95	2.2
	2	47726	1.37	5.79	60	61024	0.019	7.0	1.07	2.0
O1	1	122809	1.49	0.52	98	2987	0.013	8.5	1.04	1.8
	2	70452	1.37	1.74	60	3188	0.013	10.1	0.99	1.7
	3	324176	1.60	0.84	76	6079	0.014	10.9	0.94	1.7
S1	1	544891	1.67	0.40	27	27	0.006	11.2	0.70	2.0
	2	1206	0.71	0.69	84	27	0.006	12.6	0.67	1.9
	3	3718	0.87	0.62	58	27	0.006	14.0	0.70	1.8
S2	1	310809	1.60	0.13	95	27	0.006	10.3	0.63	2.2
S3	1	2808	0.99	0.27	39	27	0.006	4.7	0.67	3.0
	2	2808	0.99	0.27	39	27	0.006	4.7	0.67	3.0
	3	1785	0.88	0.20	4	27	0.006	6.0	0.68	2.7
S4	1	22437	1.13	0.25	99	27	0.006	15.7	0.63	1.8
	2	2232	0.78	0.23	83	27	0.006	14.2	0.64	1.9
	3	190384	1.53	0.21	100	27	0.006	10.3	0.63	2.2

**Table 5.4.** – Values of a, b,  $f_v$ ,  $SO_2$ , A, B and optical properties at 630 nm for tumor sites of PDT patients.

Pat. #	site	a [cm <sup>-1</sup> ]	b [-]	$f_v$ [%]	$SO_2$ [%]	A [cm <sup>-1</sup> ]	B [nm <sup>-1</sup> ]	$s_s^{630}$ [cm <sup>-1</sup> ]	$a_a^{630}$ [cm <sup>-1</sup> ]	$\delta^{630}$ [mm]
E6	1	704706	1.75	11.1	16	7	0.005	8.7	3.02	1.0
	2*	704706	1.75	3.89	33	16	0.005	8.7	1.65	1.4
	3*	704706	1.75	8.75	25	9	0.005	8.7	2.38	1.1
E7	1	100421	1.49	0.91	2	745	0.011	6.8	0.99	2.1
	2	306758	1.63	4.76	42	5939	0.014	8.2	1.48	1.5
	3	241450	1.53	5.83	18	4073	0.013	13.0	2.60	0.9
E8	1	10019	1.13	6.41	0	394768	0.023	6.7	1.94	1.4
	2*	10019	1.13	2.57	59	189758	0.023	6.7	0.43	3.3
	3*	10019	1.13	8.20	7	0.79	0.023	6.7	2.24	1.3
E9	1	30702	1.34	7.71	55	5083944	0.028	5.5	1.25	2.0
	2	139231	1.50	5.53	60	1405882	0.026	8.8	0.83	2.0
	3	88879	1.57	3.86	46	177409	0.022	3.6	0.85	3.0
L2	1	1169888	1.82	0.97	54	44	0.006	9.7	1.14	1.6
	2	215957	1.62	4.04	64	712	0.012	6.3	0.97	2.2
	3 <sup>†</sup>	586656	1.74	30.9	100	817	0.009	8.0	3.85	0.9
L3	1	109379	1.42	2.87	38	2699	0.012	11.5	2.40	1.0
	2 <sup>†</sup>	123227	1.44	9.66	32	2903	0.011	11.5	4.88	0.6
	3	138920	1.46	2.80	47	1441	0.010	11.5	2.60	1.0
O1	1	61291	1.40	2.17	62	683	0.012	7.5	1.29	1.7
	2	9551	1.07	3.35	63	129137	0.023	9.8	1.17	1.6
	3	17324	1.17	2.92	58	54476	0.021	9.0	1.26	1.6
S1	1	343568	1.64	0.65	52	27	0.006	8.8	0.72	2.2
	2	66111	1.37	0.69	73	27	0.006	9.4	0.69	2.2
	3	18961	1.18	0.46	89	27	0.006	9.3	0.65	2.3
S2	1	4	0.11	1.52	15	27	0.006	1.7	0.98	3.6
S3	1	104	0.42	0.62	80	27	0.006	7.0	0.67	2.5
	2	6382	1.00	0.47	67	27	0.006	10.4	0.67	2.1
	3	786	0.71	0.21	38	27	0.006	8.2	0.66	2.4
S4	1	14353	1.04	0.41	74	27	0.006	17.5	0.66	1.7
	2	55210	1.20	0.59	93	27	0.006	23.7	0.65	1.4
	3	47294	1.20	0.59	83	27	0.006	20.2	0.67	1.5

\* assumes a, b and B from site 1; <sup>†</sup> assumes a, b and B based on average  $s_s'$  and  $a_a^{dry}$  of other two sites

Calculated reduced scattering and absorption coefficients of normal and tumor sites for patient #E6 are shown in Fig. 5.17 A and B, respectively. Reduced scattering coefficients for all three tumor sites are identical since the same values of a and b were assumed to be identical for all sites as explained above.

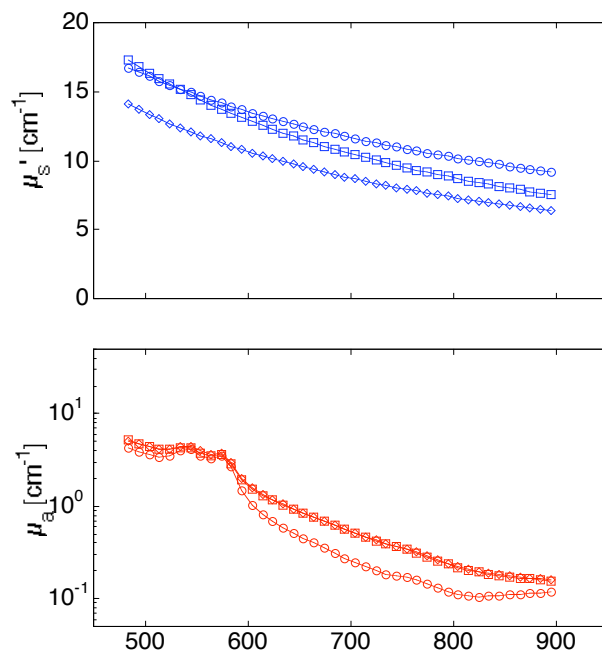


**Fig. 5.17.A.** - Optical properties of three normal sites from patient #E6. (Top) Reduced scattering coefficient. (Bottom) Absorption coefficient.

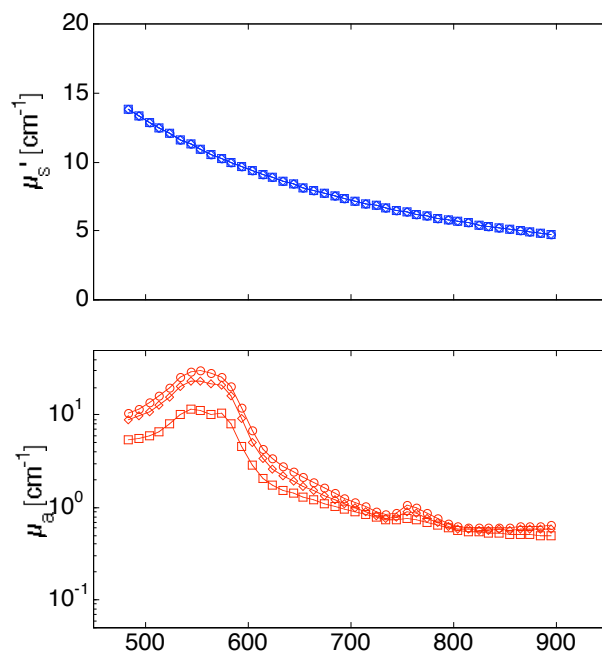


**Fig. 5.17.B.** - Optical properties of three tumor sites from patient #E6. (Top) Reduced scattering coefficient. (Bottom) Absorption coefficient. Identical reduced scattering coefficients are obtained for all three tumor sites (see text).

Blood fraction ( $f_v$ ), blood saturation ( $SO_2$ ), and reduced scattering coefficients, absorption coefficients and optical penetration depths ( $\delta$  [cm]) at 630 nm for the endoscopy screening patients (#N1-9) are shown in Figs. 5.18.A-E. Similar data for PDT patients (#E6-9, #L2-3, #O1 and #S1-4) are shown in Figs. 5.19.A-E. Normal sites are represented with circles (Figs. 5.18 and 5.19) and tumor sites are represented with inverted triangles (Fig. 5.19 only). The values for reduced scattering coefficients, absorption coefficients and optical penetration depths are also presented in tables 5.2, 5.3 and 5.4 for the normal, PDT normal and PDT tumor patients, respectively. Histograms of the optical penetration depth at 630 nm (same data as in Figs. 5.18.E and 5.19.E) are shown in Fig. 5.20 for the normal, PDT-normal (soft tissue only) and PDT-tumor (soft tissue only). PDT soft tissue patients excluded skin patients (#S1-4).

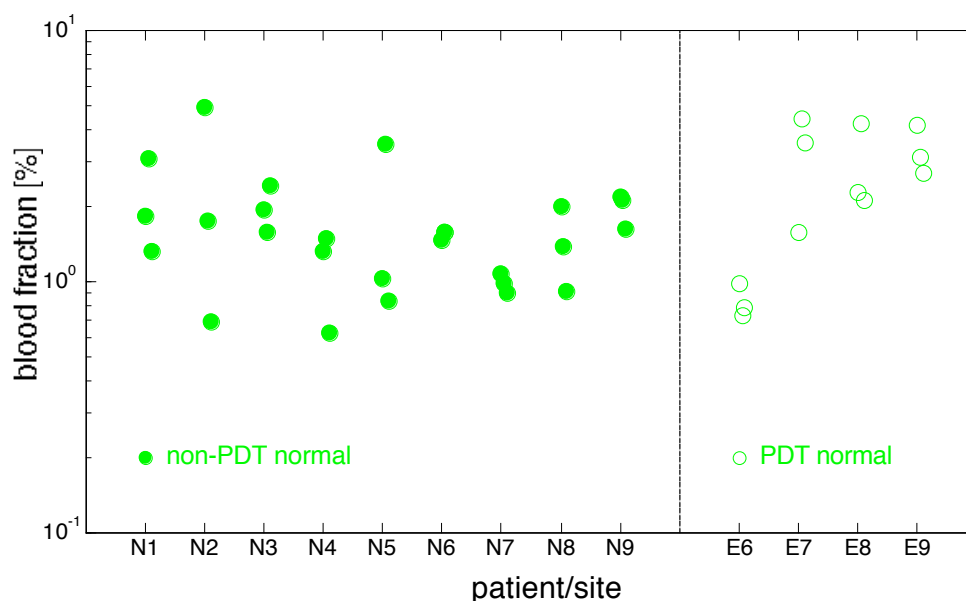


**Fig. 5.18.A** – Fraction of whole blood for normal esophageal tissue of non-PDT (patient #N1-N9) and PDT patients (patients #E6-E9).

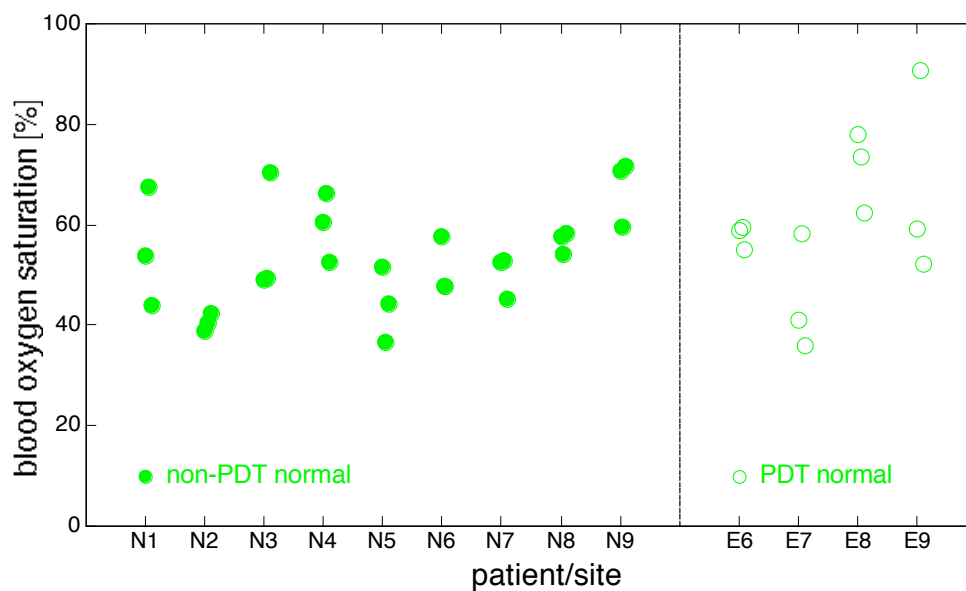


**Fig. 5.18.B** – Blood oxygen saturation for normal esophageal tissue of non-PDT (patient #N1-N9) and PDT patients (patients #E6-E9).

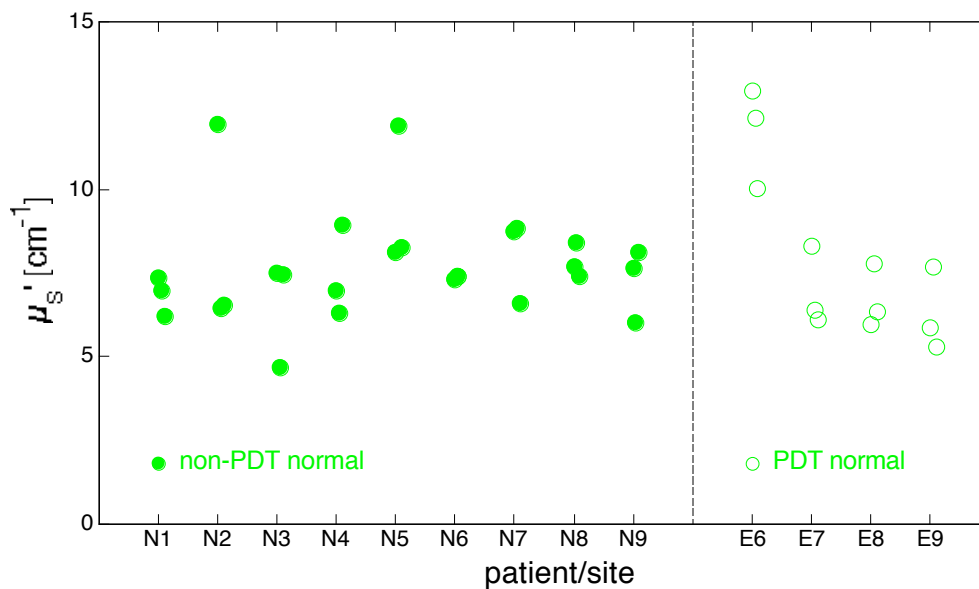


**Fig. 5.18.C** – Reduced scattering coefficient ( $\mu_s'$ ) at 630 nm for normal esophageal tissue of non-PDT (patient #N1-N9) and PDT patients (patients #E6-E9).

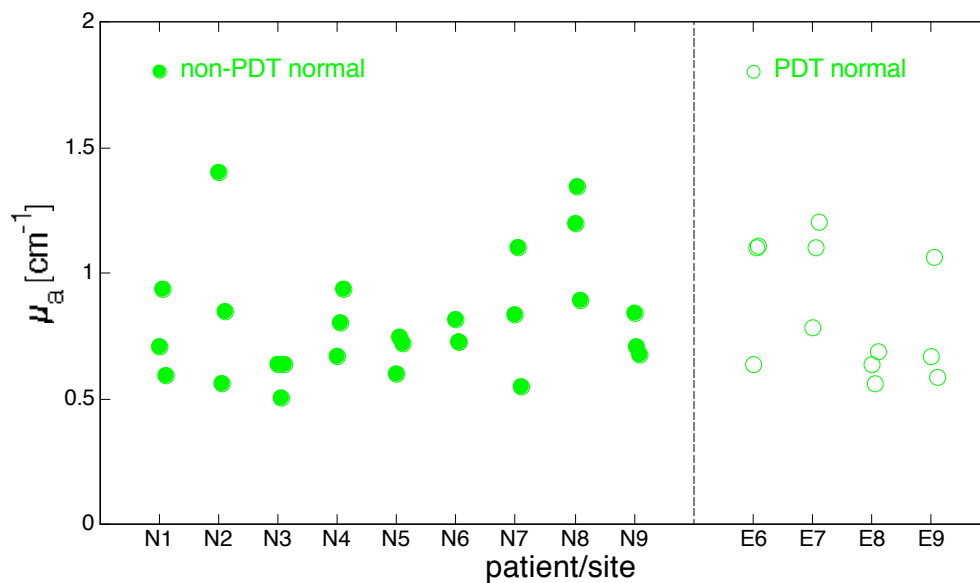


**Fig. 5.18.D** – Absorption coefficient ( $\mu_a$ ) at 630 nm for normal esophageal tissue of non-PDT (patient #N1-N9) and PDT patients (patients #E6-E9).

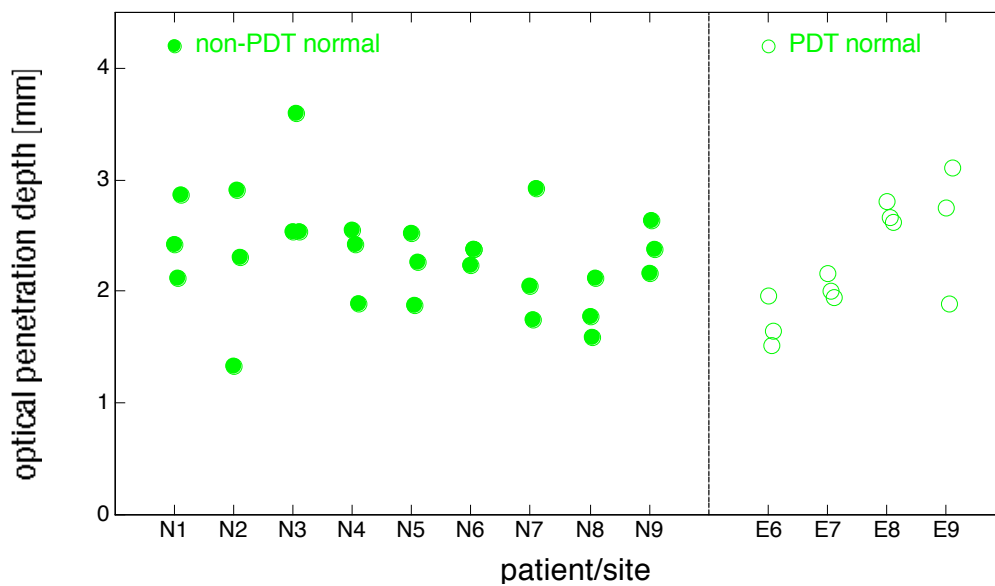


**Fig. 5.18.E** – Optical penetration depth ( $\delta$ ) at 630 nm for normal esophageal tissue of non-PDT (patient #N1-N9) and PDT patients (patients #E6-E9).

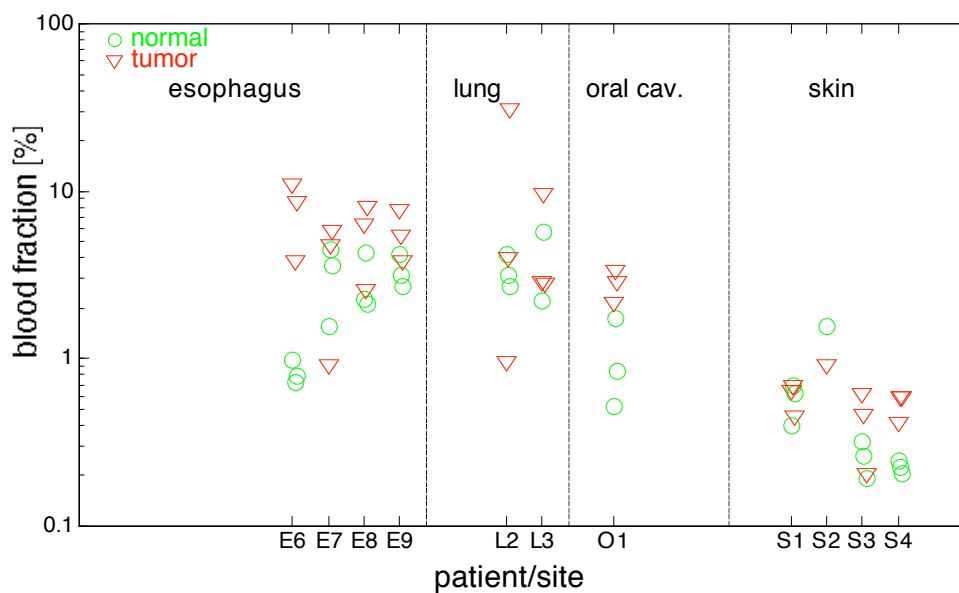


**Fig. 5.19.A** – Fraction of whole blood for normal (O) and tumor (∇) sites of esophageal, lung, oral cavity and skin PDT patients.

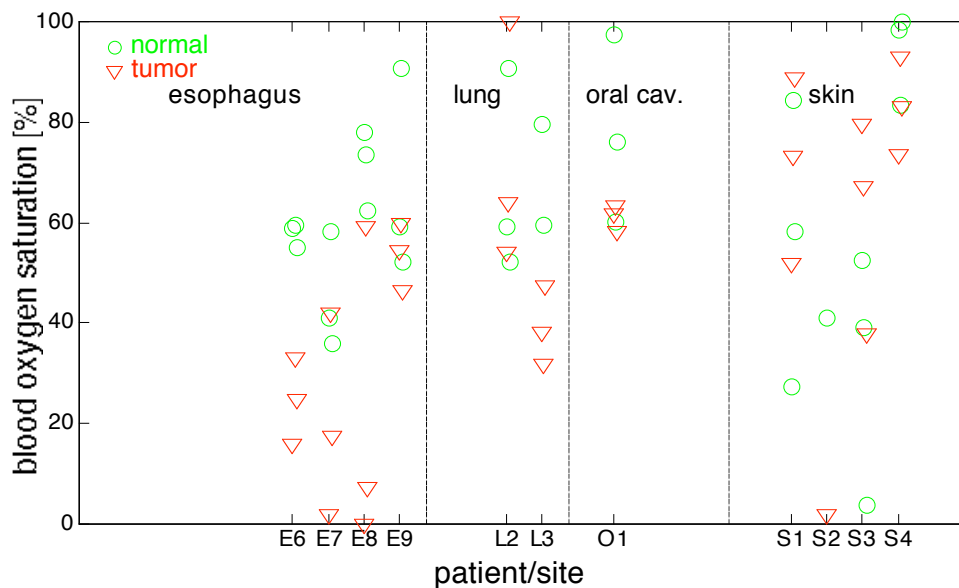


**Fig. 5.19.B** – Blood oxygen saturation for normal (O) and tumor (∇) sites of esophageal, lung, oral cavity and skin PDT patients.

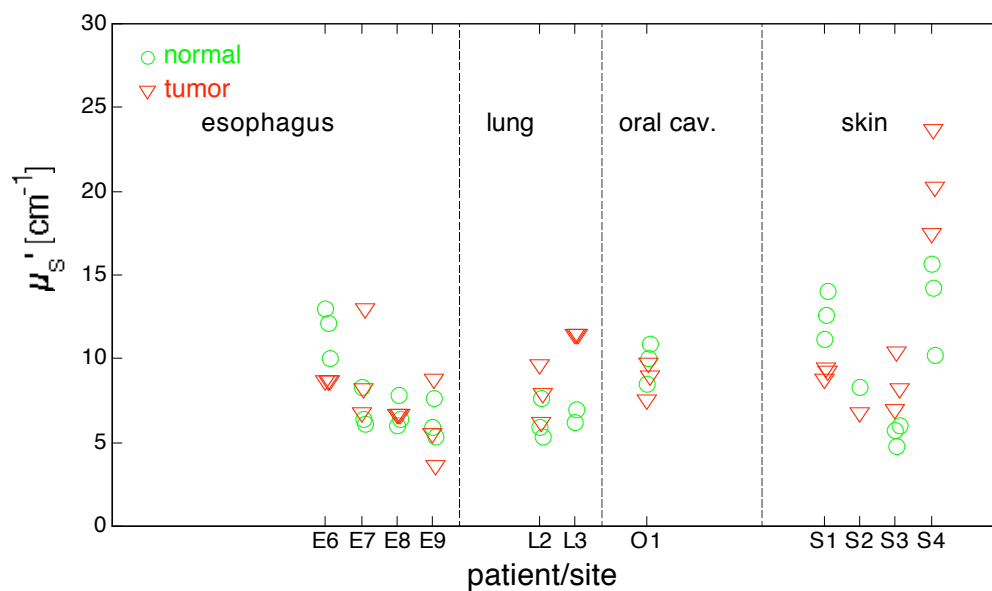


**Fig. 5.19.C** – Reduced scattering coefficient ( $\mu_s'$ ) at 630 nm for normal (O) and tumor ( $\nabla$ ) sites of esophageal, lung, oral cavity and skin PDT patients.

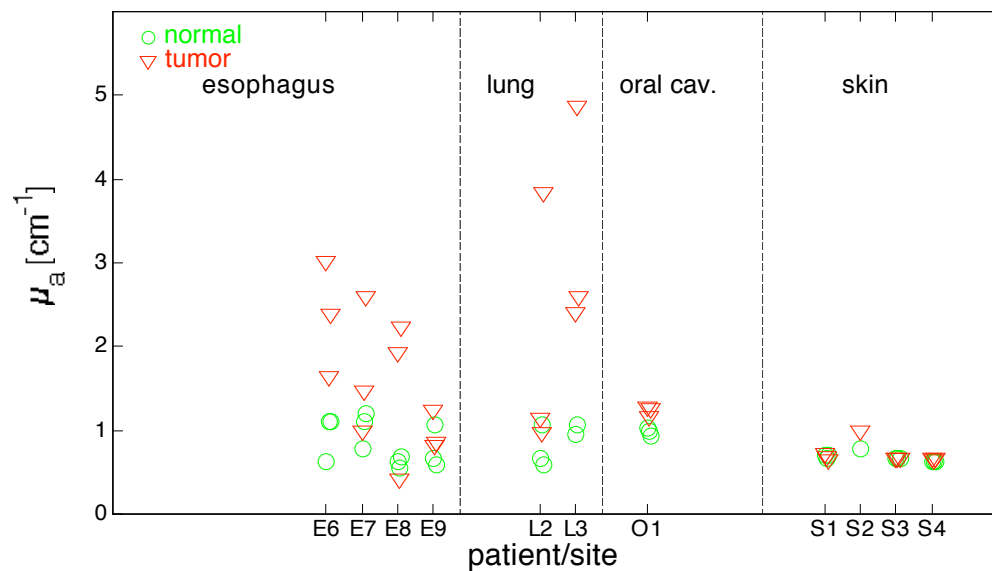


**Fig. 5.19.D** – Absorption coefficient ( $\mu_a$ ) at 630 nm for normal (O) and tumor ( $\nabla$ ) sites of esophageal, lung, oral cavity and skin PDT patients.

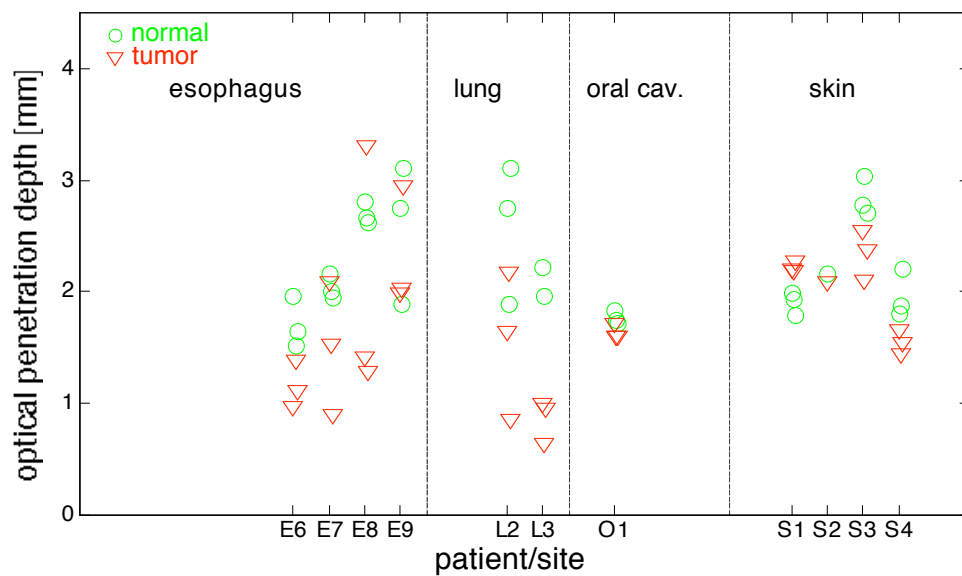


**Fig. 5.19.E** - Optical penetration depth ( $\delta$ ) at 630 nm for normal (O) and tumor (V) sites of esophageal, lung, oral cavity and skin PDT patients.

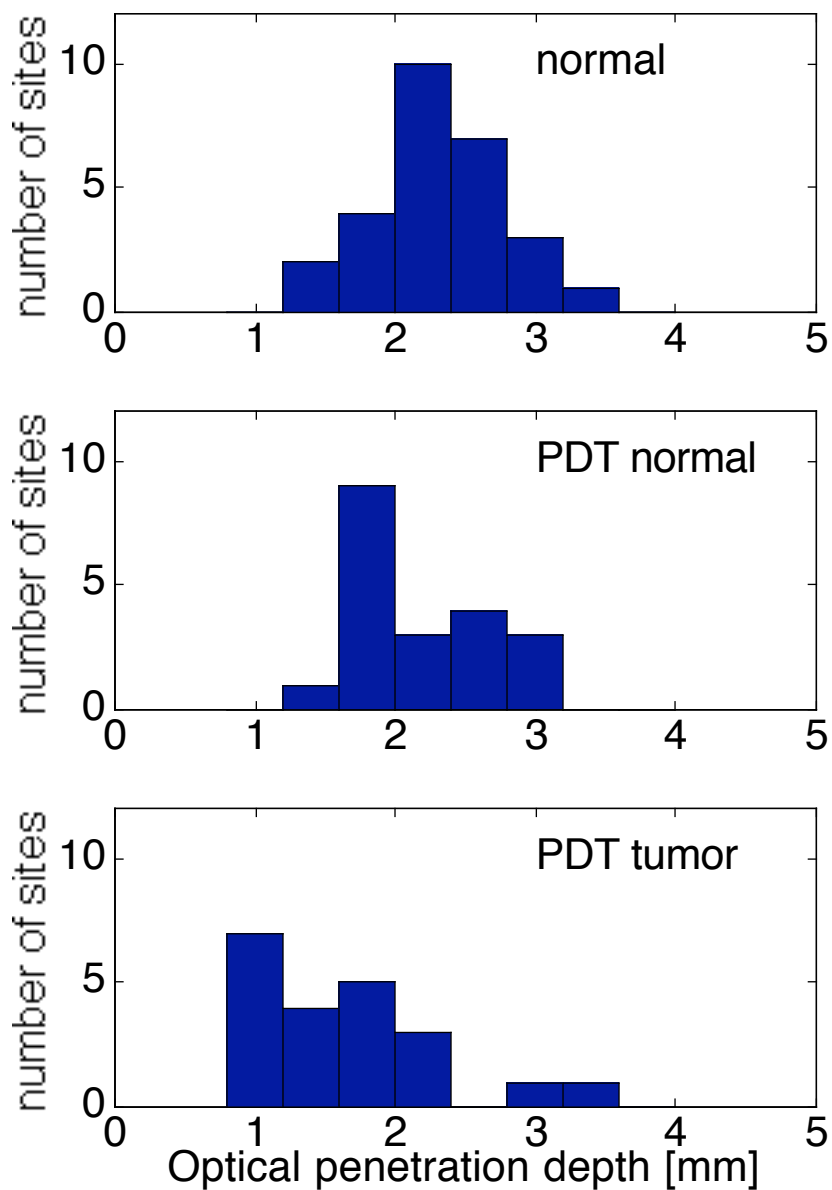


**Fig. 5.20.** - Histograms of optical penetration depth at 630 nm of the esophageal screening and soft-tissue PDT patients. Data is also presented in Figs. 5.18.E and 5.19.E.

Mean and standard deviations for blood fraction ( $f_v$ ), blood oxygen saturation ( $SO_2$ ), and reduced scattering coefficients ( $s'$ ), absorption coefficients ( $a$ ) and optical penetration depths ( $\delta$ ) at 630 nm are shown in table 5.5. Only the PDT soft tissue patients

(esophageal #E6-9, lung #L2-3 and oral cavity #O1) are included in this table. Skin patients (#S1-4) are excluded since the skin architecture is quite different from that of soft tissue [37]. No statistics were performed in the skin patient data because of the small sample population.

**Table 5.5.** – Mean and standard deviations for  $f_v$ ,  $SO_2$ , and  $a_s$ ,  $s'$  and  $\delta$  at 630 nm. PDT patient data exclude measurements in skin (see text).

	non-PDT normal	PDT normal (soft tissue only)	PDT tumor (soft tissue only)
$f_v$ [%]	$1.72 \pm 0.93$	$2.60 \pm 1.49$	$6.15 \pm 6.34$
$SO_2$ [%]	$54 \pm 10$	$65 \pm 16$	$42 \pm 24$
$s'$ at 630 nm [ $cm^{-1}$ ]	$7.7 \pm 1.5$	$7.8 \pm 2.3$	$8.4 \pm 2.3$
$a$ at 630 nm [ $cm^{-1}$ ]	$0.80 \pm 0.23$	$0.87 \pm 0.22$	$1.87 \pm 1.10$
$\delta$ at 630 nm [mm]	$2.3 \pm 0.5$	$2.2 \pm 0.5$	$1.6 \pm 0.7$

Two-sample t tests [90] were performed to compare results for normal esophageal tissue of non-PDT against PDT patients and to compare normal against tumor sites for PDT soft tissue patients. Significant difference was found between non-PDT normal and PDT normal tissue for  $f_v$  and  $SO_2$  with p-values  $<0.03$  and  $<0.01$ , respectively. No significant difference was found for the other parameters. Comparison between PDT normal and PDT tumor sites showed significant difference between all parameters except  $s'$  with p-values  $<0.02$ ,  $<0.003$ ,  $<0.001$  and  $<0.002$  for  $f_v$ ,  $SO_2$ ,  $a$  and  $\delta$ , respectively.

## 5.5 Discussion

One of the big challenges in making endoscopic measurements is the dimension constraint imposed on the optical fiber probe. Typical diameter of a working channel for commercial endoscopes is 2-3 mm [91]. Our first attempt was to use a single bare 600- $\mu$ m-diameter optical fiber for both delivery and collection of light. Unfortunately the sampling volume of this fiber configuration limits its ability to determine the absorption coefficient [60]. Furthermore, when using a single fiber the specular reflection of the optical fiber tip is an important component of the detected signal and fiber-tissue contact becomes an important issue, increasing the variation in the data [92]. An alternative approach for the endoscopic measurements was the development of the two-fiber probe described in section 5.3.1. This probe used two fibers, one as source and the other as detector, separated 2.5 mm apart in a side viewing configuration, which allowed a greater sampling volume and eliminated fiber specular reflection contamination on the detected signal.

Development of the empirical forward light transport model in section 5.3.3 lead to the use of a probe specific model, rather than the use of a theoretical model that adequately modeled the geometry and boundary conditions of the probe. Figure 5.1 shows the impact of different boundaries on the detected signal of a Monte Carlo simulation when an ideal optical fiber is used to collect light from a semi-infinite medium. The optical fiber index of refraction perturbs the medium boundary and the optical fiber numerical aperture limits the fiber cone of collection. With an actual optical fiber probe the material surrounding the optical fiber (i.e., metal supports, plastic tubing) will aggravate the changes in the medium boundary. Furthermore, the optical fiber collection efficiency (described in Chapters 3 and 4, and determined by the fiber cone of collection) is a function of the tissue optical properties which adds more complexity to the model. Since the empirical model is based on measurements with the actual probe in samples with known optical properties all these issues get lumped in the transport function. The disadvantage is the fact that the model is specific for a particular probe and ideally calibration has to be done to each probe that is made. Normalization of the data

and the model by the measurement of a solid standard (also used to account for day-to-day variations in the system) helped overcome this calibration issue as long as the probes were alike in configuration.

The ability to determine two parameters, the reduced scattering coefficient ( $\mu_s'$ ) and the absorption coefficient ( $\mu_a$ ), with one spectral reflectance measurement is only possible because of the spectral nature of the tissue components and the assumptions stated in Eqs. 5.9, 5.10 and 5.11. In a typical experimental setup two independent (or orthogonal) measurements have to be made to determine two independent variables. In our case we only have one measurement, but composed of more than 400 spectral points that are not completely orthogonal to each other. Nevertheless there exists enough information to derive the two optical properties if a priori information about the tissue components is known. For this we assume that the tissue absorption coefficient is composed of absorption from dry tissue ( $\mu_a^{\text{dry}}$ ), water ( $\mu_a^{\text{water}}$ ), oxy- and deoxy-blood ( $\mu_a^{\text{oxy}}$  and  $\mu_a^{\text{deoxy}}$ ) and that the reduced scattering coefficient behaved as  $a\lambda^{-b}$ .

As with any fitting routine, starting with the appropriate initial values for the fitting parameters helps avoiding reaching local minima (which leads to incorrect answers) in the minimization routine. Using the isobestic spectral points and leaving the blood oxygen saturation ( $\text{SO}_2$ ) out of the initial fitting helped the appropriate determination of the parameter  $b$  for the reduced scattering as well as establishing better guesses for the other initial parameters. Occasionally the determination of  $b$  with the limited number of data points (the isobestic points) resulted in non-physiological values for the optical properties. In these cases new initial parameters were attempted. Unique values for all parameters that corresponded to physiological values for the optical properties were always obtained.

This approach presented results comparable to the use of more traditional models, such as the diffusion theory combined with adding doubling for *in vitro* measurements as shown in Fig. 5.15. Disagreement was found in the spectra below 650 nm as it should be expected since diffusion theory fails when the reduced mean free path ( $1/(\mu_a + \mu_s')$ ) is comparable with the source-detector separation and when  $\mu_a$  is comparable to  $\mu_s'$ .

Literature values for bovine muscle at 630 nm have  $\mu_s'$  ranging from 4.4 to 7  $\text{cm}^{-1}$  [36] and  $\mu_a$  ranging from 0.4 to 3.5  $\text{cm}^{-1}$  [36], which are in agreement with the results obtained with the method presented in this study.

Residuals shown in Figs.5.16.A to F were typical for all the sites measured and were always below 20% for most spectral ranges. Recall that some of the tumor sites were blood saturated (highlighted in table 5.4) and assumptions of different tumors sites to have the same  $\mu_s'$  and same  $\mu_a^{\text{dry}}$  were made. These results obtained for blood saturated sites should be considered only as estimates since the above assumptions have no scientific basis. Nevertheless all blood saturated sites presented higher results for blood content. Blood oxygen saturation results were compromised in these sites since it relied mainly in the presence and magnitude of the deoxy-blood peak at 780 nm which is a small spectrum feature compared to the absorption bands in the 500–600 nm range. It should be noted that the results for  $\text{SO}_2$  in this work represent the mixed arterio-venous blood oxygen saturation which explain the low average values shown in table 5.5 as opposed to the arterious blood oxygen saturation typically in the 90 to 98% range. Reconstruction of the optical properties for all sites is direct with the use of values in tables 5.2-4 and Eqs. 5.9-11.

Comparison of non-PDT normal, PDT normal and PDT tumor patients are given in Figs. 5.18 and 5.19 with summaries presented in Fig. 5.20 and table 5.5. The mean value of  $f_v$  and  $\text{SO}_2$  were respectively 50 and 20% greater for the PDT normal (soft tissue only) compared to the non-PDT normal with p-values of  $<0.03$  and  $<0.01$ . In contrast the absorption coefficient at 630 nm was statistically the same for both patient populations. The reason for this discrepancy may be the fact that the PDT normal population was composed of many tissue types and the non-PDT normal population was composed of esophageal tissue only. Blood fraction of PDT tumor sites was more than 2 times greater than in PDT normal tissues ( $p < 0.02$ ). This is probably due to the increased vascularization typical of tumor tissue [93]. The increased blood fraction accounted for a 2-fold higher absorption coefficient ( $p < 0.001$ ). Blood oxygen saturation was 50% lower ( $p < 0.003$ ) for PDT tumor compared to PDT normal sites. No significant difference was

found between non-PDT normal, PDT normal and PDT tumor reduced scattering coefficient. As a consequence the optical penetration depth for PDT tumor patients was 38% smaller than  $\delta$  for the PDT normal patients ( $p < 0.002$ ). These results will greatly influence the drug concentration measurements as discussed in the next chapter. Reduced scattering and absorption coefficients determined in this work are comparable to results obtained by other authors for esophagus ( $s' = 7.0 \pm 2.3 \text{ cm}^{-1}$  and  $a = 0.27 \pm 0.14 \text{ cm}^{-1}$  at 630 nm [55]), bronchial submucosa ( $s' = 12.4 \pm 0.7 \text{ cm}^{-1}$  and  $a = 1.8 \pm 0.2 \text{ cm}^{-1}$  at 633 nm [94]) and bronchial tumor ( $s' = 12.5 \pm 0.7 \text{ cm}^{-1}$  and  $a = 1.2 \pm 0.2 \text{ cm}^{-1}$  at 633 nm [94]).

Interestingly, Intralipid showed a non-linear relation between concentration and scattering coefficient as determined by collimated transmission measurements and shown in Fig. 5.8. Correction of the reduced scattering coefficient in Fig. 5.9 by the values of Fig. 5.8.A and by the dilution from the stock solution (Intralipid 20%) made all curves collapse to a single curve for the reduced scattering coefficient of the stock Intralipid (not shown).

## Chapter 6

# Determination of drug concentration and photodynamic dose in esophagus, lung, oral cavity and skin cancer patients undergoing photodynamic therapy treatment

### 6.1 Introduction

Optical determination of drug concentration *in vivo* can provide tools for assessment of dosimetry [14], pharmacokinetics [27, 28] and functional studies (such as gene expression [95]) in biological systems. In many applications the drug is fluorescent hence drug concentration can possibly be determined using fluorescence spectroscopy. If the fluorophore is in a non-scattering medium the measured fluorescence is typically a linear function of the fluorophore concentration. Figure 6.1 shows the emission spectrum of different concentrations of the photosensitizer Photofrin diluted in water (top curve) for excitation with a 440-nm nitrogen-dye laser and detection with an optical multichannel analyzer through an optical fiber. If the peak fluorescence at 630 nm is plotted as a function of the fluorophore concentration a simple linear correlation between fluorophore concentration and relative fluorescence intensity is obtained (Fig. 6.1. bottom). This linear relation fails when the fluorophore concentration reaches high levels. In this case aggregation between drug molecules quenches the fluorescence [96].

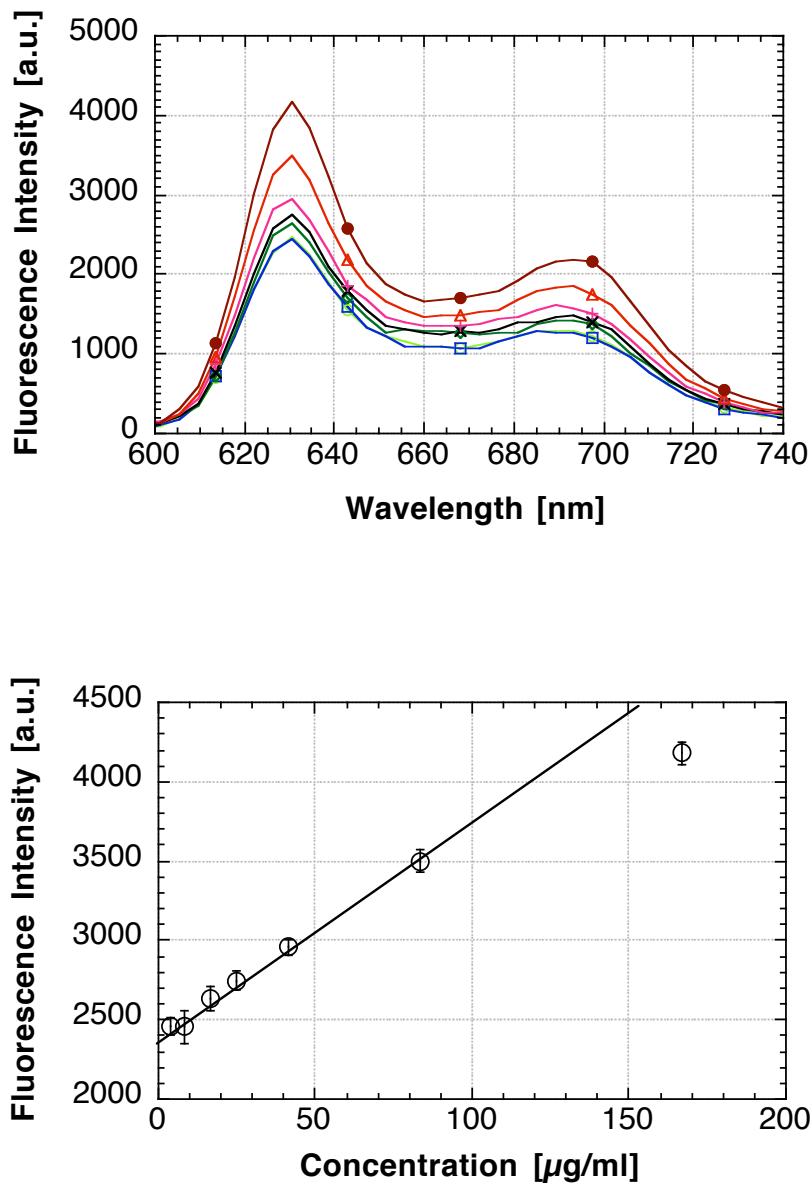


**Fig. 6.1.** – Relation between relative fluorescence intensities and Photofrin concentration in a water and excitation at 440 nm. (TOP) Spectra of increasing concentration of Photofrin in aqueous solution. (BOTTOM) Peak fluorescence at 630 nm as a function of photosensitizer concentration

One difficulty in determining the drug concentration arises from the light transport that affects the excitation and emission light when the drug is in an absorbing or scattering media. For example in Fig. 6.2 the same amount of a fluorophore (Photofrin)

was placed in three beakers containing water, water plus Intralipid (scattering agent) or water plus Intralipid plus ink (absorbing agent) and fluorescence was excited with an argon ion laser (488 nm). The observed fluorescence values through a long-pass filter (to reject the excitation light at 488 nm) for the three different media have different intensities. Different scattering and absorption coefficients from different tissues would modulate the fluorescence intensities observed *in vivo* in the same manner.

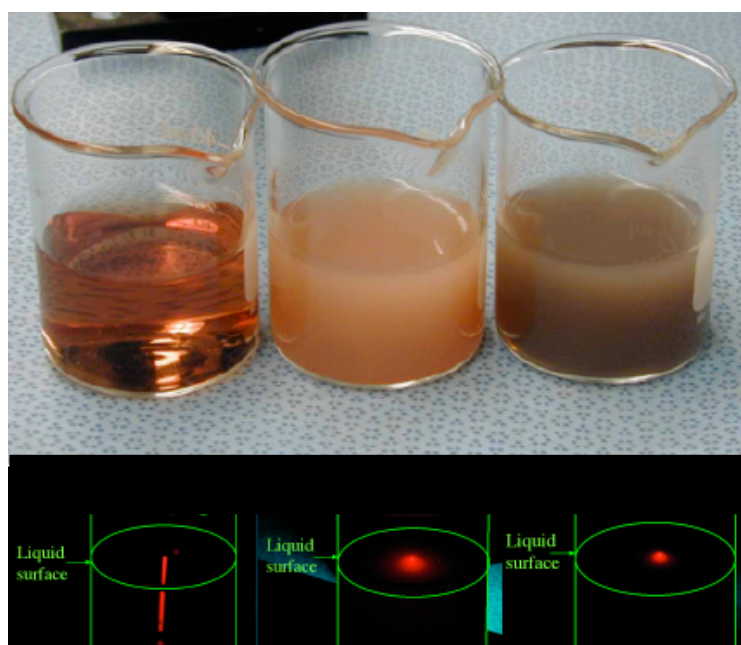


**Fig. 6.2.** – Photographs of fluorescence of Photofrin from three different media. In a clear medium (left) excitation light goes through the sample and emission comes as a line from across the sample. In a turbid medium (center) excitation light creates a diffusion glow ball at the sample surface. In a turbid/absorbing medium (right) the fluorescence glow ball is decreased in size and intensity due to the absorption of excitation and emission light.

Methods to model fluorescence measurements from turbid media have been proposed to correct the effect of optical properties. The Kubelka-Munk [32], Beer's law [97], diffusion [98] and photon migration [33] theories of light transport are amongst these models. Most of these models do not retrieve quantitative fluorescence information and require empirical calibration of the system. Typically, measurements of the fluorophore at different concentrations in tissue phantoms are made to relate fluorophore concentrations to the measured fluorescence. Recently Gardner *et al.* [22] studied the

recovery of intrinsic fluorescence from measured fluorescence. Using a non-fiber-optic based system they determined fluorophore concentration with an error of  $\pm 15\%$  over a limited range of optical properties ( $\mu_s'$  from 7.5 to 25  $\text{cm}^{-1}$  and  $\mu_a$  from 1.5 to 17  $\text{cm}^{-1}$ ).

Pogue and Burke [35] have demonstrated that small-diameter optical fibers minimize the effects of the absorption coefficient on the fluorescence measurements. Although this effect improved the ability of the system to determine drug concentration, low scattering coefficients still pose a problem. This arrangement also requires the use of an empirical calibration.

In this study we used an optical fiber to measure fluorophore concentration in turbid media. The measured fluorescence was corrected by a light transport factor obtained from Monte Carlo simulations. A Monte Carlo model for the determination of fluorescence by an optical fiber was developed. This model was validated with an analytical expression for the absorbing-only case and with experiments for the absorbing-only and turbid cases. This model assumes that the fluorophore is uniformly distributed over the sample volume and that the tissue is homogenous.

It should also be noted that the fluorescence quantum yield, a parameter that relates the number of emission photons produced to the number of absorbed excitation photons, depends on the microenvironment of the drug. In the present model the quantum yield was assumed to be constant. Knowledge of the optical properties of the medium is also required. Reflectance measurements were used for the determination of the tissue optical properties for the patients undergoing PDT treatment using the empirical transport model described in chapter 5.

Another aspect of this report is the determination of the photodynamic dose. Patterson, Wilson and Graff [13] demonstrated that the margin of necrosis corresponds to a threshold value for the number of photons absorbed by photosensitizer per gram of tissue, or [ph/g], independent of the light exposure parameters (irradiance, wavelength or exposure time) used to obtain this threshold. This threshold value is called the PDT threshold dose, and is known to vary for different photosensitizers and different tissues over the range of  $10^{18}$ - $10^{20}$  ph/g [13]. Patterson, Wilson and Graff's work illustrated that

despite variation between patients in the optical properties of a tissue or the accumulation of photosensitizing drug in a tissue, there was a practical dosimetry factor that predicted the onset of necrosis. In this study tissue, the depth of necrosis was predicted by calculating the photodynamic dose as a function of tissue depth and using the threshold dose as a guide to necrosis achievement. The photodynamic dose was determined from the optical penetration depth (chapter 5) and the drug concentration calculated from fluorescence measurements described in this chapter.

## 6.2 Theory

### 6.2.1 Determination of photosensitizer concentration from fluorescence

Normally, photosensitizers are administered as mg photosensitizer per kg body weight of patient, or [mg/kg]. But the key factor is how much photosensitizer accumulates in the tissue,  $C$  [mg/g]. If the body were simply a bag of water, the administered drug would distribute uniformly. But in reality, the pharmacokinetics of photosensitizer distribution in the body varies from tissue to tissue. This study seeks to determine the amount of photosensitizer concentration accumulated in a tissue to ensure that sufficient photosensitizer is present for treatment.

Photosensitizing drugs are often fluorescent which offers a means of assaying the amount of photosensitizing drug. One uses a shorter wavelength of light,  $\lambda_x$  [nm], to excite the photosensitizer fluorescence that emits at longer wavelengths, denoted  $\lambda_m$  [nm]. For an optically homogeneous tissue with a uniform distribution of fluorescent photosensitizer, the observed fluorescence,  $F$  [W/cm<sup>2</sup>], at wavelength  $\lambda_m$  escaping the tissue into an optical fiber in response to a broad uniform irradiance is:

$$\begin{aligned}
 F &= \int_V E_{0x} T_x \ln(10) \epsilon C \Phi_f T_m \eta_c dV \\
 &= E_{0x} \ln(10) \epsilon C \Phi_f \eta_c \int_V T_x T_m dV = E_{0x} \ln(10) \epsilon C \Phi_f \eta_c \chi
 \end{aligned} \tag{6.1}$$

where

$E_{ox}$	[W/cm <sup>2</sup> ]	irradiance of excitation light onto the tissue surface,
$T_x$	[dimensionless]	light transport factor for excitation light,
$\epsilon$	[cm <sup>-1</sup> /(mg/g)]	extinction coefficient of photosensitizing drug,
$C$	[mg/g]	concentration of photosensitizing drug,
$\Phi_f$	[dimensionless]	energy efficiency for conversion of absorbed excitation energy into emitted fluorescence energy which depends on the wavelength $\lambda_m$ ,
$T_m$	[1/cm <sup>2</sup> ]	light transport factor for escape of fluorescence at surface,
$V$	[cm <sup>3</sup> ]	Integration volume accounting for the optical fiber dimensions and geometry of excitation and collection,
$\eta_c$	[dimensionless]	collection factor to account for the numerical aperture of the fiber (see chapter 3 and 4),
$\chi$	[cm]	lumped effective transport length for excitation into and emission out of tissue. $\chi = \int_V T_x T_m dV$

The above Eq. 6.1 indicates that an effective transport length  $\chi$  characterizes the penetration of excitation light into tissue and the escape of fluorescence out of tissue. The term  $\chi$  depends on the optical properties of the tissue at  $\lambda_x$  and  $\lambda_m$  and on the area of collection of the detector as well as the geometry of collection. Gardner *et al.* [22] demonstrated the role of  $\chi$  in fluorescence spectroscopy of light-scattering tissue phantoms with a non-fiber based system. By rearranging Eq. 6.1, the observed photosensitizer fluorescence specifies the concentration of photosensitizer according to:

$$C = \frac{F}{E_{ox} \ln(10) \epsilon \Phi_f \eta_c \chi} \quad (6.2)$$

Consider two tissues with the same concentration  $C$  of photosensitizer, but one tissue is highly inflamed and the other is normal. In the inflamed tissue the high blood content attenuates penetration and escape of light and the value of  $\chi$  is decreased. The observed fluorescence  $F$  is lower in the inflamed tissue than the  $F$  observed in the normal tissue. But the factor  $\chi$  in Eq. 6.2 corrects for the differences in  $F$  so that  $C$  may be the same for both tissues.

The factor  $\Phi_f$  can vary several fold depending on the microenvironment of the photosensitizer. For example, the photosensitizer could be dissolved in an aqueous phase, adsorbed on a protein or aggregated with another photosensitizer. The quenching of fluorescence by the microenvironment is a variable that awaits experimental comparison of observed fluorescence,  $F$ , versus the true concentration  $C$  determined by chemical extraction from biopsied tissue samples and subsequent well-controlled assay.

## 6.2.2 Determination of oxidizing radicals

The number of oxidizing species that attack the cell at the necrosis margin during PDT was offered by Jacques [14-16] for a planar geometry:

$$R_{th} = E_0 k t \exp\left(\frac{-z_{necrosis}}{\delta}\right) \epsilon C \frac{\lambda}{hc} \Phi_T \Phi_{\Delta} f_R \quad (6.3)$$

where

$E_0$	[W/cm <sup>2</sup> ]	irradiance of treatment light onto the tissue surface,
$t$	[s]	exposure time for treatment light,
$\delta$	[cm]	optical penetration depth of treatment light,
$k$	[dimensionless]	augmentation of light at surface due to backscatter from tissue,
$z_{necrosis}$	[cm]	depth of the margin for zone of necrosis,
$\epsilon$	[cm <sup>-1</sup> /(mg/g)]	extinction coefficient of photosensitizing drug,
$C$	[mg/g]	concentration of photosensitizing drug,

$h$	[J s]	Plank's constant,
$c$	[m/s]	speed of light,
$\lambda$	[m]	wavelength,
$\Phi_T$	[dimensionless]	quantum efficiency for triplet formation,
$\Phi$	[dimensionless]	quantum efficiency for generation of oxidizing species,
$f_R$	[dimensionless]	fraction of oxidizing species that attack critical sites that contribute to cell death, and $1-f_R$ is the fraction of oxidizing species that attack non-critical sites such as the extracellular matrix,
$R_{th}$	[ph/g]	threshold concentration of critical oxidizing attacks for cell death.

The quantum efficiency  $\Phi$  describes the efficiency for an excited state photosensitizer to transfer its energy to molecular oxygen to create singlet oxygen or to generate some other type of oxidizing species. This  $\Phi$  is usually dependent on the tissue concentration of oxygen [9]. An example of how to determine the product  $\Phi_T\Phi f_R$  is shown in chapter 2 for a common cellular molecular species (NADPH).

## 6.3 Material and Methods

### 6.3.1 Fluorescence measurements

A nitrogen-dye laser (Fig. 6.3) operating at 440 nm wavelength, 4 ns pulse duration, 10 Hz repetition rate, 20 J/pulse energy (Laser Science, Cambridge, MA) was used to excite Photofrin fluorescence that emits in the 550-805 nm range. Excitation and collection were made through a single 600-  $\mu$ m core-diameter disposable optical fiber (Ceramoptec, Longmeadow, MA) using the biopsy channel of an endoscope or by direct contact to skin. The proximal end of the fiber was connected with a SMA connector to a mixed fiber bundle with a central 300  $\mu$ m optical fiber (which guided the excitation light from the laser) surrounded by twelve 100  $\mu$ m optical fibers that routed the fluorescence to

the detector. The detector was an optical multichannel analyzer (OMA, Princeton Instrument, Trenton, NJ) with an intensified gated diode array with 512 elements. The resolution was 2 nm per bin. Excitation light backscattered to the detector was rejected with a 530 nm long-pass glass filter (#OG530, Schott, Duryea, PA). Data was transferred to a computer through a GPIB connection. Collection time was set for 100 ms; 20 accumulations were typically used, for a total collection time of 2 seconds per measurement. Each bin of fluorescence collection was 2 nm.

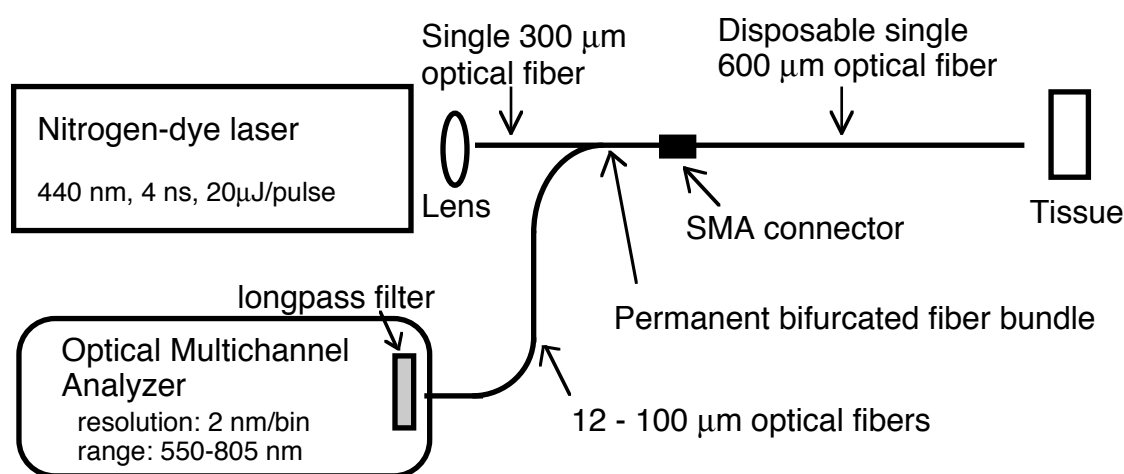


**Fig. 6.3.** – Fluorescence system setup. A nitrogen pumped dye laser excites tissue fluorescence, which is collected through the same, disposable, 600- $\mu\text{m}$  core diameter optical fiber and detected with an OMA system.

### 6.3.2 Experimental validation of the model

Fluorescence samples were prepared using rhodamine 6G as the fluorophore agent. Absorbing-only samples were made with different concentrations of India ink (No. 4415, Higgs, Lewisburg, TN) and 7.5 g/ml of rhodamine. Reagents were diluted in 90% ethanol. Fluorescence measurements were taken with the optical fiber immersed 1-cm deep in the samples mimicking an infinite medium. Samples were 2 cm in diameter and 4 cm in height. Five measurements were taken per sample.

Scattering samples were prepared using white latex paint (Behr ultra pure white No. 8050, Behr Process Corporation, Santa Clara, CA) as scattering element. Stock solution was made by mixing 10 ml of paint in 590 ml of 90% ethanol. Three sets of different paint concentration were prepared with three different absorptions each

according to table 6.1. Background absorption was obtained by adding India ink (No. 4415, Higgs, Lewisburg, TN). Final rhodamine concentration was 1.2 g/ml. Five measurements were taken per sample.

**Table 6.1.** – Composition of optical phantoms

Sample	Solvent (90% EtOh) [ml]	Paint (in 90% EtOh) [ml]	Ink (in 90% EtOh) [ml]	rhodamine (in 90% EtOh) [ml]	Final volume [ml]
Ab1	35	0	5	4	44
Ab2	30	0	10	4	44
Ab3	25	0	15	4	44
S11	0	80	0.0	1	81.0
S21	0	80	0.3	1	81.3
S31	0	80	0.6	1	81.6
S12	40	40	0.0	1	81.0
S22	40	40	0.3	1	81.3
S32	40	40	0.6	1	81.6
S13	64	16	0.0	1	81.0
S23	64	16	0.3	1	81.3
S33	64	16	0.6	1	81.6

The absorption coefficients of the stock ink and rhodamine were determined with a UV-VIS spectrophotometer (model 8452A, Hewlett-Packard, Palo Alto, CA). The optical properties of the stock white paint were determined by added-absorber spatially resolved steady-state diffuse reflectance measurements [83] as discussed in Appendix A. The optical properties of all phantoms at excitation (440 nm) and emission (630 nm) wavelengths are shown in table 6.2. These values were used in the Monte Carlo simulation to determine the lumped parameter  $\eta_c\chi$ .

**Table 6.2.** – Optical properties of phantoms at excitation (440 nm) and emission (630 nm) wavelengths

Sample	$r_s^{ex}$ [cm <sup>-1</sup> ]	$a_0^{ex}$ [cm <sup>-1</sup> ]	$a_f^{ex}$ [cm <sup>-1</sup> ]	$r_s^{em}$ [cm <sup>-1</sup> ]	$a_0^{em}$ [cm <sup>-1</sup> ]	$a_f^{em}$ [cm <sup>-1</sup> ]
Ab1	0	1.204	0.081	0	0.840	0.033
Ab2	0	2.408	0.081	0	1.680	0.033
Ab3	0	3.612	0.081	0	2.520	0.033
S11	77.6	1.830	0.011	69.3	1.270	0.008
S21	77.6	0.468	0.011	69.3	0.325	0.008
S31	77.6	0.925	0.011	69.3	0.642	0.008
S12	38.8	1.830	0.011	34.6	1.270	0.008
S22	38.8	0.468	0.011	34.6	0.325	0.008
S32	38.8	0.925	0.011	34.6	0.642	0.008
S13	15.5	1.830	0.011	13.8	1.270	0.008
S23	15.5	0.468	0.011	13.8	0.325	0.008
S33	15.5	0.925	0.011	13.8	0.642	0.008

### 6.3.3 Patients

One patient with Barrett’s esophagus (patient #E1), six patients with esophageal tumor (#E2 to #E9), three patients with lung tumor (#L1 to #L3), one patient with an oral cavity tumor (#O1) and four patients with skin cancer (#S1 to #S4) were recruited for this study. These patients were scheduled to receive standard FDA and off-label PDT treatment protocols. All patients were intravenously administered 2 mg/kg body weight of Photofrin II (Axcan – Acandipharm Inc.) 48 hours prior to activation by 630-nm laser light. Three measurements of clinically evaluated normal sites and three tumor sites were taken per patient. Nine non-PDT patients (#N1 to #N9) undergoing endoscopic screening were measured to check the fluorescence background signal from endogenous porphyrins.

Consent to take part in the dosimetry study was obtained from all patients. A study protocol was defined and approved by the Hospital IRB Committee. Detailed written and oral information on the dosimetry protocol was given to the patients prior to enrollment (See Appendix C). The measurements extended the PDT procedure by an average of 10 minutes.

### 6.3.4 Patient measurements

The 4-ns excitation pulse duration and the gated detector allowed fluorescence measurements to be made in the presence of the white illumination of the endoscope, so that the physician could observe the placement of the optical fiber during the procedure. Three normal sites and three tumor sites, as assessed by the physician, were measured. The total fluorescence measurement procedure took about 10 minutes. Typical raw fluorescence spectra of normal and tumor tissue are shown in Fig. 6.4. Measurement of a standard Rhodamine 6G solution (1.25 mg/ml in ethanol, Exciton) in a cuvette was taken before data collection to correct for day-to-day variations in the system. The fiber was placed orthogonal to the outside surface of the cuvette and five measurements were taken and averaged.

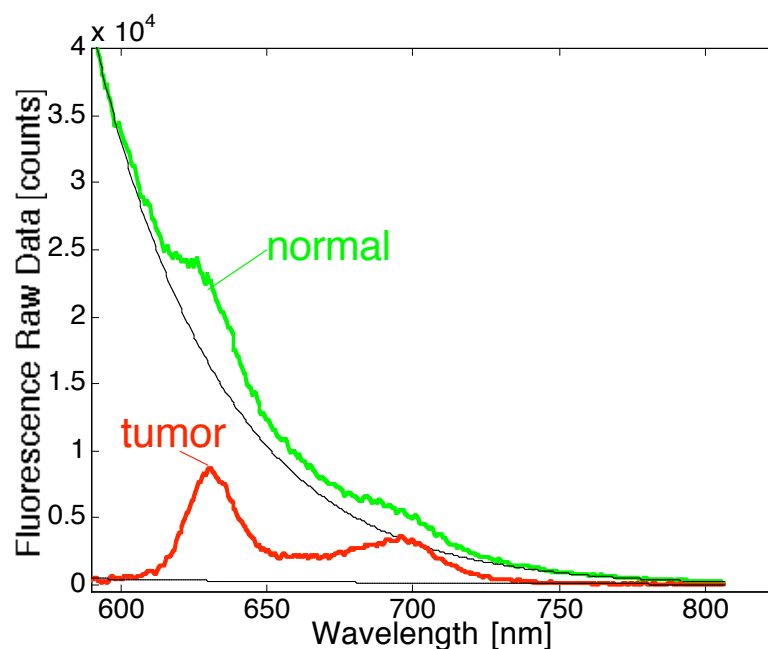


**Fig. 6.4.** – Typical *in vivo* fluorescence raw data from normal and tumor tissue. Thin black curves are a fit of the data for 580-600 nm and 750-805 nm by one side of a Gaussian curve that represents the background tissue autofluorescence.

### 6.3.5 Fluorescence Analysis

The photosensitizer fluorescence is typically weaker than the autofluorescence of the tissue. Autofluorescence of tumor sites were in most cases weaker than the

autofluorescence of normal sites. Fluorescence data from 580 to 600 nm and from 750 to 805 nm were fitted by one side of a Gaussian to yield the autofluorescent background (Fig. 6.4, thin black curves). The data from 580 to 600 nm and from 750 to 805 nm were chosen for the curve fit because no signal from the photosensitizer should be present in this spectral region. Curve fit was made as follows:

1. Initialize the variables  $A$ ,  $\lambda_0$  and  $B$  that define the magnitude, the central wavelength and the width of the Gaussian curve, respectively.
2. Generate the predicted autofluorescence curve (pAF) based on Eq. 6.4.

$$pAF = A \exp\left(\frac{(\lambda - \lambda_0)^2}{B}\right) \quad (6.4)$$

3. Minimize the square error between the predicted curve and the fluorescence data ( $F$ ) for the range of interest

$$err = \text{sqrt}\left(\sum_{\lambda=580nm}^{600nm} (pAF(\lambda) - F(\lambda))^2 + \sum_{\lambda=750nm}^{805nm} (pAF(\lambda) - F(\lambda))^2\right) \quad (6.5)$$

4. Update the values of  $A$ ,  $\lambda_0$  and  $B$
5. Iterate until  $err$  is less than  $10^{-4}$ .

This Gaussian curve was subtracted from the fluorescence data to yield a difference spectrum due to photosensitizer (Fig. 6.5).

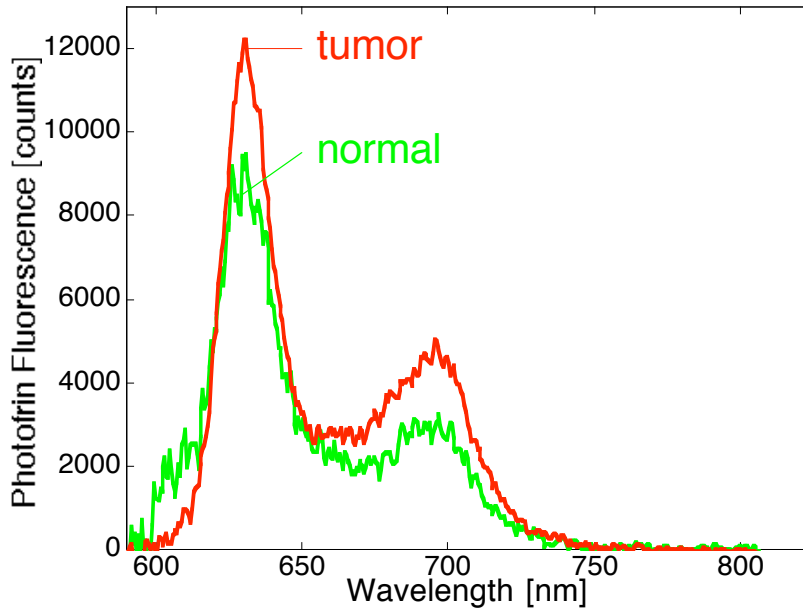


**Fig. 6.5.** – Typical *in vivo* photosensitizer fluorescence spectrum for normal and tumor tissue after subtraction of tissue autofluorescence.

A fluorescence score, FS, was defined to compare data between patients. The fluorescence spectrum after subtraction of the tissue autofluorescence yielded  $F_{\text{tissue}}(\lambda)$  which was normalized by the peak value of the Rhodamine 6G standard fluorescence at 555 nm,  $F_{\text{rh}}(555 \text{ nm})$ , and multiplied by the counts obtained from the Rhodamine 6G standard at 555 nm on the day of calibration of the instrument,  $10^5$  [counts/2-nm bin].

$$FS(\lambda) = \frac{10^5}{F_{\text{rh}}(555\text{nm})} F_{\text{tissue}}(\lambda) \quad (6.6)$$

To simplify the calibration of the instrument only the fluorescence at 630 nm was determined (FS(630 nm)).

### 6.3.6 Fluorescence Monte Carlo code

Fluorescence scores as described above do not account for the influence of the optical properties on transport of the excitation and emission photons through the

medium. A Monte Carlo simulation was developed to understand the light transport function of the normal and tumor tissue. This model used optical properties derived from the reflectance measurements described in chapter 5.

For simplicity, the photosensitizer was assumed to be uniformly distributed and with a fluorescence quantum yield of 1. Excellent discussions on Monte Carlo simulations can be found elsewhere [40, 42]. In brief, excitation photons ( $\geq$  than 1,000,000) were randomly launched uniformly within the radius of the fiber forming a collimated beam into a homogenous medium. Simulations were made for infinite or semi-infinite media and boundary conditions were assigned depending on the medium geometry and the optical fiber probe configuration. Each photon was assigned a initial weight  $W(1-r_{sp})$  at launch, where  $r_{sp}$  is the specular reflectance at the fiber tip. The photon was propagated in the medium by steps with a random stepsize  $s^{ex} = -\ln(rnd)/(a_0^{ex} + a_f^{ex} + s^{ex})$ , where  $rnd$  was a pseudo-random number uniformly distributed between 0 and 1,  $a_0^{ex}$  was the background absorption coefficient of the sample,  $a_f^{ex}$  was the absorption coefficient of the fluorophore and  $s^{ex}$  was the scattering coefficient of the medium at the excitation wavelength.

After every propagation step of an excitation photon the weight of the photon was partitioned in three ways. The weight was multiplied by  $s^{ex} / (a_0^{ex} + a_f^{ex} + s^{ex})$  and was saved with the position of the photon for further propagation of the excitation light. Part of the weight was converted into background absorbed excitation light by multiplying the weight by  $a_0^{ex} / (a_0^{ex} + a_f^{ex} + s^{ex})$ . The remaining  $a_f^{ex} / (a_0^{ex} + a_f^{ex} + s^{ex})$  was converted into fluorescence.

At this point, a fluorescence photon with weight  $W_f = W a_f^{ex} / (a_0^{ex} + a_f^{ex} + s^{ex})$  and emission wavelength was propagated with a new random step size  $s^{em} = -\ln(rnd)/(a_0^{em} + a_f^{em} + s^{em})$ , where  $a_0^{em}$  was the background absorption coefficient of the sample,  $a_f^{em}$  was the absorption coefficient of the fluorophore and  $s^{em}$  was the scattering coefficient of the medium at the emission wavelength. After each propagation step, the fluorescence photon was either absorbed with weight  $W_f(a_0^{em} + a_f^{em}) / (a_0^{em} + a_f^{em} + s^{em})$  or scattered with a new weight  $W_f' = W_f s^{em} / (a_0^{em} + a_f^{em} + s^{em})$ . The fluorescence photon was

propagated until totally absorbed according to the roulette method [40, 42, 74] or until escape.

The excitation photon resumed propagation with its remaining weight from its current position. This cycle of propagating the excitation photon, generating an emission photon, propagating the emission photon and then resuming propagation of the excitation photon was done until the excitation photon was totally absorbed according to the roulette method [40, 42, 74] or until it escaped. Reemission of the fluorescence photons was neglected.

The change in the direction of propagation after each propagation step was chosen according to the Henyey-Greenstein scattering function. The average cosine of the angle of photon deflection by a single scattering event (or anisotropy,  $g$ ) was set to 0.83. Different anisotropies were tested to evaluate the model dependence on this parameter. The first fluorescent emission event had direction selected isotropically.

When an excitation or emission photon crossed the air/sample boundary in the semi-infinite medium simulation with any escaping angle then the variable  $R_{\text{air}}$  (refer to Fig. 3.1 for geometry) was incremented by a value  $W(1-r_i)$  or  $W_f(1-r_i)$  where  $r_i$  is the internal Fresnel specular reflection for unpolarized light. When an excitation photon crossed a sample/fiber boundary with an escaping angle smaller than the half angle defined by the NA of the fiber (e.g.,  $\text{NA} = 0.39$ ), the escaping photon weight incremented the variable  $R_{\text{core}}$  by a value  $W(1-r_i)$ . If an emission photon crossed a sample/fiber boundary with an escaping angle smaller than the half angle, the escaping photon weight incremented the variable  $F_{\text{core}}$  by a value  $W_f(1-r_i)$ . If an excitation photon crossed a sample/fiber boundary with an escaping angle greater than the half angle, the escaping photon weight incremented the variable  $R_{\text{clad}}$  by a value  $W(1-r_i)$ . If an emission photon crossed a sample/fiber boundary with an escaping angle greater than the half angle, the escaping photon weight incremented the variable  $F_{\text{clad}}$  by a value  $W_f(1-r_i)$ . Escaping angles ( $\theta_{\text{out}}$ ) were corrected according to Snell's law to account for the refractive index mismatched at the boundary ( $\theta_{\text{out}} = \sin^{-1}(n_s \sin(\theta_{\text{in}})/n_f)$ , where  $\theta_{\text{in}}$  is the angle of the photon at the boundary,  $n_s$  is the refractive index of the sample, and  $n_f$  is the refractive index of

the fiber). The photon was returned to the tissue with the remaining weight ( $r_i W$  or  $r_i W_f$ ) and continued to propagate until being terminated according to the roulette method [40, 42] to conserve energy.

The lumped parameter  $\eta_c \chi$  was determined by rearranging Eq. 6.2 and using the fluorophore absorption coefficient  $\mu_{af}^{ex} = \epsilon C \ln(10)$ .

$$\eta_c \chi = \frac{F_{core}}{E_{0x} \Phi_f \mu_{af}^{ex}} \quad (6.7)$$

Ratio of the core fluorescence to the incident irradiance ( $F_{core}/E_{0x}$ ) was simply the ratio of the photon weights collected within the core of the fiber to the total weight of all photons launched. This follows from the assumption that the quantum yield of fluorescence ( $\Phi_f$ ) was assumed to be 1.

In a real application the concentration of the fluorophore is unknown and so is  $\mu_{af}^{ex}$ . Nevertheless we found that variations on the lumped parameter  $\eta_c \chi$  are negligible when the  $\mu_{af}^{ex}$  is at least 10-fold less than the background absorption  $\mu_{a0}^{ex}$ . Drug concentration *in vivo* is typically less than 5 g/ml corresponding to an absorption coefficient of  $0.05 \text{ cm}^{-1}$  at 440 nm. Typical absorption coefficient of tissue at 440 nm is approximately  $10 \text{ cm}^{-1}$ . Tests on the variations of the lumped parameter  $\eta_c \chi$  as a function of  $\mu_{af}^{ex}$  were done for typical tissue optical properties by assuming  $\mu_{a0}^{ex} = 10 \text{ cm}^{-1}$ ,  $\mu_{a0}^{em} = 0.5 \text{ cm}^{-1}$ ,  $\mu_s^{ex} = 15 \text{ cm}^{-1}$ ,  $\mu_s^{em} = 10 \text{ cm}^{-1}$  and varying  $\mu_{af}^{ex}$  from  $0.05$  to  $10 \text{ cm}^{-1}$  (g was assumed to be 0.9). For all phantoms simulations the index of refraction of the sample ( $n_s$ ) and fiber ( $n_f$ ) were set to 1.335 and 1.458, respectively. Simulations for patient data assumed  $n_s$  equal to 1.38 [99].

The Monte Carlo code was also tested against the analytical expression (Eq. 6.8) derived for the total fluorescence escaping the media for the absorbing only case [100].

$$\frac{F}{E_x} = \frac{\Phi_f}{2} \frac{\mu_{af}^{ex}}{\mu_{af}^{ex} + \mu_{a0}^{ex}} \left( 1 + \frac{\mu_{af}^{em} + \mu_{a0}^{em}}{\mu_{af}^{ex} + \mu_{a0}^{ex}} \operatorname{Ln} \left( \frac{\mu_{af}^{em} + \mu_{a0}^{em}}{\mu_{af}^{em} + \mu_{a0}^{em} + \mu_{af}^{ex} + \mu_{a0}^{ex}} \right) \right) \quad (6.8)$$

where

$F$	$[\text{W}/\text{cm}^2]$	total fluorescence escaping the medium,
$E_x$	$[\text{W}/\text{cm}^2]$	excitation source,
$\Phi_f$	[dimensionless]	quantum efficiency of fluorescence,
$\mu_{af}^{ex}$	$[\text{cm}^{-1}]$	fluorophore absorption coefficient at excitation wavelength,
$\mu_{a0}^{ex}$	$[\text{cm}^{-1}]$	background absorption coefficient at excitation wavelength,
$\mu_{af}^{em}$	$[\text{cm}^{-1}]$	fluorophore absorption coefficient at emission wavelength,
$\mu_{a0}^{em}$	$[\text{cm}^{-1}]$	background absorption coefficient at emission wavelength.

### 6.3.7 Calculating drug concentration from the measured fluorescence

With  $\eta_c \chi$  determined by Monte Carlo simulations, Eq. 6.2 was modified to calculate the drug concentration based on a single wavelength of emission. This was done to simplify the calibration procedure of the OMA system because the fluorescence spectra have to be converted from arbitrary units to the same units of  $E_{ox}$   $[\text{W}/\text{cm}^2]$ .

$$C = \frac{F_{630}^{sample}}{E_{0x} \ln(10) \epsilon \Phi_f^{630} \eta_c \chi} \frac{F_{cal}^{rhoda \min e}}{F_{max}^{rhoda \min e} \text{calib}_{630}} \frac{\lambda_{ex}}{\lambda_{em}} \quad (6.9)$$

where

$F_{630}^{sample}$	[counts]	fluorescence of the sample at 630 nm
$F_{max}^{rhoda \min e}$	[counts]	maximum fluorescence of the standard rhodamine 6G at 555 nm same day the sample measurements were taken

$F_{cal}^{rhoda\ min\ e}$	[counts]	maximum fluorescence of the standard rhodamine 6G at 555 nm same day the OMA calibration was made (5100 counts per pulse)
calib <sub>630</sub>	[counts/(W/cm <sup>2</sup> )]	OMA calibration at 630nm
$\lambda_{ex}$	[nm]	excitation wavelength
$\lambda_{em}$	[nm]	emission wavelength
E <sub>0x</sub>	[W/cm <sup>2</sup> ]	energy of excitation pulse (see text)

E<sub>0x</sub> in W/cm<sup>2</sup> was determined for the 15 J laser pulses of the N<sub>2</sub>-dye laser with 4-ns pulse width divided by the area of the fiber face. The OMA system was calibrated by shining collimated 630 nm light with known irradiance direct into the 600- $\mu$ m optical fiber using a neutral density filter to avoid detector saturation. A value of calib<sub>630</sub> = 22x10<sup>10</sup> counts/(W/cm<sup>2</sup>) was obtained for 5 accumulations of 100 ms acquisition time at

630 nm. The term  $\frac{F_{cal}^{rh}}{F_{max}^{rh} calib_{630}}$  converted the fluorescence from counts to the same units

as E<sub>0x</sub> and to account for day-to-day variations in the system. The term  $\frac{\lambda_{ex}}{\lambda_{em}}$  ensured that photons with different energies (excitation and emission photons) were properly weighted.

For the rhodamine phantom measurements, the extinction coefficient ( $\epsilon$ ) at excitation wavelength (440 nm) was 3.17 cm<sup>-1</sup>(mg/ml)<sup>-1</sup> [101] and the total quantum yield of fluorescence in methanol was 0.95 [102]. Since the fluorophore concentration was determined using only the emission wavelength at 630 nm the quantum yield was normalized by the fluorescence spectrum of rhodamine given a final quantum yield of fluorescence at 630 nm of 0.0022 [per nm].

For the patient measurements the extinction coefficient ( $\epsilon$ ) of Photofrin diluted in water was measured with a diode array spectrophotometer (HP8452A, Hewlett-Packard, Palo Alto, CA). At the excitation wavelength (440 nm),  $\epsilon$  had a value of 10.8 cm<sup>-1</sup>(mg/ml)<sup>-1</sup> (Fig. 6.6). Based on cell culture measurements by Kvam and Moan [103]  $\Phi_f$

of Photofrin was assumed to be 0.08. The quantum yield of fluorescence at 630 nm for Photofrin, determined by normalizing  $\Phi_f$  by the fluorescence spectrum, was 0.00089 [per nm]. It is acknowledged that the microenvironment influences  $\Phi_f$ , which may change its value. Since the sites where the fluorescence and reflectance (see chapter 5) measurements were taken were not exactly the same, no correlation between the spectra could be assumed. Because of this the average  $\eta_c\chi$  at 630 nm for three normal sites or three tumor sites was assumed for use in correcting normal and tumor tissue fluorescence, respectively.

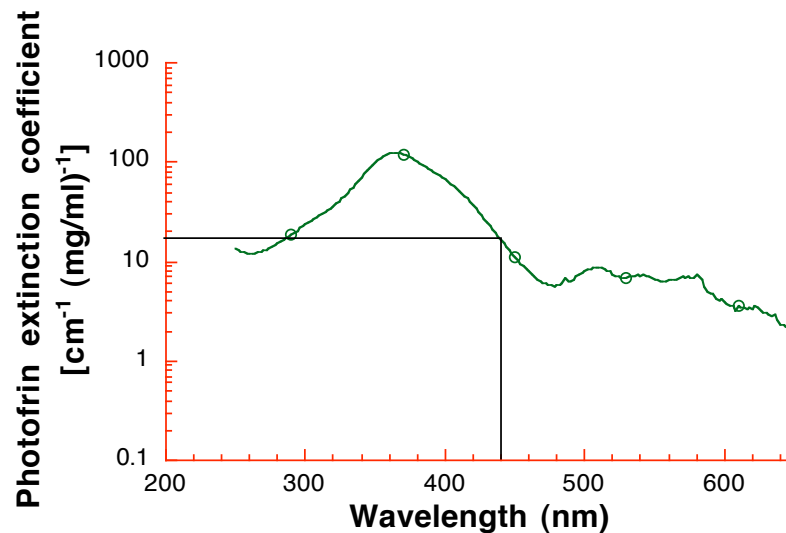


Fig.6.6. – Extinction coefficient ( $\epsilon$ ) of Photofrin diluted in water.  $\epsilon_{440} = 10.8 [\text{cm}^{-1} (\text{mg/ml})^{-1}]$  from figure.

## 6.4 Results

### 6.4.1 Tests of the Monte Carlo code

Results for the Monte Carlo tests are shown in table 6.3. The non-fluorescence case (tests #1 and #2) was setup by setting the fluorophore absorption at excitation and emission to zero. The scattering coefficients for excitation and emission were assumed to be identical for all tests and denoted  $s_s$ . Results for the non-fluorescence case were

compared to literature values [104] obtained using the adding-doubling (AD) method [40, 41]. The fluorescence for the absorbing only case (tests #3 to #5) were compared to the results from Eq. 6.8. For tests #6 and #7 the only absorber was the fluorophore. Since  $\Phi_f$  was assumed to be one for the MC simulations the results for these two tests are equivalent to one minus the total reflection for the semi-infinite case in Ref. #104. Test #8 is one example of results obtained with the MC code when absorption and scattering are considered.

**Table 6.3.** – Results for Monte Carlo code tests. Absorption and scattering coefficients are in  $\text{cm}^{-1}$ . Reflectance results for the Monte Carlo code are compared to the adding-doubling (AD) method. Fluorescence results for the Monte Carlo code are compared to Eq. 6.8. The parameter  $g$  is the average cosine or anisotropy. Index of refraction of the sample is ns.

Test #	$\mu_{af}^{ex}$	$\mu_{a0}^{ex}$	$\mu_{af}^{em}$	$\mu_{a0}^{em}$	$\mu_s$	$g$	$n_s$	MC Reflec	AD [104]	MC Fluor	Eq. 6.8
1	0	1	0	1	99	0.875	1.0	0.4398	0.4397		
2	0	1	0	1	99	0.5	1.4	0.5319	0.5321		
3	10	0	0	1	0	0	1.0			0.3801	0.3800
4	1	0	0	10	0	0	1.0			0.0234	0.0235
5	7	3	0	5	0	0	1.0			0.1577	0.1577
6	1	0	0	0	9	0	1.0		0.5851	0.5864	
7	1	0	0	0	9	0	1.4		0.7155	0.7162	
8	0.5	0.5	0	1	99	0	1.4	0.6322		0.0673	

The dependence of the lumped parameter  $\eta_c \chi$  on the ratio between the absorption coefficient of the fluorophore ( $\mu_{af}^{ex}$ ) and the total absorption coefficient at excitation ( $\mu_{af}^{ex} + \mu_{a0}^{ex}$ ) is shown in Fig. 6.7. Small changes are observed if  $\mu_{af}^{ex} \ll \mu_{af}^{ex} + \mu_{a0}^{ex}$ .

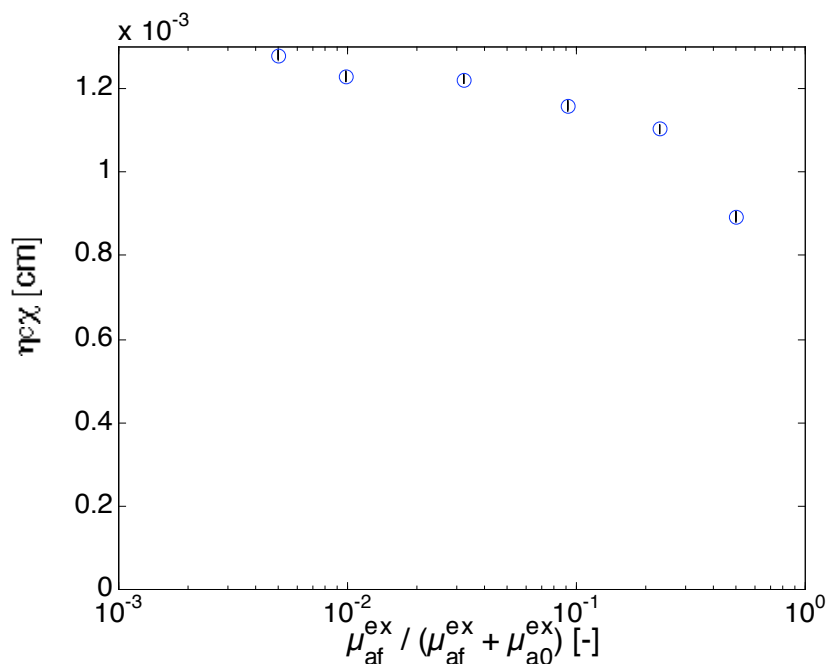


**Fig. 6.7** – Dependence of the lumped parameter  $\eta c \chi$  on the ratio between the absorption coefficient of the fluorophore and the total absorption coefficient at excitation.

## 6.4.2 Validation of model with phantoms

Concentration of rhodamine 6G in absorbing-only and turbid phantoms are shown in table 6.4.

**Table 6.4.** – Fluorescence scores and rhodamine concentration for tissue phantoms. The standard deviation for measured concentration was  $\pm 0.3$  and  $\pm 0.05$  g/ml for the absorbing-only samples and the scattering samples respectively.

Sample	FS [a.u.]	FS/ $\eta c \chi$ [a.u.]	$C_{measured}$ [g/ml]	C [g/ml]
Ab1	2,192	277,440	8.2	7.5
Ab2	1,656	258,350	7.6	7.5
Ab3	1,415	261,510	7.7	7.5
S11	3131	39786	1.18	1.2
S21	4367	36583	1.08	1.2
S31	3844	38557	1.14	1.2
S12	2047	43092	1.27	1.2
S22	2700	38652	1.14	1.2
S32	2118	35504	1.05	1.2
S13	1066	32486	0.96	1.2
S23	1371	32165	0.95	1.2
S33	1294	33788	1.00	1.2

### 6.4.3 Results from patient measurements

Comparison between normalized fluorescence for one normal site of PDT (patient #E6) and non-PDT (patient #N1) patients is shown in Fig. 6.8. The photosensitizer (Photofrin) fluorescence spectrum is shown in the 600 to 750 nm range of the PDT patient spectrum. Subtraction of the tissue auto fluorescence was performed according to section 6.3.5.

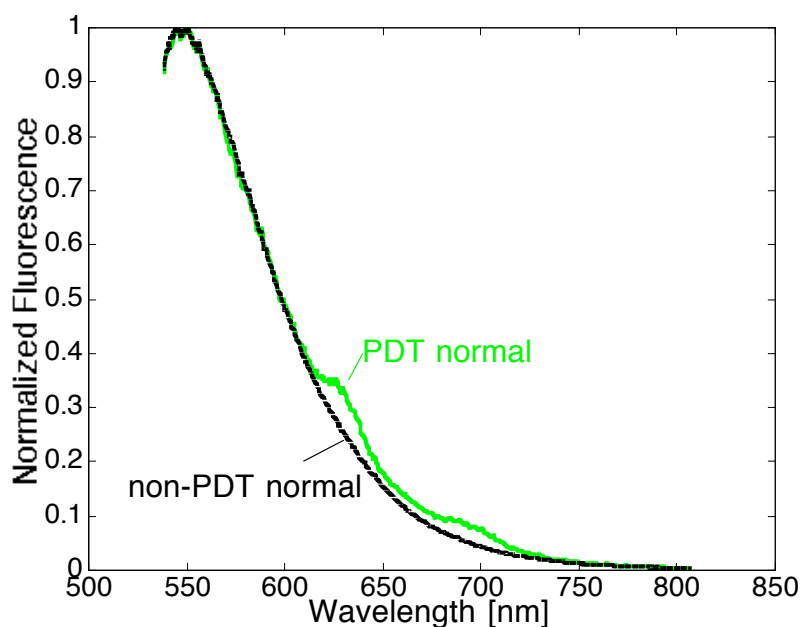


**Fig. 6.8** – Comparison between normalized fluorescence for normal tissue of PDT (solid line) and non-PDT (dashed line) patients.

An example of the determination of tissue Photofrin concentration is shown in Fig.6.9 for patient #E6. Fluorescence scores, FS, for three normal and three tumor sites are corrected by the factor  $\eta_c\chi$  determined from Monte Carlo simulations to yield the fluorophore concentration,  $C$  in mg/ml, using equation 6.6. Optical properties of the tissue were determined by reflectance spectroscopy as described in chapter 5.

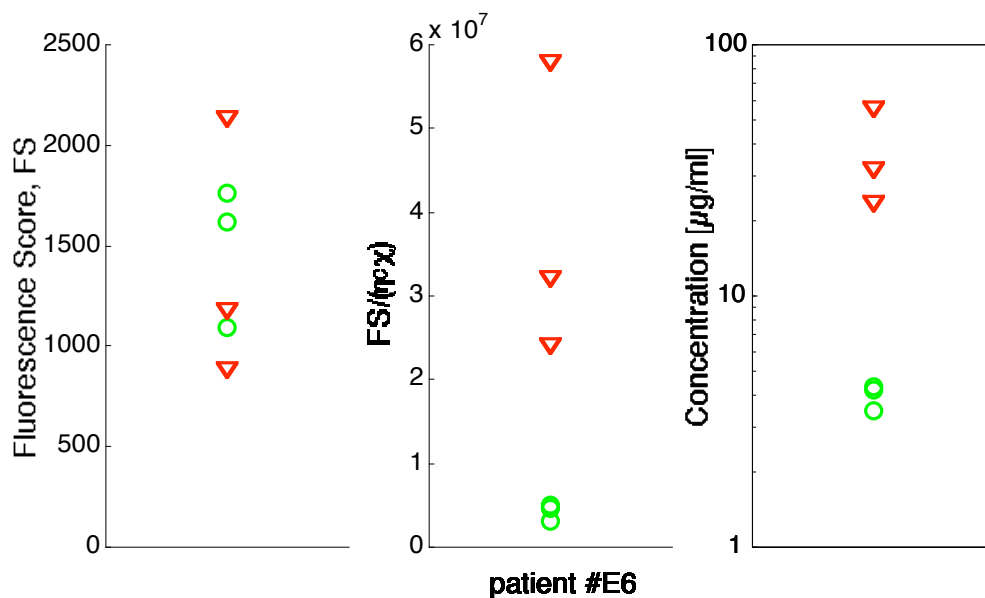


**Fig. 6.9.** – Example of the conversion of fluorescence scores into drug concentration for one patient. LEFT: fluorescence score for normal and tumor sites of patient #E6. CENTER: fluorescence score after correction by the light transport factor and the fiber field of view ( $\eta_c\chi$ ). RIGHT: drug concentration *in situ*

Fluorescence scores ( $FS_{630}$ ), corrected fluorescence and drug concentration for all patients are shown in Fig. 6.10.

Figure 6.11 shows histograms of the calculated drug concentration for normal and tumor sites for the soft tissue patients. Soft tissue patients are a subset of the data that excludes the skin patient data. The graphs show the logarithm base 10 of the concentration since the range of values obtained span through 2-3 orders of magnitude. Mean and standard deviation of normal and tumor sites fluorescence scores and of normal and tumor sites drug concentration are shown in table 6.5. Data is shown for all patients and for soft tissue patients only. P-values for two-sample t-test [90] between normal and tumor populations are also shown.

**Table 6.5.** – Mean and standard deviation of normal and tumor sites fluorescence scores at 630 nm ( $FS_{630}$ ) and of normal and tumor sites drug concentration.

	FS <sub>630</sub> [counts]		Drug Concentration [ g/ml]	
	all patients	soft tissue	all patients	soft tissue
Normal	970 ± 800	1010 ± 840	6.0 ± 6.6	6.5 ± 7.3
Tumor	1450 ± 930	1590 ± 970	13.6 ± 13.0	15.0 ± 14.3
p-value	< 0.04	< 0.05	< 0.005	< 0.025

Using Eq. 6.3 the photodynamic dose can be calculated for different depths in the tissue as shown in Fig. 6.12. These values can be compared with the threshold determined by Patterson *et al.* to evaluate which sites would produce necrosis and at which depth. For this example the light dose ( $E_{0t}$ ) was assumed to be 100 J/cm<sup>2</sup>, the optical penetration depth ( $\delta$ ) was 2 mm, the backscattering parameter  $k$  was assumed to be 2. The concentrations are shown in Fig.6.6.c and the extinction coefficient of photofrin is shown in the materials and methods section. The terms  $\Phi_T$ ,  $\Phi$  and  $f_R$  were assumed to be unity. The term  $b$  equals  $\lambda/hc$  as described in the materials and methods section. Values are calculated at the surface, 2, 4 and 6 mm depth.

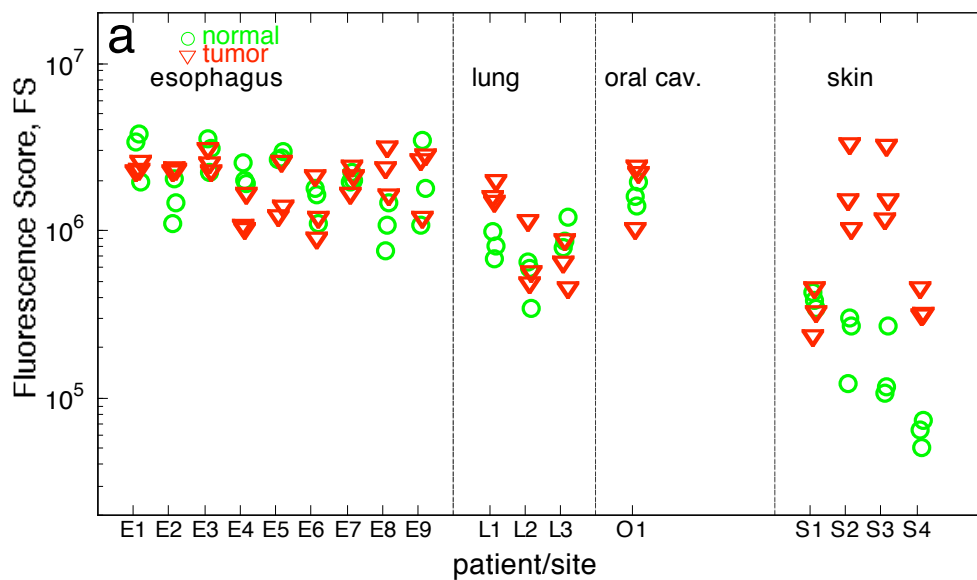


Fig. 6.10.A – Fluorescence scores for all patients.

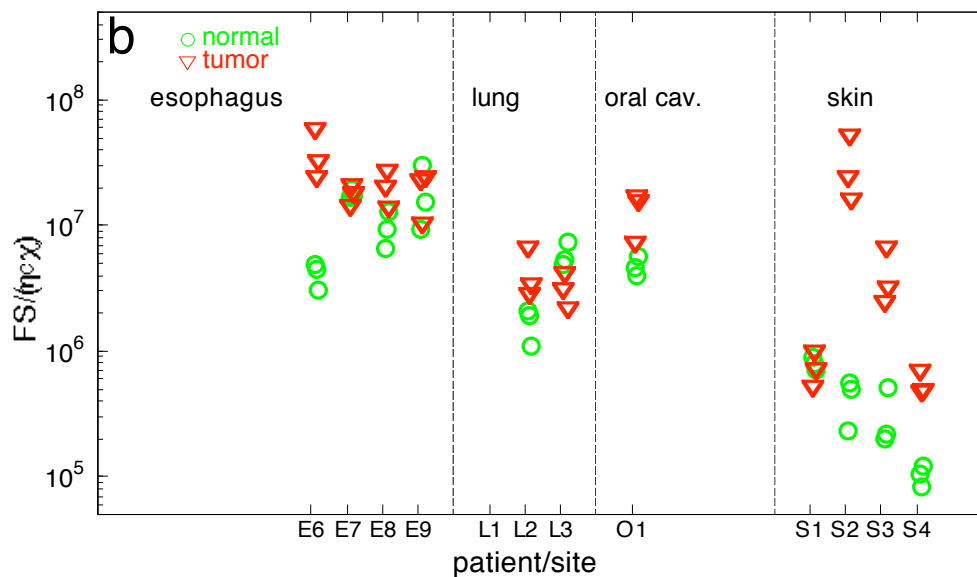
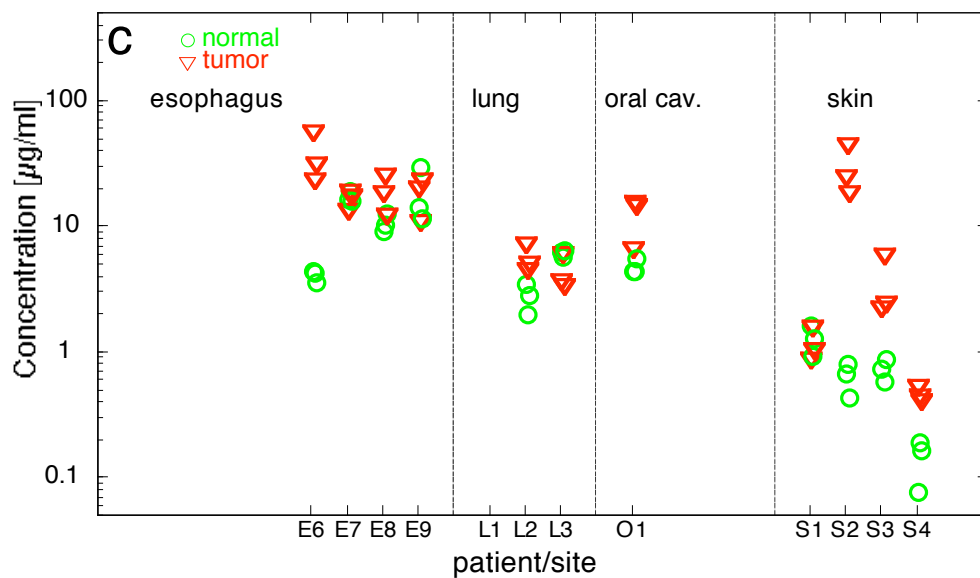
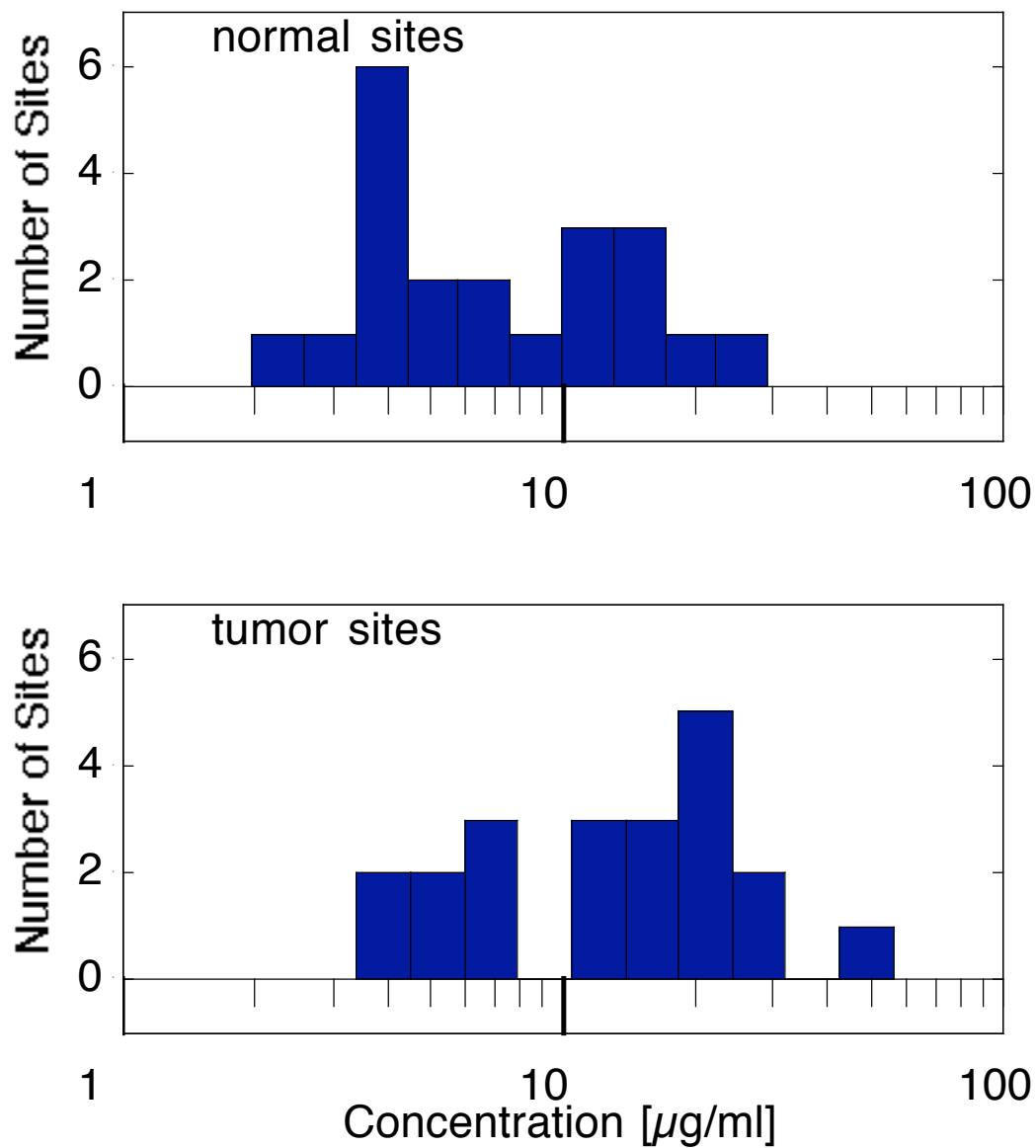


Fig. 6.10.B – Corrected fluorescence for all patients. Measurements of the optical properties of the first 5 esophageal and first lung patient were not possible due to the configuration of the previous reflectance probe hence data points for these patients are not shown.



**Fig. 6.10.C** – Drug concentration for all patients. Measurements of the optical properties of the first 5 esophageal and first lung patient were not possible due to the configuration of the previous reflectance probe hence drug concentrations for these patients are not shown.



**Fig. 6.11.** – Distribution of logarithm of drug concentration for normal and tumor tissue sites from Fig.6.10.C. The log of the concentration is used because the values span more than two orders of magnitude.

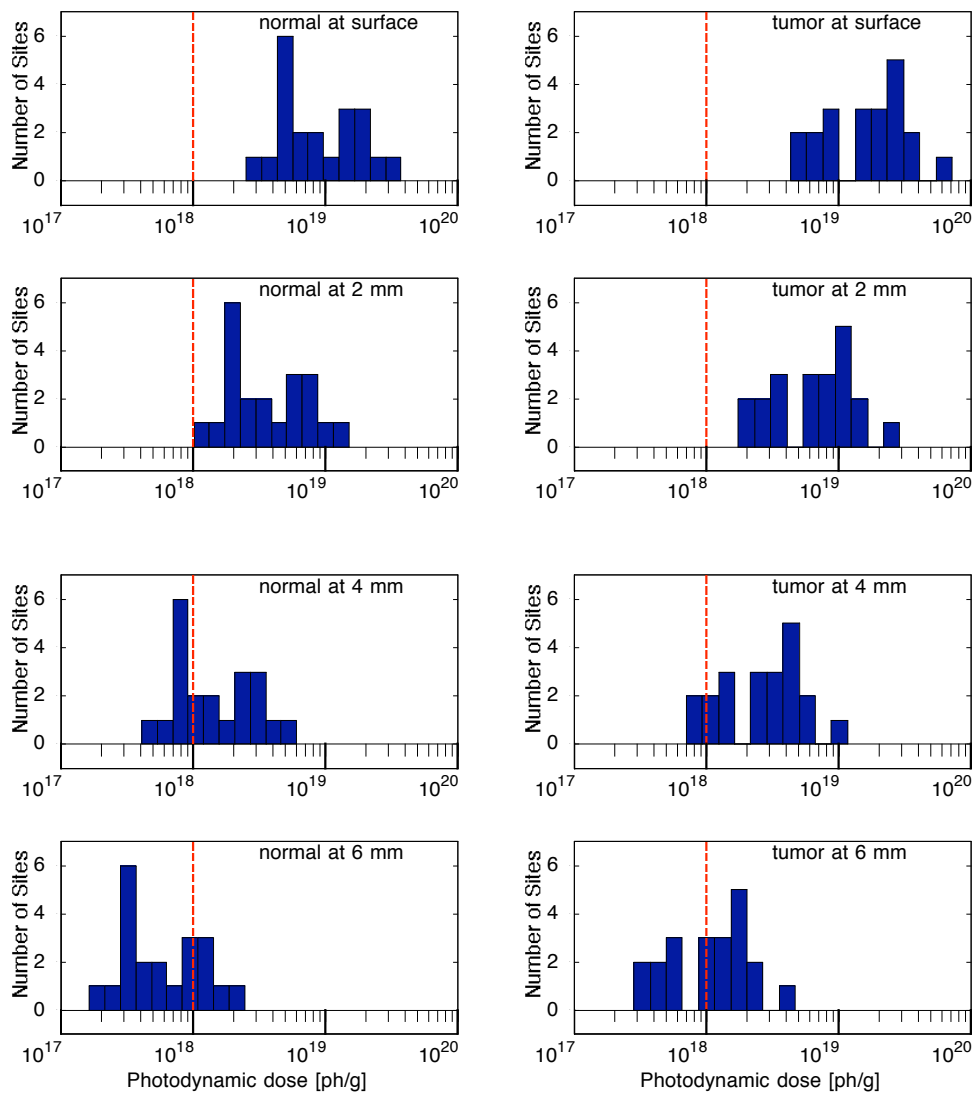


**Fig. 6.12.** – Photodynamic dose at different depths determined using Eq. 6.3. Red line is the threshold photodynamic dose ( $10^{18}$  [ph/g]) for tissue necrosis determined by Patterson *et al.* [13]. Tissue sites with photodynamic dose above the threshold would become necrotic.

## 6.5 Discussion

The key aspect of the calculation of drug concentration in this study was the lumped parameter  $\eta_c\chi$ . A fluorescence Monte Carlo code for optical fibers determined this parameter. The most important difference between other fluorescence Monte Carlo codes and the one presented in this report was the generation, propagation and extinction of emission photons for every excitation scattering event. A fluorescence Monte Carlo code where a single emission event was randomly determined based on the ratio of fluorophore to background absorption coefficients (at excitation wavelength) for each excitation photon was also tested. In this code if an emission event occurred all the excitation photon weight was converted into an emission photon that was then propagated. Although the total fluorescence escaping the tissue boundary in both codes were the same we found discrepancies of 2-3 fold in the amount of fluorescence that coupled to the optical fiber depending on the optical properties. Pogue and Burke [35] showed that, on average, collection of fluorescence light by a 600  $\mu$ m diameter optical fiber was characterized by an average of one and a half scattering events for excitation and less than one scattering event for emission photons. This effect, which is mainly due to geometrical constraints, could explain the discrepancies between the two codes since in the latter many of the emission events started after the excitation photon had been scattered few times, thus being unable to return to the fiber and be collected.

Measurements of fluorophore concentrations from tissue phantoms showed agreement with the true concentration of fluorophore added to the samples as shown in table 6.3. The mean error for the absorbing-only samples was 4% and for the turbid samples was 10%. In all but one case the model underestimated the fluorophore concentration for the scattering phantoms. One or a combination of the actual fluorophore characteristics (extinction coefficient or fluorescence quantum yield) may have differed slightly from the literature values used in the model by approximately 10%. The use of excitation at 440 nm instead of using the peak absorption at 420 nm for Photofrin in the patient measurements proved to be a good way to diminish the tissue autofluorescence

due to proteins and endogenous porphyrins since these are expected to have higher absorption at 420 nm. In fact we performed fluorescence measurements in 9 esophageal patients that were not administered Photofrin and no fluorescence from endogenous porphyrins were observed as shown for one site of patient #E6 and one site of patient #N1 in Fig. 6.8.

When comparing fluorescence scores obtained from relative fluorescence measurements, sometimes little discrimination between the fluorescence from normal and tumor tissues was observed as shown in Fig. 6.10.A. However, if these data points are corrected by the factor  $\eta_c\chi$  that depends on the optical properties of the tissue, the true drug concentration can be recovered (Fig. 6.10.C). Unfortunately, as described in chapter 5, the first generation single-fiber reflectance probe did not provide enough information to retrieve optical properties, consequently fluorescence spectra from the first five esophageal patients (#E1 to #E5) and the first lung patient (#L1) could not be used to extract fluorophore concentrations. Fluorescence data for the remaining patients was corrected by  $\eta_c\chi$  (Fig. 6.10.B).

Although the observed fluorescence of the normal and tumor tissues were similar, the tumor sites had typically higher blood contents (see chapter 5). Consequently the  $\eta_c\chi$  correction for fluorescence was higher for tumors (Fig. 6.10.B). Mean value of drug concentration (table 6.5) of tumor sites was approximately 2-fold greater than normal sites ( $p < 0.005$ ). In contrast, the fluorescence score for tumor was only 1.5-fold greater than the fluorescence for normal sites ( $p < 0.04$ ). Difference in p-values emphasizes that greater separation between normal and tumor sites can be achieved if the *in situ* drug concentration is used instead of the fluorescence score. Determining drug concentration from the corrected fluorescence is achieved by proper calibration of the fluorescence system and with knowledge of the characteristics of the fluorophore, such as extinction coefficient and quantum yield of fluorescence. In general, these parameters are strongly influenced by the microenvironment within which the fluorophore resides or to which the fluorophore is bound (i.e.,  $\Phi_f = 0.03, 0.07$  and  $0.08$  for Photofrin in PBS, 10% plasma and

in cells, respectively [103]). Studies should be performed to better understand these parameters for the particular fluorophore in use.

The goal in this study was to develop a system and model that can reliably measure absolute fluorophore concentration of tissues through endoscopy. For that reason optical fibers were used. The model needed to correct the fluorescence signal for the optical properties of the tissue that influence the detected fluorescence. Gardner *et al.* [22] have demonstrated a similar model where they used empirical expressions based on Monte Carlo simulations to correct the fluorescence data. This model was not suited for optical fibers and was limited to one-dimensional light delivery. Pogue and Burke [35] demonstrated a fiber optic method where small diameter optical fibers were used to diminish the effects of the absorption coefficient in the measurements. In this method the fluorescence still needed to be corrected for the scattering coefficient and calibration could be particularly complex due to non-linear behavior of the measured fluorescence for low scattering coefficients as shown in their study. This would be problematic for soft tissues such as the esophagus and photosensitizers fluorescing in the near infrared, which presents low scattering coefficients [36]. Other authors have proposed methods where the fluorescence spectral shape measured through optical fibers could be recovered but no quantitative analysis could be made [28-32].

The limitations of the method in this study are first the need for *a priori* information about tissue optical properties. Determination of tissue optical properties is straightforward and might be done using the steady-state diffuse reflectance method of chapter 5 or using time domain [47-49] or frequency domain methods [49, 50]. A second limitation is the assumption of uniform optical properties and the tissue to be homogeneous. The Monte Carlo code could be modified to accommodate tissue geometries other than homogeneous. The particular tissue geometry could be determined by imaging techniques such as optical coherence tomography [105], MRI [106] or CT [107]. A third limitation is the time spent in the Monte Carlo simulations, which will diminish with faster computers. A fourth limitation is that the absorption coefficient of the fluorophore must be small relative to the background tissue absorption coefficient

(Fig. 6.7) since the lumped parameter  $\eta_c\chi$  is dependent on this relation. In most practical cases the fluorophore concentration in the tissue is small and this usually does not impose a problem. A typical value of Photofrin concentration in tissue is 5 g/ml, accounting for a fluorophore absorption coefficient of approximately  $0.025 \text{ cm}^{-1}$  relative to a typical background absorption coefficient of  $10 \text{ cm}^{-1}$  at the excitation wavelength. Finally, the major limitation is the influence of the microenvironment on the fluorophore extinction coefficient and fluorescence quantum yield. A possible way to overcome this limitation is to compare the results of this method (spectrofluometric assay) on tissue biopsies in which the actual fluorophore concentration is known by chemical extraction. This may allow better approximations for these unknown values.

Nevertheless the use of the present method for determination of drug concentration in tissue may provide insight into the dosimetry of photodynamic therapy. As an example, the photodynamic dose based on Eq. 6.3 was determined for all the patient sites (Fig. 6.12). Comparison of the photodynamic dose at different depths with the threshold photodynamic dose determined by Patterson *et al.* [13] show that at the surface, all tissue sites would become necrotic. At 6 mm depth practically no normal tissues would become necrotic whereas almost half of the tumor sites would still be affected by the PDT treatment. The values obtained for the tissue photosensitizer concentration (Figs. 6.10 and 6.11) spanned more than two orders of magnitude showing large patient-to-patient variability and reinforcing the need for appropriate dosimetry in PDT.

## 6.6 Conclusion

The uncorrected relative fluorescence data showed greater overlap between normal and tumor tissue for most types of cancer than the corrected fluorescence. Notably, the two lung-cancer patients exhibited almost no Photofrin fluorescence in the normal tissue. The significance of this finding is unclear and more patient data is required before clear conclusions about lung uptake can be made. The fluorescence corrected for optical properties was typically larger for the tumor sites compared to normal sites. This

was expected due to the localization properties of the drug. It should be noted that this increase could only be observed after correction for the optical properties (Fig. 6.10.C). This may be explained by the influence of blood on excitation and emission of the drug fluorescence in tumors. The next step in this work will be to correlate the correct fluorescence with actual drug concentration in the tissue and establish a calibration model to obtain absolute *in vivo* drug concentration. This will be done by extracting biopsies from patients, chemically extracting the drug to obtain true concentration and correlating these corrected fluorescence data.

A system and model to measure the relative drug concentration *in vivo* for patients undergoing endoscopic PDT was presented, along with preliminary results on eleven patients. All the patients had late stage cancer with bulk and/or large tumors. These are the most appropriate situation for the present model, since the model assumes a uniform medium. A more elaborate model should be developed for cases with multi-layered tissues. Studies should be made to better understand the interactions of the fluorophore with the microenvironment to better predict this behavior which would help in the development of new models.

## **Chapter 7**

### **General discussion and conclusions**

This dissertation has presented photochemical and optical methods, as well as instrumentation, based on optical reflectance and fluorescence spectroscopy for quality control of photodynamic therapy. The parameters measured for PDT quality control were the drug accumulation and the optical penetration depth. These methods were tested *in vitro* in photochemical assays and in tissue-simulating phantoms. Pilot clinical trials were conducted and *in vivo* measurements were performed on patients undergoing endoscopic screening for esophageal diseases or photodynamic therapy of esophagus, lung, oral cavity and skin. Because of the remote location of some of these tissue sites (e.g., esophagus and lung) the instruments developed used optical fibers. Models were designed to understand light propagation from optical fibers to tissue and vice versa. These models were used to improve the design of instrumentation and to allow existing well-established theories to accurately analyze data by the implementation of empirical and Monte Carlo based corrections. The *in vivo* measured optical penetration depth and drug concentrations were compiled as histograms to demonstrate patient-to-patient variability (Figs. 5.20 and 6.11). The parameters were also used to determine the photodynamic dose (Fig.6.12). These histograms represent the first attempt to establish population distribution curves for these parameters. Such information should be of interest to the Food and Drug Administration in its evaluation of protocols for prescription of drug light doses used to treat PDT patients.

### **7.1. Photochemical assay for determination of quantum efficiency of oxidation**

Photooxidation and photobleaching during PDT (Photodynamic therapy) were studied in a model system using NADPH as the target substrate and Photofrin II as the photosensitizer. The efficiency of NADPH oxidation per photon absorbed by photosensitizer was determined as a function of substrate concentration. Both the efficiency of photosensitizer photobleaching and the spectral changes were measured. The influences of sodium azide, a singlet oxygen scavenger, and albumin on these efficiencies were determined. The kinetics of changes in absorbance (340nm) and fluorescence (440nm excitation; 540-800nm emission) were measured to assay oxidation of NADPH and photobleaching of Photofrin. The efficiency of oxidation increased (0.002; 0.004; 0.0049; 0.005) with increasing NADPH (in aqueous solution) concentration (0.4; 1; 3.5; 10mM) approaching a stable value of 0.005. Using typical values for quantum efficiency of Photofrin triplet state generation and efficiency of singlet oxygen production, a value for the efficiency of interaction between singlet oxygen and NADPH was obtained (0.025).

### **7.2. Collection efficiency of a single optical fiber**

If optical fibers are used both for delivery and collection of light, two major factors affect the measurement of collected light: (1) the light transport in the medium that describes the amount of light returning to the fiber, and (2) the light coupling to the optical fiber which depends on the angular distribution of photons entering the fiber. Chapter 3 discusses experimental and theoretical studies on the dependence of the efficiency of light coupling into a single optical fiber on the optical properties of the medium. A Monte Carlo model was developed and an analytical expression was derived to determine the optical fiber collection efficiency. For highly scattering tissues, the efficiency is predicted by the numerical aperture (NA) of the fiber. The collection efficiency was shown to be a problem intrinsic to the usage of optical fibers in turbid

media. This results from the fact that the angular distribution of the photons returning to the optical fiber is different for different optical properties. The distribution behaves as  $\cos(\theta_a)\sin(\theta_a)$ , and the amount of collected light behaves as  $\sin^2(\theta_a)$  for high reduced scattering samples ( $\mu_s' > 7 \text{ cm}^{-1}$ ). For lower scattering, such as in soft tissues, photons arrive at the fiber from deeper depths and the coupling efficiency could increase 2-3 fold above that predicted by the NA.

### **7.3. Collection efficiency of multiple fibers**

The concept of the collection efficiency of the optical fiber described in chapter 3 was expanded to multi-fiber geometries. The dependence of the collection efficiency on optical properties was verified by comparing experimental data to a simple diffusion model and to a Monte Carlo-corrected diffusion model. Mean square errors were 7.9% and 1.4% for the diffusion and the Monte Carlo corrected model, respectively. The efficiency of coupling was shown to be highly dependent on the numerical aperture (NA) of the optical fiber. However, for lower scattering, such as in soft tissues, the efficiency of coupling for multiple fiber probes could be 2-3 fold smaller than that predicted by fiber NA. Multi-fiber and single-fiber geometries were shown to behave very differently. For single-fiber probes there is a significant increase in the collection efficiency for low-scattering samples relative to that for high-scattering samples. For multiple fiber probe there is a corresponding significant decrease in the collection efficiency for low-scattering samples. The collection efficiency can be used as a practical guide for choosing optical fiber based systems for biomedical applications.

### **7.4. Determination of optical properties with reflectance spectroscopy**

Chapter 5 established an experimental method for determination of optical properties *in vivo*. The model was based on an empirical light transport function and was very robust. The main variable affecting the optical penetration depth of treatment light and the depth of treatment was blood perfusion. The fraction of blood ranged from 0.1% to 30% and was typically greater for tumor tissue than for normal tissue in a given

patient. The increased blood fraction accounted for a higher absorption coefficient hence a reduced optical penetration depth in tumor tissue. Reduced scattering coefficients of normal tissue sites were in general higher than that of tumor tissue sites for a given patient. Although normal tissue showed an increased reduced scattering coefficient and tumor tissue showed an increased absorption coefficient for a given patient, the patient-to-patient variability was considerable. That variability explained the large range of optical penetration depth obtained for both normal and tumor tissues. Values of  $\delta$  ranged from 1.3-3.6 mm for the overall normal sites and from 0.6-3.6 mm for the tumor sites. The mean value for the non-PDT patients was 2.3 mm with a standard deviation of 0.5 mm. The mean value for the normal sites of the PDT patients was 2.2 mm with a standard deviation of 0.5 mm. The mean value for the tumor sites was 1.6 mm with a standard deviation of 0.7 mm.

### **7.5. Determination of drug concentration and photodynamic dose *in vivo***

A system and model to measure the relative drug concentration *in vivo* for patients undergoing endoscopic PDT was presented in chapter 6, along with preliminary results on 11 patients. All the patients had late-stage cancer with bulky tumors. These are the more appropriate cases for the use of the present model because it assumes homogeneous semi-infinite tissue. A more elaborate model should be developed for cases of multi-layered tissues. Fluorescence measurements from tissue were corrected by the light transport of the excitation and emission light derived from Monte Carlo simulations. Measurements in tissue simulating scattering phantoms had a mean error of 10%. The non-corrected relative fluorescence data showed little difference between normal and tumor tissue for most types of cancer. The fluorescence corrected for optical properties was typically larger for the tumor sites compared to normal sites. This was expected due to the localization properties of the drug. It should be noted that this increased fluorescence could only be observed after correction for the optical properties since most of the excitation and emission of the drug fluorescence is diminished in the tumor tissue

due to light absorption by blood. The drug concentrations span over 2 orders of magnitude. The next step in this work will be to correlate the correct fluorescence with actual drug concentration in the tissue and elaborate a calibration model to obtain absolute drug concentration values. We expect to accomplish that by extracting biopsies from the patients, chemically extracting the drug concentration information from the tissues and correlating them with the corrected fluorescence data. Studies should be made to better understand the chemical-physical interactions between the fluorophore and the microenvironment to better predict these interactions which would help in the development of new models.

## Bibliography

- [1] B. W. Henderson and T. J. Dougherty, "How does photodynamic therapy work?," *Photochem. Photobiol.*, vol. 55, pp. 145-157, 1992.
- [2] R. Ackroyd, C. Kelty, N Brown and M. Reed, "The history of photodetection and photodynamic therapy," *Photochem. Photobiol.*, vol. 74, pp. 656-669, 2001.
- [3] J. Moan, K. Berg, E. Kvam, A. Westen, Z. Malik, A. Ruck and H. Scheneckenburger, "Intracellular localization of photosensitizers." In *Photosensitizing Compounds: Their Chemistry, Biology and Clinical Use*. pp. 95-107. Wiley, Chichester, UK, 1989.
- [4] M. L. Agarwal, M. E. Clay, E. J. Harvey, H. H. Evans, A. R. Antunez and N. L. Oleinick, "Photodynamic therapy induces rapid cell death by apoptosis in L5178Y mouse lymphoma cells," *Cancer Res.*, vol. 51, pp. 5993-5996, 1991.
- [5] D. Kessel and Y. Luo, "Mitochondrial photodamage and PDT-induced apoptosis," *J. Photochem. Photobiol. B*, vol. 42, pp. 89-95, 1998.
- [6] W. M. Star, H. P. A. Marijnissen, A. E. van der Berg-Block, J. A. C. Versteeg, K. A. P. Franken and H. S. Reinhold, "Destruction of rat mammary tumor and normal tissue microcirculation by hematoporphyrin derivative photoradiation observed in vivo in sandwich observation chambers," *Cancer Res.*, vol. 46, pp. 2532-2540, 1986.

- [7] M. W. R. Reed, T. J. Wieman, D. A. Schuschke, M. T. Tseng and F. N. Miller, "A comparison of the effects of photodynamic therapy on normal and tumor blood vessels in the rat microcirculation," *Radiat. Res.*, vol. 119, pp. 542-552, 1989.
- [8] B. W. Henderson and V. H. Fingar, "Relationship of tumor hypoxia and response to photodynamic treatment in an experimental mouse tumor," *Cancer Res.*, vol. 47, pp. 3110-3114, 1987.
- [9] B. W. Henderson and V. H. Fingar, "Oxygen limitation of direct tumor cell killing during photodynamic treatment," *Photochem. Photobiol.*, vol. 49, pp. 299-304, 1989.
- [10] B. J. Tromberg, A. Orenstein, S. Kimel, S. J. Baker, J. Hyatt, J. S. Nelson and M. W. Berns, "In vivo tumor oxygen tension measurements for the evaluation of the efficiency of photodynamic therapy," *Photochem. Photobiol.*, vol. 52, pp. 375-385, 1990.
- [11] A. Maier, U. Anegg, B. Fell, P. Rehak, B. Ratzenhofer, F. Tomaselli, O. Sankin, H. Pinter, F. M. Smolle-Juttner and G. B. Friehs, "Hyperbaric oxygen and photodynamic therapy in the treatment of advanced carcinoma of the cardia and the esophagus," *Lasers Surg. Med.*, vol. 26, pp. 308-315, 2000.
- [12] B.W. McIlroy, A. Curnow, G. Buonaccorsi, M. A. Scott, S. G. Bown and A. J. MacRobert, "Spatial measurement of oxygen levels during photodynamic therapy using time-resolved optical spectroscopy," *J Photochem Photobiol B*, vol. 43, pp. 47-55, 1998.
- [13] M. S. Patterson, B. C. Wilson and R. Graff, "In vivo tests of the concept of photodynamic threshold dose in normal rat liver photosensitized by aluminum chlorosulphonated phthalocyanine," *Photochem. Photobiol.*, vol. 52, pp. 343-349, 1990.
- [14] S. L. Jacques, "Simple theory, measurements, and rules of thumb for dosimetry during photodynamic therapy," in *Photodynamic Therapy: Mechanisms*, T. J. Dougherty, *Proc. SPIE*, vol. 1065, pp. 100-108, 1989.

- [15] S. L. Jacques, "Laser-tissue interactions: photochemical, photothermal, photomechanical," *Surgical Clinics of North America*, vol. 72, pp. 531-558, 1992.
- [16] S. L. Jacques, "Light distributions from point, line and plane sources for photochemical reactions and fluorescence in turbid biological tissues," *Photochem. Photobiol.*, vol. 67, pp. 23-32, 1998.
- [17] W. M. Star, "Diffusion theory of light transport," in *Optical-Thermal Response of Laser Irradiated Tissue*, A. J. Welch and M. J. C. van Gemert, Eds. New York: Plenum Press, 1995, pp. 131-206.
- [18] B. C. Wilson and S. L. Jacques, "Optical reflectance and transmittance of tissues: principles and applications," *IEEE J. Quantum Electronics*, vol. 26, pp. 2186-2199, 1991.
- [19] W. M. Star, J. P. Marijnissen and M. J. van Gemert, "Light dosimetry in optical phantoms and in tissues: I. Multiple flux and transport theory.," *Phys Med Biol*, vol. 33, pp. 437-454, 1988.
- [20] R. R. Anderson, H. Beck, U. Bruggemann, W. Farinelli, S. L. Jacques, J. A. Parrish, "Pulsed photothermal radiometry in turbid media: internal reflection of back-scattered radiation strongly influences optical dosimetry," *Applied Optics*, vol. 28, pp. 2256-2262, 1989.
- [21] R. Baumgartner, N. Fuchs, D. Jocham, H. Stepp and E. Unsold, "Pharmacokinetics of fluorescent poliporphyrin photofrin II in normal rat tissue and rat bladder tumor," *Photochem. Photobiol.*, vol. 55, pp. 569-574, 1992.
- [22] C. M. Gardner, S. L. Jacques and A. J. Welch, "Fluorescence spectroscopy of tissue: recovery of intrinsic fluorescence from measured fluorescence," *Applied Optics*, vol. 35, pp. 1780-1792, 1996.
- [23] T. S. Mang, T. J. Dougherty, W. R. Potter, D. G. Boyle, S. Somer and J. Moan, "Photobleaching of porphyrins used in photodynamic therapy and implications for therapy," *Photochem. Photobiol.*, vol. 45, pp. 501-506, 1987.

- [24] G. Bittiroli, A. C. Croce, R. Ramponi and P. Vaghi, "Distribution of di-sulfonated aluminum phthalocyanine and Photofrin II in living cells: a comparative fluorometric study," *Photochem. Photobiol.*, vol. 55, pp. 575-585, 1992.
- [25] D. Bellnier, K. Ho, R. K. Pandey, J. Missert and T. J. Dogherty, "Distribution and elucidation of the tumor-localizing component of hematoporphyrin derivative in mice," *Photochem. Photobiol.*, vol. 50, pp. 221-228, 1989.
- [26] D. Bellnier and T. J. Dogherty, "A preliminary pharmacokinetic study of intravenous Photofrin in patients," *J. Clin. Laser Med. Surg.*, vol. 14, pp. 311-314, 1996.
- [27] D. Kessel, "Pharmacokinetics of N-aspartyl chlorin e6 in cancer patients," *J. Photochem. Photobiol. B*, vol. 39, pp. 81-83, 1997.
- [28] D. R. Braichotte, G. A. Wagnieres, R. Bays, P. Monnier and H. E. van den Bergh, "Clinical pharmacokinetics studies of Photofrin by fluorescence spectroscopy in the oral cavity, the esophagus and the bronchi," *Cancer*, vol. 75, pp. 2768-2778, 1995.
- [29] S. Andersen-Engels, J. Ankerst, J. Johansson, K. Svanberg and S. Svanberg, "Laser-induced fluorescence in malignant and normal tissue of rats injected with BPD," *Photochem. Photobiol.*, vol. 57, pp. 978-983, 1993.
- [30] M. Sinaasappel and H. J. C. M. Sterenberg, "Quantification of the hematoporphyrin derivative by fluorescence measurement using a dual-wavelength excitation and dual-wavelength detection," *Applied Optics*, vol. 32, pp. 541-548, 1993.
- [31] S. Lam, J. Hung and B. Palcic, "Mechanism of detection of early lung cancer by ratio fluorometry," *Lasers Life Science*, vol. 3, pp. 67-73, 1991.
- [32] A. J. Durkin, S. Jaikumar, N. Ramanujam and R. Richards-Kortum, "Relation between fluorescence spectra of dilute and turbid samples," *Applied Optics*, vol. 33, pp. 414-423, 1994.
- [33] J. Wu, M. S. Fled and R. P. Rava, "An analytical model for extracting intrinsic fluorescence in turbid media," *Applied Optics*, vol. 32, pp. 3585-3595, 1993.

- [34] A. J. Welch, C. Gardner, R. Richards-Kortum, E. Chan, G. Creiswell, J. Pfefer and S. Warren, "Propagation of fluorescence light," *Lasers Surg. Med.*, vol. 21, pp. 166-178, 1997.
- [35] B. W. Pogue and G. Burke, "Fiber-optic bundle design for quantitative measurement from tissue," *Applied Optics*, vol. 37, pp. 7429-7436, 1998.
- [36] W.-F. Cheong, S. A. Prahl and A. J. Welch, "A review of the optical properties of biological tissue," *IEEE J. Quantum Electron.*, vol. 26, pp. 2166-2185, 1990.
- [37] M. J. van Gemert, S. L. Jacques, H. J. Sterenborg and W. M. Star, "Skin optics," *IEEE Trans Biomed Eng.*, vol. 36, pp. 1146-1154, 1989.
- [38] I. S. Saidi, S. L. Jacques and F. K. Tittel, "Mie and Rayleigh modeling of visible-light scattering in neonatal skin," *Applied Optics*, vol. 34, pp. 7410-7418, 1995.
- [39] S. L. Jacques and S. A. Prahl, "Modeling optical and thermal distributions in tissue during laser irradiation," *Lasers Surg Med.*, vol. 6, pp. 494-503, 1987.
- [40] S. A. Prahl, *Light Transport in Tissue*, PhD dissertation, University of Texas, Austin, Texas, USA, 1988.
- [41] S. A. Prahl, M. J. C. van Gemert, and A. J. Welch, "Determining the optical properties of turbid media by using the adding-doubling method," *Applied Optics*, vol. 32, pp. 559-568, 1993.
- [42] L. Wang, S. L. Jacques and L. Zheng "MCML – Monte Carlo modeling of light transport in multi-layered tissues," *Comp. Meth. Prog. in Biomed*, vol. 47, pp. 131-146, 1995.
- [43] T. J. Farel and M. S. Patterson, "A diffusion theory model of spatially resolved, steady-state diffuse reflectance for the noninvasive determination of tissue optical properties *in vivo*," *Med. Phys.*, vol. 19, pp. 879-888, 1992.
- [44] J. W. Pickering, C. J. M. Moes, H. J. C. M. Sterenborg, S. A. Prahl, and M. J. C. van Gemert. "Two integrating spheres with an intervening scattering sample," *J. Opt. Soc. Am. A*, vol. 9, pp. 621-631, 1992.

- [45] J. W. Pickering, S. A. Prahl, N. van Wieringen, J. F. Beek, H. J. C. M. Sterenborg, and M. J. C. van Gemert. "Double-integrating-sphere system for measuring the optical properties of tissue," *Applied Optics*, vol. 32, pp. 399-410, 1993.
- [46] J. W. Pickering, S. Bosman, P. Posthumus, P. Blokland, J. F. Beek, and M. J. C. van Gemert. "Changes in the optical properties (at 632.8 nm) of slowly heated myocardium," *Applied Optics*, vol. 32, pp. 367-371, 1993.
- [47] M. S. Patterson, B. Chance and B. C. Wilson, "Time resolved reflectance and transmittance for the non-invasive measurements of optical properties," *Applied Optics*, vol. 28, pp. 2331-2336, 1989.
- [48] S. Andersson-Engels, R. Berg, A. Persson and S. Svanberg, "Multispectral tissue characterization with time-resolved detection of diffusely scattered white light," *Opt. Lett.*, vol. 18, pp. 1697-1699, 1993.
- [49] E. M. Sevick, B. Chance, J. Leigh, S. Nioka and M. Maris, "Quantitation of time- and frequency resolved optical spectra for the determination of tissue oxygenation," *Anal. Biochem.*, vol. 195, pp. 330-351, 1991.
- [50] S. Fantini, M. A. Franceschini-Fantini, J. S. Maier, S. A. Walker, B. Barbieri and Enrico Gratton, "Frequency-domain multichannel optical detector for noninvasive tissue spectroscopy and oximetry," *Optical Engineering*, vol. 34, pp. 32-42, 1995.
- [51] A. A. Oraevsky, S. L. Jacques and F. K. Tittel, "Measurement of tissue optical properties by time-resolved detection of laser-induced transient stress," *Applied Optics*, vol. 36, pp. 402-415, 1997.
- [52] J. A. Viator, *Characterization of photoacoustic sources in tissue using time domain measurements*, PhD dissertation, Oregon Health & Science University, Portland, Oregon, USA, 2001.
- [53] A. M. K. Nilsson, R. Berg and S. Andersson-Engels, "Measurements of the optical properties of tissue in conjunction with photodynamic therapy," *Applied Optics*, vol. 34, pp. 4609-4619, 1995.
- [54] B.-M. Kim, M. Ostermeyer, S. L. Jacques, D. A. Levy, P. Chakrabarti, J. H. Torres, A. C. von Eschenbach, S. Rastegar and M. Motamedi, "Transurethral fiber optics

- for in vivo optical property determination: Human and animal trials,” in *Laser-Tissue Interaction VII*, S. L. Jacques, *Proc. SPIE*, vol. 2681, pp. 303-309, 1996.
- [55] R. Bays, G. Wagnieres, D. Robert, D. Braichotte, J.-F. Savary, P. Monnier and H. van den Bergh, “Clinical determination of tissue optical properties by endoscopic spatially resolved reflectometry,” *Applied Optics*, vol. 35, pp. 1756-1766, 1996.
- [56] A. Kienle, L. Lilge, M. S. Patterson, R. Hibst, R. Steiner and B. C. Wilson, “Spatially resolved absolute diffuse reflectance measurements for noninvasive determination of the optical scattering and absorption coefficients of biological tissues,” *Applied Optics*, vol. 35, pp. 2304-2314, 1996
- [57] M. G. Nichols, E. L. Hull and T. H. Foster, “Design and testing of a white-light, steady-state diffuse reflectance spectrometer for the determination of optical properties of highly scattering systems,” *Applied Optics*, vol. 36, pp. 93-104, 1997.
- [58] J. R. Mourant, T. Fuselier, J. Boyer, T. M. Johnson and I. J. Bigio, “Predictions and measurements of scattering and absorption over broad wavelength ranges in tissue phantoms,” *Applied Optics*, vol. 36, pp. 949-957, 1997.
- [59] J. R. Mourant, I. J. Bigio, D. A. Jack, T. M. Johnson and H. D. Miller, “Measuring absorption coefficients in small volumes of highly scattering media: source-detector separations for which path length do not depend on scattering properties,” *Applied Optics*, vol. 36, pp. 5655-5661, 1997.
- [60] T. P. Moffitt and S. A. Prahl, “Sized-fiber reflectometry for measuring local optical properties,” *IEEE J. Sel. Top. Quantum Electron.*, vol. 7, pp. 952-958, 2001.
- [61] B. W. Henderson and A. C. Miller, “Effects of scavengers of reactive oxygen and radical species on cell survival following photodynamic treatment in vitro: comparison to ionizing radiation,” *Radiat Res.*, vol.108, pp. 196-205, 1986.
- [62] C. Hadjur, G. Wagnieres, F. Ihringer, P. Monnier and H. J. van den Bergh H.J., “Production of the free radicals O<sub>2</sub>·- and ·OH by irradiation of the photosensitizer zinc(II) phthalocyanine,” *Photochem Photobiol B*, vol. 38, pp. 196-202, 1997.
- [63] R.D. Glickman, S.J. Jacques, J.A. Schwartz, T. Rodriguez, K.W. Lam and G. Buhr, “Photodisruption increases the free radical reactivity of melanosomes isolated from

- retinal pigment epithelium,” in *Laser-Tissue Interaction VII*, S. L. Jacques, *Proc. SPIE*, vol. 2681, pp. 460-467, 1996.
- [64] S.U. Egorov, V.F. Kamalov, N.I. Koroteev, A.A. Kransnovsky Jr., B.N. Toleutaev and S.V. Zinukov, “Rise and decay kinetics of photosensitized singlet oxygen luminescence in water. Measurements with nanosecond time-correlated single photon counting technique”, *Chem. Phys. Lett.*, vol.163, pp. 421-424, 1989.
- [65] E. Reddi, G. Jori, M.A.J. Rodgers and J.D. Spikes, “Flash photolysis studies in homogeneous and microheterogeneous aqueous dispersions”, *Photochem. Photobiol.*, vol. 38, pp. 639-645, 1983.
- [66] C.R. Lambert, E. Reddi, J.D. Spikes, M.A.J.Rodgers and G. Jori, “The effects of porphyrin structure and aggregation state on photosensitized process in aqueous and micellar media”, *Photochem. Photobiol.*, vol. 44, pp. 565-601, 1986.
- [67] B. W. Pogue, J. D. Pitts, M.-A. Mycek, R. D. Sloboda, C. M. Wilmot, J. F. Brandsema and J. A. O’Hara, “In vivo NADH fluorescence monitoring as an assay for cellular damage in photodynamic therapy,” *Photochem. Photobiol.*, vol. 74, pp. 817-824, 2001.
- [68] A. Baker and J. R. Kanofsky, “Quenching of singlet oxygen by biomolecules from L1210 leukemia cells,” *Photochem. Photobiol.*, vol. 55, pp. 523-528, 1992.
- [69] S. L. Jacques, “Reflectance spectroscopy with optical fiber devices and transcutaneous bilirubinometers,” in *Biomedical Optical Instrumentation and Laser-Assisted Biotechnology*, A.M. Verga Scheggi et al., Eds., Netherlands: Kluwer Academic Publishers, pp. 83-94, 1996.
- [70] D. R. Braichotte, J. F.Savary, P. Monnier and H. E. van den Bergh, “Optimizing light dosimetry in photodynamic therapy of early stage carcinomas of esophagus using fluorescence spectroscopy,” *Laser Surg. Med.*, vol. 19, pp. 340-346, 1996.
- [71] W. B. Pogue and T. Hasan, “Fluorophore quantitation in tissue-simulating media with confocal detection,” *IEEE J.Quantum Electron.*, vol. 2, pp. 959-964, 1997.
- [72] L. S. Saidi, *Transcutaneous optical measurement of hyperbilirubinemia in neonates*, PhD dissertation, Rice University, Houston, Texas, USA (1992).

- [73] E. Hecht, *Optics*, 3<sup>rd</sup> Edition, Massachusetts: Addison-Wesley, pp. 111-121, 1998.
- [74] S. A. Prahl and S.L. Jacques, "Monte Carlo Simulations," [Online]. Available: <http://omlc.ogi.edu/software/mc/>, 2000.
- [75] M. Young, *Optics and lasers: including fibers and optical waveguides*, 4<sup>th</sup> Revised Edition, New York: Springer-Verlag, pp. 250-252, 1992.
- [76] Optical fiber catalog, CeramOptec Industries, Inc., [Online] Available: <http://www.ceramoptec.com/>, 2002.
- [77] Melles Griot product catalog, page 4.13, 1999.
- [78] S. T. Flock, S. L. Jacques, B. C. Wilson, W. M. Star and M. J. C. van Gemert, "Optical properties of Intralipid: A phantom medium for light propagation studies," *Laser Surg. Med.*, vol. 12, pp. 510-519, 1992.
- [79] M. Keijzer, S. L. Jacques, S. A. Prahl and A.J. Welch, "Light distributions in artery tissue: Monte Carlo simulations for finite-diameter laser beams," *Lasers Surg. Med.*, vol. 9, pp. 148-154, 1989.
- [80] M. Canpolat and J. R. Mourant, "Particle size analysis of turbid media with a single optical fiber in contact with the medium to deliver and detect white light," *Applied Optics*, vol. 40, pp. 3792-3799, 2001.
- [81] S. L. Jacques, "Modeling light transport in tissue," in *Biomedical Optical Instrumentation and Laser-Assisted Biotechnology*, A. M. Verga Scheggi *et al.*, eds. Netherlands: Kluwer Academic Publishers, pp. 21-32, 1996.
- [82] P. R. Bargo, S. S. Prahl and S. L. Jacques, "Collection efficiency of a single optical fiber in turbid media," *Applied Optics*, vol. 42, pp. 3187-3197, 2003.
- [83] B. C. Wilson, "Measurement of tissue optical properties: methods and theories," in *Optical-Thermal Response of Laser Irradiated Tissue*, A. J. Welch and M. J. C. van Gemert, Eds. New York: Plenum Press, pp. 233-274, 1995.
- [84] L. G. Henyey and J. L. Greenstein, "Diffuse radiation in the galaxy," *The Astrophysical J.*, vol. 93, pp. 70-83, 1941.
- [85] A. N. Witt, "Multiple scattering in reflection nebulae. I. A Monte Carlo approach," *The Astrophysical J.*, vol. 35, pp. 1-6, 1977.

- [86] V. G. Peters, D. R. Wyman, M. S. Patterson and G. L. Frank, "Optical properties of normal and diseased human breast tissues in the visible and near infrared," *Phys. Med. Biol.*, vol. 35, pp. 1317-1334, 1990.
- [87] M. S. Patterson, E. Schwartz and B. C. Wilson, "Quantitative reflectance spectrophotometry for the noninvasive measurement of photosensitizer concentration in tissue during photodynamic therapy," in *Photodynamic Therapy: Mechanisms*, T. J. Dougherty, *Proc. SPIE*, vol. 1065, pp. 115-122, 1989.
- [88] W. J. Ride, "The scattering of light by turbid media – part I," *Proc. Roy. Soc. (London)*, vol. A131, pp. 451-464, 1931.
- [89] W. G. Egan and T. Hilgeman, "In situ separation of scattering and absorption in fluids," *Applied Optics*, vol. 20, pp. 727-729, 1981.
- [90] D. S. Moore and G. P. McCabe, *Introduction to the practice of statistics*, 2<sup>th</sup> Edition, New York: W. H. Freeman and Company, pp. 529-557, 1993.
- [91] Endoscopes Catalog, Olympus America, Inc., [Online] Available: [http://www.olympusamerica.com/msg\\_section/msg\\_gastro\\_g.asp](http://www.olympusamerica.com/msg_section/msg_gastro_g.asp), 2003.
- [92] T. P. Moffitt and S. A. Prael, "The specular reflection problem with a single fiber for emission and collection," *Proc. SPIE: Saratov Fall Meeting*, 2002.
- [93] A. Abramsson, O. Berlin, H. Papayan, D. Paulin, M. Shani and C. Betsholtz, "Analysis of mural cell recruitment to tumor vessels," *Circulation*, vol. 105, pp. 112-117, 2002.
- [94] J. Qu, C. MacAulay, S. Lam and B. Palcic, "Optical properties of normal and carcinomatous bronchial tissue," *Applied Optics*, vol. 33, pp. 7397-7405, 1994.
- [95] A. Furtado and R. Henry R., "Measurement of green fluorescent protein concentration in single cells by image analysis," *Anal. Biochem.*, vol. 310, pp. 84-92, 2002.
- [96] H. Toledano, R. Edrei and S. Kimel, "Photodynamic damage by liposome-bound porphycenes: comparison between in vitro and in vivo models" *J Photochem Photobiol B*, vol. 42, pp. 20-27, 1998.

- [97] R. Richards-Kortum, R. P. Rava, M. Fitzmaurice, L. L. Tong, N. B. Ratliff, J. R. Kramer and M. S. Feld, "A one-layer model of laser-induced fluorescence for diagnostic of disease in human tissue: applications to atherosclerosis," *IEEE Trans. Biomed. Eng.*, vol. 36, pp. 1222-1231, 1989.
- [98] A. E. Profio, S. Xie and K.-H. Shu, "Diagnosis of tumors by fluorescence: quantification of photosensitizer concentration," in *Photodynamic Therapy: Mechanisms II*, T. J. Dougherty, *Proc. SPIE*, vol. 1203, pp. 12-18, 1990.
- [99] G. Muller and A. Rogan, eds., *Laser-Induced Interstitial Thermotherapy*, vol. Pm25, SPIE Press, Bellingham, WA, 1995.
- [100] S. A. Prahl and P. R. Bargo, "Comparison of an analytical expression for the total fluorescence escaping a semi-infinite absorbing only medium with Monte Carlo and experimental results," manuscript in preparation.
- [101] S. A. Prah, "Rhodamine 6G," [Online]. Available: <http://omlc.ogi.edu/spectra/PhotochemCAD/html/rhodamine6G.html>, 2000.
- [102] R. F. Kubin and A. N. Fletcher, "Fluorescence quantum yield of rhodamine dyes," *J. Lumin.*, vol. 27, pp. 445-462, 1982.
- [103] E. Kvam and J. Moan, "A comparison of three photosensitizers with respect to efficiency of cell inactivation, fluorescence quantum yield and DNA strand breaks," *Photochem. Photobiol.*, vol. 52, pp. 769-773, 1990.
- [104] A. F. Fercher, "Optical coherence tomography," *J. Biomedical Opt.*, vol. 1, pp. 157-173, 1996.
- [105] R. B. Buxton, *An Introduction to Functional Magnetic Resonance Imaging: Principles and Techniques*, Cambridge: Cambridge University Press, 2001.
- [106] P. M. Silverman, *Multislice Computed Tomography: Principles, Practice, and Clinical Protocols*, Lippincott Williams & Wilkins Publishers, 2002.

# Appendix A

## Calibration of stock solutions

### A.1 Stock solutions of chapters 3 and 5

Stock Intralipid-20% (Liposin II, Abbott Laboratories, North Chicago, IL) was calibrated with the added absorber technique [83]. Intralipid-20% was diluted 3:1 and separated into three 150-ml samples. Ink and water were added to each of the three samples. Samples 1, 2 and 3 received 0, 250 and 500  $\mu$ l of stock India ink, respectively, and 500, 250 and 0  $\mu$ l of water (final  $\mu$  of approximately 0.001, 0.1 and 0.2  $\text{cm}^{-1}$ ). To characterize the stock India ink (No. 4415, Higgs, Lewisburg, TN), stock ink was diluted 40:1 into a 2-ml cuvette (1 cm pathlength) and the absorbance was measured with a spectrophotometer (8452A, Hewlett-Packard, Palo Alto, CA). An absorption coefficient ( $\mu_a$ ) of 58  $\text{cm}^{-1}$  at 630 nm was determined from this measurement. Measurements of light transport as a function of source/detector separation were taken with two 400-  $\mu$ -dia. optical fibers (FT400ET, 3M-Thorlabs, Newton, NJ) immersed 1 cm deep in the solutions (dimensions: 6-cm diameter by 5-cm height). A tungsten-halogen white lamp (LS-1, Ocean Optics, Inc., Dunedin, FL) connected to one of the optical fibers was used as the light source. The detector, connected to the other fiber, was a spectrometer (S2000, Ocean Optics, Inc., Dunedin, FL). Measurements in the visible/NIR range were taken for fiber separations of 1.75, 2.75, 3.75, 4.75 and 5.75 mm in all samples. Each set of data points (5 fiber separation x 3 samples per wavelength) was fitted with a minimum square fitting routine to the solution of the steady-state diffusion equation<sup>25</sup> for an infinite

medium. The two fitting parameters were the Intralipid reduced scattering coefficient ( $\mu_s'$ ) and the Intralipid absorption coefficient ( $\mu_a$ ). Values of  $0.01 \text{ cm}^{-1}$  and  $200 \text{ cm}^{-1}$  at 630nm were determined for the Intralipid-20% absorption and reduced scattering coefficients, respectively.

## A.2 Stock solutions of chapter 4 and 6

The optical properties of the samples were determined by added-absorber spatially resolved steady-state diffuse reflectance measurements [83]. For chapter 4 samples had 1.03  $\mu\text{m}$  diameter latex microspheres (5100B, Duke Scientific, Palo Alto, CA) at 8% concentration, no added absorber and low concentrations of added-absorber (yielding absorption coefficients of 0.1, 0.3 and  $0.7 \text{ cm}^{-1}$  at 630 nm). For chapter 6 samples had 10 ml of white paint (Behr ultra pure white No. 8050, Behr Process Corporation, Santa Clara, CA) dissolved in 590 ml of 90% ethanol, no added absorber and low concentrations of added-absorber (yielding absorption coefficients 0.1, 0.3 and  $0.6 \text{ cm}^{-1}$  at 630 nm). The absorber was India ink (No. 4414, Higgs, Lewisburg, TN). Two 400-  $\mu\text{m}$ -diameter optical fibers (FT400ET, Thorlabs, Newton, NJ) polished flat at both ends were inserted vertically side by side within the liquid samples to a depth of approximately half of its height (1.5 cm deep). The fiber faces were carefully aligned to the same depth and the fibers were pointing to the bottom of the container. One fiber was held fixed in the sample and was connected at to a tungsten-halogen white lamp (LS-1, Ocean Optics, Inc., Dunedin, FL). The other fiber was held by a translation stage and connected to a diode array spectrophotometer (S2000, Ocean Optics, Inc., Dunedin, FL). The initial fiber separation was measured with a caliper (2.0 mm). The diffuse reflectance was measured at the initial fiber separation and for increasing fiber separations in 4 radial steps increments of 1.0 mm. The expected range of reduced scattering coefficients was determined by Mie scattering theory [38] for the microspheres and vary from approximately 20 down to  $10 \text{ cm}^{-1}$  across the visible spectrum of light (empty circles in Fig. A.1). Samples were assumed to be a homogeneous and infinite. Each set of 20 spectra (5 fiber separations x 4 samples (no ink, and 3 increments in ink)) was fitted with

a minimum square fitting routine to the solution of the steady-state diffusion equation [17] for an infinite medium. The sample with no added absorber had an absorption coefficient composed of just the baseline microspheres and water absorption coefficients ( $\mu_a^0$ ). The added absorber samples were assumed to have absorption coefficients composed of the  $\mu_a^0$  plus the added titrated ink absorption. All 4 samples were assumed to have the same reduced scattering coefficient ( $\mu_s'$ ). The two fitting parameters were the reduced scattering coefficient and the baseline absorption coefficient for the original solution without ink. Values of  $0.01 \text{ cm}^{-1}$  and  $20 \text{ cm}^{-1}$  at  $630 \text{ nm}$  were determined for the absorption and reduced scattering coefficients, respectively. Results are shown in Fig. A.1 along with the absorption coefficient of water (dashed line) and the absorption coefficient of the smallest aliquot of ink for comparison.

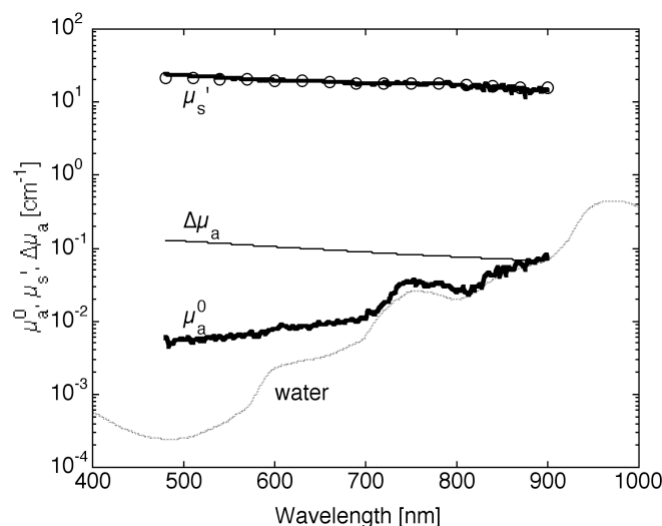


**Fig. A.1** – Optical property spectra determined for the  $1.03 \mu\text{m}$  diameter microspheres solution at a concentration of 8%. Absorption coefficients of water (dashed line) and the lowest ink aliquot are shown for comparison. Empty circles represent the reduced scattering coefficients determined by Mie theory for this sphere diameter.

## Appendix B

### Matlab code to determine coefficients $C_1$ , $C_2$ and $L_1$

```

% master.m

% Determine forward transport for acrylamide matrix

clear
close all

%%%%%%%%
% Set wavelength range
%%

nm = [485:925]';

%%%%%%%%%%
load expdatawave5                % --> testT a s nm, testT is an 8x8xlength(nm) data matrix
                                  %                already in a musp, mua grid. Parameters
                                  %                a and s are the grid for mua and musp

%%%%%%%%%%
% redefine mua
mua(1:10)      = [0.01:0.01:0.1]';
mua(11:65)    = linspace(.11,8,55)';
mua(66:80)    = linspace(8.1461,15,15)';
%%%%%%%%%%
Na = length(a);
Ns = length(s);

figure(1);clf                    % plot 8x8 data for 630nm (I = 147)
imagesc(s,a,log10(testT(:, :, 147)))
colorbar
set(gca, 'fontsize',16)
xlabel('μ_s [cm^-^1]', 'fontsize', 16)
ylabel('μ_a [cm^-^1]', 'fontsize', 16)
%title('log10(mT)')
axis xy

figure(10); clf
y = testT(11, :, 147);

```



```

figure(1);clf
imagesc(s,a,log10(testT(:,1)))
colorbar
set(gca, 'fontsize',16)
xlabel('μ_s [cm^-^1]', 'fontsize', 16)
ylabel('μ_a [cm^-^1]', 'fontsize', 16)
%title('log10(mT)')
axis xy

Ta = zeros(Na,1);
for l = 147:152%:step:N
for i = 1:Ns
    k = 0;
    Ta = testT(:,i,l);
    clear TTa MMA
    TTa = 0;
    MMA = 0;
    for j = 1:Na
        if Ta(j) ~= 0
            k = k+1;
            TTa(k) = Ta(j);
            MMA(k) = a(j);
        end
    end
end

%figure(3); clf
%semilogy(MMa, TTa, ['o' sym(i)])
%hold on
%drawnow
if 1
flag = 0;
if max(MMa) > 4.0
    flag = flag+1;
    const1 = 2;
    rate1 = 1;
    const2 = .01;
    %rate2 = 1;

    cnt = 0;
    data = TTa;
    passmua = MMA;
    if flag == 1
        start = [const1 rate1 const2];
    else
        start = result;
    end
    result = fmins('fitExpmaa1', start, options, [], data);
    resultsExpmaa1(i,:) = result;
else
    resultsExpmaa1(i,:) = [0 0 0];
end
end

```

```

        end
        %figure(3)
        %text(4,0.5, sprintf('s = %4.2f', s(i)));
%       set(gca, 'fontsize', 16)
%       text(4, 5e-4, '\mu_a [cm^-^1]', 'fontsize', 16)
%       ylabel('M [a.u.]')
%       testT(:,i,l) = resultsExpmaa1(i,1)*exp(-mua*resultsExpmaa1(i,2))+resultsExpmaa1(i,3);
%       pause % SLJ
    end

%%%%%%%%% Exp
C1(:,l) = resultsExpmaa1(:,1);
L1(:,l) = resultsExpmaa1(:,2);
C2(:,l) = resultsExpmaa1(:,3);
%L2 = resultsExpmaa(:,4);
end
testT(isnan(testT)) = 0;

figure(4);clf
imagesc(s,mua,log10(testT(:,:,147)))
colorbar
xlabel('\mu_s" [cm^-^1]')
ylabel('\mu_a [cm^-^1]')
% title('log_1_0(M)')
axis xy

figure(3)
set(gca, 'fontsize', 16)
xlabel('\mu_a [cm^-^1]')
ylabel('M [a.u.]')
text(6, 0.08, 'C_1 exp(-\mu_a L_1) + C_2', 'fontsize', 16)
text(6, 0.001, 'C_1 exp(-\mu_a L_1)', 'fontsize', 16)
% figure(5);clf
% imagesc(s,mua,log10(testT(:,:,length(nm))))
% colorbar
% xlabel('musp')
% ylabel('mua')
% title('log10(mT)')
% axis xy

%%%%%%%%%%%%%%
% Find polynomial coefficients and smooth coefficients for C1, C2 and L1 to eliminate
%%%%%%%%%%
warning off
for k = 147%:N % wavelength
    figure(6); clf
    semilogy(s, C1(:,k), 'ro')
    hold on
    semilogy(s, L1(:,k), 'gs')
    semilogy(s, C2(:,k), 'bd')
    hold on

```

```

n = C1(:,k);
fitC1(k,:) = polyfit(s(n>1e-3), n(n>1e-3), 4);
newC1(:,k) = polyval(fitC1(k,:), s);
plot(s, newC1(:,k), 'k-')

%%%%% C2
n = C2(:,k);

if k < N-5
    m = mean(C2(:,k:k+5)');
else
    m = mean(C2(:,k-5:k)');
end

fitC2(k,:) = polyfit(s(n<1.3*m & n > .7*m), n(n<1.3*m & n > .7*m), 15);
newC2(:,k) = polyval(fitC2(k,:), s);
plot(s, newC2(:,k), 'k-')
% plot(s, m, 'm')

n1 = L1(:,k);
fitL1(k,:) = polyfit(s(n<1.3*m & n > .7*m), n1(n<1.3*m & n > .7*m), 15);
newL1(:,k) = polyval(fitL1(k,:), s);

if k < N-5
    m1 = mean(L1(:,k:k+5)');
else
    m1 = mean(L1(:,k-5:k)');
end
plot(s, newL1(:,k), 'k-')
% plot(s, m1, 'c')

set(gca, 'fontsize', 16)
xlabel('μ_s" [cm^-^1]')
ylabel('Coefficients')
axis([0 35 5e-3 3])
drawnow
minmusp(1,k) = min(s(C1(:,k)>1e-3));
maxmusp(1,k) = max(s(C1(:,k)>1e-3));
% pause
end
warning on

mua2 = [0.05:0.05:10]';
for i = 1:length(s)
    if s(i) > minmusp(1,147) & s(i) < maxmusp(1,147)
        map(:,i) = newC1(i,147)*exp(-mua2*newL1(i,147))+newC2(i,147);
    else
        map(:,i) = zeros(size(mua2));
    end
end

end

```

```

figure(7);clf
imagesc(s,mua2,log10(map(:,:)))
colorbar
xlabel('μ_s [cm^-^1]')
ylabel('μ_a [cm^-^1]')
% title('log_1_0(M)')
axis xy
% save mapcoeff nm s mua C1 L1 C2 newC1 newL1 newC2 minmusp maxmusp

%%%%%%%%%%%%%%
%%%%%%%%%%%%%%
%%%%%%%%%%%%%%function err = fitExpmue1(start, y)

global passmue cnt

cnt = cnt+1;

const1 = start(1);
rate1 = start(2);
const2 = start(3);
%rate2 = start(4);

x = passmue;
py = const1*exp(-x*rate1)+const2;

err = sum(((py-y)./y).^2);

if const1<0; err = err*10;end
if rate1 <0; err = err*10;end
if const2<0; err = err*10;end

if 1
if rem(cnt,50) == 0
    figure(3);clf
    semilogy(x,y, 'o')
    hold on

    xx = [0.05:0.05:10];
    pyy = const1*exp(-xx*rate1)+const2;
    plot(xx, pyy, 'k-')

    % SLJ
    pyy = y - const2;
    plot(x, pyy, 'rd')
    pyy = const1*exp(-xx*rate1); % slow
    plot(xx, pyy, 'r-')
%
    pause
    drawnow
end
end

```

**Appendix C**  
**Study consent form**



9205 SW Barnes Rd.  
Portland, OR 97225

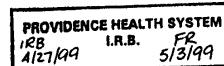
(503) 216-2109  
Fax: (503) 216-2422

Director  
Kenton W. Gregory, M.D.

### Informed Consent for Research Study

Title: Fluorescence, Reflectance and Photoacoustic Imaging in Photodynamic Therapy (PDT) with Porfimer Sodium (99-42)

Principal Investigator: Steven Jacques, PhD  
Co-Investigators: Paulo Bargo, MS  
Teresa Goodell, RN, MSN



#### Background and Purpose

You have been invited to take part in this research study because you are going to have a photodynamic therapy (PDT) procedure. This study will test two investigational optical fibers (probes); the investigational fibers are not approved by the Food & Drug Administration (FDA). The PDT treatment and procedure are approved by the FDA.

The new fiber will try to measure the amount of Photofrin (the drug used in PDT) that is in your tissues and how deeply the PDT treatment penetrated into your tissues. There is reason to believe that these measurements might allow for more accurate PDT treatment in the future. These measurements are not currently done during routine PDT procedures. The measurements taken for this study will not affect your PDT procedure – the measurements will be collected and analyzed to see if standards can be developed for use in the future.

The investigational fibers are very similar to commercially available fibers that are used in the PDT procedure to deliver the laser light to the tissues.

The purposes of this study are to 1) test the effectiveness of the fibers in measuring Photofrin concentration in both healthy and diseased tissues and depth of treatment in diseased tissues 2) test the investigational fibers for safety; and 3) collect information (measurements.)

Approximately 40 patients will take part in this study.



OREGON GRADUATE INSTITUTE  
— of —  
SCIENCE & TECHNOLOGY



#### Measurement Procedure

The measurements involve placing two different optical fibers on the diseased area and surrounding healthy tissue to take measurements during your PDT procedure. The measurement procedures will take from 1 minute to as long as 30 minutes, but most measurements are expected to take 5 minutes or less. The measurements may be repeated if you have followup endoscopies for PDT.

The measurements are done by shining cool laser light down the optical fiber. You will not feel the laser light used to take the measurements. This type of measurement does not heat the tissue or cause discomfort. It may prolong your treatment by several minutes. Aside from the optical measurements, the PDT treatment will proceed as described in the information you were given on PDT.

Patient's Initials/Date \_\_\_\_\_

### **Potential Risks and Side Effects**

The measurements may prolong the endoscopy or bronchoscopy that is a normal part of PDT. The measurements are expected to take about 5 minutes. If the measurements take more than 5 to 10 minutes, it is possible that you will require medication for a longer time to help you remain comfortable during the procedure. In any case, you will not receive more than the safe recommended total amount of medication.

There is a very small risk that the optical fibers used to take the measurements could break, causing a hole (puncture) or bleeding. The risk of breakage is no greater with these fibers than with standard FDA-approved optical fibers. All fibers are coated with a substance that keeps them from falling apart in case of a break in the fiber. Pressure from the optical fiber against the tissue might cause bleeding. Any bleeding is expected to be minor, and not require any treatment. If serious bleeding occurs, hospitalization or a blood transfusion may be necessary. This risk is no greater than the risk of bleeding usually encountered with routine endoscopy or bronchoscopy.

### **General Information**

Your taking part in this study is voluntary. You may refuse to take part or even decide to stop taking part without affecting your present PDT treatment or future medical care. Your taking part in this study may be stopped without your consent if, in your doctor's judgement, this is in your best interest or if the study is stopped.

### **Benefits and Alternatives**

You may choose not to take part in this study. You will not benefit directly from taking part in this study. This study will collect information that may lead to more effective PDT treatments for others in the future.

### **Confidentiality**

Your confidentiality will be protected to the extent permitted by law. The study investigators, representatives of the FDA or the Providence Health System Institutional Review Board (IRB) may review your medical records; however, they are obligated to keep the information confidential. Your name will not be revealed should the results of this study be published. However, complete confidentiality cannot be guaranteed.

### **Costs and Compensation**

You are responsible for and must pay the costs of your routine medical care, the PDT treatment, the drug Photofrin® and any other medications you receive. However, these costs may be covered, at least in part, by medical insurers or Medicare. You will not be paid for taking part in this study. You will not be charged for the investigational fibers used to take measurements.

### **Liability**

Should you suffer any injury as a result of taking part in this research study, all of

**Patient's Initials/Date** \_\_\_\_\_

the necessary medical facilities are available for treatment, insofar as is reasonably possible. Providence Health System is not the sponsoring agency of this research project and will not assume financial responsibility for such treatment, or provide financial compensation for such injury. You are responsible for the costs of medical care for injury resulting from treatment in this study; however these costs may be covered, at least in part, by most insurance companies or Medicare.

#### **New Information**

If new scientific developments occur or if your doctor feels that taking part in this study is no longer in your best interest, you will be told and you will be removed from the study.

#### **Questions**

Any questions I have about this research study have been or will be answered by Dr. Steven L. Jacques at (503) 216-4092 or Teresa T. Goodell, RN, - Study Coordinator - at (503) 216-2040. Any questions I have concerning my rights as a research subject or whom to contact in the event of a research related injury will be answered by the Providence Health System Institutional Review Board at (503) 215-6512.

#### **Patient's Consent**

I have been offered the chance to ask questions about this study. I have read this consent form and my questions have been answered to my satisfaction.

My signature below means that I freely agree to take part in this research study and that the conditions stated in this consent form are acceptable to me. I will receive a copy of this signed consent form.

Patient's Signature \_\_\_\_\_

Patient's Printed Name \_\_\_\_\_

Date \_\_\_\_\_

Physician's Signature \_\_\_\_\_

Physician's Printed Name \_\_\_\_\_

Date \_\_\_\_\_

Signature of Witness \_\_\_\_\_

Printed Name of Witness \_\_\_\_\_

Date \_\_\_\_\_

Relationship to Patient \_\_\_\_\_

**Patient's Initials/Date** \_\_\_\_\_